Superlattices and Quantum Spin Hall States in Graphene and Hexagonal Boron Nitride Heterostructures

by

Javier Daniel Sanchez-Yamagishi

Submitted to the Department of Physics
in partial fulfillment of the requirements for the degree of

Doctor of Philosophy
in Physics
at the Massachusetts Institute of Technology

February 2015

Signature of Author: _____

Javier Daniel Sanchez-Yamagishi
Department of Physics
January 29th, 2015

Certified by: _____

Pablo Jarillo-Herrero
Professor of Physics
Thesis Supervisor

Accepted by: _____

Krishna Rajagopal
Professor of Physics
Associate Department Head for Education

Superlattices and Quantum Spin Hall States in Graphene and Hexagonal Boron Nitride Heterostructures

by Javier Daniel Sanchez-Yamagishi

Submitted to the Department of Physics
in partial fulfillment of the requirements for the degree of
Doctor of Philosophy
in Physics

Abstract

Two-dimensional (2d) layered materials, such as graphene and hexagonal boron nitride (hBN), can be isolated separately and then stacked together to form heterostructures with crystalline interfaces between the layers. In this thesis, I present a series of experiments which explore the quantum transport of electrons in heterostructures made from graphene and hBN. Depending on the relative alignment, or "twist", between the layers, a crystal of hBN can be either a non-perturbing substrate for the graphene, or a method to induce a band gap and superlattice potential for the graphene electrons. In the case of two stacked graphene layers, a relative twist can electronically decouple the layers from each other, despite a tiny 0.34nm interlayer spacing.

This twist-dependent physics can be used to realize new electronic states in graphene, especially in the presence of strong magnetic fields and electron-electron interactions. By applying a strong tilted magnetic field to graphene which is decoupled from its hBN substrate, we are able to realize a quantum spin Hall state and measure its electronic properties. An analogous bilayer quantum spin Hall state is also realized in twisted bilayer graphene, by taking advantage of the twist decoupling between the layers and the effects of electron-electron interactions. A different set of experiments explores the competition of a magnetic field with the effects of the superlattice potential which arises when a graphene sheet is nearly aligned to its hBN substrates. The large superlattice potential allows us to study graphene transport in Hofstadter's butterfly—the fractal spectrum for electrons under the simultaneous influence of a lattice and a magnetic field.

Thesis Supervisor: Pablo Jarillo-Herrero
Title: Professor of Physics

Acknowledgments

Over the last six years, I have been lucky to have an immense amount of support and help to complete this thesis work. I believe science to very much be a human endeavor; and thanks to many humans, my time here at MIT has been formative, productive, and fun.

I first want to acknowledge my advisor, Pablo Jarillo-Herrero, for being a true mentor throughout my PhD work, starting from the day he called me to tell me I was accepted to MIT. Pablo's energy and enthusiasm for science has been both a great inspiration and an asset. He has always supported me in taking an independent lead in my research, yet at the same time offered key guidance that has kept me from going astray. I also appreciate the extra effort he takes towards his students' professional development, whether it be helping prepare for talks, reflecting on PhD progress, or planning for a future career. I am very grateful to have had him as an advisor.

All of the experiments in this thesis were team projects, giving me the opportunity to work with many great people who I would like to acknowledge. My first teammate was Leonardo Campos, who was also my first close friend at MIT. Leonardo taught me how to make graphene and, just as importantly, how to enjoy life in the Brazilian way. For both, I am forever indebted to him. Next was Thiti Taychatanapat, who taught me how to measure (carefully). With him, I measured the quantum Hall effect for the first time and began my explorations in the world of twisted bilayer graphene. In the middle of my PhD, I had the great fortunate to team up with two amazing postdocs, Andrea Young and Benjamin Hunt, to work on the quantum spin Hall and graphene-hBN superlattice projects. Working so closely together with them was one of the most intensely fun and intellectually stimulating parts of my time here at MIT. I thank them both for being great mentors and friends. In recent years, I've had a great time working with a new graduate student, Jason Luo, as we've made constant progress trying out new ideas and exploring the world of twisted bilayer graphene together. His work was instrumental in the last set of twisted bilayer experiments, which is presented at the end of this thesis.

The collaboration most important to this thesis work comes from our Japanese hBN growers, Takashi Taniguchi and Kenji Watanabe at Japan NIMS. Without their hBN crystals, not a single one of the experiments in this thesis would have been possible.

Other collaborators essential to this thesis work are Brian Leroy, Matthew Yankowitz and Jiamen Xue at the U of Arizona STM lab, who revealed what the atoms of our graphene devices were up to. One of the great benefits of being at MIT is getting to collaborate with their undergraduates. I've had a wonderful time working with some very enthusiastic and intelligent students, including Ken Van Tilburg, Danny Bulmash and Sang Hyun Choi. I thank them all for the contributions they have made to my thesis work and also for being my test subjects in learning how to be a teacher. I also acknowledge my other thesis committee members, Leonid Levitov and Liang Fu, who have been a constant source of ideas and feedback on new data over the course of my PhD.

I want to thank the members of the Jarillo-Herrero group who I've worked side-by-side with over the years. These include Joel Wang, Britt Baugher, Michele Zaffalon, Hadar Steinberg, Tchefor Ndukum, Nathan Gabor, Valla Fatemi, Qiong Ma and Hugh Churchill. I have learned so much from all of these people, and I appreciate them both their scientific comradery and friendship. I also thank the members of the wider building 13 and physics community for their support and friendship throughout my PhD: Allen Hsu, KiKang Kim, Mario Hofmann, Wenjing Fang, Shiahn Chen, Vitor Manfrinato, Paulo Araujo, Apratim Sahay, Robin Chisnell, Alex Frenzel, Justin Song, Evelyn Tang, Andrew Potter, Rahul Nandkishore, David Mross, and our group administrator Monica Wolf.

My time at MIT was thoroughly enriched by some great institutions and groups that I had the chance to participate in, such as the Physics Graduate Student Council, MIT Graduate Student Council, Sidney Pacific dorm, and the Thirsty Ear. I have great respect and admiration for the people I've met in these organizations; from them I have learned at least some things about how to be a leader and to make change happen. In this respect, I want to especially thank Todd Schenk, Ulric Ferner, Nan Gu, Matt Walker, Wendy Lam, Aalap Dighe, Ellan Spero, Kendall Nowocin and Matt Haberland.

It was a long path to MIT, and as long of one to make it to the end. Fortunately, I did not have to travel it alone. I want to thank my old friends Jordan and Brian, who made the trek with me from South Jersey, to New Brunswick, and then MIT (with some detours). Their success along the way has always been a constant motivation and inspiration for me throughout my PhD.

Finally, I want to thank both my family and my fiancée Lisa for their constant love and support throughout. No matter how difficult grad school could get, I knew that I had my team to back me up. I especially want to thank my parents for believing in me and giving me the tools to make it here today.

Contents

Abstract 3

Acknowledgments 4

List of Figures 11

1 Introduction & Background 29
- 1.1 Prologue . . . 29
- 1.2 Thesis introduction . . . 31
- 1.3 Graphene basics . . . 33
  - 1.3.1 Where it comes from . . . 33
  - 1.3.2 Electronic structure . . . 34
  - 1.3.3 Graphene quantum Hall effect . . . 35
  - 1.3.4 hBN, van der Waals heterostructures, and superlattices . . . 37

2 Quantum Spin Hall State in Monolayer Graphene 41
- 2.1 Introduction - graphene and topological insulators . . . 41
- 2.2 Background . . . 42
  - 2.2.1 Quantum spin Hall - two copies of the quantum Hall effect . . . 42
  - 2.2.2 Quantum spin Hall states . . . 43
  - 2.2.3 Charge neutral graphene in a strong magnetic field . . . 44
- 2.3 Experiment details . . . 46
- 2.4 Tunable symmetry breaking and helical edge transport in a graphene quantum spin Hall state . . . 46

3 Massive Dirac Fermions and Hofstadter's Butterfly in Graphene-hBN Superlattices 57
- 3.1 Introduction - superlattices and insulating states . . . 57
- 3.2 Background . . . 59
  - 3.2.1 Opening a gap. Breaking graphene's sublattice symmetry. . . . 59
  - 3.2.2 Superlattices and magnetic fields - Hofstadter's butterfly . . . 61
- 3.3 Experiment details . . . 64

3.4 Massive Dirac Fermions and Hofstadter Butterfly in a van der Waals Heterostructure . . . 66
3.5 Epilogue . . . 74

4 Edge States in Twisted Bilayer Graphene 75
4.1 Introduction - twisted bilayer graphene . . . 75
4.2 Background . . . 78
4.2.1 Twisted bilayer graphene . . . 78
4.2.2 Experimental regimes: low twist, high twist . . . 81
4.3 Experiment details . . . 82
4.3.1 Questions to answer . . . 82
4.3.2 Devices and measurements . . . 82
4.4 Quantum Hall effect, screening, and layer-polarized insulating states in twisted bilayer graphene . . . 83
4.5 Broken symmetry states and quantum spin Hall in twisted bilayer graphene 89
4.5.1 Let's realize a TwBLG quantum spin Hall state . . . 89
4.5.2 Measurements of the N=0 LL in high quality TwBLG . . . 90
4.5.3 Contact resistance, gating and QSH . . . 96
Contact resistance due to contacts . . . 97
Beating the p-n junctions and measuring a QSH state . . . 98
4.5.4 Conclusion - broken symmetries and quantum spin Hall state in TwBLG . . . 102
4.6 Final notes . . . 102
4.6.1 Unanswered questions. . . . 102
4.6.2 Future directions . . . 104

A Fabrication Details 105
A.1 Overview . . . 105
A.2 Flake transfer methods . . . 105
A.2.1 PC-based pick-up method . . . 107
A.2.2 MMA-based transfer method . . . 110
A.2.3 PVA-based transfer method . . . 111
A.3 Additional nanofabrication details . . . 112
A.3.1 Source materials . . . 112
A.3.2 Contacts . . . 112

B Additional details for graphene quantum spin Hall state experiment 115
B.1 Fabrication . . . 115
B.2 Conductance measurements . . . 115
B.3 Capacitance measurements . . . 116
B.4 Additional data . . . 116

C Additional details for graphene-hBN superlattice experiments **125**
C.1 Zero and low-field transport measurements . . . 125
C.2 Moire superlattices . . . 125
C.3 Theoretical model for Hofstadter spectrum of monolayer graphene on hBN . . . 129
C.4 Landau level spectrum . . . 130
C.5 Gap measurements . . . 133
C.5.1 Temperature dependence of conductivity at B=0 . . . 133
C.5.2 Magnetic field dependence of the gap . . . 133
C.6 Capacitance measurements . . . 134
C.6.1 Principle of measurement . . . 134
C.6.2 Additional capacitance measurements . . . 134
C.7 Extracting an upper bound on the gap $\Delta\mu$ from gate dependence of transport and capacitance . . . 135

D Additional details for twisted bilayer graphene experiments **145**
D.1 Fabrication details . . . 145
D.2 Contact geometry for TwBLG quantum Hall study . . . 145
D.3 Displacement field, density and screening . . . 146
D.4 Magnetoresistance measurement and background subtraction for TwBLG quantum Hall study . . . 148
D.5 Consistency between zero and high magnetic field measurements . . . 149

E Basic electronic theory of twisted bilayer graphene **151**
E.1 Geometry . . . 151
E.2 Continuum model . . . 153
E.3 Different families of commensurate structures . . . 156
E.4 Conclusions from basic electronic theory . . . 156

Bibliography **159**

List of Figures

1.1 Superlattices and Quantum Spin Hall States in Graphene and Hexagonal Boron Nitride Heterostructures 32

1.2 **How we make graphene. a**) Crystals of natural graphite. Large flake is approximately 2cm long. **b)** Graphite exfoliated onto a piece of tape. **c)** Flake of monolayer graphene (lightest color). Scale bar is 10um. . . 33

1.3 **Graphene electronic structure. a)** Graphene is made up of two inequivalent sublattices labeled A and B. **b)** Graphene band structure. Conduction and valence band meet at conical points. Valley quantum numbers K and K' differentiate the two inequivalent sets of Dirac cones. **c)** Fermi surfaces in K-space appear as circles centered at the corners of the first Brilloin zone. **d)** Graphene's massless Dirac dispersion. 34

1.4 **Graphene's charge density can be easily changed by the field effect. Left,** a graphene field effect device is made by forming a capacitor between a sheet of graphene and a metallic gate. The induced charge density n, will be proportional the applied gate voltage V_g and the gate capacitance C. In the original graphene studies the dielectric was the SiO_2 substrate and the gate was heavily doped Si. **Right,** conductance measurement of a graphene device as a function of applied gate voltage. The conductance reaches a minimum at the charge neutrality point. . . 35

1.5 **The quantum Hall effect in graphene.** **a)** The quantum Hall effect is a 2d electronic state where the bulk is localized and metallic edge states propagate in only one direction. **b)** Dispersion of Landau level bands as they approach the edge of the sample. When the Fermi level lies within a Landau gap, the only states that cross the Fermi level will be at the edge. **c)** Graphene Landau level spectrum as a function of magnetic field. **d)** Two probe measurement of a single quantum Hall edge state. An applied source-drain voltage will impose a transverse voltage between the two edges of the sample that will result in current flow. **e)** Two-probe conductance measurement of graphene as a function of applied gate voltage at $B = 4.0$ T. Conductance is measured by applying a small oscillating voltage and measuring the resulting current that flows through the sample. 38

1.6 **Van der Waals heterostructures are made by stacking 2d layered materials.** **Left)** Stack made of graphene and hBN flakes. **Right)** When two layers are mismatched, there will be an emergent periodic moiré pattern. In this case, the two layers have a lattice mismatch of 10%. 38

2.1 Realizing a quantum spin Hall state in monolayer graphene on hBN . . . 41

2.2 **From the quantum Hall edge states to the quantum spin Hall state.** Top cartoons are schematics of different edge state configurations. Bottom plots show dispersion of bands going from the bulk to the edge of the sample. **a)** Quantum Hall edge state. **b)** Two copies of quantum Hall edge states with opposite chiralities. Scattering between the modes can lead to the opening of a gap. **c)** The quantum spin Hall state has two edge modes with opposite chiralities and opposite spin polarizations. The crossing of the modes is protected by an extra symmetry of the system. 42

2.3 **The Zeeman effect in graphene leads to co-existing electron-like and hole-like bands with opposite spin polarizations.** 43

2.4 **Device schematic for graphene quantum spin Hall studies.** . . . 47

2.5 **Quantum spin Hall state in monolayer graphene in extreme tilted magnetic fields.** **a**, Conductance of device A at $B_\perp$=1.4T for different values of B_T. As B_T increases, the insulating state at ν=0 is gradually replaced by a high conductance state, with an accompanying inversion of the sign of $\partial G_{cnp}/\partial T$ (additional data in Figures B.3 and B.4). Inset: G_{cnp} as a function of B_T for Device A. Left to right: $B_\perp$=0.75 (cyan), 1.0, 1.4, 1.6, 2.0, 2.5, 3.0, and 4.0 T. **b,** Capacitance (dark lines) and dissipation (faded lines) of device B at $B_\perp$=2.5T. The low dissipation confirms that the measurements are in the low-frequency limit, so that the dips in capacitance can be safely interpreted as corresponding to incompressible states. **c,** Conductance under the same conditions. The absence of a detectable change in capacitance, even as the two-terminal conductance undergoes a transition from an insulating to a metallic state suggests that the conductance transition is due to the emergence of gapless edge states. 48

2.6 **Nonlocal two-terminal transport in the quantum spin Hall regime.** **a,** Schematic of four distinct two-terminal measurement topologies available in a four-terminal device. Hollow circles indicate floating contacts while filled, colored circles indicate measurement contacts. Each variation probes two parallel conductance paths between the measurement contacts with a variable number of segments on each path, indicated by black edges. **b**, Two-terminal conductance measurements of Device A for $B_\perp$=1.4T, color-coded to the four different measurement configurations. Dashed curves are taken at B_T=1.4T; solid curves are taken at B_T=34.5T (QSH regime). In the QSH regime, G_{cnp} depends strongly on the number of floating contacts (see Figure B.5 for similar data for sample C). Inset: AFM phase micrograph of Device A. Scale bar: 1 micron. **c**, G_{cnp} for eighteen different contact configurations based on cyclic permutations of the topologies shown in **a**. Data are plotted against two model fits. In a numerical simulation based on a diffusive model (black circles), the graphene flake was assumed to be a bulk conductor with the conductivity left as a fitting parameter ($\sigma = 3.25e^2/h$ for the best fit). The QSH model is Eq. 1, and has no fitting parameters. The dashed line indicates a perfect fit of data to model. Note that the measured G_{cnp} never reaches the value predicted by the QSH model, indicating either contact resistance or finite backscattering between the helical edge states. **d**, Schematic of bulk order and edge state spin texture in the fully polarized QSH regime. Arrows indicate the projection of the electron spin on a particular sublattice, with the two sublattices indicated by hollow and filled circles. The edge state wavefunctions are evenly distributed on the two sublattices and have opposite spin polarization, at least for an idealized armchair edge[107]. 50

2.7 **Symmetry-driven quantum phase transition. a** Capacitance (top) and conductance (bottom) of device A at $B_\perp$=1.1T. The central dip in capacitance does not change with B_T at any point during the transition, implying that the bulk gap does not close. **b**, Bulk spin order in the three transition regimes. The balls and arrows are schematic representations of the spin and sublattice texture of the ground state wavefunctions and do not represent individual electrons; the electron density within the ZLL at ν=0 is two electrons per cyclotron guiding center. The insets in **b** show details of the relative alignment of the electron spins on the two sublattices. At large B_T, the bulk electron spins are aligned with the field (top panel), resulting in an emergent U(1) spin-rotation symmetry in the plane perpendicular to B_T. As the total magnetic field is reduced below some critical value (with $B_\perp$ held constant), the spins on opposite sublattices cant with respect to each other while maintaining a net polarization in the direction of B_T (middle panel). This state spontaneously breaks the U(1) symmetry, rendering local rotations of the electron spins energetically costly. At pure perpendicular fields (bottom panel), the valley isospin anisotropy energy overwhelms the Zeeman energy and the canting angle θ is close to 90°, defining a state with antiferromagnetic order. **c**, Low energy band structure in the three phases[107]. ϵ is the energy and x is the in-plane coordinate perpendicular to the physical edge of the sample. The intermediate CAF phase smoothly interpolates between the gapless edge states of the QSH phase (top panel) and the gapped edge of the perpendicular field phase (bottom panel) without closing the bulk gap. Colors indicate spin texture of the bands projected onto the magnetic field direction, with red corresponding to aligned, blue antialigned, and black zero net spin along the field direction. 53

2.8 **Spin textured edge states of the CAF phase. a,** Temperature dependence in the intermediate field regime for device C at $B_\perp$=5.9T and B_T=45.0T. The conductance peaks shows a metallic temperature coefficient, while the state at charge neutrality remains insulating. **b,** Nonlocal two-terminal conductance of device A at $B_\perp$=1.6T and B_T=26.1T. Color coding indicates contact geometry following the scheme in Figure 2.6a. The height of the conductance peaks depends strongly on the configuration of floating contacts, indicating their origin in the gapped, counterpropagating edge states of the CAF phase. **c,** Schematic band diagram, including spin order, of the CAF edge states. For the electron and hole bands nearest to zero energy, the canting angle inverts near the sample edge, leading to counterpropagating edge states with inverted CAF spin texture. The dashed gray line indicates the Fermi energy, ϵ_F, in the regime corresponding to one of the conductance peaks. **d**, Schematic of bulk order and edge state spin texture in the CAF regime, following the convention of Figure 2.6d. **e**, Differential conductance, dI/dV_{SD}, of device C in the QSH regime ($B_\perp$=2.7 T, B_T=45.0 T) in units of e^2/h. A constant source-drain voltage, V_{SD}, along with a 100μV, 313 Hz excitation voltage, are applied to one contact and the AC current measured through the second, grounded contact. **f**, dI/dV_{SD} of device C in the CAF regime ($B_\perp$=5.9T, B_T=45.0T) in units of e^2/h. In both **e** and **f**, a symmetry is observed upon reversing both V_{SD} and carrier polarity. . . 54

3.1 **"Hofstadter's Butterfly" Energy spectrum of a square lattice in a magnetic field.** Vertical axis is magnetic field in units of flux quanta per unit cell (0 to 1). Horizontal axis is energy with the bandwidth of a single Bloch band. 57

3.2 Insulating state and Hofstadter butterfly in graphene-hBN heterostructures 58

3.3 **Breaking graphene's sublattice symmetry results in a band gap at the Dirac point.** 60

3.4 **Graphene stacked on hBN form a moiré pattern due to their lattice mismatch.** Atomic stacking arrangement changes smoothly across the superlattice unit cell, resulting in a sign oscillation of the mass term $m(r)$. Mismatch is exaggerated to make moiré easier to see 61

3.5 **The length scale of a moiré superlattice depends sensitively on the twist angle between the graphene and hBN.** Plots shows the dependence of the wavelength of a graphene-hBN superlattice on the relative twist angle between the two crystal lattices. 62

3.6 Wannier plot of allowed gaps as a function of superlattice filling fraction n/n_0 and the flux quanta per superlattice unit cell ϕ/ϕ_0. Plotted lines are for $s = 0, \pm1, \pm2$ and $t = -10$ to 10. Black lines are $s = 0$, red lines are $s = -1$ and blue lines are $s = 1$. 63

3.7 **Device fabrication steps for a graphene-hBN superlattice sample.** A-D are optical images and E/F are AFM images of the fabrication steps for the devices. Scale of optical images is 32.5um wide **(A)** Etched graphite bar on Si/SiO_2 wafer serves as a local backgate. **(B)** After transfer of 7 nm-thick hBN flake, wrinkles in hBN are visible. **(C)** After graphene transfer (dash line depicts graphene boundary). **(D)** Final contacted and etched device (graphene strips are false colored red). **(E)** AFM image of graphene (red false color) on hBN. Large wrinkles in hBN are visible (1-80nm in height), forming a triangular structure **(F)** AFM image of final contacted and etched device. Each of the four devices are seperated from the others via a wrinkle in the graphene/hBN. 65

3.8 **Insulating states and superlattice minibands in a graphene/hBN heterostructure.** **(A)** Schematic of the moiré pattern for graphene (gray) on hBN (red and blue), for zero misalignment angle and an exaggerated lattice mismatch of $\sim 10\%$. The moiré unit cell is outlined in green. Regions of local quasi-epitaxial alignment lead to opposite signs of the sublattice asymmetry, $m(\vec{r})$, in different regions. **(B)** Low temperature (T=150 mK) conductivity near charge neutrality of four heterostructure devices (A1, A2, B1 and B2). The CNP offset V_0=37, 37, 46 and 42 mV, respectively. Left inset: Measurement schematic. Right inset: AFM image. Scale bar is 3 μm. **(C)** Resistance over a larger gate range. Finite-density resistance peaks indicate full filling of the lowest superlattice miniband in two of the four measured devices (A1 and A2) within the experimentally-accessible density range. 66

3.9 **Hofstadter butterfly.** **(A)** Two-terminal magnetoconductance of device A1 up to 45 T. **(B)** In Wannier's theory [227], energy gaps in the Hofstadter spectrum are confined to linear trajectories $\phi/\phi_0 = (n/n_0 - s)/t$, where s and t are integers denoting the superlattice miniband filling index [137] and quantized Hall conductance of the gapped state, respectively. Grey lines indicate gaps for $-4 \leq s \leq 4$, with colored overlays indicating features observed in (A). Black: gaps requiring no broken symmetry; Blue: broken-symmetry states for the central Landau fan. Red: symmetry broken states belonging to superlattice ($s \neq 0$) Landau fans. Gaps intersect at $\phi/\phi_0 = 1/q$, with q an integer (orange); $\phi = \phi_0$ at 29T. **(C)** Theoretical Hofstadter energy spectrum for the fully spin- and sublattice-split $N = 0$ Landau level [119] (more details in Appendix sec:App-Hoff-Koshino). Black points indicate regions of dense energy bands; intervening spectral gaps are color-coded to the associated two-terminal conductance $G = 2$ (red), 1 (purple) and 0 (grey) in units of e^2/h. **(D)** Conductance traces within the $N = 0$ LL at B=43T (top) and B=19 T (bottom). Shaded rectangles are color-coded to the expected two-terminal conductance from the Hofstadter model of (C). The emergence of Hofstadter minigaps, characterized by a non-monotonic sequence of quantized conductance plateaus, is evident in the 43T data, where $\phi > \phi_0$. At 19T, the quantum Hall sequence is the standard monotonic $G = |\nu|e^2/h$. Peaks between plateaus are due to diffusive transport in this wide-aspect-ratio device. 68

3.10 **Magnetocapacitance of semimetallic and insulating graphene devices.** **(A)** Capacitance of a typical semimetallic graphene device. The zero-energy Landau level forms at $\sim$ 0.15T, appearing as a local maximum at the CNP ($V_g = 34.5$ mV). **(B)** Capacitance of an insulating graphene device (B2) under similar conditions. In contrast to (A), the density of states is at a local minimum for all fields at charge neutrality ($V_g = 44$ mV). **(C)** Capacitance of device B2 at B=2.0 T and **(D)** 13.5 T. Cyclotron gaps are shaded grey ($\nu = \pm 2$ labeled) and broken-symmetry gaps are shaded green. **(E)** Fractional quantum Hall (FQH) states in the $N = 0$ LL. The incompressible features at $\nu = \pm\frac{5}{3}$ are of similar strength to the other FQH states. 70

3.11 **Energy gaps of the zero-field insulator. (A)** Conductivity of the insulator device A1 at a series of temperatures. **(B)** Arrhenius plot of σ_{CNP} for all four devices. Lines are fits to $\sigma_{CNP}(T) \propto \exp(-\Delta/2T)$, giving Δ_{A1}=321 K, Δ_{A2}=268 K, Δ_{B1}=194 K, and Δ_{B2}=189 K. **(C)** Correlation of observed band gaps with moiré wavelength λ. Circles: thermal activation gap (Figure 3.9B); error bars are estimated from the uncertainty in the range of simply-activated behavior. Triangles: width in gate voltage of insulating state. λ is extracted from the period of the Hofstadter oscillations for A1 and A2, and from STM measurements for B1 and B2. Inset: Scanning tunneling topography image of B2 (5 nm scale bar). **(D)** Schematic band structure for semimetallic graphene. **(E)** Schematic band structure for an insulating graphene-hBN heterostructure, showing the band gap and moiré minibands. 72

4.1 **A moiré emerges when twisting a graphene bilayer**. 75

4.2 **It is possible to realize a new type of quantum spin Hall state in twisted bilayer graphene.** 77

4.3 **Decoupling of layers in twisted bilayer graphene is controlled by the twist angle**. Lattice structure of twisted bilayer graphene for twist angles $\theta = 20°$ and 3° (left and right respectively). The twist angle controls the overlap of the Fermi surfaces for the bottom and top layers (blue and red circles, respectively). 78

4.4 **Twisting separates the Dirac cones coming from each layer**. Left, comparison of TwBLG band structure for zero coupling (black lines) and nonzero coupling (blue lines). Right, band structure near the K point shows two isolated Dirac cones, one coming from each layer. A van Hove singularity forms where the two cones meet and hybridize. 79

4.5 **Two different types of TwBLG devices**. All devices consist of a stack of hBN-graphene-graphene-hBN with dual top and bottom gates. **Left**, Device with graphite bottom gate, metal contacts on the top surface of the TwBLG, and a top gate overlapping with leads. **Right,** Edge-contacted device with AuPd bottom gates. Contact bottom gates lie underneath the metal-TwBLG interface. 83

4.6 Twisted bilayer graphene device structure and zero magnetic field resistance measurements. (a) Twisted bilayer graphene lattice with twist angle θ. (b) Twist angle separates the Fermi surface of each layer in K-space. (c) Schematic of a dual-gated twisted bilayer device with h-BN gate dielectric insulators. Dual-gates allow for independent control of the carrier density and displacement field D. (d) Zero-magnetic field resistance R at the charge neutrality point at different values of D. The resistance at the charge neutrality point decreases with increasing D. Peaks have been offset in density for clarity. 84

4.7 Quantum Hall effect, Landau level (LL) crossings, and screening in twisted bilayers. (a) Schematic of twisted bilayer LL spectrum. LLs are 8-fold degenerate (g=8) due to spin, valley & layer degeneracy. Displacement field D breaks layer degeneracy (g=4). (b) $1/R_{xy}$ as a function of total filling factor ν_{tot} at $B = 9$T. At $D = 0$, steps in $1/R_{xy}$ of $8e^2/h$ are observed (black line); at D/ϵ_0=−145 mV/nm, new steps of $4e^2/h$ develop. (c) Diagram of inter-layer screening. The applied field D is screened by charge imbalances Δn and by the inter-layer dielectric constant ϵ_{GG}. The total screened field E_{tot} induces an inter-layer potential difference ΔV. (d) LL energy spectra of upper and lower graphene layers (red and blue lines respectively) as a function of inter-layer potential difference ΔV. LL crossings are indicated by black dots. $N_{U(L)}$ is the LL index of the upper (lower) layer. (e) Simulated density of states for twisted bilayer as a function of ν_{tot} and ΔV. (f) Measured longitudinal resistance R'_{xx} with background subtracted, as a function of D and ν_{tot} at $B = 4$T. Peaks in R'_{xx} cross as a function of D, indicating the crossing of LLs. Black dots are theoretical fits to the LL crossings, from which the interlayer capacitance is extracted. 85

4.8 Insulating states in twisted bilayer at $\nu_{tot} = 0$. (a) Longitudinal resistivity ρ_{xx} as a function of D and ν_{tot} at B=9T. At $\nu_{tot} = 0$, two insulating regimes are observed, one at $D = 0$ and another at high D, with a low ρ_{xx} region separating them. (b) Temperature dependence at B=9T and $\nu_{tot} = 0$ of ρ_{xx} vs D shows non-metallic behavior. Temperature increases going from the top light blue curve to bottom red curve as 0.3, 1, 4, 8, 10, and 12K, respectively. (c) Magnetic field dependence of $\nu_{tot} = 0$ insulating states. Resistivity double minima approach each other with slope 7.5 mV/nmT (dashed red lines). Both insulating states disappear at low B. (d) Schematic of $\nu_{tot} = 0$ edge states at nonzero ΔV when D is applied. The zeroth LLs are split apart, resulting in counter-propagating edge states in the absence of interactions (intersecting solid lines). The insulating state at high D indicates inter-layer coupling between these edge states, which may open a gap at the edge (dashed lines). 87

4.9 **Broken symmetry states in TwBLG.** 2-probe conductance colorplots of a dual-gated twisted bilayer graphene device (called "Portal") as a function of topgate voltage (TG) and backgate voltage (BG). **a**) Dashed lines indicate $\nu_{tot} = \pm 4$ plateaus which frame the zero total density line. **b)** Zoom-in on the TwBLG zeroth Landau level. A complex sequence of conductance plateaus are observed due to the broken spin-valley-layer degeneracy in the zeroth Landau level due to electron-electron interaction effects and the applied electric field. 91

4.10 **Measurement of broken symmetry plateau sequence. a)** 2-probe conductance map of "Portal" as a function of symmetric and antisymmetric gate voltages. **b)** Same dataset with contact resistance removed by fitting to $\nu_{tot} = \pm 4$ plateaus. Circled numbers indicate value of plateau in units of e^2/h. **c)** Line cuts through $\nu_{tot} = \pm 4$ plateaus showing BG dependence of contact resistance. **d)** Symmetric voltage line cuts through data in (b) show conductance plateaus at all integer values from -4 to +4. 93

4.11 **Schematic conductance map for TwBLG with broken symmetry states.** Numbers indicate the filling factor on layers one and two as ν_1, ν_2. 94

4.12 **Electron-hole bilayer edge states can be protected. Left,** Raw conductance near the zero-density line. Black to red lines correspond to cuts near $\nu_{tot} = 0$ where $TG + c_{BT}BG$=-25mV to +25mV. Bilayer cartoons show hypothesized edge states for each of the conductance regimes. **Right,** comparison of edge configurations for (2,-2) and (1,-1) states. The (2,-2) has the full spin degeneracy; and backscattering via interlayer tunneling is not prevented. For the (1,-1) state, the opposite spin polarizations of each layer prevents backscattering via interlayer tunneling. . . 94

4.13 **The protected electron-hole bilayer states onset near 5T. a)** Magnetic field dependence of conductance along the $\nu_{tot} = 0$ line. **b)** Conductance of the (-1,1) and (1,-1) states (blue and red lines) as a function of magnetic field. 96

4.14 **The zeroth Landau level of TwBLG looks similar for different samples.** Raw 2-probe conductance colormaps of the TwBLG zeroth Landau level in three different samples called "Portal", "Octopus" and "Buendia". For comparison, data is plotted in terms of "Density"= $C_{TG}V_{TG} + C_{BG}V_{BG}$ and "Displacement field"= $C_{TG}V_{TG} - C_{BG}V_{BG}$. . . 97

4.15 **Contact doping can introduce a gate-dependent contact resistance. a)** Graphene doping profile for negative gate voltages. Gold contacts (yellow squares) induce a local p-type doping in the graphene. **b)** Doping profile for positive gate voltages. p-n junctions are created at the graphene-gold interface. **c)** Edge state configuration for p-type graphene where the outer region has the same sign charge carriers as the inner region. **d)** When the inner region has the opposite sign charge carriers as the outer, the edge states may not be able to equilibrate across the insulating $\nu = 0$ state[9]. 99

4.16 **Contact gates can be used to control the effects of contact resistance. a)** Conductance colorplots of the zeroth Landau level for sample "Buendia" with gate control of the contact doping. P-type contacts results in clear measurements of the negative density conductance plateaus and strong suppression of the positive density plateaus. The converse is true for n-type contacts. **b)** Density line cuts for p-type (red) and n-type (blue) contacts. **c)** Cartoon of device. The primary region is defined where the topgate and backgate overlap. The contact topgates (cTG) and global backgate control the doping of the TwBLG leading up to the metal leads. 100

4.17 **Contacts of a single doping type cannot simulatenously contact well both layers of a bilayer QSH state.** 101

4.18 **Contact effects limit the conductance of the (1,-1) and (-1,1) plateaus**. **a)** Density traces for p-type contacts cutting through the (1,-1) state (blue) and the (-1,1) state (black). The conductance remains pinned to $1e^2/h$ when transitioning from the (-1,0) to (-1,1) state (black). **b)** Similar line cuts for n-type contacts. **c-f)** Zoom-in plots of the datasets from Figure 4.16 looking at the transitions from the $\nu_{tot} = \pm 1$ states to the (1,-1) and (-1,1) states. 101

4.19 **Simultaneous p-type and n-type contacts are the most effective in measuring the QSH state conductance.** cTG scans in different plataeu regions. (-1,0) state at (TG,BG)=(0.38,0.04); (-1,1) state at (TG,BG)=(0.75,-0.167) ; (0,1) state at (TG,BG)=(0.71,0.12) 103

A.1 **Fabrication steps for a monolayer graphene quantum spin Hall device.** The data measured from this device is presented in Figure 2.5 and 2.6. Optical images (a-c) and atomic force microscopy (AFM) phase images (d-f) **a)** An etched graphite flake serves as a local backgate electrode. **b)** After transfer of hBN and graphene flakes. **c)** Nanolithography is used to attach gold electrodes to the graphene. The next step is to etch the flake into its final shape. **d)** AFM phase image of a graphene flake (purple false color) on top of hBN on top of a graphite bar (gray false color). Bubbles and wrinkles are evident in the stack. The rectangle (dashed lines) indicates the location of the final device in a flat region of the graphene. **e)** AFM phase image of the final etched device with four contacts. Dark rectangle is etched graphene flake. Polymer residue can be observed towards the bottom of the graphene flake, this is removed in a subsequent AFM tip cleaning step. **f)** AFM image of device after tip cleaning process. 106

A.2 Micromanipulator transfer setup. Under the microscope (Bausch & Lomb Microzoom II) there is a heated stage that holds the substrate. To the right is a micromanipulator (Karl Suss) that has been modified to hold a glass slide at a controllable tilt with respect to the stage. 108
A.3 **MMA-based transfer method.** Step 110
A.4 **PVA-based transfer method. a)** Silicon chip with PVA and PMMA spun on. **b)** Tape window for supporting polymer film. **c)** With tape for depositing flake material. **d)** After suspending membrane. **e)** After placing washers and fixing with backing tape layer. **f)** Other side of window with tape backing layer. 113

B.1 **Physical parameters of measured samples**. The studied devices consisted of sequentially stacked flakes of thin graphite, h-BN, and monolayer graphene on an insulating Si wafer with 285nm of thermally-grown SiO_2. The bottom graphite layer serves as a local gate electrode as well as to screen charge inhomogeneity in the graphene. The table lists the details of the samples discussed in the Section 2.4 (Samples A, B, and C), as well as for additional samples which are presented in this appendix (Samples D-I). 117
B.2 **Images of measured devices.** False color AFM images of the devices enumerated in Table B.1. Dashed lines outline the graphene boundary. Black scale bars correspond to 1 μm. 117
B.3 **Conductance as a function of $B_\perp$, B_T, and gate voltage for samples A, B and C.** Coloring of lines from blue to red indicates increasing B_T, with $B_\perp$ as indicated at the top of each panel. 118
B.4 **G_cnp as a function of $B_\perp$ and B_T for samples A, B and E.** Correspondingly higher values of B_T are required to induce the transition for higher values of $B_\perp$. For Sample A, the curves correspond to (blue to red) $B_\perp$=0.75, 1, 1.2, 1.4, 1.6, 2, 2.5, 3, 3.5, and 4T. For Sample B, the curves correspond to (blue to red) $B_\perp$=1, 1.5, 2, 2.5, 3, and 3.5 T. For Sample E, the curves correspond to (blue to red) $B_\perp$=0.9, 1, 1.1, 1.2, 1.3, 1.4, and 1.5T. 119

B.5 **Nonlocal measurements for sample C in the QSH and CAF regime.** In Section 2.4, evidence for conduction via edge states in the QSH and CAF regimes is provided by nonlocal transport measurements in Sample A (Figures 2.6b and 2.8b). Due to conduction through counter-propagating edge states, interrupting an edge with a floating contact decreases the 2-terminal conductance much more than would be expected in a diffusive transport model. Here we provide an additional example of this behavior for sample C. **a,** Schematic of distinct 2-terminal measurement topologies with different number of floating contacts (hollow circles). **b,** QSH regime, $B_\perp$=2.7T and B_T=45T. **c,** CAF regime, $B_\perp$=5.9T and B_T=45T. Curves are color coded according to the measurement schematics, as in the main text. Due to a small gate leak in one of the contacts, these specific nonlocal measurements underestimate the conductance by a scale factor which was adjusted for by fitting the $\nu = -1$ plateau to a conductance of e^2/h. 120

B.6 **Double conductance peaks in seven different samples.** A generic feature of the intermediate regime between the insulating and metallic QSH regimes is the appearance of double conductance peaks close to $\nu = 0$. The figure shows two-terminal conductance vs. backgate voltage V_G. Purely perpendicular magnetic field only ($B_\mathrm{T} = B_\perp$, black lines) results in an insulating state at $\nu = 0$. Increasing the total magnetic field while keeping the perpendicular component constant ($B_\mathrm{T} > B_\perp$, red lines), induces a transition to the CAF with associated double conductance peak feature. Samples are ordered from left to right by descending aspect ratio. 121

B.7 **Temperature dependence of the charge-neutrality point conductivity for Sample B. a-c,** Gate sweeps for sample B at constant $B_\perp$ = 2.5T and B_T = 2.5T, 26.5T and 34.5T for a, b, and c, respectively. **d,** Conductance at the charge neutrality point as a function of temperature for the data in a, b, and c. A clear insulating dependence ($\partial G/\partial T > 0$) is observed for $B_\perp = B_\mathrm{T}$. With increased B_T, in the intermediate regime, the double conductance peaks between $\nu = 0$ and $\nu = \pm 1$ display a weakly metallic temperature dependence ($\partial G/\partial T < 0$) while G_{cnp} is very weakly insulating. In the QSH regime ($B_\mathrm{T} \gg B_\perp$), where the conduction is along edge channels, the temperature dependence at $\nu = 0$ is metallic. 121

B.8 **Schematic of the capacitance bridge-on-a-chip in tilted magnetic field.** The magnetic field points up in the schematic. Beige: sample stage, showing axis of rotation (red arrows). Purple: graphene sample mount. Blue: transistor mount with 90° bend. The HEMT is mounted on the face angled 90° from the graphene sample mount and with the plane of its 2D conduction channel perpendicular to the sample stage axis of rotation. A single wire bond connects the two mounts, from the graphite back gate to the balance point of the capacitance bridge. The transistor is gated by applying V_g to the balance point/graphite back gate through a 100 MΩ chip resistor. Combined with total capacitance of the balance point to ground (~ 3 pF), this sets the low frequency cutoff for the measurement at ~ 1 kHz. The density of electrons in the graphene sample is determined by the DC voltage difference between the graphene sample and the graphite back gate, namely by $V_s - V_g$. In the data presented in Section 2.4, this is compensated for, and all capacitance measurements are shown as a function of the graphite gate voltage relative to grounded graphene. All components shown in black are at room temperature. . . . 122

B.9 **Tilted-field magnetotransport in zero-field insulating monolayer graphene.** In a fraction of devices having the identical geometry to those presented in Section 2.4, we find that rather than a conductivity of $\sim e^2/h$ at charge neutrality these devices instead exhibit insulating behavior at the CNP at zero applied magnetic field. We ascribe this insulating behavior to the opening of a bandgap at the CNP due to the effect of an aligned hBN substrate (see Chapter 3). The top panel shows resistance of the device in zero magnetic field. This device has a resistance of 825 kΩ at the CNP in zero magnetic field and T=.3K. As with the devices described in Chapter 2, the insulating state becomes stronger in a perpendicular magnetic field. In the bottom panel, solid lines are gate sweeps at constant $B_\perp$=1, 2 and 3T and $B_\mathrm{T} = B_\perp$. Dashed lines are for the corresponding sequence of $B_\perp$=1, 2 and 3T but with B_T=45T for each. Data taken at 0.3K. Semiconducting graphene samples do not show any sign of QSH-type physics, at least up to 45T. Even for $B_\perp$=1T and B_T=45T, the conductance at the CNP increases only slightly, from 0.02 e^2/h with zero in-plane field to $0.14e^2/h$ with B_T=45T. This is understandable, as even neglecting interaction effects, closing a moiré-induced band gap of $\Delta = 10$ meV requires a Zeeman field of nearly $\Delta/(g\mu_B) \approx 85$ T. We note that in these samples, the ground state at $B_\mathrm{T} = B_\perp$ may not be an antiferromagnet. 123

C.1 **Magnetotransport measurements of insulating graphene devices.** **(A)** Conductance of device A1 as a function of gate voltage and magnetic field. **(B)** Conductance trace at $V_g = 40$ mV, showing that G_{CNP} is a monotonically decreasing function of $|B|$. **(C)** Gate sweeps at low field of the four devices, at B=100 (red), 200 (blue) and 300 mT (tan) . Well-quantized $\nu = \pm 2$ plateaus appear at $B \lesssim 100$ mT for all devices. 126

C.2 **Zero-field transport and field-effect mobility of insulating graphene devices.** Conductivity vs. gate voltage for the four devices discussed in main text. Dashed lines are low-density tangents whose slope corresponds to the field-effect mobility 127

C.3 **Additional zero-field-insulating graphene-hBN device.** Data for this (fifth) device, CTA1, are shown in black and compared with the four devices studied in the Section 3.4. The data ranges are the same as in Figure 3.8B of Chapter 3 but on a semilog scale. The CNP offset V_0=37, 37, 46 and 42 mV respectively for A1, A2, B1 and B2, as in Figure 3.8B, and V_0=32 mV for CTA1. 127

C.4 **Magnetotransport and superlattice Dirac points.** Top to bottom: devices A1, A2 and B2. 129

C.5 **Fits to Landau level crossings of Hofstadter spectrum and Hofstadter oscillations.** Magnetotransport of samples A1 (top) and A2 (bottom) plotted as a function of $1/B$. Dashed lines are a fit to the Landau level crossings with the equation $B_0/B = q$, where q is an integer and B_0 is the flux quantum per superlattice unit cell. B_0 is equal to 28.7 T and 57.0 T for samples A1 and A2 respectively. 130

C.6 **STM topography map of sample B2.** Topography map taken at a sample voltage of 0.3 V and a constant tunnel current of 100 pA. The scale bars for both images are 5 nm. 131

C.7 **Calculated Hofstadter spectrum, Hall conductivity, and Wannier diagram for the N=0 LL with fully broken spin and valley symmetry.** (A) Hofstadter butterfly spectrum calculated from a tight binding model with an additional valley and spin splitting. (B) The same data, with gaps color-coded to reflect the quantized Hall conductance. The numbers indicate the corresponding value of the Hall conductance. The dashed curves mark constant density within the energy spectrum, specifically integer multiples of n_0. (C) Wannier diagram for the N=0 Landau level. The depicted features are gaps, color coded as in (B). Gapped features follow linear trajectories [213, 217, 227]. 131

C.8 **Landau level energy spectrum for $-5 < N < -5$. (A)** LL spectrum for $m^* = 0$ as a function of magnetic field, showing the zero mode and $\sqrt{B}$ dependence of the cyclotron energies. **(B)** Splitting of the zero mode with increasing $\Delta = 2m^* v_F^2$. Black curves indicate valley degenerate LLs, while red and blue indicate sublattice polarized levels in which the valley degeneracy has been lifted. Within these calculations, which neglect the Zeeman splitting, the black levels are fourfold degenerate while the red and blue levels are twofold degenerate. **(C)** LL spectrum with $\Delta = 60$ meV showing the sublattice polarized zero mode, which does not disperse with magnetic field. 136
C.9 **Temperature dependence of conductivity from 200K to 2K.** Normalized conductivity plotted against 1/T. All samples exhibit a strong temperature dependence at high temperatures (200K to 20K) and a weaker dependence for $T < 20$K. 137
C.10 **Arrhenius fits.** Data (black symbols) and high temperature fits (red line). Measured values of Δ are presented in the legend for each sample along with the spread in gap values (in parentheses) due to uncertainty in the range of the high temperature regime. These gap values appear in Figure 3.11C. 138
C.11 **Variable-range hopping (VRH) fits.** Data (black symbols) and intermediate temperature fits (blue lines) to a VRH model $\sigma(T) \propto \exp(-\sqrt{T^*/T})$. Fits have $T^* = 1681$, 1764, 441 and 576K for samples A1, A2, B1 and B2 respectively. 139
C.12 **Dependence of Arrhenius gap on magnetic field.** Gap extracted by fitting to Arrhenius behavior from 10 K to 50 K at different magnetic fields. Gaps for all samples exhibit nonmonotonic behavior, with an apparent minimum at $B \simeq 0.25$ T (gray dashed line). 139
C.13 **Schematic of high-sensitivity capacitance measurement.** 140
C.14 **Capacitance and loss of the insulating graphene capacitor in the $N = 0$ Landau level at 13.5T** Capacitance is shown in red and loss in grey. 140

C.15 **Capacitance and loss of the semimetallic and insulating graphene-hBN capacitors. (A)** The same measurement of the capacitance of the semimetallic graphene capacitor depicted in Figure 3.10A of the main text, alongside a concurrent measurement of the loss signal. The measurement frequency was 173.5 kHz. A parasitic background capacitance C_p=2 pF was subtracted from the capacitance signal after a rotation of $\delta = -7.2°$. The scale of the capacitance color bar is twice as large as that of the loss. **(B)** The same measurement of the capacitance of the insulating graphene capacitor (device B1) depicted in Figure 3.10B, alongside a concurrent measurement of the loss signal. The measurement frequency was 56.2 kHz. A parasitic background capacitance C_p=57 fF was subtracted from the capacitance signal after a rotation of $\delta = -1.1°$. The scale of the capacitance color bar is five times as large as that of the loss. 141

C.16 **Comparison of transport and capacitance at 45 T.** Top: transport measurement. Features are similar to the measurement in Figure 3.9C, top panel (at 43T). Bottom: capacitance and loss measurement at 45 T. Measurement frequency was 48 kHz. Shaded rectangles indicate normal quantum Hall states at filling factors $\nu = 0, \pm 1$ and ± 2, as in Figure 3.9C. Colored arrows indicate bulk insulating states associated with Hofstadter minigaps in the $N = 0$ LL for $\phi/\phi_0 > 1$. 142

C.17 **Estimate of zero-field gap from chemical potential change $\Delta\mu(\Delta V)$.** Simultaneous measurement of zero-field capacitance (red) and conductivity (blue) of device B2. Over a range of gate voltage ΔV, $\Delta\mu = e\Delta V - \int (C/C_{geom}) dV$ (Equation C.14); that is, the shaded red rectangle minus the area indicated by the purple outline. Here, C_{geom}=22.2 fF is indicated by a dashed red line. Thus, $\Delta\mu = e\Delta V$ serves as an upper bound on the magnitude of the gap. 143

D.1 Optical images of twisted bilayer graphene devices before topgate fabrication. Etched graphene flakes are outlined, with the bottom graphene flake highlighted in red and the top graphene flake highlighted in blue. The inset shows the same devices after fabrication of topgate electrodes 146

D.2 **(a)** Background subtracted longitudinal resistance R'_{xx} at B=4T, as a function of the displacement field D and filling factor ν_{tot}, neglecting the graphene chemical potential. The layer degenerate crossings do no occur at $D = 0$ and the filling factors do not match the correct crossings. **(b)** Same R'_{xx}, but with D and ν_{tot} calculated to include the graphene chemical potential and the screening properties of the twisted bilayer. Layer degenerate crossings now occur at $D = 0$ and at integer multiples of filling factor 8. The plot in (b) is the same data that appears in Figure 4.7f. 147

D.3 **(a)** Measured longitudinal resistance R_{xx} as a function of V_T and V_B. **(b)** Same R_{xx} data as a function of displacement field D and total filling factor ν_{tot} with log color scale. **(c)** R_{xx} line-scans corresponding to the dashed lines in (b). **(d)** Same R_{xx} data, but with the background subtracted. Crossings visible in (d) occur in the same location as in (b). 148

E.1 Commensurate twisted bilayer graphene superlattice 152
E.2 **SE-odd and SE-even structures have different interlayer couplings**. Plots of Brillouin zones for the unrotate (red) and rotated layer (blue). Black dots are constructed by adding reciprocal superlattice vectors to a K-point in layer 2 and represent interlayer scattering processes. **Left)** In SE-odd structures, the superlattice does not couple $\boldsymbol{K}$ into $\boldsymbol{K}^\theta$. **Right)** In a SE-even structure, the sublattice couples $\boldsymbol{K}$ into $\boldsymbol{K}^\theta$. . . . 153
E.3 States in layer 1 near the $\boldsymbol{K}$ point couple to states in layer 2 with added momentum of 0,$-\boldsymbol{G_1}$, or $-\boldsymbol{G_1}-\boldsymbol{G_2}$. 155
E.4 Low energy band structure for twisted bilayer graphene. 155
E.5 Fermi velocity reduction with twist angle 156
E.6 Dependence of superlattice wavelength on twist angle. Wavelength is normalized to the value of the moiré wavelength at the same twist angle. 157

Chapter 1

Introduction & Background

1.1 Prologue

IN the field of electronic transport, we seek to understand how electrons in materials behave and move in response to an applied voltage. This movement can be chaotic; the electrons will jostle off of crystal defects, bounce from uneven edges of the sample, and move in all directions. It is not possible to follow this mess on the individual electron level. Instead, we measure the average rate of electrons that pass from one side of the sample to the other; we call this the electric *current*. Typically, the larger the applied voltage across the material, the larger the current. By taking the ratio of the two we can understand how much resistance the current flow in a material has to the applied voltage:

$$resistance = \frac{voltage}{current}.$$

This single number, the resistance, sums up the contribution of many different factors in the complex classical and quantum dynamics of electrons. As physicists, we are interested in understanding the underlying dynamics, but all we see is the aggregate behavior. Oftentimes, it can feel like listening to an orchestra where every musician is out of sync: just a lot of incoherent sounds without any sense of order. We would not be able to tell if they were playing Vivaldi, putting on the national anthem, or just performing a sound check. In the case of electrons, the underlying music we often cannot see is that of quantum mechanics, which governs the dynamics of small things. These interesting quantum effects are often obscured in a single resistance measurement.

Sometimes, though, things can be different. For example, take a single sheet of graphite and cool it down to a very low temperatures, let's say a fraction of 1 Kelvin. Then apply a magnetic field perpendicular to the plane and measure its resistance. The resistance will begin to wiggle, a tiny amount at first, then increasingly more with larger field, until suddenly it flatlines at a value of exactly

$$resistance = \frac{h}{e^2} = 25,812.81\Omega.$$

In this equation, h is Planck's constant and e is the charge of an electron. Both are fundamental constants of nature. This is the equivalent of the musicians in the orchestra

abruptly starting to play in synchronization. In an instant, there is no question that something special is happening, even if we do not know exactly what notes or instruments we are listening to. We can clearly hear that there is a fundamental order and beauty at work. The same is true for the resistance, only when the electrons are heavily constrained or forced to work together will weird quantum behavior be revealed.

The search for weird quantum behavior sometimes involves pushing experiments to extremes. In the case of this thesis, it will require low temperatures, high magnetic fields, and pristine crystal interfaces. In all cases though, the primary measurement will be simple, the value of the resistance.

1.2 Thesis introduction

In this thesis, I describe a series of interconnected experiments which explore three different themes in graphene transport. The first theme is the building of new electronic devices made by stacking 2-dimensional layered materials. The second theme explores the effects of electron-electron interactions, which can lead to unusual many-body ground states of the electron wavefunction. The last theme is the engineering of 1-dimensional edge modes, where the value of a quantum number is locked to the electron's direction. These themes come together in both the search for new quantum phenomena and the effort to engineer new types of quantum states.

All the experiments I discuss will involve electrons conducting through graphene, which is the most famous example of a 2-dimensional (2d) layered material[64]. 2d layered materials have a layered structure, with weak van der Waals-like adhesion between the layers and strong covalent bonds in-plane. These covalent bonds are so strong that graphene can be suspended in a free-standing structure despite being only one atom thick[25, 150]. Moreover, it is actually possible to peel an individual graphene sheet off a substrate and stack it onto another 2d layered material, creating an atomically perfect interface under ambient conditions[224]. Repeating the process creates a vertical heterostructure of 2d layered materials, called a van der Waals heterostructure. This thesis explores how the electronic properties of these heterostructures can depend sensitively on the coupling at the interfaces of dissimilar 2d layered materials. For example, a mismatch between the lattices of the materials will cause an superlattice structure to arise, which can strongly affect electron transport in the combined material.

Electron-electron interactions will also lead to emergent electronic behavior, as electrons can lower their mutual Coulomb repulsion energy if they develop correlations in their wavefunction. Interaction effects play an important role when the electron kinetic energy is quenched, for example by a magnetic field. This can lead to polarizations of the electron quantum numbers, leading to complicated and unpredictable behavior if there are many degrees of freedom. The experiments in this thesis explore the effects of electron-electron interactions, and also take advantage of it to build new types of 1-dimensional electronic states.

The 1-dimensional edge states of the quantum Hall effect play a central role throughout these thesis. We will see that these chiral edge states can be combined together to build unique new types of 1d electronic states, where a quantum number is tied to the direction of propagation. This work opens the door to building new quantum circuits, realized through the combination of the quantum Hall effect and electron-electron interactions in a van der Waals heterostructure.

This thesis is divided into three chapters which explore the above themes. Each of the chapters presents a different experiment. They are:

- Realization of a quantum spin Hall state in monolayer graphene. (Chapter 2)
- Observation of massive Dirac Fermions and Hofstadter's butterfly in graphene-hBN superlattices. (Chapter 3)

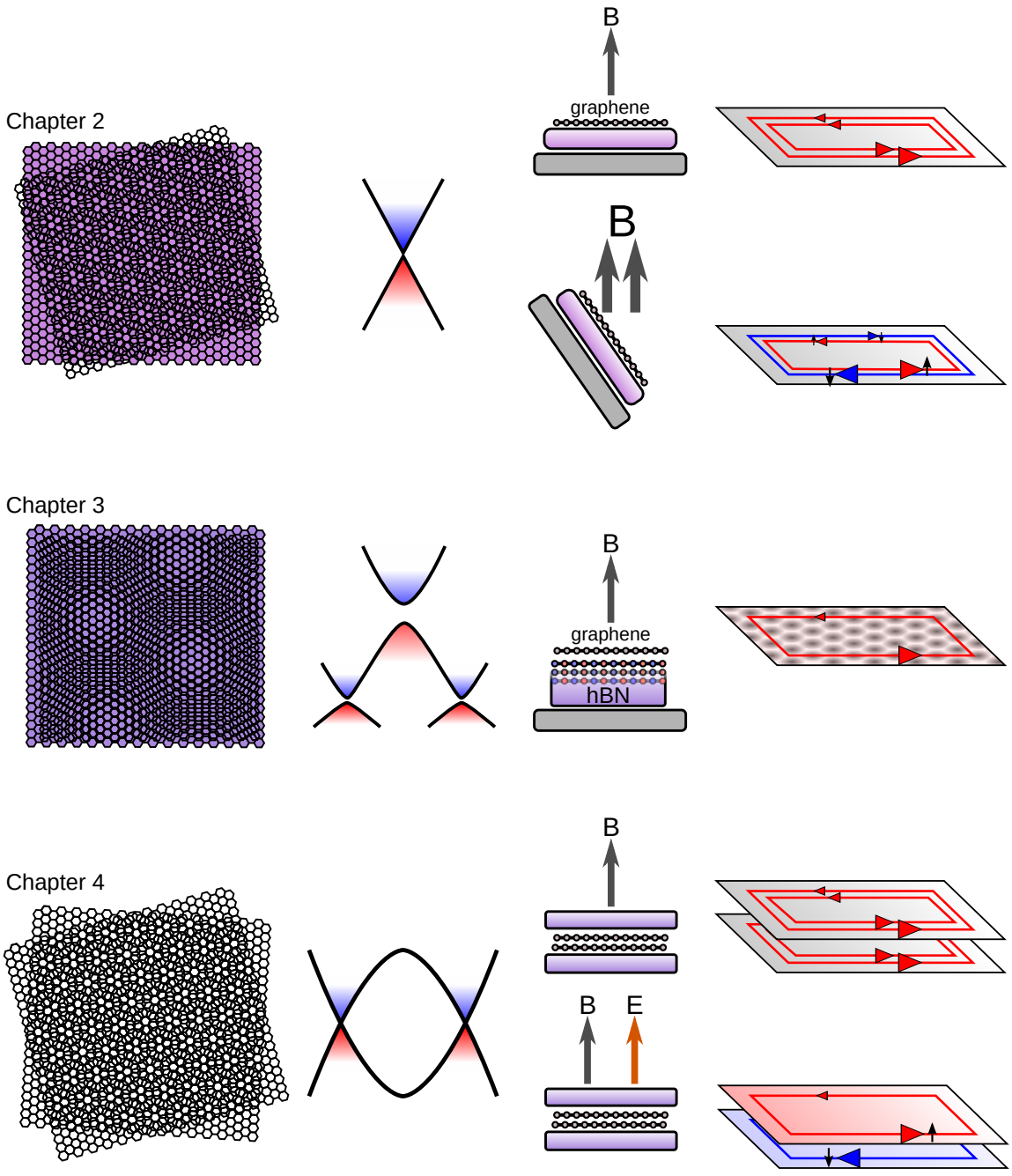

Figure 1.1. Superlattices and Quantum Spin Hall States in Graphene and Hexagonal Boron Nitride Heterostructures

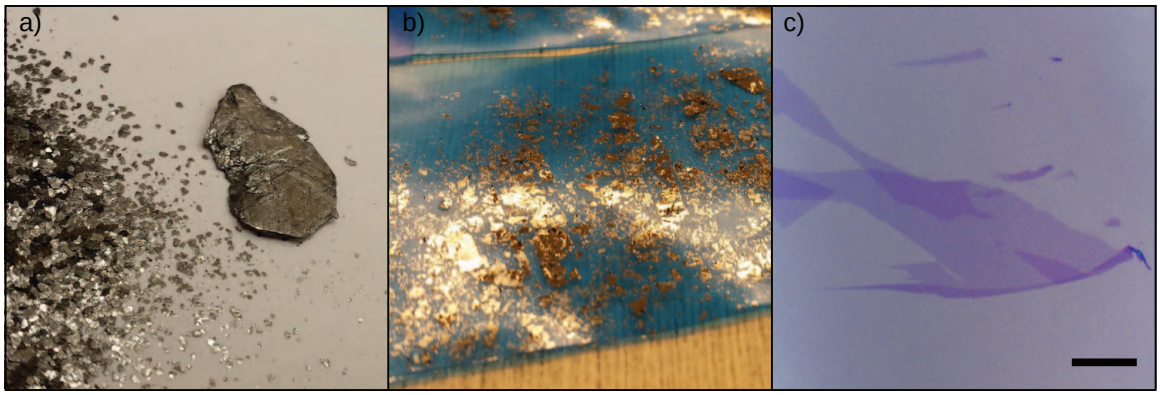

Figure 1.2. How we make graphene. **a**) Crystals of natural graphite. Large flake is approximately 2cm long. **b)** Graphite exfoliated onto a piece of tape. **c)** Flake of monolayer graphene (lightest color). Scale bar is 10um.

- Exploration of edge states in twisted bilayer graphene (Chapter 4)

The remainder of this chapter will introduce some of the basic concepts about graphene, the quantum Hall effect, and van der Waals heterostructures, which will be relevant for the rest of the thesis.

1.3 Graphene basics

1.3.1 Where it comes from

Graphene can be made by isolating single layers from graphite (Figure 1.2). All the graphene devices in this thesis were made from natural graphite that came from a mine in India. There, they were originally formed after millennia of extreme pressure and temperatures in the Earth's crust. It is unlike most of the other commonly studied materials in solid state physics, where naturally available materials are often too disordered for quantum transport studies. In many cases, years to decades of material science effort are necessary to produce material of acceptable quality. Graphene research has also been aided by the high quality of synthetic graphite, which used to be a by-product of making steel ("Kish Graphite")[165]. Recently, synthetically grown monolayers of graphene have also begun to approach the device quality made from mechanically exfoliated graphite layers[178].

To isolate the graphene, we gently rub thin flakes of graphite onto a substrate such as SiO_2 or a polymer membrane. In the process, some monolayer graphene flakes are liberated and transfer to the substrate. We then use an optical microscope to manually search for single-atom-thick flakes that are 10-50μm in lateral size. Once identified, we transfer the graphene flakes onto other substrates for further processing.

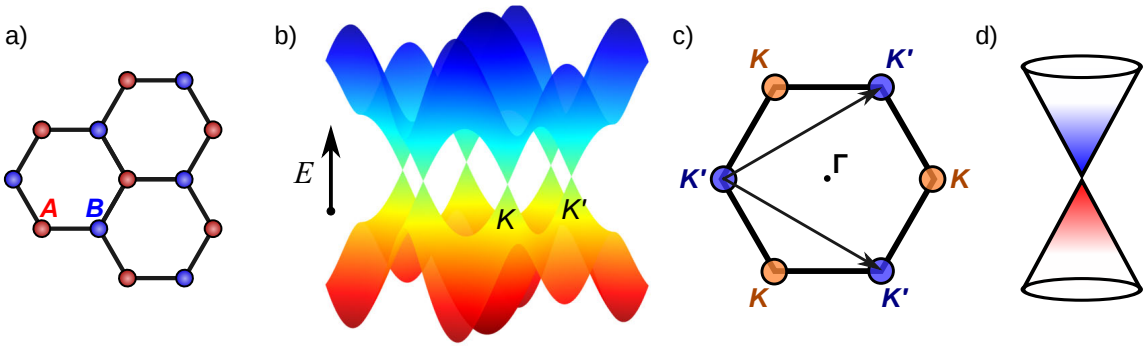

Figure 1.3. Graphene electronic structure. **a)** Graphene is made up of two inequivalent sublattices labeled A and B. **b)** Graphene band structure. Conduction and valence band meet at conical points. Valley quantum numbers K and K' differentiate the two inequivalent sets of Dirac cones. **c)** Fermi surfaces in K-space appear as circles centered at the corners of the first Brilloin zone. **d)** Graphene's massless Dirac dispersion.

■ 1.3.2 Electronic structure

Graphene is a honeycomb lattice of carbon atoms. The unit cell has a two atom basis which form two inequivalent sublattices, labeled A and B. Performing a simple tight binding calculation produces the band structure in Figure 1.3[27, 222]. The most striking feature is that the conduction and valence band touch at the corners of the Brillouin zone. Emerging from each point is a conical energy dispersion. These high symmetry points of the band structure can be divided into two inequivalent sets which are labeled as the K and K' valleys, and are called the "Dirac" points.

Expanding the bandstructure around the Dirac points results in a linear energy dispersion given by $E(k) = \pm\hbar v_F k$, where the graphene Fermi velocity, v_F, is 300x slower than the speed of light. The electron wavefunctions will be in equal superpositions of both the A and B sublattices, but with a definite phase that is tied to which Dirac point it originates from (K or K') and what its momentum is relative to that Dirac point. Since the Dirac cones originating from the K and K' points are degenerate in energy, we typically just consider a single Dirac cone where the electrons have an additional "valley" quantum number that keeps track of whether they originate from the K or K' point. This valley degeneracy will be in addition to the typical spin degeneracy, which results in a total 4-fold degenerate Dirac cone.

Graphene does not have a band gap. In this sense it is consider a semi-metal since the conduction and valence band touch at the Dirac points, which is protected by the sublattice symmetry of the graphene lattice. Breaking the sublattice symmetry will open a band gap at the Dirac points and change the dispersion from massless to massive. We will explore this idea further in Chapter 3.

Because graphene does not have a band gap, there is no energy barrier to adding

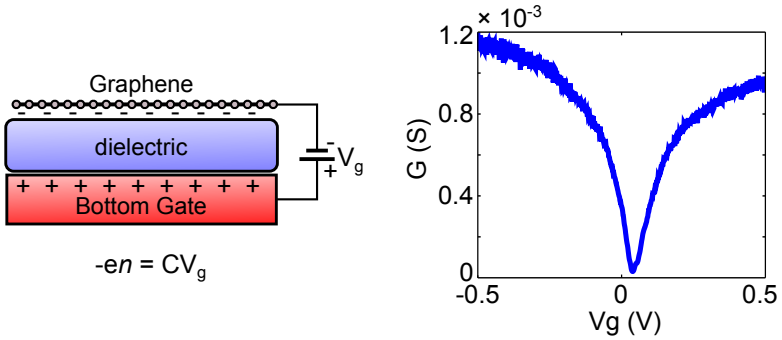

Figure 1.4. Graphene's charge density can be easily changed by the field effect. Left, a graphene field effect device is made by forming a capacitor between a sheet of graphene and a metallic gate. The induced charge density n, will be proportional the applied gate voltage V_g and the gate capacitance C. In the original graphene studies the dielectric was the SiO_2 substrate and the gate was heavily doped Si. **Right,** conductance measurement of a graphene device as a function of applied gate voltage. The conductance reaches a minimum at the charge neutrality point.

or removing charge. The charge density can be easily modulated by the electric field effect[169], which is a large factor in graphene's popularity. Field effect control is accomplished by forming a capacitor between a sheet of graphene and a gate electrode and applying a voltage between the two (see Figure 1.4, left). Charge neutral graphene has its Fermi level located at the Dirac point and will shift up or down as the charge density is changed. A typical measurement of the conductance as a function of gate voltage is shown in Figure 1.4. The conductance has a minimum at the charge neutrality point which increases rapidly as charge carriers are added to the graphene. Often the gate voltage at which the charge neutrality point is observed will be displaced from zero, due to extrinsic sources of charge doping, as well as from the work function difference between the graphene and the gate electrode[68].

■ 1.3.3 Graphene quantum Hall effect

An essential element to this thesis is the quantum Hall effect; it is the platform for most of the experiments I will discuss. The quantum Hall effect (QHE) is a topological state of matter that occurs in 2-dimensional electronic systems with broken time-reversal symmetry (typically caused by a perpendicular magnetic field)[70]. It is a bulk insulating state with a set of 1-dimensional metallic modes along the edge of the sample (Figure 1.5a). It is called a topological state of matter because its Hall conductivity is quantized in a way that only depends on the wavefunction topology[217]. As a result, it is insensitive to the specific details of the sample such as its size, shape, or disorder distribution. In all cases, the Hall conductivity of the QHE will be exactly quantized to an integer multiple of e^2/h, corresponding to the number of ballistic edge modes along the sample perimeter.

Understanding the quantum Hall effect in graphene begins by looking at the bulk energy spectrum. In a perpendicular magnetic field, the graphene electronic spectrum

will be broken up into discrete Landau levels separated by gaps. When the Fermi level is located within one of the gaps, the quantum Hall effect will be observed. The Landau levels are centered at a series of energies, E_{LL}, given by the following equation:

$$E_{LL} = \pm v_F \sqrt{2e\hbar B|N|}, \text{ with } N = 0, \pm 1, \pm 2. \tag{1.1}$$

A plot of the spectrum can be seen in Figure 1.5c. The Landau level spectrum can be understood from a simple semi-classical argument by considering the quantization of cyclotron orbits. For normal materials with a parabolic dispersion, this results in a constant energy spacing between levels given by $\hbar\omega_c$, where $\omega_c = eB/m_c$ is the cyclotron frequency and the cyclotron mass m_c is constant. In graphene, m_c instead increases linearly with the energy[1], resulting in a decreasing gap size. Each of these Landau levels are highly degenerate, holding a charge density given by the number of flux quanta that pierce the sample: $n_{LL} = B/\Phi_0$, where $\Phi_0 = h/e$ is the magnetic flux quantum. In addition, each Landau level has an extra 4-fold degeneracy due to the spin and valley symmetries. Because of graphene's unique massless Dirac dispersion, its Landau level structure departs from a typical parabolic dispersion in two important ways. One way is that there is a level at zero energy. The second way is that there is a square root dependence on the Landau energy level index N, so the first energy gap, between $N = 0$ and $N = \pm 1$, is much bigger than all the other gaps. This fact, paired with the large graphene Fermi velocity, means that the quantum Hall effect can be observed in this Landau level gap even at room temperature[170].

One way we can see how the quantum Hall effect comes about is by considering the dispersion of Landau levels at the edge of a sample[84]. The confining potential of the edge will cause the electronic states to disperse in energy up or down depending on whether they originate from electron-like or hole-like bands, respectively. These edge states carry current in a direction determined by the cross product between the confining electric field at the edge and the perpendicular magnetic field. Hence, the edge states will propagate in only one direction along the edge of the sample; we say that the edge state is *chiral*. If the Fermi level lies within a gap (Figure 1.5b), it will intersect these edge modes, each of which will form a ballistic 1-dimensional mode with a conductance e^2/h times the degeneracy of the mode[2]. The number of edge modes that cross the Fermi level will be equal to the number of filled Landau levels relative to zero energy, which is denoted by the filling factor $\nu = n/n_{LL}$, where n is the charge density. Imposing a current through the sample will cause a voltage difference between the two edges of the

[1] In graphene, the cyclotron mass is different than the effective band mass (which is infinite) or the rest mass (which is zero). Following the equation $m_c = (\hbar^2/2\pi)\partial S_k(E)/\partial E$, where $S_k = \pi k^2$ is the area in k-space of the Fermi surface, we can see that the cyclotron mass goes as $m_c = E/v_f{}^2$. Note that the sign of the cyclotron mass switches sign from the conduction to valence band. To estimate the magnetic field dependence, we relate the Fermi energy to the number of filled Landau levels using the relations $E = \hbar v_F \sqrt{\pi n}$ and $n \propto n_{LL} N$, where N is the Landau level index and $n_{LL} = B/\Phi_0$ is the charge density per Landau level. The result is that $m_c \propto \frac{1}{v_F}\sqrt{\hbar e B N}$ and the Landau level gaps will be given by $\hbar\omega_c \propto v_F\sqrt{\hbar e B/N}$. The same energy spacing relation can be derived from Equation 1.1.

[2] A nice derivation for this result can be found in section 3.1 of Reference 72

sample, resulting in a Hall voltage given by:

$$V_H = (h/\boldsymbol{\nu} e^2) I \tag{1.2}$$

where I is the current, and V_H is the Hall voltage that develops transverse to the sample. In a 2-probe measurement, the source-drain voltage drop in the quantum Hall effect will be the Hall voltage, so the measured conductance will be $G = I/V_H = (e^2/h)\boldsymbol{\nu}$. This can be understood from a ballistic 1d conductor model, where the chemical potential of a ballistic conductor is equal to the metallic contact that it leaves from. When there is an applied voltage difference between the source-drain contacts (Figure 1.5d), there will be a resulting chemical potential difference between the edge states on either side of the sample. The edge states with a higher chemical potential will carry more current, resulting in a net current given by Equation 1.2. Since each of the Landau levels in graphene are 4-fold degenerate, and zero energy occurs in the middle of the zeroth Landau level, the sequence of Hall plateaus will be given by the filling factors $\nu = \pm 2, \pm 6, \pm 10$, etc. An example of this type of measurement is presented in Figure 1.5e. Because the quantum Hall effect is tied to the charge density as well as the band structure (whether it is electron-like or hole-like), it can be used as a characterization tool to understand a new material

The quantum Hall effect will only be observed if the Landau level gap is much larger than the energy scale of temperature and disorder. In terms of temperature scale, the Landau levels gaps go as: $E_{LL} = 421\text{K}/\sqrt{B(T)}$, while the scale of disorder in clean graphene-hBN samples can be lower than 10 K. For very clean samples, it is also possible to observe the effects of electron-electron interactions (about 10x smaller energy scale than the Landau level gaps[242]), which will split the Landau level spin and valley degeneracies. This will be discussed further in next chapter.

■ 1.3.4 hBN, van der Waals heterostructures, and superlattices

Graphene fabrication technology has progressed in discrete jumps. A handful of breakthroughs have caused great improvements in device quality, or have opened the door to a wider range of device geometries. The first graphene devices were supported on SiO_2 substrates[168, 169, 250], where device qualities quickly plateaued. This was due to charge disorder caused by contamination from the fabrication process and from the the polar SiO_2 substrate itself[141, 249]. Removing the substrate by suspending the graphene[21, 48] was the next fabrication breakthrough, and still provides the highest quality graphene devices[108, 142]. For comparison, the charge disorder of graphene on a SiO2 substrate results in a energy fluctuation at the Dirac point of about 100meV [236], while the level of energy fluctuations in suspended graphene can be as low as 1meV[142]. A drawback of the suspended technique is that the device geometry is severely limited by the mechanical stability of the suspended graphene membrane. In addition, high quality samples require a current annealing process which is laborious and difficult to perform reliably.

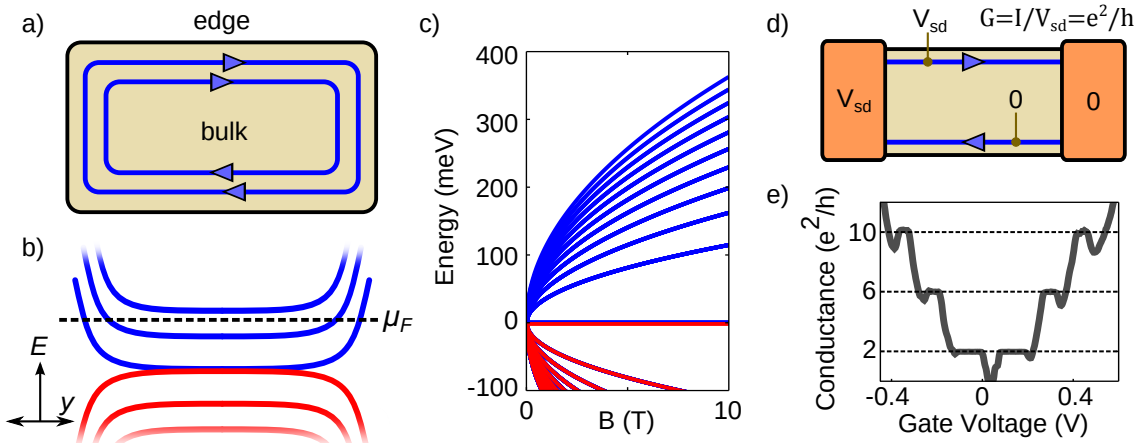

Figure 1.5. The quantum Hall effect in graphene. a) The quantum Hall effect is a 2d electronic state where the bulk is localized and metallic edge states propagate in only one direction. **b)** Dispersion of Landau level bands as they approach the edge of the sample. When the Fermi level lies within a Landau gap, the only states that cross the Fermi level will be at the edge. **c)** Graphene Landau level spectrum as a function of magnetic field. **d)** Two probe measurement of a single quantum Hall edge state. An applied source-drain voltage will impose a transverse voltage between the two edges of the sample that will result in current flow. **e)** Two-probe conductance measurement of graphene as a function of applied gate voltage at $B = 4.0$ T. Conductance is measured by applying a small oscillating voltage and measuring the resulting current that flows through the sample.

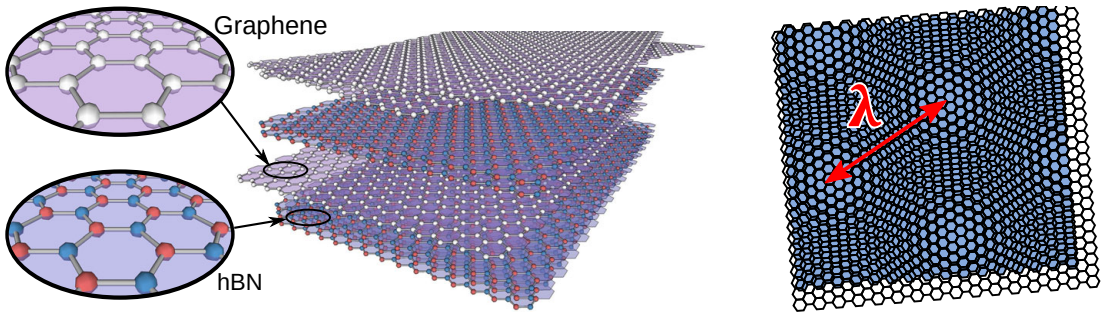

Figure 1.6. Van der Waals heterostructures are made by stacking 2d layered materials. Left) Stack made of graphene and hBN flakes. **Right)** When two layers are mismatched, there will be an emergent periodic moiré pattern. In this case, the two layers have a lattice mismatch of 10%.

For this thesis, the most important fabrication breakthrough was the discovery that hexagonal boron nitride (hBN) is a good substrate for graphene[43]. hBN is the sister material of graphene, it has the same hexagonal lattice except it is made of boron and nitrogen atoms (Figure 1.6, left). The breaking of the hexagonal sublattice symmetry causes hBN to be an insulator with a bandgap of 6 eV[228]. Most importantly, it has an inert structure without dangling bonds at the surface. Consequently, it provides a exceptionally flat electrostatic potential for supporting graphene with minimal extrinsic charge disorder. The variation of the Dirac point energy for graphene-on-hBN-on-SiO_2 is about 10meV[236], an order of magnitude improvement compared to using just SiO_2. All the experiments I will discuss in this thesis rely on clean graphene devices which are supported or completely encapsulated by hBN. The low amounts of charge disorder will enable us to observe the quantum Hall effect at very low magnetic fields and to observe the electron-electron interaction effects which are integral to this thesis.

Contained within the hBN breakthrough was another discovery of equal importance: that graphene could be transferred onto a hBN flake under ambient conditions to create an atomically perfect interface[82]. Graphene and hBN flakes in an uncontrolled environment are covered in a layer of absorbed molecules, but somehow the flakes can be forced together in such a way that these molecules are pushed out from between them. The interface somehow is able to self-clean[120]. Generalizing this concept, what we have is a new way to build material heterostructures. Instead of growing a crystalline heterostructure layer by layer in a ultra high vacuum chamber, materials can instead be grown separately, isolated into individual layers, and then recombined to form heterostructures. Since the original demonstration of a graphene-hBN heterostructure, this concept of van der Waals heterostructures has been applied to many other combinations of 2d layered materials[63].

The properties of a van der Waals heterostructure will depend not only on the properties of the constituent layers, but also on how they couple at their crystal interfaces. The nature of the interface will depend on the relative alignment between the layers, which can be controlled in the stacking technique. For example, misalignment between two layers caused by a relative twist or lattice mismatch will result in a long range moiré pattern to appear when looking at the interface (Figure 1.6). This moiré will cause a long range modulation of the interlayer couplings, which could greatly affect the electronic properties of the combined heterostructure. In Chapter 3, we will see how the relative alignment between the graphene and its hBN substrate can even introduce a bandgap at the graphene Dirac point. In the case of two stacked graphene layers, the relative twist angle between the layers will control the degree to which the monolayers hybridize. I will discuss experiments exploring this idea in Chapter 4, where we will see that a relative twist can completely decouple the layers from each other, despite their sub-nanometer spacing.

Chapter 2

Quantum Spin Hall State in Monolayer Graphene

2.1 Introduction - graphene and topological insulators

IN 2004, Novoselov and Geim demonstrated the electric field effect in graphene[168]. The following year, Kane and Mele published a study of spin-orbit interactions in graphene[104], and in turn began a separate chapter for condensed matter physics. They discovered that spin-orbit interactions cause intrinsic graphene to become a bulk insulator with a pair of metallic 1d edge modes. Unlike the quantum Hall effect, the two edge modes of this state propagate in opposite directions with opposite spin polarizations. They called it the quantum spin Hall effect. Diving deeper, Kane and Mele identified a number, a topological invariant, which differentiated this state from other insulators within the same symmetry class. These were the beginnings a new field that would grow to explore a wide class of related electronic states called "topological insulators".

Graphene is not normally a topological insulator. Its intrinsic spin-orbit interaction

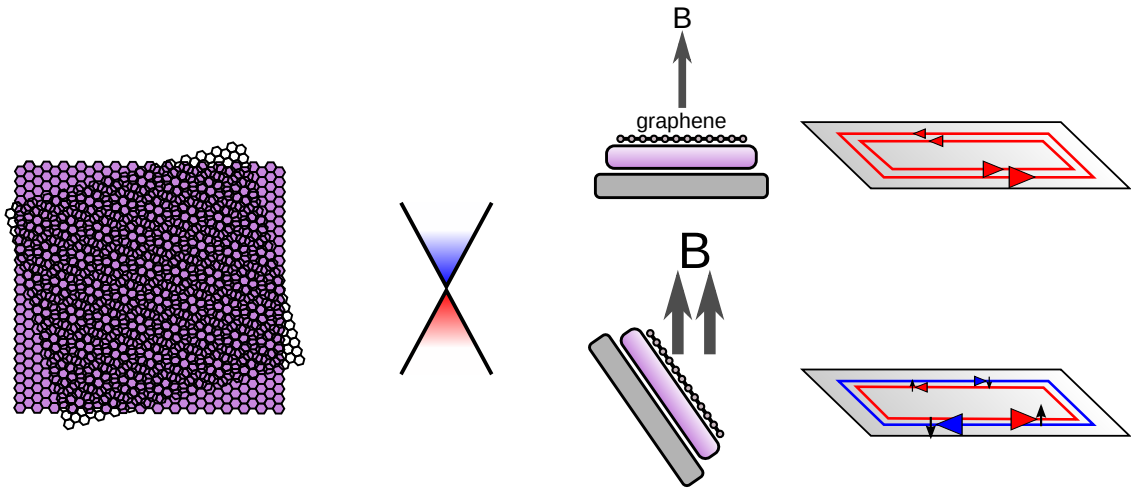

Figure 2.1. Realizing a quantum spin Hall state in monolayer graphene on hBN

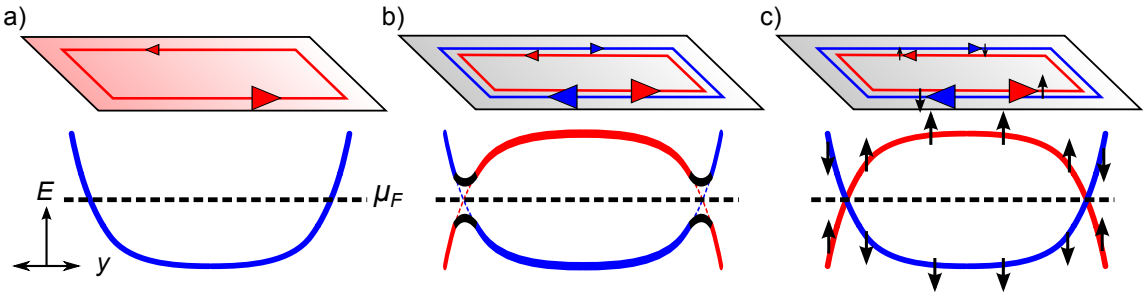

Figure 2.2. From the quantum Hall edge states to the quantum spin Hall state. Top cartoons are schematics of different edge state configurations. Bottom plots show dispersion of bands going from the bulk to the edge of the sample. **a)** Quantum Hall edge state. **b)** Two copies of quantum Hall edge states with opposite chiralities. Scattering between the modes can lead to the opening of a gap. **c)** The quantum spin Hall state has two edge modes with opposite chiralities and opposite spin polarizations. The crossing of the modes is protected by an extra symmetry of the system.

is exceedingly weak, corresponding to an energy scale of about 1μeV[153, 241], much smaller than the scale of temperature or disorder in experiments. Instead, other 2d[117] and 3d topological insulators[93, 233] were discovered in materials with heavy elements and strong spin-orbit coupling.

In this chapter, we will see an alternative way to realize a quantum spin Hall state in graphene. Unlike the original proposal by Kane and Mele, this 2d topological insulator state is fundamentally based upon the graphene quantum Hall effect. I will show how we can induce a quantum spin Hall state in charge neutral graphene by applying a large magnetic field to a clean graphene device. The result is a new type of 2d topological insulator which is realized in the presence of strong electron-electron interactions. This work also maps out a clear boundary point in the phase diagram for the correlated ground states of graphene in a magnetic field.

■ 2.2 Background

■ 2.2.1 Quantum spin Hall - two copies of the quantum Hall effect

In the quantum Hall effect, metallic edge modes surround the insulating bulk of a 2d electron gas (Figure 2.2a)[70]. The edge modes are chiral—electrons can only propagate in one direction around the edge of the sample. As such, disorder cannot backscatter the charge carriers since the oppositely moving mode is too far away, on the other side of the sample. This is the origin of the dissipation-less transport observed in the quantum Hall effect.

Now imagine two superimposed copies of the quantum Hall effect, each copy with a single edge state but with opposite chirality (Figure 2.2b). In this case, electrons traveling on the edge can backscatter since the counterpropagating modes are right on top of each other. If the scattering is a coherent coupling process, the edge modes can even completely gap out. This is will happen if there is no extra symmetry that protects

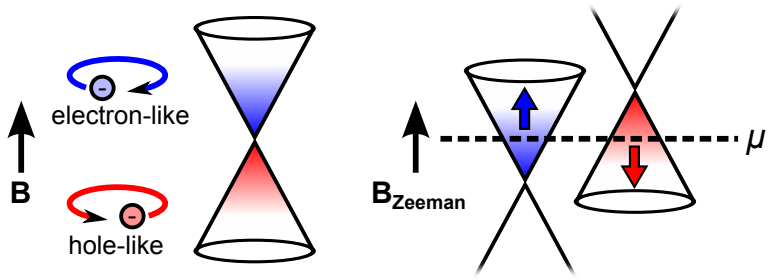

Figure 2.3. The Zeeman effect in graphene leads to co-existing electron-like and hole-like bands with opposite spin polarizations.

the degenerate crossing of the edge modes. But, if there is an extra symmetry of the system that maps the two edge modes into each other, such as a flipping of their spin polarization and propagation direction, then the crossing can be protected, in which case backscattering will not occur (Figure 2.2c). This is an illustrative example of a "symmetry-protected" topological insulator in 2d: a quantum spin Hall (QSH) state. In the original formulation of the QSH state[104], the relevant symmetry was time-reversal, but this concept has since been generalized to other symmetries as well, such as crystal symmetries[60].

We see then that we could build a QSH state from two copies of the quantum Hall effect, if the copies had opposite chiralities as well as opposite spin polarizations. How can this be done? Following a semiclassical argument, the chirality of a quantum Hall edge state originates from the sign of a band's cyclotron mass. This determines the direction electrons will orbit in a magnetic field: like an electron or like an oppositely charged hole (Figure 2.3, left). Intuitively then, to build a QSH state we need co-existing electron- and hole-like bands, with opposite spin polarizations. Typically, we associate electron and hole-like behavior with the conduction and valence bands, respectively, so we can also think of a semi-metal where the conduction and valence bands overlap.

Neutral graphene becomes an overlapping semi-metal when its spin degeneracy is split by the Zeeman effect. This is because the conduction and valence bands meet at the neutrality point, so the shifting of the two spin polarizations in energy necessarily leads to an overlap (Figure 2.3, right). Moreover, the electron-like and hole-like bands will have opposite spin polarizations. This is the exactly the recipe we want to build a QSH state. Applying a perpendicular magnetic field will lead to a quantum Hall effect in each of the electron-like and hole-like bands with the resulting system being in a QSH state.

■ 2.2.2 Quantum spin Hall states

The study of the quantum spin Hall states has its origin in research on spintronics and the quantum Hall effect. The latter was driven by the following question: can a quantum Hall-like system be realized in the absence of a magnetic field[83]? Investigations towards

this end overlapped with research into the electronic control of spin currents, where the quantum spin Hall effect was the natural extrapolation from studies of the spin Hall effect in materials with spin-orbit coupling[105, 159, 160, 207, 232]. Further developments in the latter work led to a prediction for a quantum spin Hall state in HgTe[17], a narrow gap semiconductor with strong spin-orbit coupling. Subsequently, the group of Laurens Molenkamp reported the observation of the predicted quantum spin Hall state at zero magnetic field[117]. Their primary observation was that for a specific thickness of the HgTe quantum well the system would turn from a band insulator to a conductor with conductance approximately $2e^2/h$. In addition, they saw that the conductance was independent of sample width, but was sensitive to the measurement geometry along the edge[187]. This provided clear evidence for the existence of edge states. Since this initial discovery, another quantum spin Hall system has been demonstrated in InAs/GaSb quantum wells[47, 116].

Much of the interest in quantum spin Hall states is due to its potential use for quantum computing. Specifically, it is a proposed platform for realizing topologically-protected qubits[164] in the form of Majorana bound states [62]. Majorana bound states were originally proposed by Kitaev to arise in a 1-dimensional spinless superconductor[114], but other solid state systems have since been proposed to host them as well[5, 193, 194]. A quantum spin Hall state is spinless in the sense that it lacks a spin degeneracy. Moreover, the counterpropagating modes can undergo s-wave pairing since they have opposite spins. All that is required is the help of a proximal s-wave superconductor to couple them[61, 62]. The final step is to create a boundary where the Majorana bound states will live, which can be provided by gapping out a portion of the quantum spin Hall state with a local ferromagnet. This method has yet to be demonstrated, but Majorana bound states have been reported instead in 1d nanowires coupled to a superconductor[158, 161]. Nonetheless, work still continues to realize a Majorana bound state in a quantum spin Hall system, since their realization in a 2d structure opens itself to potentially more geometric flexibility in building topologically protected circuits.

■ 2.2.3 Charge neutral graphene in a strong magnetic field

Let us now discuss more concretely what happens to neutral graphene in a magnetic field. As we saw in the first chapter, monolayer graphene has a unique Landau level spectrum due to its massless Dirac dispersion. Importantly, it has a Landau level at zero energy which is four-fold degenerate, due to the spin and valley degrees of freedom. This zeroth Landau level is half-filled for charge-neutral graphene. In the first observation of the graphene quantum Hall effect, transport in this zeroth Landau level appeared as a peak in the longitudinal resistance and a passing through zero of the Hall conductance[168, 250]. One expectation was that with higher magnetic fields and cleaner samples the Zeeman effect could be used to split the zeroth Landau level, causing a transition to a QSH state at charge neutrality[1, 59]. This would appear as a quantized total conductance of $2e^2/h$ as transport occurs through a pair of protected ballistic edge states.

A quantum spin Hall state has not been observed for neutral graphene in a purely perpendicular magnetic field. Instead, multiple groups have observed a deep insulating state develop[22, 29, 30, 49, 242, 246, 247]. Initially, there was some confusion as to the origin of this effect, with different groups reporting varying behavior in disordered graphene devices. Fabrication improvements have increased the quality of devices dramatically over the years, with both the development of suspended graphene and graphene on hBN substrates. As the sample quality has improved, the insulating state has become the consistently observed behavior [22, 49, 242]. Moreover, in higher quality samples the insulating state is observed to onset at lower magnetic fields, indicating an intrinsic behavior.

We now understand that this insulating state arises due to exchange interactions breaking the degeneracy of the zeroth Landau level, leading to a gap at charge neutrality. This degeneracy breaking occurs because the electrons can lower their mutual Coulomb repulsion if they adopt a many-body wavefunction which is spatially anti-symmetric. In a system with a spin-degeneracy, this will cause the electrons to polarize their spins in the same direction, a phenomenon called "quantum Hall ferromagnetism" [103]. The situation is more complex in graphene; the polarization can point in any direction in the nearly SU(4) symmetric spin-valley space. The direction chosen will depend sensitively on the relative scale of small symmetry-breaking terms. The most obvious is the Zeeman effect, which naively would always cause the spin polarized state to be favored. Exchange interactions would then enhance the Zeeman splitting of the zeroth Landau level, leading to a QSH state (which has a spin polarized bulk). We know this is not the case. In fact, measurements of the insulating state in a titled field demonstrate that the ground state is spin *unpolarized*[242].

Clearly then, there are other symmetry breaking effects in the zeroth Landau level which are stronger than the Zeeman effect. These arise from the unique structure of the graphene zeroth Landau level, where the two different valley polarizations, K and K', each occupy a different sublattice. This is a departure from the zero magnetic field case, where the electron wavefunctions are always in an equal sublattice superposition. In the zeroth Landau level though, a valley polarized state corresponds to all the electrons occupying only one sublattice to form a charge density wave. Many possible ground states have been proposed by analyzing the symmetry breaking effects of short-range Coloumb interactions, optical phonon modes, and Zeeman splitting[6, 7, 39, 71, 102, 107, 166, 167, 175, 237]. One simple result is that all the proposed ground states are insulating, except for the QSH state. Regardless of what the true ground state is though, an analysis of its phase diagram shows that the spin ferromagnet state (QSH) is the favored state in the limit of infinite Zeeman effect. Since an in-plane magnetic field only affects the Zeeman effect, and not any of the other symmetry-breaking terms, a route forward to the QSH state becomes clear: apply a very large in-plane magnetic field.

■ 2.3 Experiment details

Our strategy for realizing a graphene quantum spin Hall (QSH) state was to apply a large *tilted* magnetic field to charge neutral graphene. The small perpendicular field would induce the quantum Hall effect, while the large in-plane component would provide the Zeeman splitting to invert the bands. A major limitation to this experiment was the weakness of the Zeeman splitting in graphene ($g \sim 2$) compared to the other symmetry-breaking terms which were driving the system into an insulating state. To tip the balance in favor of the Zeeman splitting, we would require the largest magnetic fields currently available to humans (30 to 45T continuous field at the National High Magnetic Field Lab). Since a majority of the total field would be required to tilt in-plane, the samples would need to have a fully developed quantum Hall effect at a low perpendicular field ($<$1T). Correspondingly, we would need high quality graphene devices with minimal amounts of charge disorder. All of the devices consisted of stacks of graphene separated by a thin hBN layer from an underlying graphite flake that served as a gate electrode (Figure 2.4). The additional role of the graphite was to screen charge disorder, most importantly from the underlying SiO2, but also within the hBN or on top of the graphene as well[181, 185]. In addition, we thought that the graphite could partially screen the Coulomb interactions which cause the insulating state at charge neutrality, and hence reduce the required Zeeman splitting. This latter idea is yet to be proven experimentally.

Even with the proximal graphite gate to screen disorder, it was still necessary to make graphene devices that were free of polymer residue and that lay flat on the hBN without ripples or bubbles. In practice, we fabricated a large quantity of devices and used statistics to our advantage. This was aided by a quick turn-around characterization in a top-loading He3 system which we used to check the quality of the quantum Hall effect. A major fabrication breakthrough was the discovery by the Vandersypen group at Delft that the graphene on hBN flakes could be mechanically cleaned by contact mode AFM[76]. Previously we had to rely on a unreliable heat annealing process which only occasionally produced completely clean transferred flakes.

Once the devices were initially characterized, the final measurements were performed at the National High Magnetic Field Lab. In addition to the standard transport measurements, we also performed capacitance measurements as well. Capacitance is a useful probe of bulk density of states and bulk conductivities, as opposed to transport which is sensitive to the most conductive path from the source to the drain electrodes. By measuring the capacitance we could verify whether a state was a bulk insulator even while transport indicated metallic conduction (for example while measuring the quantum Hall effect). See the Appendix B.3 for more information.

■ 2.4 Tunable symmetry breaking and helical edge transport in a graphene quantum spin Hall state

The text in this section originally appeared in the publication Young, Sanchez-Yamagishi, Hunt, et. al. [243]

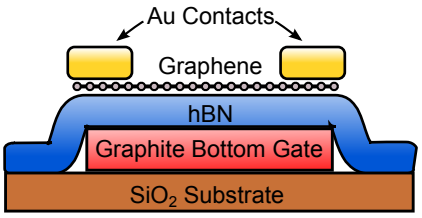

Figure 2.4. Device schematic for graphene quantum spin Hall studies.

Low-dimensional electronic systems have traditionally been obtained by electrostatically confining electrons, either in heterostructures or in intrinsically nanoscale materials such as single molecules, nanowires, and graphene. Recently, a new paradigm has emerged with the recognition that certain gapped systems, known as symmetry protected topological (SPT) phases[31, 189], can host robust surface states that remain gapless as long as the relevant global symmetry remains unbroken. The nature of the charge carriers in SPT surface states is intimately tied to the symmetry of the bulk, resulting in one- and two-dimensional electronic systems with novel properties. For example, time reversal symmetry (TRS) endows the massless charge carriers on the surface of a three-dimensional topological insulator with helicity, locking the orientation of their spin relative to their momentum[86, 183]. Weakly breaking this symmetry generates a gap on the surface,[32] resulting in charge carriers with finite effective mass and exotic spin textures[235]. Analogous manipulations have yet to be demonstrated in two-dimensional topological insulators, where the primary example of a SPT phase is the quantum spin Hall (QSH) state[47, 118]. Here, we demonstrate experimentally that charge neutral monolayer graphene displays a QSH state[1, 59] when it is subjected to a very large magnetic field angled with respect to the graphene plane. Unlike in the TRS case[118], the QSH state presented here is protected by a symmetry of planar spin-rotations that emerges as electron spins in a half-filled Landau level are polarized by the large magnetic field. The properties of the resulting helical edge states can be modulated by balancing the applied field against an intrinsic antiferromagnetic instability[89, 102, 106], which tends to spontaneously break the spin-rotation symmetry. In the resulting canted antiferromagnetic (CAF) state, we observe transport signatures of gapped edge states, which constitute a new kind of one-dimensional electronic system with tunable band gap and associated spin-texture[107].

In the integer quantum Hall effect, the topology of the bulk Landau level (LL) energy bands requires the existence of gapless edge states at any interface with the vacuum. The metrological precision of the Hall quantization can be traced to the inability of these edge

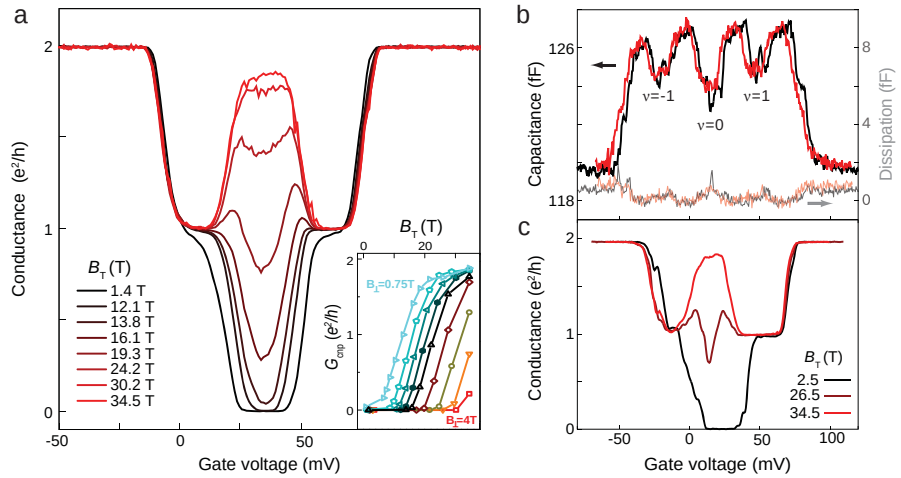

Figure 2.5. Quantum spin Hall state in monolayer graphene in extreme tilted magnetic fields. **a**, Conductance of device A at $B_\perp$=1.4T for different values of B_T. As B_T increases, the insulating state at ν=0 is gradually replaced by a high conductance state, with an accompanying inversion of the sign of $\partial G_{cnp}/\partial T$ (additional data in Figures B.3 and B.4). Inset: G_{cnp} as a function of B_T for Device A. Left to right: $B_\perp$=0.75 (cyan), 1.0, 1.4, 1.6, 2.0, 2.5, 3.0, and 4.0 T. **b,** Capacitance (dark lines) and dissipation (faded lines) of device B at $B_\perp$=2.5T. The low dissipation confirms that the measurements are in the low-frequency limit, so that the dips in capacitance can be safely interpreted as corresponding to incompressible states. **c,** Conductance under the same conditions. The absence of a detectable change in capacitance, even as the two-terminal conductance undergoes a transition from an insulating to a metallic state suggests that the conductance transition is due to the emergence of gapless edge states.

states to backscatter due to the physical separation of modes with opposite momentum by the insulating sample bulk. In contrast, counterpropagating boundary states in a symmetry-protected topological (SPT) insulator coexist spatially but are prevented from backscattering by a symmetry of the experimental system[86, 183]. The local symmetry that protects transport in SPT surface states is unlikely to be as robust as the inherently nonlocal physical separation that protects the quantum Hall effect. However, it enables the creation of new electronic systems in which momentum and some quantum number such as spin are coupled, potentially leading to devices with new functionality. Most experimentally realized SPT phases are based on TRS, with counterpropagating states protected from intermixing by the Kramers degeneracy. However, intensive efforts are underway to search for topological phases protected by symmetries other than TR in new experimental systems[94, 111].

Our approach is inspired by the similarity between the TRS QSH state and overlapping electron- and hole-like copies of the quantum Hall effect, with the two copies having opposite spin polarization. This state is protected by spin conservation rather than the orthogonality of states in a Kramers doublet[86], as with the TRS QSH observed in strong spin-orbit systems. Nevertheless, it is expected to reproduce the characteristic

experimental signatures of the TRS QSH, with gapless helical edge states enclosing an insulating bulk[1, 59]. Two requirements are necessary for realizing such a QSH state. First, the spin-orbit coupling must be weak, so that spin remains a good quantum number. Second, the energy gap between electron- and hole-like Landau levels must be small enough to be invertible by the Zeeman splitting. Both of these conditions are met in graphene, a gapless semimetal with very weak spin-orbit coupling[153]. The graphene LL structure is characterized by the existence of a fourfold spin- and valley-degenerate LL at zero energy(zLL)[200]. Near the sample boundary, the zLL splits into one positively dispersing (electron-like) and one negatively dispersing (hole-like) mode per spin projection. Consequently, a spin-symmetry protected QSH state is expected when the spin degeneracy is lifted by an external magnetic field, resulting in a bulk energy gap at charge neutrality and electron-like and hole-like states with opposite spin polarization that cross at the sample edge[1, 59].

Experimentally, charge neutral monolayer graphene does not exhibit the expected phenomenology of the QSH state, becoming strongly insulating instead at high magnetic fields[29]. While the precise nature of this insulating state has remained elusive, its origin can be traced to the strong Coulomb interactions within the graphene zLL. At integer filling factors, ν, the Coulomb energy is minimized by forming antisymmetric orbital wavefunctions, forcing the combined spin/valley isospin part of the wavefunction to be symmetric. The resulting possible ground states lie on a degenerate manifold of states fully polarized in the approximately SU(4)-symmetric isospin space[237], encompassing a variety of different spin- and valley- orders. In the real experimental system, the state at any given filling factor (such as $\nu = 0$) is determined by the competition between SU(4) symmetry-breaking effects. The most obvious such anisotropy is the Zeeman effect, which naturally favors a spin-polarized state, but the sublattice structure of the zLL adds additional interaction anisotropies[6] that can favor spin unpolarized ground states characterized by lattice scale spin- or charge-density wave order[89, 102, 106, 167]. This interplay can be probed experimentally by changing the in-plane component of magnetic field, which changes the Zeeman energy but does not affect orbital energies, and previous observations indeed confirm that the state responsible for the ν=0 insulator is spin unpolarized[242]. However, the spin polarized QSH state can be expected to emerge for sufficiently large in-plane field, manifesting as an incompressible conducting state at charge neutrality.

Figure 2.5a shows two terminal conductance measurements of a high quality graphene device fabricated on a thin hBN substrate, which itself sits atop a graphite local gate. As the total magnetic field (B_T) is increased with $B_\perp$ held constant, the initially low charge neutrality point conductance (G_{cnp}) increases steadily before finally saturating at $G \sim 1.8\ e^2/h$ for the largest total field applied. Evidence for a similar transition was recently reported in bilayer graphene[138], where the additional orbital degeneracy of the zero Landau level leads to a conductance of $4e^2/h$. We note that although superficially similar, the structure and transport properties of the resulting edge modes are likely to be heavily influenced by the additional degeneracy, particularly when many

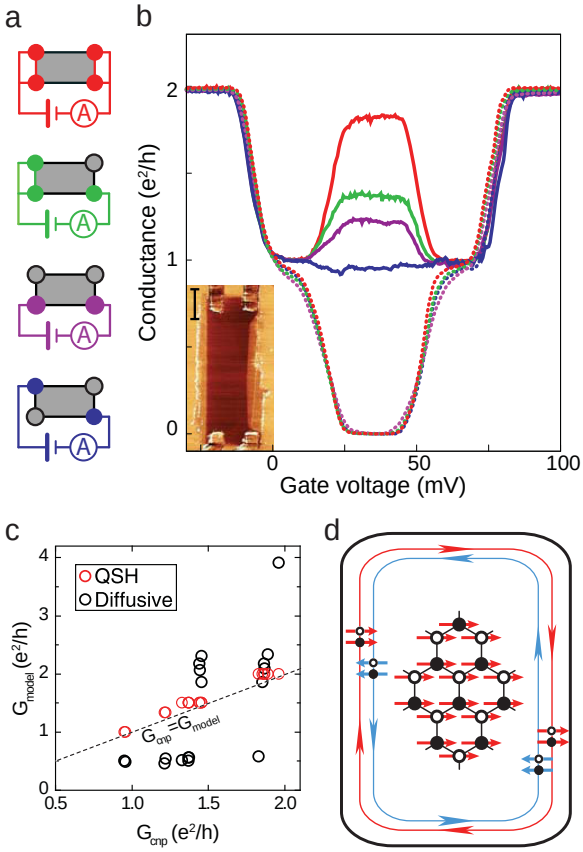

Figure 2.6. Nonlocal two-terminal transport in the quantum spin Hall regime. a, Schematic of four distinct two-terminal measurement topologies available in a four-terminal device. Hollow circles indicate floating contacts while filled, colored circles indicate measurement contacts. Each variation probes two parallel conductance paths between the measurement contacts with a variable number of segments on each path, indicated by black edges. **b**, Two-terminal conductance measurements of Device A for $B_\perp$=1.4T, color-coded to the four different measurement configurations. Dashed curves are taken at B_T=1.4T; solid curves are taken at B_T=34.5T (QSH regime). In the QSH regime, G_{cnp} depends strongly on the number of floating contacts (see Figure B.5 for similar data for sample C). Inset: AFM phase micrograph of Device A. Scale bar: 1 micron. **c**, G_{cnp} for eighteen different contact configurations based on cyclic permutations of the topologies shown in **a**. Data are plotted against two model fits. In a numerical simulation based on a diffusive model (black circles), the graphene flake was assumed to be a bulk conductor with the conductivity left as a fitting parameter ($\sigma = 3.25e^2/h$ for the best fit). The QSH model is Eq. 1, and has no fitting parameters. The dashed line indicates a perfect fit of data to model. Note that the measured G_{cnp} never reaches the value predicted by the QSH model, indicating either contact resistance or finite backscattering between the helical edge states. **d**, Schematic of bulk order and edge state spin texture in the fully polarized QSH regime. Arrows indicate the projection of the electron spin on a particular sublattice, with the two sublattices indicated by hollow and filled circles. The edge state wavefunctions are evenly distributed on the two sublattices and have opposite spin polarization, at least for an idealized armchair edge[107].

body reconstructions of the edge states are taken into account[59, 143].

To distinguish the role of the edges and the bulk in this conductance transition, we also measure the capacitance between the graphene and the graphite back gate under similar conditions. Capacitance (C) measurements serve as a probe of the bulk density of states (D) via $C^{-1} = C_G^{-1} + (Ae^2D)^{-1}$, where C_G is the geometric capacitance and A is the sample area. Simultaneous capacitance and transport measurements from a second graphene device show that quantized Hall states within the zLL at $\nu = 0$ and $\nu = \pm 1$ are associated with minima in the density of states (Figure 2.5b-c). As the total field is increased, the capacitance dip at $\nu = 0$ remains unaltered even as conductance increases by several orders of magnitude. This implies that the high field $\nu = 0$ state has an incompressible bulk, consistent with the hypothesis of a ferromagnetic QSH state with conducting edge states and a bulk gap.

We probe the nature of the edge states through nonlocal transport measurements in which floating contacts are added along the sample edges[187]. Unlike the chiral edge of a quantum Hall state, which carries current in only one direction, the QSH edge can carry current either way, with backscattering suppressed by the conservation of spin within the helical edge sates. Because the carriers do not maintain their spin coherence within a metal contact, contacts equilibrate the counterpropagating states so that each length of QSH edge between contacts must be considered as a single h/e^2 resistor. The two-terminal conductance results from the parallel addition of the two edges connecting the measurement probes,

$$G = \frac{e^2}{h}\left(\frac{1}{N_1+1} + \frac{1}{N_2+1}\right), \tag{2.1}$$

where N_1 and N_2 are the number of floating contacts along each edge. Figure 2.6b shows the results of nonlocal two-terminal conductance measurements for the four distinct two-terminal measurement geometries available in a four-terminal device (Figure 2.6a). Repeating the measurement for 18 cyclic permutations of the available contact configurations, we find that the results are well fit by the simple model of Eq. 2.1 (Figure 2.6c) despite large variations in the effective bulk aspect ratio. Notably, G_{cnp} is always less than the value expected from the QSH model, suggesting some small but finite amount of backscattering or contact resistance. The combination of bulk incompressibility and nonlocal transport signatures of counterpropagating edge states lead us to conclude that the high field metallic state observed indeed displays a QSH effect.

The QSH state realized here is equivalent to two copies of the quantum Hall effect, protected from mixing by the U(1) symmetry of spin rotations in the plane perpendicular to the magnetic field. As such, it constitutes a topologically nontrivial state that is clearly distinct in its edge state properties from the insulating state at fully perpendicular field. What kind of transition connects the two states? Capacitance measurements in the intermediate conductance regime reveal that the bulk gap does not close as the total field is increased (Figure 2.7a). This rules out a conventional topological phase transition, in which case the bulk gap is required to close[26]; the transition must thus

occur by breaking the spin-symmetry on which the QSH effect relies. In fact, a canted antiferromagnetic state (Figure 2.7b) that spontaneously breaks this symmetry is among the theoretically allowed $\nu = 0$ states[89, 102, 106]. Within this scenario, the canting angle is controlled by the ratio of the Zeeman energy, $g\mu_B B_T$, and the antiferromagnetic exchange coupling, which depends only on $B_\perp$. The observed conductance transition results from the edge gap closing (Figure 2.7c) as the spins on the two graphene sublattices are slowly canted by the in-plane magnetic field, with the fully polarized QSH state emerging above a critical value of B_T[107]. In the language of SPT insulators, the antiferromagnetic instability breaks the spin symmetry below this critical field, allowing the counterpropagating edge states to backscatter and acquire a gap[205].

Experimentally, the sub-critical field regime is characterized by high conductance peaks appearing symmetrically between $\nu = 0$ and $\nu = \pm 1$. We observe $G > e^2/h$ peaks in many samples with widely varying aspect ratios (Figure B.6), which is inconsistent with diffusive bulk transport in a compressible Landau level[2]. Variable temperature measurements indicate that the peaks are metallic, even when the state at $\nu = 0$ is still strongly insulating (Figure 2.8a). Moreover, the peaks exhibit the nonlocal transport behavior of counterpropagating edge states (Figure 2.8b); in particular the peak conductance is always strictly less than e^2/h when the two edges are interrupted by a floating contact. These results indicate that the conductance peaks are due to edge state transport in the canted antiferromagnetic state. The high conductance of these edge states, despite proximity to the strongly disordered etched graphene edge, implies that backscattering is at least partially suppressed. This is consistent with the the theory of the CAF band structure shown in Figure 2.8c-d[107], in which the interpolation between the gapless QSH and gapped AF edge structure is achieved via a new kind of one-dimensional edge state in which counterpropagating modes have oppositely-canted AF spin texture. Interestingly, existing theories of the CAF state are only rigorously applicable to the zero carrier density regime, in which case the CAF edge modes exist as excited states. The fact that we can access the CAF edge states via gating is somewhat surprising, as it implies that this spectrum is stable to small populations of the edge bands.

Questions remain about the precise nature of the QSH and CAF boundary modes. The measured G_{cnp} never reaches $2e^2/h$ even at the highest values of B_T, despite some of the devices showing a flat plateau around charge neutrality. Naively, backscattering within the QSH edge mode requires flipping an electron spin, for example by magnetic impurities, although such a process should be energetically unfavorable at high magnetic fields. More trivially, we cannot exclude that weakly conducting charge puddles connect the two edges (but not source and drain contacts), leading to backscattering across the bulk in the QSH regime. Spin-orbit effects may also play a role by spoiling the spin-symmetry upon which the helical edge states rely. While the intrinsic spin-orbit coupling in graphene is thought to be weak[153], the helical states may be uniquely sensitive to spin relaxation. Alternatively, the large Rashba-type spin-orbit coupling induced in the graphene under the gold contacts[140] may gap out the edge states near

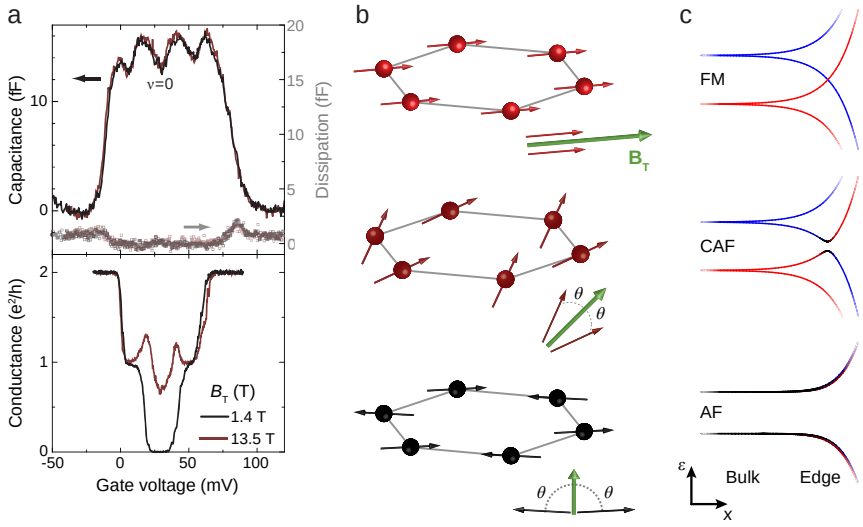

Figure 2.7. Symmetry-driven quantum phase transition. **a** Capacitance (top) and conductance (bottom) of device A at $B_\perp$=1.1T. The central dip in capacitance does not change with B_T at any point during the transition, implying that the bulk gap does not close. **b**, Bulk spin order in the three transition regimes. The balls and arrows are schematic representations of the spin and sublattice texture of the ground state wavefunctions and do not represent individual electrons; the electron density within the ZLL at ν=0 is two electrons per cyclotron guiding center. The insets in **b** show details of the relative alignment of the electron spins on the two sublattices. At large B_T, the bulk electron spins are aligned with the field (top panel), resulting in an emergent U(1) spin-rotation symmetry in the plane perpendicular to B_T. As the total magnetic field is reduced below some critical value (with $B_\perp$ held constant), the spins on opposite sublattices cant with respect to each other while maintaining a net polarization in the direction of B_T (middle panel). This state spontaneously breaks the U(1) symmetry, rendering local rotations of the electron spins energetically costly. At pure perpendicular fields (bottom panel), the valley isospin anisotropy energy overwhelms the Zeeman energy and the canting angle θ is close to 90°, defining a state with antiferromagnetic order. **c**, Low energy band structure in the three phases[107]. ϵ is the energy and x is the in-plane coordinate perpendicular to the physical edge of the sample. The intermediate CAF phase smoothly interpolates between the gapless edge states of the QSH phase (top panel) and the gapped edge of the perpendicular field phase (bottom panel) without closing the bulk gap. Colors indicate spin texture of the bands projected onto the magnetic field direction, with red corresponding to aligned, blue antialigned, and black zero net spin along the field direction.

the graphene/contact interface, contributing a QSH-specific contact resistance which lowers the plateau conductance. The effects of mixed armchair and zigzag edges on helical edge transport have also not been addressed by current theoretical treatments.

Nonlinear transport measurements provide some additional insight into the nature of backscattering in the edge states. In both the QSH and CAF regimes, the nonlinear transport data is invariant under simultaneous inversion of the carrier density and source-drain bias, V_{SD} (Figures 2.8e-f). The data thus respects charge conjugation symmetry within the graphene, possibly implying that the inelastic processes probed by large V_{SD} are native to the electronic system. Notably, the nonlinear conductance is not invariant under reversal of source drain bias alone. We can understand this lack

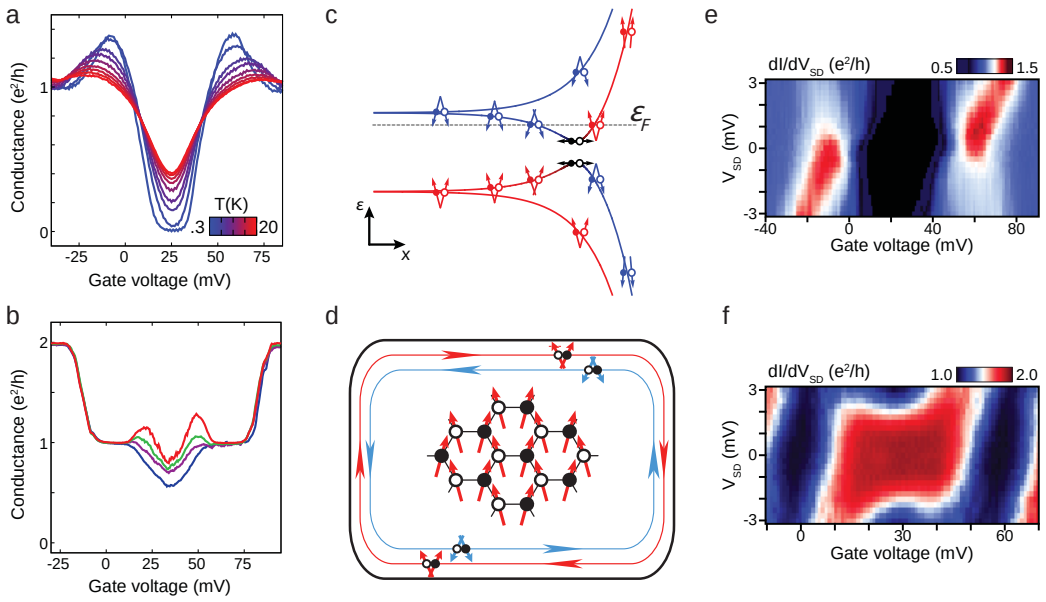

Figure 2.8. Spin textured edge states of the CAF phase. a, Temperature dependence in the intermediate field regime for device C at $B_\perp$=5.9T and B_T=45.0T. The conductance peaks shows a metallic temperature coefficient, while the state at charge neutrality remains insulating. **b,** Nonlocal two-terminal conductance of device A at $B_\perp$=1.6T and B_T=26.1T. Color coding indicates contact geometry following the scheme in Figure 2.6a. The height of the conductance peaks depends strongly on the configuration of floating contacts, indicating their origin in the gapped, counterpropagating edge states of the CAF phase. **c,** Schematic band diagram, including spin order, of the CAF edge states. For the electron and hole bands nearest to zero energy, the canting angle inverts near the sample edge, leading to counterpropagating edge states with inverted CAF spin texture. The dashed gray line indicates the Fermi energy, ϵ_F, in the regime corresponding to one of the conductance peaks. **d**, Schematic of bulk order and edge state spin texture in the CAF regime, following the convention of Figure 2.6d. **e**, Differential conductance, dI/dV_{SD}, of device C in the QSH regime ($B_\perp$=2.7 T, B_T=45.0 T) in units of e^2/h. A constant source-drain voltage, V_{SD}, along with a 100μV, 313 Hz excitation voltage, are applied to one contact and the AC current measured through the second, grounded contact. **f**, dI/dV_{SD} of device C in the CAF regime ($B_\perp$=5.9T, B_T=45.0T) in units of e^2/h. In both **e** and **f**, a symmetry is observed upon reversing both V_{SD} and carrier polarity.

of symmetry as a natural consequence of dissipative edge transport in our time-reversal noninvariant system, where, in contrast to topological insulators, the counterpropagating edge states can be spatially separated. Within this picture, reversing V_{SD} changes the current carried by the inner and outer counterpropagating edge states. If dissipation differs between the two states on a single edge and the two physical graphene edges are inequivalent, reversing V_{SD} can be expected to result in different conductance.

The current experiments present the first proof of the CAF-QSH crossover in monolayer graphene. In addition, they enable the study of QSH physics in a versatile material platform, enabling new experiments. Most importantly, the high-field graphene QSH system differs from the conventional TRS QSH state through the crucial role of interactions, which lead to the spontaneous breaking of spin symmetry that generates the gapped CAF edge states. We note that in this chapter we have discussed experimental results in the context of mean-field treatments of interactions in the graphene zero Landau level[106, 107]. Crucially, this treatment neglects the potential for the spin-ferromagnetic (or CAF) order parameter to reconstruct near the sample boundary[59, 102], possibly leading to a qualitative change in the nature of the edge charge carriers. These results should inspire more careful future work, both experimental and theoretical, to both understand the true nature of the edge states and to use them as a building block for realizing novel quantum circuits.

Chapter 3

Massive Dirac Fermions and Hofstadter's Butterfly in Graphene-hBN Superlattices

3.1 Introduction - superlattices and insulating states

WE could not have realized a graphene quantum spin Hall state without hexagonal boron nitride (see previous chapter). Highly crystalline, chemically inert, and atomically flat, it seemed like the perfect match for performing pristine graphene studies. The initial discovery of hexagonal boron nitride (hBN) as a substrate for graphene[43] quickly resulted in a series of new results that were enabled by the order of magnitude

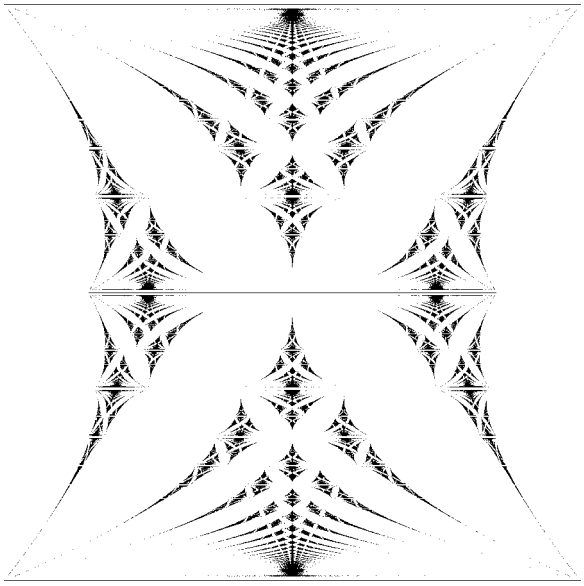

Figure 3.1. "Hofstadter's Butterfly" Energy spectrum of a square lattice in a magnetic field. Vertical axis is magnetic field in units of flux quanta per unit cell (0 to 1). Horizontal axis is energy with the bandwidth of a single Bloch band.

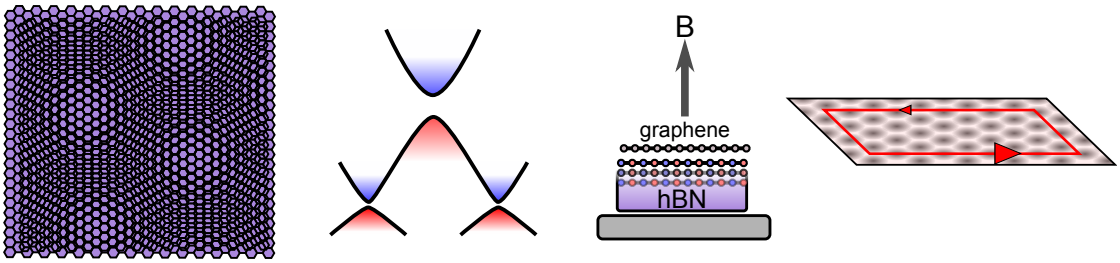

Figure 3.2. Insulating state and Hofstadter butterfly in graphene-hBN heterostructures

improvement in sample quality[42, 78, 181, 192, 215, 242]. For all these studies, the hBN was treated as the ideal substrate and dielectric material, without any interactions with the graphene. Lurking in the background though was the knowledge that the hBN does not provide a truly flat electric potential. This was already observed in the first STM studies, where graphene on hBN was found to form a topographic moiré pattern and to have a density of states modulation many nanometers in length[44, 236]. As studies of graphene-hBN heterostructures intensified, it did not take long for departures from pristine graphene behavior to appear, forcing the field to seriously consider the coupling between the graphene and hBN.

In this chapter, I describe experiments that show how hBN can drastically change the electronic properties of graphene. The primary experimental observations are the opening of a band gap at the graphene Dirac point, as well as the transport signatures of a superlattice potential. These effects can be understood in terms of two different types of hBN-induced symmetry breaking terms: a sublattice asymmetric term due to the difference in boron and nitrogen atomic potentials, and a long wavelength potential modulation due to the lattice mismatched graphene and hBN.

The sublattice symmetry of the carbon hexagonal lattice is the origin of graphene's celebrated massless Dirac dispersion. From an applications perspective, it also is the primary barrier to inducing a bandgap in graphene, with much effort devoted towards methods of overcoming it[199]. The work in this chapter was the first to demonstrate a transport gap in graphene induced by the breaking of sublattice symmetry.

The lattice mismatch between the graphene and hBN results in an emergent long-wavelength potential modulation called a moiré superlattice potential. The result is a perturbation on the low energy states which "folds" the graphene band structure into the smaller superlattice Brillouin zone, generating new replicas of the Dirac cone at higher energies ("superlattice" Dirac points)[240]. In a magnetic field, an even richer electronic structure emerges, where commensuration effects between the magnetic length scale and the superlattice wavelength results in a complex sequence of spectral gaps. This seemingly self-referential pattern of gaps as a function of magnetic field has been termed "Hofstadter's Butterfly," after Douglas Hofstadter who empirically described the fractal spectrum for a square lattice potential under the influence of a magnetic field [92](see Figure 3.1). Since its first description, it has continued to be a fascinating example

of emergent phenomena as well as one the first cases of a fractal structure appearing in condensed matter physics. It also helps its popularity that it has an aesthetically beautiful figure, a catchy title, and an eponym who happens to be a Pulitzer prize winning author[91].

The conclusion from this chapter is that hBN can be both an ideal non-perturbing substrate for graphene, or a way to provide an atomically precise modulation of the graphene up to length scales of 14nm (the largest graphene-hBN superlattice wavelength). The effect is determined by the rotational alignment between the two crystals. This system offers one of the first demonstrations of the power of the van der Waals heterostructures paradigm. By stacking van der Waals materials, new electronic materials can be made both with the combined properties of the individual sheets and with the emergent properties from the interface couplings.

3.2 Background

3.2.1 Opening a gap. Breaking graphene's sublattice symmetry.

The opening of a bandgap in graphene is highly desirable for electronics applications such as digital logic devices or radio-frequency transistors[199]. It would also be useful for nanotechnology devices, since electrostatic gates could then be used to deplete and confine charge carriers in graphene as has been done for GaAs quantum dot circuits[179]. There have been many proposed strategies for opening a gap in graphene, such as confining graphene into nanoribbons[33, 85, 130, 239] or modifying it chemically [35, 54]. Unfortunately, these methods often introduce a large amount of disorder or too severely modifies the graphene, with the device having greatly reduced mobilities and conductivities.

An alternative route towards a graphene bandgap can be arrived by considering the graphene lattice symmetries. The graphene honeycomb has two sublattices which are equivalent and map into each other by inversion. This sublattice/inversion symmetry protects the linear Dirac dispersion centered at the graphene K and K' points. We can see this by considering the low energy Hamiltonian of graphene in the vicinity of the K (K') point:

$$H = v_F \boldsymbol{\sigma} \cdot \boldsymbol{p} + m^* v_F^2 \hat{\sigma}_Z, \tag{3.1}$$

where v_F is the Fermi velocity, $\boldsymbol{p} = (p_x, p_y)$ is the momentum in the graphene plane, $\boldsymbol{\sigma} = (\sigma_x, \sigma_y)$, and the Pauli matrices $\{\sigma_i\}$ operate in the basis of the two sublattice occupations. Since the σ_Z term is asymmetric under sublattice inversion, the mass prefactor m^* must be zero for a system with sublattice symmetry (e.g. graphene). By considering the energy eigenvalues of the above Hamiltonian, it follows simply that the spectrum must be gapless if this mass term is zero (Figure 3.3):

$$E(\boldsymbol{p}) = \pm\sqrt{v_F^2 |\boldsymbol{p}|^2 + (m^* v_F^2)^2}.$$

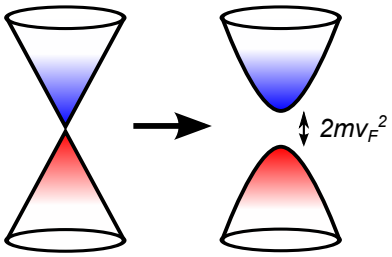

Figure 3.3. Breaking graphene's sublattice symmetry results in a band gap at the Dirac point.

By a similar analysis, we can understand that materials with hexagonal lattices without inversion symmetry will feature band gaps, such as hexagonal boron nitride and transition metal dicalgonides[225].

Another motivation for realizing a graphene mass term is that it can give rise to the transport of topological currents. The gapping of the Dirac dispersion endows the band with a nonzero Berry curvature which will have an associated valley Hall effect at zero magnetic field [234]. An applied charge current will then result in an all-electrical generation of a transverse valley current. This could have interesting applications for realizing "valleytronics", where the valley quantum degree of freedom is used for encoding information[188].

So then, how to break the graphene's sublattice symmetry? Given the requirement for an atomic-scale potential modulation, this would likely require the use of a precise atomic decoration method, or the use of another crystalline material in close proximity to the graphene. This could be accomplished by mechanically transferring or epitaxially growing the graphene onto a substrate which can break the symmetry (the latter idea is patented by Loren Pfeiffer[180]). Prior to the experimental results discussed in this chapter, spectroscopic gaps at the graphene Dirac point where observed by various ARPES studies for epitaxially grown graphene. This includes graphene grown on SiC substrates [253] as well as on ruthenium [56]. In both cases the authors invoke the breaking of sublattice symmetry by the underlying substrate as the cause of the bandgap.

Given hBN's similarity to graphene and its broken inversion symmetry, it may seem like the ideal substrate to epitaxially gap out graphene. In fact, ab-initio calculations predict that epitaxially stacking graphene onto hBN will result in an induced bandgap of 53meV[69]. There is only one problem, graphene and hBN are not lattice matched; the hBN is 1.8% larger. In addition, the weak van der Waals forces between the graphene and hBN are not enough to force long-range epitaxy[190]. Instead, they form an incommensurate interface, with a resulting moiré pattern that is observed in STM measurements[236]. The moiré is due to the graphene-hBN stacking smoothly changing in a periodic pattern (Figure 3.4). The result is that the mass term, which parametrizes the sublattice symmetry breaking, will oscillate and change sign across the superlattice unit cell. Ab-initio calculations predict that the average effect will be

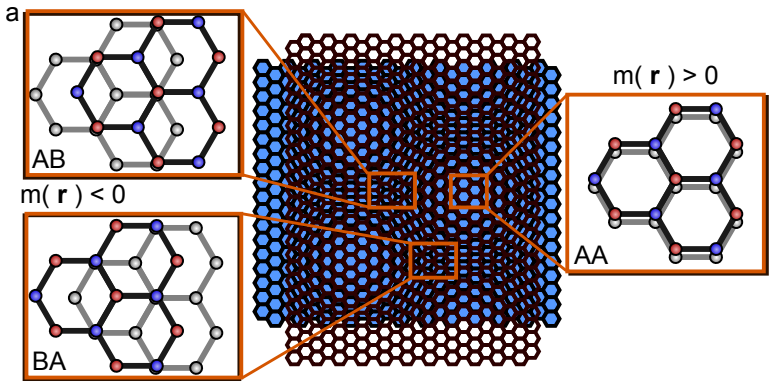

Figure 3.4. Graphene stacked on hBN form a moiré pattern due to their lattice mismatch. Atomic stacking arrangement changes smoothly across the superlattice unit cell, resulting in a sign oscillation of the mass term $m(r)$. Mismatch is exaggerated to make moiré easier to see

an average small gap of 4 meV [190]. The gap arising in graphene-hBN superlattices were further explored by Kinderman et al. [113] within a tight binding model, where it was found that a perpendicular electric field could also be used to increase the gap as well (from 5 to 10meV). Such small predicted gaps are within the realm of observation for ultra clean graphene-hBN samples (disorder energy scale ∼1meV). None of these predicted gaps are of a large enough size though to make graphene useful as a digital transistor, but are of fundamental interest for demonstrating the controlled and precise modification of graphene's properties.

■ 3.2.2 Superlattices and magnetic fields - Hofstadter's butterfly

In addition to locally breaking the graphene sublattice symmetry, the hBN also introduces a potential modulation on the length scale of the moiré superlattice. The wavelength of the moiré superlattice is given by [240]:

$$\lambda = \frac{(1+\delta)a}{\sqrt{2(1+\delta)(1-cos\theta)+\delta^2}},$$

where a is the graphene lattice constant, δ is the lattice mismatch between the hBN and the graphene, and θ is the relative rotation angle between the two lattices. The largest wavelength is for $\theta = 0$, which has a value of of 14nm. At the densities relevant for transport measurements ($1e11\text{cm}^{-2}$ to $1e13\text{cm}^{-2}$), the Fermi wavelength ($\lambda_F = 2\sqrt{\pi/n}$) will be about 100nm to 10nm in size. This is typically much larger than the length scale of the superlattice perturbation (Figure 3.5), and hence there should be very little effect on the low energy band structure except at very low twist angles.

The first direct evidence of hBN modifying the graphene electronic structure came from STM measurements[240]. The authors observed high energy dips in the local density of states, which correlated with the observed moiré wavelength as $E = \hbar v_F|\boldsymbol{G}|/2 = 2\pi\hbar v_F/\sqrt{3}\lambda$, where G is the smallest reciprocal superlattice vector. This can be un-

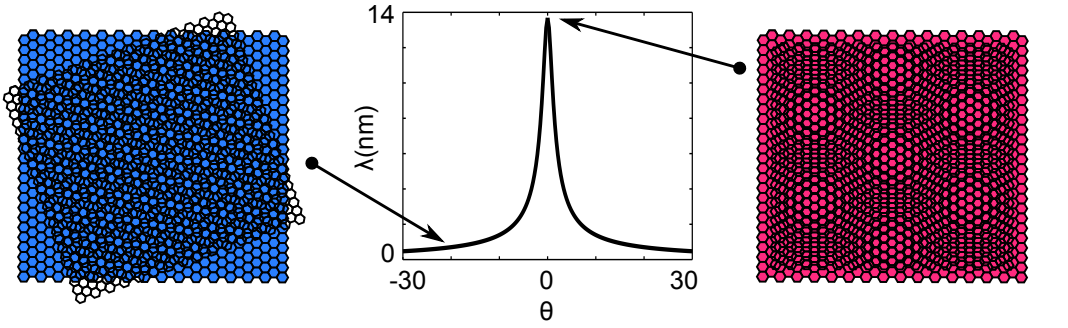

Figure 3.5. The length scale of a moiré superlattice depends sensitively on the twist angle between the graphene and hBN. Plots shows the dependence of the wavelength of a graphene-hBN superlattice on the relative twist angle between the two crystal lattices.

derstood as arising from scattering processes off the superlattice potential which causes a zone folding of the graphene bandstructure into the reduced superlattice Brillouin zone[176, 177]. The result is a high-energy replication of the zero energy Dirac point which appear as dips in the local density of states.

The behavior of electrons under the simultaneous influence of a magnetic field and a periodic potential is both a fascinating and classic problem[13][92]. Two of the main approaches start by considering a Bloch band under the influence of a magnetic field, or a Landau level in a periodic potential. Either way, the greatest departures from the initial energy structure occurs when the magnetic length $l_B = \sqrt{\hbar/eB}$ is comparable to the length scale of the periodic potential. For atomic scale potentials, this would correspond to a magnetic field of $10,000$T. But, for a superlattice in the 10 nanometer range, a magnetic field of only 40T would be necessary. An additional requirement for observing these effects is that the energy scale of the periodic potential and the Landau level gaps be greater than the disorder.

The interest in this regime originates from the empirical studies by Hofstadter [92] of the spectrum for a square lattice in a magnetic field. There he found a surprisingly rich structure of subband splittings in the electronic spectra, which he observed to have a self-referential, or fractal, structure of gaps (Figure 3.1). This structure originates from the curious fact that for rational values of flux quanta per unit cell $\phi/\phi_0 = p/q$, a Bloch band of states will divide into q subbands, while a Landau level under the influence of a periodic potential will be divided up into p subbands. The details of the different gap sizes will depend on the specific details of the periodic potential, with the square lattice having been proven rigorously to produce a fractal spectrum[137].

Transport measurements are only sensitive to electronic states near the Fermi level, and hence do not directly access spectral gaps. Instead, it is possible to measure the Hall conductance at a given charge density whenever the sample is in a bulk gapped state. As originally described by Wannier[227], gaps induced by a magnetic field and a periodic potential are constrained to follow straight lines as a function of charge density and magnetic field:

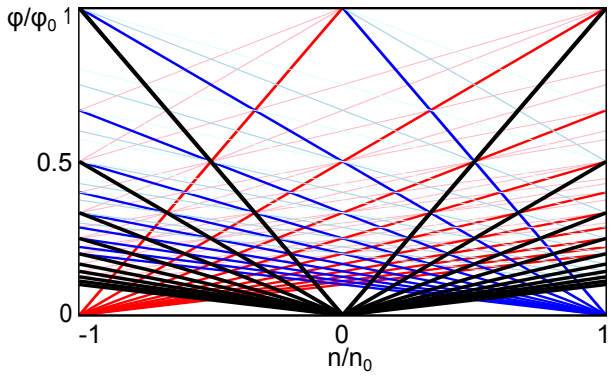

Figure 3.6. Wannier plot of allowed gaps as a function of superlattice filling fraction n/n_0 and the flux quanta per superlattice unit cell ϕ/ϕ_0. Plotted lines are for $s = 0, \pm 1, \pm 2$ and $t = -10$ to 10. Black lines are $s = 0$, red lines are $s = -1$ and blue lines are $s = 1$.

$$(n/n_0) = t(\phi/\phi_0) + s \tag{3.2}$$

Here, n/n_0 is the filling fraction of the superlattice unit cell, ϕ/ϕ_0 is the flux quanta per superlattice unit cell, s is the Bloch band filling index (analogous to the Landau level index), and t specifies the Hall conductivity of the system such that $\sigma_{xy} = te^2/h$ [217]. It is interesting to consider that Hofstadter's work predated the discovery of the quantum Hall effect in 1980[115], but it was the analysis by TKKN[217] of the problem of a periodic potential in a magnetic field that established the value t as the topological invariant for the quantum Hall system.

An example of a Wannier plot of possible gaps is shown in Figure 3.6. Even Wannier himself noted that replotting Hofstadter's butterfly in this way results in an "esthetic loss," since it is the varying energy gap structure which gives the most striking fractal appearance [227]. Fortunately, this recursive pattern becomes more evident in a transport measurement, since the Hall conductivity will be different for different gaps[217]. In addition, the gap size can be indirectly visualized, since it affects how the transport measurement behaves if the gap is changing its value relative to the energy scale of disorder and temperature. A picture can be painted by considering that the recursive structure is based on a "skeleton" defined by the fractional sequence $\phi/\phi_0 = 1/q$ (see Figure 3.1). These points act as an effective zero magnetic field. Emerging from them will be new magneto-oscillations and a repetition of the butterfly structure as a function of the magnetic field, δB, measured relative to the point $1/q$ [28]. Very roughly speaking, the subband gap size will increase with the effective magnetic field δB, with the associated transport features starting as Shubnikov-de Haas oscillations and then transitioning to a full blown quantum Hall effect. In this sense then the fractal structure will be apparent in a transport measurement as a function of density and magnetic field as a series of repeating Landau "fans" that emanate from points where $\phi/\phi_0 = 1/q$, some with apparently negative sign of magnetic field as well. In the end though, numer-

ical calculations will be necessary since the details of the spectrum and the transport features will depend on the very specific nature of the periodic potential.

Experimental studies of Hofstadter's butterfly have been primarily focused on two-dimensional electron gases in GaAs[4, 66, 149, 195], where the 2DEG layer was located only ∼30nm from the crystal surface. This allows for a periodic electrostatic gate to be made on top to provide the superlattice modulation. These studies were able to successfully demonstrate many of the features expected of Hofstadter's butterfly, such as the splitting of Landau levels into subbands[195] and their specific Hall plateau sequence[4, 217].

Compared to these GaAs 2DEG studies there are a couple of new things that the graphene-hBN system can bring to the table. One of the most important is the ability to electrostatically tune the graphene carrier density over a wide range without sacrificing the sample quality. This allows for the exploration of a wide range of features in density space, and produces nice looking colorplots (which is one of graphene's great strengths). Since the graphene-hBN superlattice is defined by pristine crystals, the resulting periodic potential should be disorder-free in comparison to lithographically-defined features. This opens the possibility of exploring more delicate effects in the presence of a periodic potential, such as interaction-driven states including the fractional quantum Hall effect.

■ 3.3 Experiment details

Our discovery of a bandgap in a graphene-hBN heterostructure was an accident. While attempting to realize a monolayer quantum spin Hall state (see previous chapter), we fabricated and measured a large quantity of graphene on hBN devices with local graphite backgates. One set was different than all the others: they displayed deep insulating states at the charge neutrality point. Intriguingly, the same day we made the measurements, an arxiv posting from the Goldharber-Gordon group revealed a similar behavior in their samples[8]. This mystery was deepened, and eventually resolved, by our observation of superlattice potential effects which connected the insulating states with the graphene-hBN moiré. A fortuitous circumstance was that these devices all originated from the same graphene flake (Figure3.3), but with wrinkles dividing the different regions, resulting in slightly different twist angles for each device. To reach beyond the limit of one flux quanta per superlattice unit cell, it was necessary to measure in the hybrid magnet at the National High Magnetic Field lab, which has a maximum continuous output field of 45.1T (world record holder). After completion of the magnetotransport measurements, the devices were measured in a STM by our collaborators Brian Leroy and Matthew Yankowitz at University of Arizona, who determined the superlattice wavelength directly from topographic imaging.

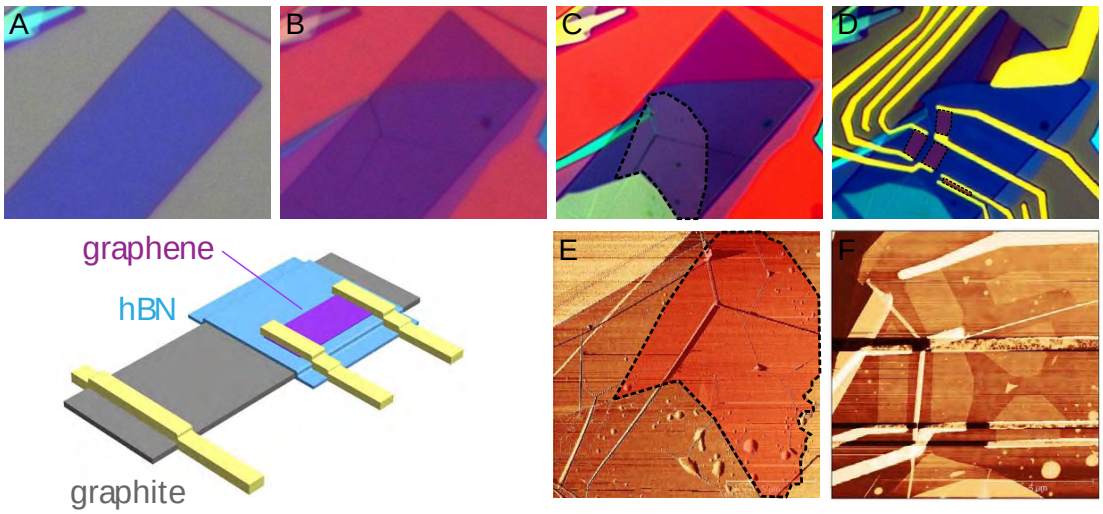

Figure 3.7. Device fabrication steps for a graphene-hBN superlattice sample. A-D are optical images and E/F are AFM images of the fabrication steps for the devices. Scale of optical images is 32.5um wide **(A)** Etched graphite bar on Si/SiO_2 wafer serves as a local backgate. **(B)** After transfer of 7 nm-thick hBN flake, wrinkles in hBN are visible. **(C)** After graphene transfer (dash line depicts graphene boundary). **(D)** Final contacted and etched device (graphene strips are false colored red). **(E)** AFM image of graphene (red false color) on hBN. Large wrinkles in hBN are visible (1-80nm in height), forming a triangular structure **(F)** AFM image of final contacted and etched device. Each of the four devices are seperated from the others via a wrinkle in the graphene/hBN.

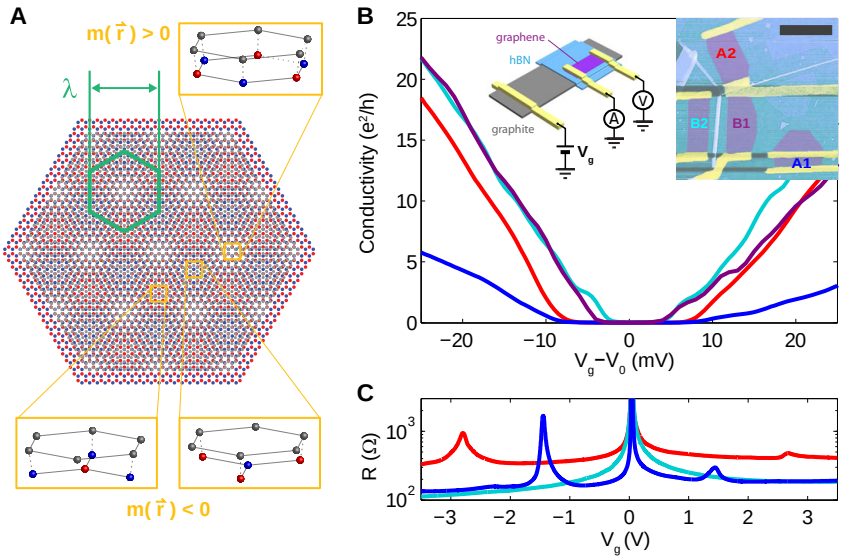

Figure 3.8. Insulating states and superlattice minibands in a graphene/hBN heterostructure. (A) Schematic of the moiré pattern for graphene (gray) on hBN (red and blue), for zero misalignment angle and an exaggerated lattice mismatch of $\sim 10\%$. The moiré unit cell is outlined in green. Regions of local quasi-epitaxial alignment lead to opposite signs of the sublattice asymmetry, $m(\vec{r})$, in different regions. **(B)** Low temperature (T=150 mK) conductivity near charge neutrality of four heterostructure devices (A1, A2, B1 and B2). The CNP offset V_0=37, 37, 46 and 42 mV, respectively. Left inset: Measurement schematic. Right inset: AFM image. Scale bar is 3 μm. **(C)** Resistance over a larger gate range. Finite-density resistance peaks indicate full filling of the lowest superlattice miniband in two of the four measured devices (A1 and A2) within the experimentally-accessible density range.

■ 3.4 Massive Dirac Fermions and Hofstadter Butterfly in a van der Waals Heterostructure

The following is the text reproduced from the publication Hunt, Sanchez-Yamagishi, Young et.al. [97]. The section following this one will then end the chapter with a few notes on new developments since the completion of this work.

Van der Waals heterostructures comprise a new class of artificial materials formed by stacking atomically-thin planar crystals. Here, we demonstrate band structure engineering in a van der Waals heterostructure composed of a monolayer graphene flake coupled to a rotationally-aligned hexagonal boron nitride substrate. The spatially-varying interlayer atomic registry results both in a local breaking of the carbon sublattice symmetry and a long-range moiré superlattice potential in the graphene. In our samples, this interplay between short- and long-wavelength effects resulted in a band structure described by isolated superlattice minibands and an unexpectedly large band gap at charge neutrality. This picture is confirmed by our observation of fractional quantum Hall states at $\pm 5/3$ filling and features associated with

the Hofstadter butterfly at ultra-high magnetic fields.

The ability to tailor the properties of electronic devices is one of the landmark achievements of modern technology, and motivates a sizable fraction of modern research in condensed matter physics. Just as crystal structure can determine the electronic properties of a material, artificial periodic superstructures can be used to modify the electronic band structure of existing materials [220]. The band structure of pristine graphene consists of linearly dispersing energy bands, which touch at two degenerate "Dirac points". This degeneracy is protected by the equivalence of the A and B triangular sublattices that make up the graphene honeycomb [222], and is responsible for graphene's semimetallic behavior. Theory suggests that the electronic properties of graphene can be tuned via external periodic potentials: long-wavelength superlattices have been predicted to lead to the formation of additional gapless Dirac points at finite energy[177], while atomic scale modulations, by breaking the A-B sublattice symmetry, may turn graphene from a semimetal into a semiconductor[69]. Experimental efforts to make high-mobility functional devices based on band structure engineering, however, have been hindered by growth and nanofabrication limitations[199].

Recently, a new approach has become available through the use of hexagonal boron nitride (hBN) as a planar crystalline substrate. hBN is isostructural to graphene, but has boron and nitrogen atoms on the A and B sublattices leading to a large band gap[121]. The weak interlayer van der Waals forces in both graphene and hBN permit the fabrication of multilayer heterostructures by sequential transfer of individual layers[43]. During the transfer process, the angular alignment of the constituent crystals (θ) can in principle be controlled, but the graphene and hBN lattices retain their natural 1.8% mismatch [69]. The beating of the mismatched lattices leads to the formation of a moiré pattern with wavelength $\lambda(\theta)$ that can be much larger than the lattice constant [240](Figure 3.8A, for more details see Appendix C.2).

The effect of the moiré on the graphene electronic structure can be decomposed into two parts[113]. The moiré pattern results in a λ-scale modulation of the graphene-hBN coupling, forming a smooth superlattice potential. More subtly, the moiré also modulates the local asymmetry between the graphene sublattices induced by the difference in potential between boron and nitrogen atoms in the hBN. The resulting A-B potential difference in the graphene, parameterized in Figure 3.8A as $m(\vec{r})$, oscillates across the superlattice unit cell [151], leading to nearly complete cancellation[113] upon spatial average. As we demonstrate, however, the absence of sublattice symmetry nonetheless has considerable experimental consequences for the electronic properties near the charge neutrality point.

We present measurements of four heterostructure devices consisting of a monolayer graphene flake on a 7 nm-thick hBN substrate (details in Section 3.3), which itself sits on top of a graphite local gate (Figure 3.8B). The proximal gate electrode serve both as an extremely flat substrate and to screen long-range potential fluctuations in the graphene[181], leading to high quality devices with field effect mobilities $\sim$100,000 $\mathrm{cm}^2/\mathrm{V}\cdot\mathrm{s}$ and well-quantized quantum Hall plateaus at fields $B \lesssim 100$ mT (for additional

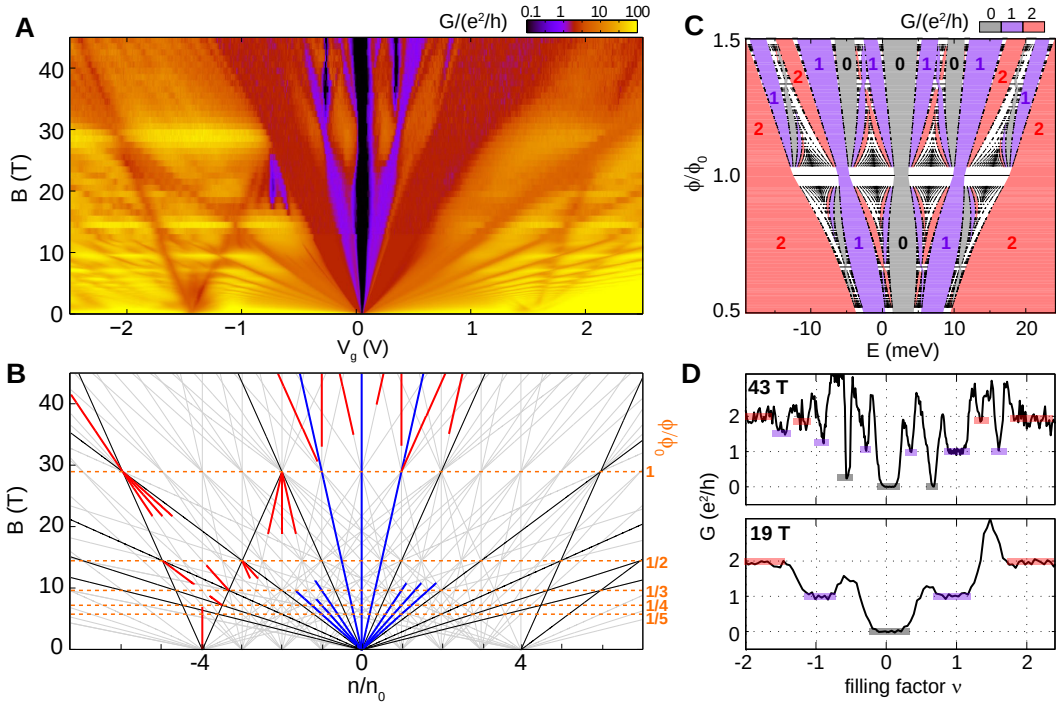

Figure 3.9. Hofstadter butterfly. **(A)** Two-terminal magnetoconductance of device A1 up to 45 T. **(B)** In Wannier's theory [227], energy gaps in the Hofstadter spectrum are confined to linear trajectories $\phi/\phi_0 = (n/n_0 - s)/t$, where s and t are integers denoting the superlattice miniband filling index [137] and quantized Hall conductance of the gapped state, respectively. Grey lines indicate gaps for $-4 \leq s \leq 4$, with colored overlays indicating features observed in (A). Black: gaps requiring no broken symmetry; Blue: broken-symmetry states for the central Landau fan. Red: symmetry broken states belonging to superlattice ($s \neq 0$) Landau fans. Gaps intersect at $\phi/\phi_0 = 1/q$, with q an integer (orange); $\phi = \phi_0$ at 29T. **(C)** Theoretical Hofstadter energy spectrum for the fully spin- and sublattice-split $N = 0$ Landau level [119] (more details in Appendix sec:App-Hoff-Koshino). Black points indicate regions of dense energy bands; intervening spectral gaps are color-coded to the associated two-terminal conductance $G = 2$ (red), 1 (purple) and 0 (grey) in units of e^2/h. **(D)** Conductance traces within the $N = 0$ LL at B=43T (top) and B=19 T (bottom). Shaded rectangles are color-coded to the expected two-terminal conductance from the Hofstadter model of (C). The emergence of Hofstadter minigaps, characterized by a non-monotonic sequence of quantized conductance plateaus, is evident in the 43T data, where $\phi > \phi_0$. At 19T, the quantum Hall sequence is the standard monotonic $G = |\nu|e^2/h$. Peaks between plateaus are due to diffusive transport in this wide-aspect-ratio device.

details see Appendix C.1). In contrast to the majority of graphene devices, which, with few exceptions[10, 181], are semimetallic with zero-field minimum conductivity $\sim 2e^2/h$, all four devices are strongly insulating near the overall charge neutrality point (CNP) (Figure 3.8B). In addition, two devices show pronounced resistance peaks at finite density (Figure 3.8C), situated symmetrically about the CNP. Notably, the devices showing additional resistance peaks also have the strongest insulating states.

We ascribe the satellite resistance peaks to the Bragg scattering of charge carriers

by the superlattice when the lowest electron and hole minibands are fully occupied [41, 182, 223, 240]. In graphene, as a consequence of the spin and valley degeneracies, full filling occurs at a density of four electrons per superlattice unit cell, $n = 4n_0$, where $1/n_0 = \sqrt{3}\lambda^2/2$ is the unit cell area (Figure 3.8A). Using the density at which the peaks are observed for devices A1 and A2, we estimate λ_{A1}=11-13.5nm and λ_{A2}=7.5-9.5nm, where the error is dominated by uncertainty in the value of the hBN dielectric constant (for additional details see Appendix C.2). Such large values of λ, not much smaller than the theoretical maximum of 14 nm, imply nearly perfect rotational alignment of the graphene and hBN, with $\theta < 2°$ for the two devices showing satellite peaks. Although we do not observe satellite peaks in devices B1 and B2, scanning tunneling topography measurements reveal moiré patterns with λ_{B1}=3.8nm and λ_{B2}=3.5nm, corresponding to close alignment with $\theta \sim 4°$ (more details in Appendix C.2).

The moiré pattern offers a unique opportunity to study the elementary problem of a charged quantum particle moving under the simultaneous influence of a periodic potential and a magnetic field[4, 13, 92, 195] in the normally inaccessible regime of more than one magnetic flux quantum (ϕ_0) per superlattice unit cell. In the absence of the superlattice, graphene is described at high fields by a set of discrete, highly degenerate Landau levels (LLs) indexed by an integer N. The periodic potential splits the flat LL bands into "Hofstadter minibands" separated by a hierarchy of self-similar minigaps[92]. Despite the intricate structure of the Hofstadter spectrum, the densities corresponding to the fractal minigaps follow simple linear trajectories as a function of magnetic field[227]. Magnetoresistance data indeed show strong effects of the superlattice (Figure 3.9A), including Landau fans originating from both the central and satellite zero-field resistance peaks. As recently demonstrated, the intersections between the central and satellite fans occur at $\phi = \phi_0/q$ (Figure 3.9B), where ϕ is the magnetic flux per superlattice unit cell and q is a positive integer [41, 182]. These intersections allow a second, independent method of measuring the unit cell area without reference to electrostatic parameters(see Appendix C.2), giving $\lambda_{A1} = 12.9 \pm 0.2$ nm and $\lambda_{A2} = 9.2 \pm 0.1$ nm.

The full development of the Hofstadter butterfly, however, is most obvious in the regime $\phi/\phi_0 > 1$, which is challenging to access in monolayer graphene. Figure 3.9D shows the conductance within the N=0 Landau level for two values of field corresponding to $\phi < \phi_0$ and $\phi > \phi_0$. At the higher field, the N=0 LL is completely reconstructed, with a nonmonotonic sequence of conductance plateaus well-matched by tight-binding calculations of the Hofstadter butterfly spectrum in which phenomenological spin and sublattice symmetry-breaking terms have been included (Figure 3.9C) (Additional details in Appendix C.3). The emergence of states with integer quantized conductance at noninteger filling of a single Landau level, severing the canonical relationship between quantized conductance and filling fraction, is the signature of the Hofstadter butterfly.

Equating the effect of the hBN substrate with that of a smooth superlattice potential explains many features of the experimental data, including the satellite resistance peaks and most features of the ultra-high B transport data. However, it fails to account for the insulating state observed at charge neutrality, which persists uninterrupted from B=0

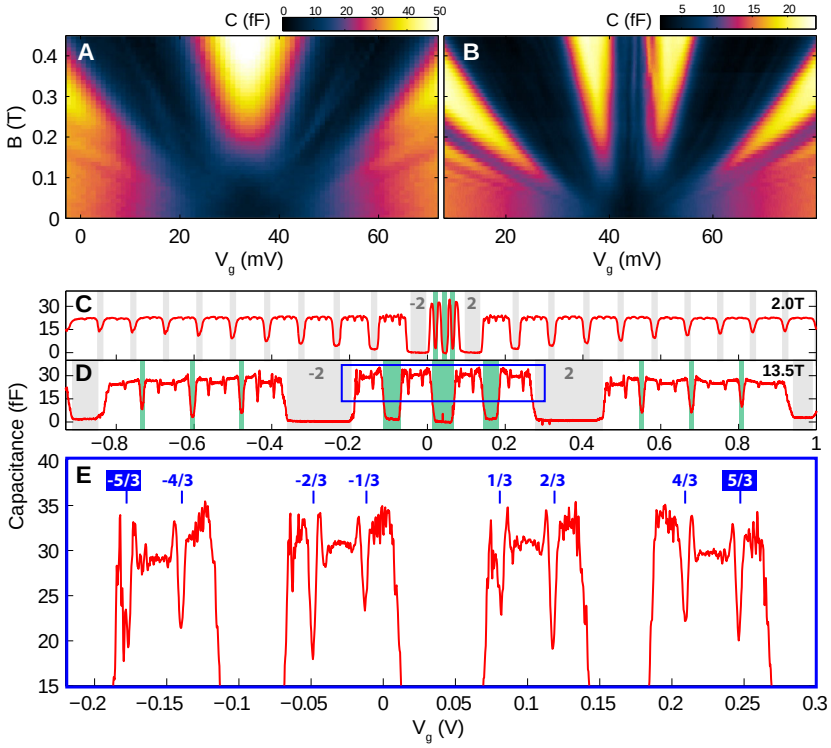

Figure 3.10. Magnetocapacitance of semimetallic and insulating graphene devices. (A) Capacitance of a typical semimetallic graphene device. The zero-energy Landau level forms at ~ 0.15T, appearing as a local maximum at the CNP ($V_g = 34.5$ mV). **(B)** Capacitance of an insulating graphene device (B2) under similar conditions. In contrast to (A), the density of states is at a local minimum for all fields at charge neutrality ($V_g = 44$ mV). **(C)** Capacitance of device B2 at B=2.0 T and **(D)** 13.5 T. Cyclotron gaps are shaded grey ($\nu = \pm 2$ labeled) and broken-symmetry gaps are shaded green. **(E)** Fractional quantum Hall (FQH) states in the $N = 0$ LL. The incompressible features at $\nu = \pm\frac{5}{3}$ are of similar strength to the other FQH states.

to 45 T. To further explore the properties of this state, we measure the capacitance of the graphene to the proximal graphite back-gate using a low-temperature capacitance bridge [12](details for capacitance measurements can be found in Appendix C.6). Capacitance measurements probe the thermodynamic density of states, $\partial n/\partial \mu$; for our parallel plate geometry, the measured capacitance $C_{meas}^{-1} = C_{geom}^{-1} + (Ae^2 \partial n/\partial \mu)^{-1}$, where C_{geom} is the geometric capacitance and A is the sample area [136]. Figure 3.10A shows magnetocapacitance data from a typical, semimetallic graphene-on-hBN device. The capacitance, and by extension the density of states, has a minimum at charge neutrality. As the field is increased, this minimum is replaced by a local maximum, signifying the formation of the zero-energy Landau level characteristic of massless Dirac fermions[65]. Capacitance measurements of an insulating graphene device reveal very different behavior (Figure 3.10B). No peak forms at the CNP at finite field, as can be

seen from the dark vertical region centered at $V_g = 41$ mV, indicating that the N=0 Landau is split into two finite-energy sublevels; in other words, a Landau level never forms at zero energy.

As we increase the field further (Figure 3.10C), additional minima in capacitance appear at all integer filling factors ν – including those not belonging to the standard monolayer graphene sequence – indicating the emergence of exchange-driven broken symmetry states [244]. Capacitance minima associated with fractional quantum Hall states appear (Figure 3.10D) at all multiples of 1/3 for -2< ν <2. Notably, this sequence includes robust features at $\nu = \pm\frac{5}{3}$ not observed in previous studies [42,57] of semimetallic monolayer graphene. These states are thought to be described by a fully spin- and sublattice-polarized Laughlin wavefunction [11,218]; their absence in semimetallic graphene is attributed[42,204] to the low energy cost of exciting charge carriers to the unoccupied, energetically-equivalent sublattice. Our observation of the $\pm\frac{5}{3}$ states suggests that sublattice symmetry is broken in our graphene-hBN heterostructures.

In the Dirac equation description of graphene, sublattice symmetry breaking can be parameterized by a mass. In our heterostructures, this mass term $m(\vec{r})$ is expected to oscillate across the moiré unit cell (Figure 3.8A). Notably, the low-density phenomenology of our insulating graphene at low fields ($\phi \ll \phi_0$), including the insulating gap, the absence of a zero-energy Landau level, and the observation of the $\nu = \pm\frac{5}{3}$ states, can be captured by a Dirac equation with a spatially-uniform global effective mass, m^*. The resulting Hamiltonian describing physics in the vicinity of the $K(K')$ point is

$$\hat{H} = v_F \boldsymbol{\sigma} \cdot \boldsymbol{p} + m^* v_F^2 \hat{\sigma}_z \tag{3.3}$$

$$= \begin{pmatrix} \pm m^* v_F^2 & v_F(p_x - ip_y) \\ v_F(p_x + ip_y) & \mp m^* v_F^2 \end{pmatrix} \tag{3.4}$$

where v_F is the Fermi velocity, $\boldsymbol{\sigma} = (\sigma_x, \sigma_y)$, and the Pauli matrices $\{\sigma_i\}$ operate in the basis of the two sublattices. The resulting energy spectrum at zero magnetic field, $E(p) = \pm\sqrt{v_F^2 p^2 + (m^* v_F^2)^2}$, features a band gap $\Delta = 2m^* v_F^2$ at charge neutrality. In a quantizing magnetic field, the Landau level spectrum is given by $E_N = \pm\sqrt{2(\hbar v_F)^2 |N| / \ell_B^2 + \left(m^* v_F^2\right)^2}$, where $\ell_B = \sqrt{\hbar/(eB)}$ is the magnetic length (see Appendix C.4). The mass term does not lift the LL degeneracy for $|N|$ >0; this is reflected in our data (Figure 3.10C) by the observation of symmetry breaking in the higher Landau levels only at higher magnetic fields, presumably due to exchange interactions, as in semimetallic graphene[244]. However, the splitting of the N=0 LL into two sublattice-polarized branches at $E_0 = \pm m^* v_F^2$ is consistent with the persistent gap at charge neutrality, as well as the observation of the $\pm\frac{5}{3}$ fractional quantum Hall states.

The observation of band gaps in samples with long wavelength moiré patterns is not likely to be coincidental. Naively, $m(\vec{r})$ nearly vanishes upon spatial average, calling into question whether a mismatched hBN substrate can open a measurable gap. Indeed, predictions for how the global parameter m^* depends on the microscopic structure of

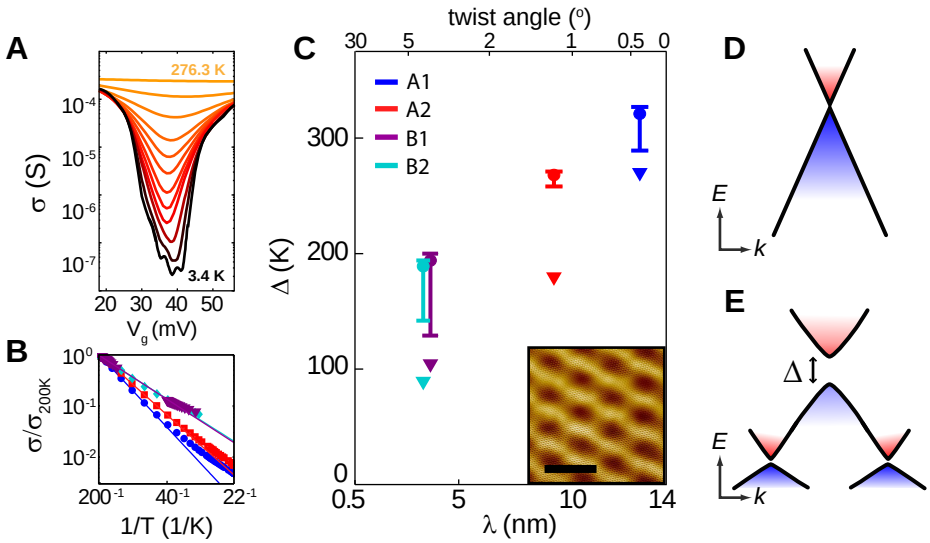

Figure 3.11. Energy gaps of the zero-field insulator. **(A)** Conductivity of the insulator device A1 at a series of temperatures. **(B)** Arrhenius plot of σ_{CNP} for all four devices. Lines are fits to $\sigma_{CNP}(T) \propto \exp(-\Delta/2T)$, giving Δ_{A1}=321 K, Δ_{A2}=268 K, Δ_{B1}=194 K, and Δ_{B2}=189 K. **(C)** Correlation of observed band gaps with moiré wavelength λ. Circles: thermal activation gap (Figure 3.9B); error bars are estimated from the uncertainty in the range of simply-activated behavior. Triangles: width in gate voltage of insulating state. λ is extracted from the period of the Hofstadter oscillations for A1 and A2, and from STM measurements for B1 and B2. Inset: Scanning tunneling topography image of B2 (5 nm scale bar). **(D)** Schematic band structure for semimetallic graphene. **(E)** Schematic band structure for an insulating graphene-hBN heterostructure, showing the band gap and moiré minibands.

$m(\vec{r})$ vary by several orders of magnitude depending on theoretical assumptions[69, 113, 190, 210]. We quantitatively assess the connection between λ and m^* by measuring the band gap using thermally-activated transport (Figure 3.11A-B) and, independently, by measuring the width in gate voltage of the insulating state, which places an upper bound on the chemical potential difference across the band gap (see Appendix C.5). Figure 3.11C shows a correlation between moiré wavelength and the measured gaps, suggesting that the interaction of the graphene flake with the closely-aligned hBN substrate is responsible for the insulating behavior. Single-particle theories of graphene on hBN [113, 190] predict $\Delta \sim 5 - 10$ meV for zero misalignment angle, for which the gap is expected to be maximal. Our measured band gaps exceed these predictions even for non-zero twist. In addition, the discrepancy between the two methods for gap determination implies that Δ depends on chemical potential, suggesting that many-body interactions may play a role in enhancing Δ[210]. However, quantitative comparison with the predicted power-law dependence of $\Delta(\lambda)$ will require more extensive data.

The ability to engineer a non-zero band mass in graphene has far-reaching implications for future experimental efforts. The possibility of an alignment-dependent mass may require a reinterpretation of experiments involving graphene-hBN heterostructures,

even as it engenders new opportunities for the design of electronic devices. The gapped spectrum and the tunability of the associated effective mass provide both a useful tool in nanoengineering based on electrostatic confinement as well as a new design parameter in the study of many-body effects in monolayer graphene.

3.5 Epilogue

In the last year since the completion and publication of the experiments in this chapter[97], progress has been made in understanding the mechanism for the insulating state observed in nearly-aligned graphene on hBN. Raman and frictional force microscopy studies on graphene-hBN heterostructures[50, 230] give evidence for a periodic strain redistribution in aligned graphene/hBN. Although the stacking arrangement has not been observed directly, the strain distribution could contribute to the observed insulating state, either through increasing the sublattice symmetry breaking effects of the hBN or via associated strain pseudo-magnetic fields which will gap out regions of the sample[81].

A massive graphene Dirac band should have a nonzero Berry curvature with an associated valley Hall effect, whereby a valley current is created by the application of a transverse charge current[234]. Recently, this effect has been observed for the first time in an aligned graphene-hBN heterostructure[79].

Contemporary to the work described in this chapter, there has also been interesting progress in realizing artificial magnetic fields in optical lattices for ultracold atoms[3, 99, 155].

Chapter 4

Edge States in Twisted Bilayer Graphene

4.1 Introduction - twisted bilayer graphene

STACKING a graphene sheet on top of another with a twist will cause a super-periodic pattern to emerge (Figure 4.1). Looking closely at the dark and light spots of the pattern will reveal that the contrast arises from different atomic stackings between the two layers. Twisting the layers further causes the pattern to shrink in size to a minimum value, and then suddenly grow again, expanding outwards until the super-periodic pattern is no longer perceptible in the field of view. This pattern is called a moiré, and arises whenever two different periodic structures are overlaid and visualized together, for example in a layered sheer fabric. Besides being aesthetically pleasing, the visual moiré corresponds to a periodic electronic coupling between the two graphene sheets on a length scale often much larger than the atomic-scale lattice constant. As a result, the arresting development of the moiré pattern also has a strong effect on the graphene electronic properties.

The above considerations are not just for fun; the stacking of two graphene layers to make "twisted" bilayer graphene is both possible and naturally occurring in various graphene growth processes. It is a unique form of crystal disorder: individual layers can have no correlation in their relative orientation, yet are each perfect planar crystals. This is made possible by graphene's mechanical structure, which has strong carbon-carbon

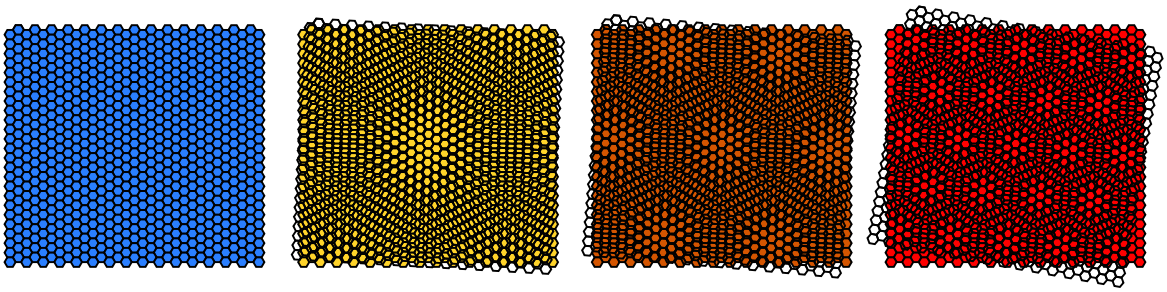

Figure 4.1. A moiré emerges when twisting a graphene bilayer.

covalent bonds in-plane and weak van der Waals like adhesion between the planes.

Twisted bilayer graphene (TwBLG) is the most generic form of the graphene bilayer. It is called "twisted" to differentiate it from the AB-stacking prevalent in highly-ordered pyrolytic graphite, which was used in all the original monolayer graphene studies[168, 169, 250]. The moiré that results from the relative twist is a periodically changing pattern of local atomic stacking configurations between the layers, and has great consequences for the electronic structure of the system. TwBLG is attractive in that it adds just the right amount of complexity to monolayer graphene, both a new layer degree of freedom and an interlayer coupling which is tunable by twist angle. These are the ingredients for a wide-range of possible electronic behaviors.

Below, I list some of the general motivations for studying the electronic properties of twisted bilayer graphene:

- **Bilayer 2DEGs in GaAs display interesting physics.** A pair of closely spaced 2-dimensional electron gases will interact via tunneling or Coulomb interactions. Many interesting phenomena have been demonstrated in this system, including indirect excitons, Coulomb drag, and interlayer exciton condensates ([52, 80, 209]). TwBLG may provide an analogous graphene-based system, where the relative twist decouples the layers enough so that the layer degree of freedom becomes a good quantum number.

- **Graphene growth typically produces twisted layers.** Because of the weak interlayer forces, most graphene production methods produce multilayers with rotational misalignments. Examples of this include chemical vapor deposition[109, 184], epitaxial growth on SiC[55], and solution-based mechanical exfoliation[90].

- **Twisted layers are technologically relevant.** Monolayer graphene has the highest mobility, as compared to other stacking of graphene. Twisting allows for multiple layers of graphene to be stacked, yet still retain the monolayer-like qualities.

- **Twisting physics is a general phenomena of van der Waals heterostructures.** As van der Waals heterostructures receive increasing attention[63, 97], the rotational alignment between stacked layers in a heterostructure will play an important role. We already discussed such effects in the previous chapter for graphene-hBN heterostructures. TwBLG offers an archetypal twisted interface to study. In fact, the theoretical approaches originally developed to describe TwBLG[134, 148] are now being applying to other types of twisted heterostructures[113].

In this chapter, I will present our quantum Hall studies in TwBLG and demonstrate its use as a platform for building unique edge states. The primary result is that the individual layers of TwBLG do not directly couple in the bulk, despite their tiny 0.34 nm interlayer spacing (Section 4.4). This occurs when the twist angle between the layers is large. By using dual electrostatic gates, we can independently control the number

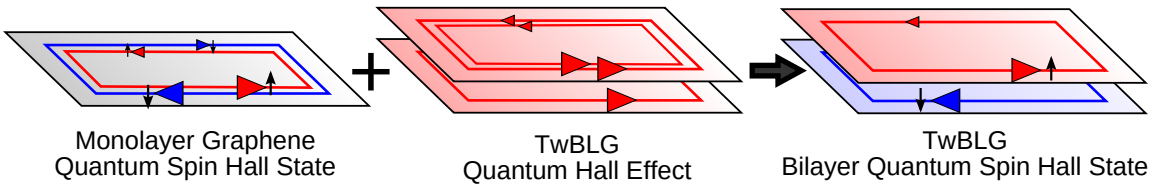

Figure 4.2. It is possible to realize a new type of quantum spin Hall state in twisted bilayer graphene.

of edge states on each layer and also observe the effects of interlayer interaction along the edge. We take advantage of this behavior to realize a bilayer form of a quantum spin Hall (QSH) state (Section 4.5). It is very similar to the QSH state I discussed previously in monolayer graphene—two coexisting edge states with opposite chiralities and opposite spin polarizations—but in this case, the two edge states occupy different layers (Figure 4.2).

To induce the monolayer graphene QSH state, we required a very large in-plane magnetic field (Chapter 2). TwBLG offers a route to create a configurable QSH state at a much lower field since it does not require a large Zeeman splitting. The proposed bilayer QSH state is also unique, because its constituent edge modes are localized on different layers and hence can be independently contacted. This is in contrast to normal QSH systems, where spin-selective leads would be necessary to accomplish the same task[23]. In TwBLG, it is also natural to consider fractional generalizations of this bilayer QSH state. By doping each edge to a fractional filling, we can envision counter-propagating fractional edge modes which are spin-protected from mixing. Recenty, theoretical proposals have considered the use of such "fractional quantum spin Hall" states to realize generalized forms of Majorana fermions[14, 34, 37, 131, 221]. These "parafermion" bound states are predicted to provide a greater range of topological protected quantum gates than are possible with just a Majorana bound state.

In the next section, I'll begin with a brief review of the twisted bilayer graphene literature relevant to our transport studies. Following that, I'll discuss our electronic transport measurements on dual-gated TwBLG devices and our study of the quantum Hall effect in TwBLG. Lastly, I will present our observation of broken-symmetry states in TwBLG and our demonstration of a bilayer quantum spin Hall state.

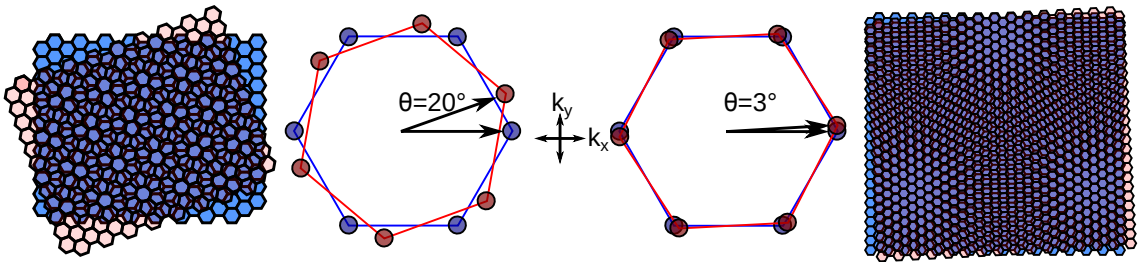

Figure 4.3. Decoupling of layers in twisted bilayer graphene is controlled by the twist angle. Lattice structure of twisted bilayer graphene for twist angles $\theta = 20°$ and $3°$ (left and right respectively). The twist angle controls the overlap of the Fermi surfaces for the bottom and top layers (blue and red circles, respectively).

4.2 Background

4.2.1 Twisted bilayer graphene

The study of twisted bilayer graphene and crystalline moirés begins with scanning tunneling microscopy (STM) studies on graphite. Highly ordered pyrolytic graphite (HOPG) was a common sample standard for early STM studies, due to the extreme flatness and ease in cleaving to make clean sample surfaces. Early on, researchers observed periodic patterns in STM topography scans on HOPG, where the size of the periodicity was much larger than the graphite lattice constant[24, 186]. It was already then inferred that this moiré was due to a rotational misalignment of the top graphene layer with respect to the rest of the graphite stack.

The first indication that rotionally misaligned graphene can result in electronic decoupling came from studies both of graphene multilayers both grown on SiC[15, 212, 231], and of graphite[127]. In both cases, monolayer graphene physics was observed, despite the presence of multiply stacked layers. This was attributed to rotational misalignment of the top layer, and was further backed up by ab-inito calculations which showed an electronic decoupling between the layers[87, 123]. We can get an intuitive picture for why this occurs by consider the shape of the Fermi surfaces in momentum space coming from each layer (Figure 4.3). The Fermi surfaces form small circles centered at the large momentum values K and K'. For a large twist angle, the circles will be separated in momentum space without any overlap. This results in a momentum mismatch between the layer Fermi surfaces, which causes the twist decoupling.

A more rigorous model for the twist-dependent coupling was first presented by Lopes dos Santos et. al. [134], who considered an interlayer coupling which retained only the nearest-neighbor hopping from an atom in one layer to the nearest atom in the other layer. From a simple continuum model they made the following predictions:

1. Twisting causes the Dirac cones from each layer to separate in momentum space by $\Delta K = sin(\theta/2)$, resulting in a decoupling between the layers at low energies (Figure E.4).

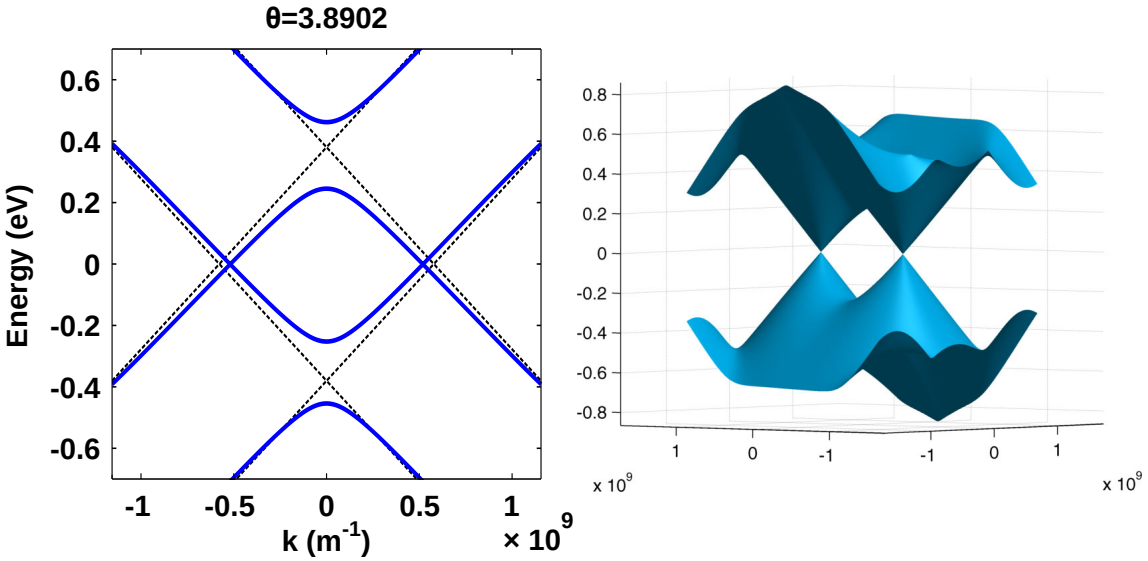

Figure 4.4. Twisting separates the Dirac cones coming from each layer. Left, comparison of TwBLG band structure for zero coupling (black lines) and nonzero coupling (blue lines). Right, band structure near the K point shows two isolated Dirac cones, one coming from each layer. A van Hove singularity forms where the two cones meet and hybridize.

2. At low twist angles, interlayer coupling will flatten the Dirac cone dispersion and correspondingly reduce the Fermi velocity

3. The spectra will feature a van Hove singularity where the Dirac cones from each layer cross and hybridize

4. A perpendicular electric field will not result in a gap (as in AB-stacked bilayer graphene[144]), but will instead simply shift the two Dirac cones resulting in a charge transfer from one layer to another.

The tight binding analysis has been further expanded beyond this initial model [133, 147, 201, 202, 203, 219], but the simple model still has been successful in explaining a majority of the observed experimental results. This model is discussed in more detail in Appendix E. An important addition was the identification by Mele[147] that there are actually two different classes of commensurate TwBLG structures which differ in their lattice symmetries, with one class of structures resulting in small gaps at the original monolayer Dirac points. Interestingly, these gapped structures are predicted to be topological crystalline insulators[111], although this has yet to be verified experimentally.

The first studies of twisted bilayer graphene came from STM studies on CVD grown graphene bilayers, which are produced in twisted form[88]. By extracting the wavelength of the moiré patterns observed in STM topography, the authors were able to determine the twist angle using the equation $\lambda = a/2sin(\theta/2)$, where a is the graphene lattice

constant and θ is the twist angle. The authors then correlated the twist angle with electronic features observed in tunneling spectroscopy measurements [129, 135]. The main departures from the expected spectrum for monolayer graphene was a suppression of the Fermi velocity for low twist angles, as well as the observation of large peaks in the density of states that were symmetrically located in energy around the Dirac point. These peaks they ascribed to the presence of van Hove singularities in the spectrum due to the hybridization between the layers. At a van Hove singularity, the density of states diverges, leading to the enhancement of electron interaction effects. Monolayer graphene also has a van Hove singularity in its bandstructure, and it has been predicted that exotic interacting states will arise if the Fermi level is aligned to the van Hove singularity[73, 146, 163]. In monolayer graphene, the van Hove singularities occur at extremely large charge densities corresponding to an additional 1/4 of an electron per unit cell. In TwBLG, the singularities are at a much lower and attainable charge density[74], and their location is controlled by the twist angle. The TwBLG van Hove singularities have been observed in ARPES measurements [173], but no study has yet to probe the electronic effects when the Fermi level is brought up to the van Hove singularity.

The number of transport studies in twisted bilayer graphene is limited compared to other graphene stackings. Part of the difficulty is was that CVD-grown twisted bilayers were not of high enough quality for many quantum transport experiments, while exfoliated graphene bilayers are stacked AB-type. One group solved this problem by searching for monolayer graphene sheets which had folded over, naturally leading to a bilayer with a rotational misalignment[196]. In a magnetic field, they observed two sets of resistance oscillations with different periods, and were able to attribute this behavior to the different charge densities on each of the layers [196, 197, 198]. This was the first demonstration of independent transport contributions from each TwBLG layer. Because the experiment had only a single electrostatic gate though, it was not possible to independently control the charge density on each layer. Another group was able to observe quantum Hall plateaus in a TwBLG device made from graphene bilayers grown on SiC and then transferred to a Si/SiO_2 substrate [124]. In this case, their data seemed more consistent with a nearly-aligned bilayer, but again the lack of dual top and bottom gates made it difficult to understand the transport behavior of the system.

With the development of the van der Waals heterostructure stacking technique[43], it suddenly became feasible to produce high quality TwBLG devices by stacking exfoliated flakes. Moreover, by encapsulating the bilayer in hBN dielectrics, it would be straightforward to make a dual-gated device with metal gate electrodes both underneath and on top of the TwBLG. Further motivating the approach, encouraging initial studies of graphene on hBN demonstrated interaction effects in the graphene quantum Hall effect at much lower magnetic field [42, 242]. The prospects were quiet hopeful that a dual-gated TwBLG device would demonstrate a wealth of interesting electronic phenomena and would contain multiple control knobs to engineer unique states (such as twist angle, charge density, interlayer electric field, etc).

4.2.2 Experimental regimes: low twist, high twist

We can roughly divide the experimental regimes in TwBLG into large-twist and low-twist structures. For large twist angles ($\theta > 5°$), the two layers are mostly decoupled at low energies, each having a monolayer graphene-like electronic spectra. Electrons in the bilayer have a new layer degree of freedom which we can couple to with an applied electric field. From this perspective, the TwBLG looks very similar to the bilayer 2DEGs studied in GaAs/AlGaAs heterostructures [20, 51, 53, 211], where an insulating spacer separates a pair of 2DEGs such that they only interact via weak tunneling or Coloumb interactions. In the case of TwBLG though, the interlayer distance can be much smaller than what is possible in a GaAs bilayer 2DEG. Smaller distances will increase the strength of interlayer Coulomb interactions, which could lead to new layer-coherent ground states[16, 152, 245]. Such states have been observed to occur in GaAs bilayers[52, 156, 162, 238].

At the edge, interlayer effects could also occur, since the interlayer decoupling may no longer apply depending on the edge geometry and the presence of disorder. We will see that this can have a strong effect on the behavior of quantum Hall edge modes in TwBLG. In addition, it is possible to realize new types of edge configurations which have no analogue in the GaAs bilayer 2DEGs. By applying an interlayer electric field to TwBLG, it possible to dope one layer with electrons, the other with holes. The resulting quantum Hall edge states will have opposite chiralities in each layer and hence will propagate in opposite directions. Such counterpropagating edge modes will be spaced by atomic distances and will form the basis of a bilayer quantum spin Hall state.

The low-twist bilayers occupy a smaller range of twist space, but are just as interesting. The effects of the moiré superlattice and the layer hybridization are predicted to drastically affect the electronic structure. The moiré superlattice will cause a zone folding of the bandstructure, resulting in replicas of the graphene Dirac points at higher energies[36]. The layer hybridization results in lower energy van Hove singularities, which could lead to new ground states due to electron-electron interaction effects[74]. At the limit of very low twist angle, distinct regions of AA and AB stacked regions will emerge. It is predicted that electrons will localize in the AA regions, corresponding to a flattening of the TwBLG bands[19, 122, 133, 191, 214, 219].

In the presence of a perpendicular magnetic field, the interplay between the moiré superlattice and the magnetic field will result in a fractal-like gap sequence known as Hofstadter's butterfly [18, 112, 157, 226]. In a transport measurement, the observation would be a fluctuating sequence of quantum Hall plateaus with in a self-referential pattern. In the previous chapter, we discussed similar effects that occur in graphene-hBN superlattices. Compared to graphene-hBN, TwBLG should produce a much more symmetric electronic structure, since the superlattice is formed at the interface of two identical graphene layers. In addition, the maximum superlattice wavelength in TwBLG is unbounded (graphene-hBN has a maximum of 14nm), so a larger range of superlattice-magnetic regimes could be reached.

4.3 Experiment details

4.3.1 Questions to answer

In the previous section, I outlined the interesting electronic behavior that could be observed in twisted bilayer graphene depending on the relative twist angle. The next sections will dive into the experimental work undertaken to explore these possibilities. This work spanned over the years from 2010 to 2014 and was designed to answer the following questions:

1. How does the quantum Hall effect look like in TwBLG?
2. In what way do electron-electron interactions break the spin, valley and layer degeneracies in the TwBLG Landau levels?
3. Can a quantum spin Hall state be realized in TwBLG?
4. Will new fractional quantum Hall edge states arise in TwBLG?
5. Does TwBLG display an exciton condensate ground state, as observed in bilayer 2DEGs?

This chapter answers the first three questions, while more future work will be necessary to answer the last two.

4.3.2 Devices and measurements

Attempting to answer the above questions required the following experimental steps: (1) produce a TwBLG stack; (2) attach metallic leads; (3) measure its resistance in a cryostat as a function of magnetic field, electrostatic gates, and temperature. A majority of our experimental work was devoted to the fabrication steps (1) and (2), with feedback from the measurement results informing our improved sample designs. In all cases, we used a polymer-based technique to stack graphene and hBN exfoliated flakes to create a layered structure consisting of hBN-Graphene-Graphene-hBN (Figure 4.5). The details of this transfer method is discussed in Appendix A. I emphasize that the TwBLG stack and specifically the graphene-graphene interface was created by physically bring into contact two separate graphene sheets through the aid of micromanipulators. The fact that this can result in a clean crystalline interface is surprising, but our measurements show that this often is the case. All devices are made with "dual-gates", consisting of both a bottom and top gate. This allows for the control of both the total charge density on the TwBLG, as well as the electric field across the bilayer.

We attached metallic leads to the TwBLG in two different methods. In one method we contacted from above, by evaporating metal through a mask onto the top of the TwBLG (Figure 4.5, Left). In the another method, contacts were made from the side by etching down through the entire stack and attaching leads along the edge (Figure 4.5, Right)[224]. In both cases the initial assumption is that the metal equally contacts

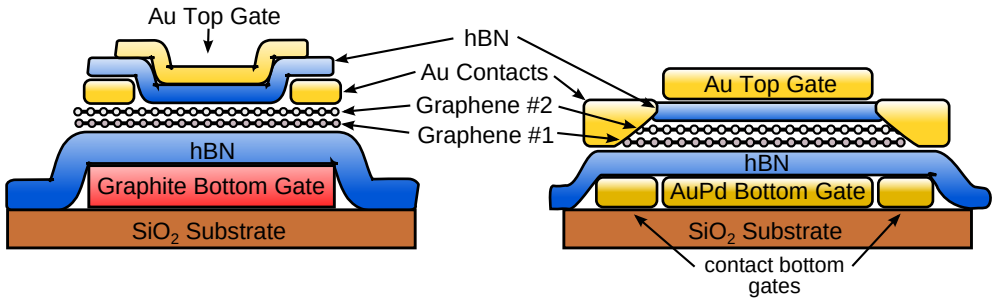

Figure 4.5. Two different types of TwBLG devices. All devices consist of a stack of hBN-graphene-graphene-hBN with dual top and bottom gates. **Left**, Device with graphite bottom gate, metal contacts on the top surface of the TwBLG, and a top gate overlapping with leads. **Right,** Edge-contacted device with AuPd bottom gates. Contact bottom gates lie underneath the metal-TwBLG interface.

both layers, although we will see later that the actual current distribution among the layers can be more complicated.

By using exfoliated flakes of graphene and encapsulating them in hBN, we were able to make devices with low amounts of charge disorder. In improved devices, the graphene was shielded from the SiO_2 by either a graphite or AuPd local bottom gate. In the latter case, metal bottom gates allowed for greater flexibility in the geometry of the gate structure, allowing for different regions to be defined by local gates.

■ 4.4 Quantum Hall effect, screening, and layer-polarized insulating states in twisted bilayer graphene

The text in this section was originally published in Sanchez-Yamagishi et. al. [192].

We investigate electronic transport in dual-gated twisted bilayer graphene. Despite the sub-nanometer proximity between the layers, we identify independent contributions to the magnetoresistance from the graphene Landau level spectrum of each layer. We demonstrate that the filling factor of each layer can be independently controlled via the dual gates, which we use to induce Landau level crossings between the layers. By analyzing the gate dependence of the Landau level crossings, we characterize the finite inter-layer screening and extract the capacitance between the atomically-spaced layers. At zero filling factor, we observe an insulating state at large displacement fields, which can be explained by the presence of counter-propagating edge states with inter-layer coupling.

The bilayer 2-dimensional electron gas (2DEG) consists of two closely spaced 2DEGs, where inter-layer Coulomb interactions and tunneling effects can lead to new behaviors which are not present in the individual layers[20, 52, 80]. In these bilayers, an insulating spacer is necessary to separate the 2DEG layers. In the case of twisted bilayer graphene,

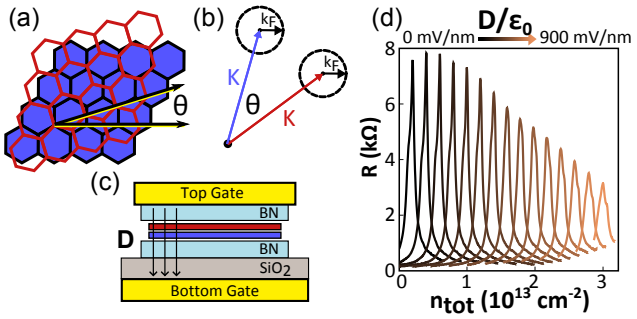

Figure 4.6. Twisted bilayer graphene device structure and zero magnetic field resistance measurements. (a) Twisted bilayer graphene lattice with twist angle θ. (b) Twist angle separates the Fermi surface of each layer in K-space. (c) Schematic of a dual-gated twisted bilayer device with h-BN gate dielectric insulators. Dual-gates allow for independent control of the carrier density and displacement field D. (d) Zero-magnetic field resistance R at the charge neutrality point at different values of D. The resistance at the charge neutrality point decreases with increasing D. Peaks have been offset in density for clarity.

the layers can be stacked directly on top of each other, yet still retain a degree of independence. This is possible because of the carbon honeycomb lattice of graphene, which results in weak coupling between the layers[46], as well as a circular Fermi surface centered at nonzero K vectors[27]. The latter is key, because a relative twist angle between the graphene bilayer lattices can cause the Fermi surfaces of the two layers to not overlap at low densities (Figure 4.4a,b). This preserves the linear Dirac dispersion in the twisted bilayer graphene[15, 87, 128, 134, 135, 196, 198], but with twice the number of Dirac cones due to the two layers[134, 196, 198].

Here, we present magnetoresistance measurements of dual-gated twisted bilayer graphene devices (twisted bilayers), which exhibit the quantum Hall effect (QHE) and magnetoresistance oscillations of two monolayer graphene (MLG) sheets conducting in parallel. As we vary the gate voltages, we observe inter-layer Landau level crossings which allow us to quantify both the layer charge transfer, as well as the finite screening effects between the layers. This incomplete screening of the applied field, due to graphene's small density of states and the close spacing between the layers, allows us to extract the inter-layer capacitance. Lastly, at high magnetic fields we observe a pattern of insulating states centered at zero density which resemble those observed in AB-stacked bilayer graphene (AB-BLG)[110, 229], but originate from layer-polarized edge modes.

Our twisted bilayer devices are fabricated using a PMMA-transfer technique to sequentially stack two separate MLG sheets such that they overlap on top of a hexagonal Boron Nitride (h-BN) flake[43, 215]. The bilayer region formed at the overlap is then contacted, and a topgate is fabricated with a h-BN flake as the dielectric insulator [1]. The final devices are measured in a He3 cryostat, with the temperature at 300mK unless otherwise noted.

[1] Additional details can be found in the Appendix D.2

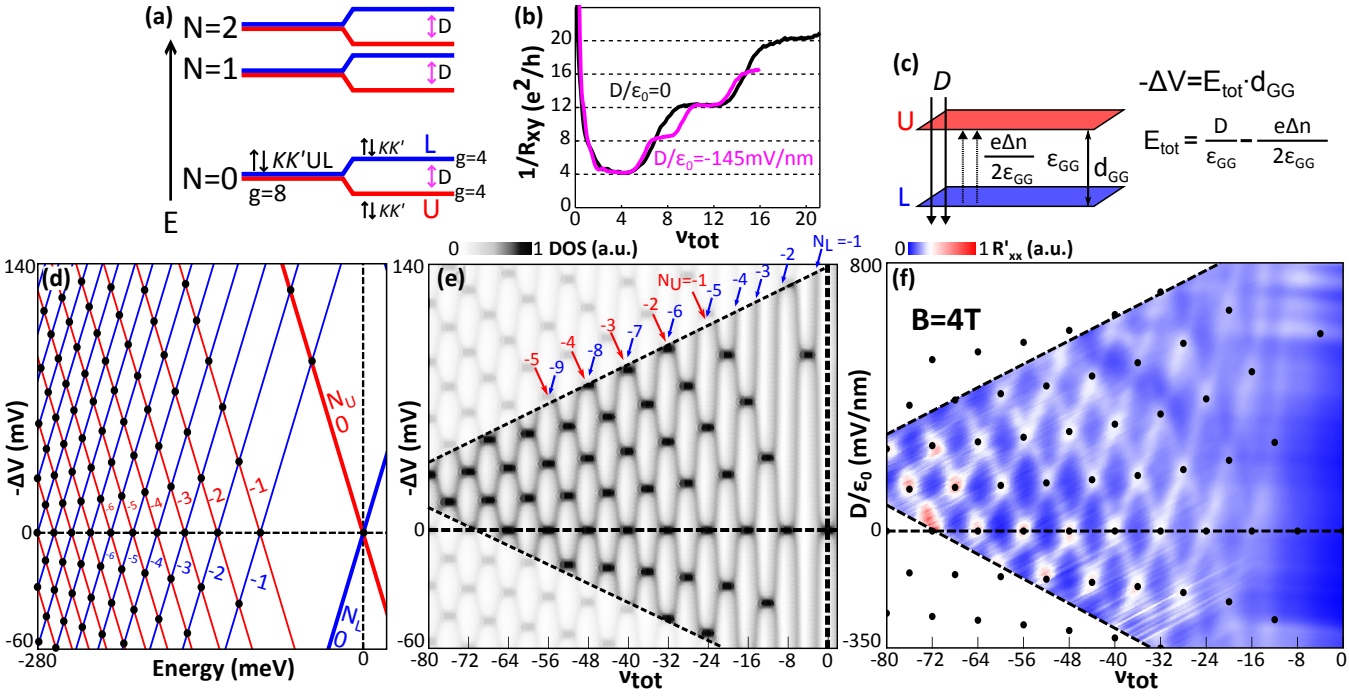

Figure 4.7. Quantum Hall effect, Landau level (LL) crossings, and screening in twisted bilayers. (a) Schematic of twisted bilayer LL spectrum. LLs are 8-fold degenerate (g=8) due to spin, valley & layer degeneracy. Displacement field D breaks layer degeneracy (g=4). (b) $1/R_{xy}$ as a function of total filling factor ν_{tot} at $B = 9$T. At $D = 0$, steps in $1/R_{xy}$ of $8e^2/h$ are observed (black line); at D/ϵ_0=−145 mV/nm, new steps of $4e^2/h$ develop. (c) Diagram of inter-layer screening. The applied field D is screened by charge imbalances Δn and by the inter-layer dielectric constant ϵ_{GG}. The total screened field E_{tot} induces an inter-layer potential difference ΔV. (d) LL energy spectra of upper and lower graphene layers (red and blue lines respectively) as a function of inter-layer potential difference ΔV. LL crossings are indicated by black dots. $N_{U(L)}$ is the LL index of the upper (lower) layer. (e) Simulated density of states for twisted bilayer as a function of ν_{tot} and ΔV. (f) Measured longitudinal resistance R'_{xx} with background subtracted, as a function of D and ν_{tot} at $B = 4$T. Peaks in R'_{xx} cross as a function of D, indicating the crossing of LLs. Black dots are theoretical fits to the LL crossings, from which the interlayer capacitance is extracted.

Using our devices' dual gates we can independently control the total carrier density n_{tot} of the twisted bilayer, as well as the displacement field D applied normal to the layers (Figure 4.4c). The total carrier density of the twisted bilayer is $en_{tot} = (C_T V_{TG} + C_B V_{BG})$, where $C_{T(B)}$ is the capacitance per unit area to ground of the top (bottom) gate, $V_{TG(BG)}$ is the potential difference between the top (bottom) gate and the graphene layer closest to it, and e is the elementary charge. The applied displacement field is $D = (C_T V_{TG} - C_B V_{BG})/2$, which induces charge and voltage differences between the layers. Further details about the calculation of the total carrier density and displacement field can be found in Appendix D.3.

We first compare our twisted bilayer samples with AB-BLG by measuring the re-

sistance of the charge neutrality point (CNP) as a function of D. In AB-BLG, a displacement field breaks the bilayer's inversion symmetry, which opens a band gap at the CNP[145, 172, 174]. This is not predicted to occur in twisted bilayers[134], and in our samples the CNP resistance decreases almost linearly as D increases (Figure 4.4d). This is a strong indication that our bilayers are not AB-stacked. Instead, the effect of D at the CNP can be explained as doping the two layers with equal and opposite charge, reducing the resistance of each individual layer. Moreover, there is evidence of a splitting of the peak resistance at the CNP with large D (Appendix D.5).

At high magnetic field B, we measure a QHE which is distinctly different from that observed in MLG[168, 250] or AB-BLG[171]. At $D = 0$, we measure the Hall resistance R_{xy} as a function of total filling factor $\nu_{tot} = n_{tot}h/eB$, where h is Planck's constant (Figure 4.7b, black line). We observe plateaus following the progression $1/R_{xy} = \nu(e^2/h)$, where $\nu = 4, 12, 20$. These steps of $8e^2/h$ between each plateau of $1/R_{xy}$ indicate the presence of 8-fold degenerate Landau levels (LLs). This 8-fold degeneracy follows from the usual spin ($\uparrow$,$\downarrow$) and valley (K,K') degeneracies found in MLG[168, 250], with an additional 2-fold degeneracy which we ascribe to the layer degree of freedom (U,L for upper and lower layer respectively)(Figure 4.7a)[40].

This layer degeneracy at $D = 0$ was observed in three different samples, and can be seen up to high filling factors in the longitudinal resistance as well. Figure 4.7f shows longitudinal resistance measurements R'_{xx}, where a smooth background has been subtracted to improve the contrast of magnetoresistance peaks (details of this process can be found in Appendix D.4). When $D = 0$, peaks in R'_{xx} are separated by $\Delta\nu_{tot} = 8$, again indicating 8-fold degenerate LLs, with this trend verified as far as $\nu_{tot} = -72$.

A property of the twisted bilayers is that the layer degeneracy can be easily broken by applying a displacement field normal to the graphene layers, resulting in 4-fold degenerate LLs, which we observe as new steps of $4e^2/h$ in $1/R_{xy}$ (Figure 4.7b, purple line). These LL splittings are also seen clearly in R'_{xx}, where each peak in R'_{xx} at $D = 0$ splits in two for $|D| > 0$ (Figure 4.7f). As D is increased further, these peaks cross with their neighbors, indicating the crossing of LLs between the layers.

To model the pattern of possible LL crossings, we consider independent MLG LL energy spectra in each layer with a potential difference ΔV between the upper and lower layer induced by D (Figure 4.7d). The upper and lower layer LLs (red and blue lines respectively), are degenerate at $\Delta V = 0$, and split in energy as $|\Delta V|$ increases, resulting in energy crossings when $-e\Delta V$ is equal to the energy spacing between two MLG LLs. This condition is satisfied when $-e\Delta V = \mathcal{E}_{LL}(N_U) - \mathcal{E}_{LL}(N_L)$, where $\mathcal{E}_{LL}(N) = \mathrm{sgn}(N)v_F\sqrt{2e\hbar B|N|}$, N_U and N_L are the LL indices for the upper and lower layer respectively, and v_F is the MLG Fermi velocity[27]. This energy plot is converted to filling factor by modeling each LL by a Lorentzian density of states with disorder broadening (Figure 4.7e). The resulting plot of two intersecting LL spectra qualitatively reproduces all the peaks in R'_{xx} presented in Figure 4.7f.

The relationship between the applied D and the induced ΔV at a crossing is determined by the inter-layer screening properties of the twisted bilayer, as D will be screened

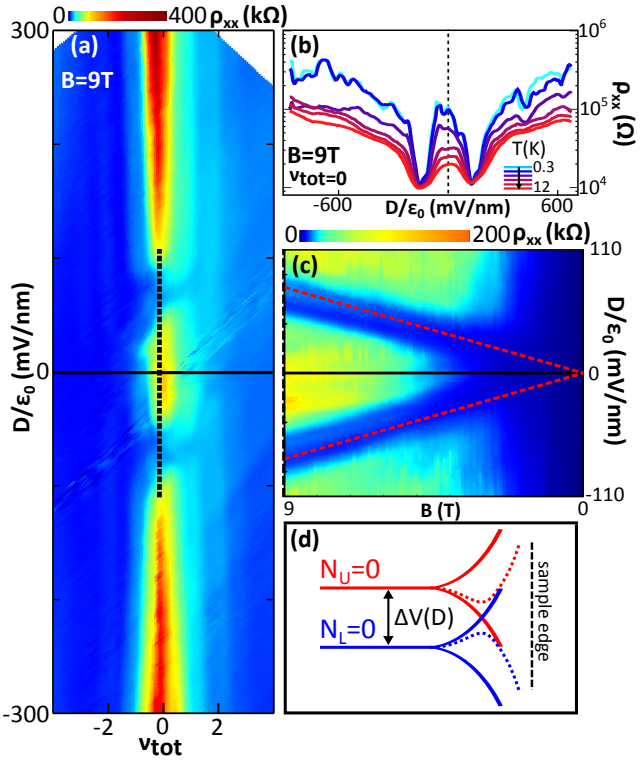

Figure 4.8. Insulating states in twisted bilayer at $\nu_{\rm tot} = 0$. (a) Longitudinal resistivity $\rho_{\rm xx}$ as a function of D and $\nu_{\rm tot}$ at B=9T. At $\nu_{\rm tot} = 0$, two insulating regimes are observed, one at $D = 0$ and another at high D, with a low $\rho_{\rm xx}$ region separating them. (b) Temperature dependence at B=9T and $\nu_{\rm tot} = 0$ of $\rho_{\rm xx}$ vs D shows non-metallic behavior. Temperature increases going from the top light blue curve to bottom red curve as 0.3, 1, 4, 8, 10, and 12K, respectively. (c) Magnetic field dependence of $\nu_{\rm tot} = 0$ insulating states. Resistivity double minima approach each other with slope 7.5 mV/nmT (dashed red lines). Both insulating states disappear at low B. (d) Schematic of $\nu_{\rm tot} = 0$ edge states at nonzero ΔV when D is applied. The zeroth LLs are split apart, resulting in counter-propagating edge states in the absence of interactions (intersecting solid lines). The insulating state at high D indicates inter-layer coupling between these edge states, which may open a gap at the edge (dashed lines).

both by free charges and the inter-layer dielectric environment (Figure 4.7c). The total screened electric field $E_{\rm tot}$ between the two graphene sheets with spacing $d_{\rm GG}$ results in the potential difference $-\Delta V = E_{\rm tot} \cdot d_{\rm GG}$. The relation then is:

$$-\Delta V = \left(D - \frac{e\Delta n}{2}\right)\frac{d_{\rm GG}}{\epsilon_{\rm GG}} = (D - \epsilon_0 E_{\rm S})\,\frac{1}{C_{\rm GG}}, \tag{4.1}$$

where $E_{\rm S}$ is the screening field due to the layer density imbalance Δn, $\epsilon_{\rm GG}$ is the inter-layer dielectric constant, and $C_{\rm GG} = \epsilon_{\rm GG}/d_{\rm GG}$ is the inter-layer capacitance per unit area.

For a high density of states material, ΔV would be effectively zero and the charge imbalance Δn would completely screen D, independent of the inter-layer capacitance

C_{GG}. Graphene though, has a small density of states, and a correspondingly small quantum capacitance which is comparable to the inter-layer capacitance of the closely-spaced graphene sheets. This leads to an incomplete charge screening of D and a dependence of Δn on C_{GG} which we can measure. When the Fermi energy lies at a LL crossing with LL indices N_U and N_L, we can determine both ΔV and Δn ($\Delta n = (N_U - N_L)4eB/h$) and use equation (4.1) to compute the D at which a crossing should be observed. We repeat this process for each crossing, and fit it to our data to extract C_{GG}. The computed crossings are overlaid as black circles on Figure 4.7f, resulting in good agreement when $C_{GG} = 6.8$ μF/cm^2 (estimated error ± 1.0 μF/cm^2). A similar analysis was repeated on two other samples with LL crossings, both resulting in an extracted capacitance of $C_{GG} = 7.5 \pm 1.0$ μF/cm^2. For comparison, the capacitance of two parallel plates separated by 0.34 nm of vacuum would be 2.6 μF/cm^2, which is less than half of our extracted capacitances (atomic force microscopy measurements indicate an inter-layer step height that varies from 0.34 to 0.41nm across our samples). Given that the inter-layer distances are only somewhat larger than the spatial extent of the graphene p_z orbitals[95], it seems likely that both the finite thickness of the graphene layer, and its polarizability[98], could increase the inter-layer capacitance. A similar magnitude of screening also occurs in AB-BLG[154, 251]. Another possible effect is Fermi velocity reduction, which has been demonstrated to occur in twisted bilayers at small twist angles [134, 135, 198, 201]. In this case, since we assume v_F to be the same as in isolated MLG, the inter-layer capacitance could be even larger than we estimate and our extracted capacitance C_{GG} sets a lower-bound on this quantity.

We now turn to the $\nu_{tot} = 0$ region, where we see evidence of coupling between edge states in the two layers. At high B-field and $\nu_{tot} = 0$, the longitudinal resistivity ρ_{xx} has two insulating regions: one at $D = 0$ and one at high D (Figure 4.8a). Both insulating states have high resistivities (> 100 kΩ) with a non-metallic temperature dependence (Figure 4.8b). A similar pattern of insulating states has been observed in AB-BLG[110, 229], but the mechanism for such states must be different in the twisted bilayers. In AB-BLG, high D opens a band gap independent of B. Such an effect does not occur in the twisted bilayers (Figure 4.4d)[134], and as seen in Figure 4.8c, the high D insulating state disappears at low B field.

This high D insulating state can be explained by the coupling of counter-propagating edge states, which can co-exist on the same edge of the twisted-bilayer sample when $\nu_{tot} = 0$. These crossings occur when $|D| > 0$, because the zeroth LL in graphene is made up of opposite chirality states with energy that diverges in opposite directions at the edge of the sample (Figure 4.8d). When the zeroth LL of the twisted bilayer is split in energy by D, the electron-like edge states in one layer (blue line) will cross the hole-like edge states in the other (red line), resulting in counter-propagating, layer-polarized edge modes. A similar scenario has been previously considered for spin-splitting in the zeroth LL in graphene, leading to spin currents[1]. In the case of twisted bilayer though, there should be a displacement-induced layer splitting of the zeroth LL, with associated "layer" current. Because the states counter-propagate along the same edge though, a

backscattering channel is available by tunneling into the other layer. Such a process could lead to 1d localization[126], or an insulating gap due to an avoided crossing of the edges states (Figure 4.8d, dotted lines), both of which could explain the insulating behavior we observe.

The high D insulating state at $\nu_{\text{tot}} = 0$ is separated by a low resistivity region from another insulating state at $D = 0$. The development of an insulating state at zero filling factor has been observed in MLG[30, 67, 248] and BLG[229, 252], and is attributed to electron-electron interaction effects which break the degeneracy of the zeroth Landau level and open a gap at zero density. Given the presence of the low resistivity transition region between the two insulating states, it is unlikely then that both the high D and $D = 0$ regions are layer-polarized states, since that would imply a continuous transition from one state to the other. The $D = 0$ state then could simply be both MLG sheets within some broken-symmetry state that does not involve the layer degree of freedom[107]. As D increases, the layer-polarized state eventually becomes more energetically favorable, leading to the transition to the high D insulating state.

These $\nu_{\text{tot}} = 0$ states indicate that layer interactions in the twisted bilayer graphene can lead to new behaviors which cannot be explained by completely independent monolayer graphene sheets conducting in parallel. In principle, this inter-layer coupling is tunable by varying the distance between the graphene layers, altering the twist angle, as well as by threading magnetic flux parallel to the layers.

4.5 Broken symmetry states and quantum spin Hall in twisted bilayer graphene

4.5.1 Let's realize a TwBLG quantum spin Hall state

Our initial magnetotransport experiments on dual-gated twisted bilayer graphene demonstrated a rather simple result: it looked like two monolayer graphene sheets conducting in parallel without any bulk hybridization effects (Section 4.4). This is despite the sub-nanometer spacing between the stacked layers. At the edges though, there was clear evidence for inter-layer tunneling, which we argued was responsible for causing an insulating state at large inter-layer electric fields.

As sample qualities improve, we expect that electron-electron interactions will play an important role in the TwBLG Landau levels, as they do for monolayer [29, 101, 242, 248] and AB-bilayer graphene[58]. In fact, already in our 2010 dataset there is evidence of broken symmetry states in the zeroth Landau level of the TwBLG. For example, looking closely at the low-density region of Figure 4.8, we can see a fine structure of step like features in the magnetoresistance which cannot be explained by pairs of monolayer quantum Hall edge states which have the full spin-valley symmetry. The confidence in this observation though would have to await both better datasets with cleaner samples, as well as an improved understanding of the broken symmetry states in the graphene zeroth Landau level. A key development came from Young et. al.[242], who showed that the $\nu = \pm 1$ states in monolayer graphene were likely to be spin ferromagnetic ground

states. The edge states at $\nu = \pm 1$ then would be expected to be spin-polarized. In addition, the completion of the monolayer graphene quantum spin Hall work discussed in Chapter 2 resulted in our appreciation for how the graphene quantum Hall effect could be used to build new types of edge states. The take-away intuition from this work was that a quantum spin Hall state is phenomenologically identical to two coexisting copies of quantum Hall edge states which are protected from mixing. So, if we could superimpose the spin polarized $\nu = 1$ and $\nu = -1$ edge states in graphene, which have opposite chiralities and opposite spin polarizations, we would then have a quantum spin Hall state.

This suggests the following experiment: dope TwBLG such that simultaneously one layer is at $\nu = 1$ and the other is at $\nu = -1$, the result would be a new type of quantum spin Hall state, albeit one where the edge states are separated by at least 0.34nm. The experimental signature of such a state would be a two probe conductance of $2e^2/h$, where spin conservation prevents the two modes from mixing with each other. In general the concept can be generalized to other broken symmetry state filling factors, or even fractional edge states, where we can study how the resulting edge modes interact with each other.

The rest of this section discusses transport measurements on high quality TwBLG devices where the disorder is reduced enough such that electron-electron interactions can fully break the symmetry of the graphene Landau levels. The result is a new set of quantum Hall plateaus whose value depends on the chirality, spin-valley occupation, and the interlayer interaction between the edge states on each layer. The primary result will be the first experimental evidence for a bilayer quantum spin Hall state.

■ 4.5.2 Measurements of the N=0 LL in high quality TwBLG

Compared to the original TwBLG devices discussed in Section 4.4, the devices discussed in this section have a local graphite or metal backgate that sits between the SiO2 substrate and the bottom of the TwBLG. This local backgate serves the important role of screening out the charger disorder from the SiO_2 substrate, resulting in greater charge homogeneity in the device.

Figure 4.9 shows two-probe conductance colorplots of a dual-gated twisted bilayer graphene device (device name "Portal") measured at a magnetic field of B =12T. Clear conductance plateaus can be observed as flat colored features in the plot, and for low gate voltage values a finely structured sequence of plateaus can be observed which appear to shift and transition with the gate voltages (Figure 4.9b). In a 2-probe measurement of the quantum Hall effect (QHE), it is expected that the conductance will exhibit steps following the sequence $G = \nu_{tot} e^2/h$ whenever the total filling factor ν_{tot} is integer valued and the graphene is in a bulk incompressible state. Here, the total filling factor is defined as $\nu_{tot} = n_{tot}/(B/\Phi_0)$, where n_{tot} is the total charge density on the bilayer and $\Phi_0 = h/e$ is the magnetic flux quantum.

To analyze this dataset, we begin by transforming to a more illuminating coordinate space consisting of symmetric and antisymmetric combinations of the top and bottom

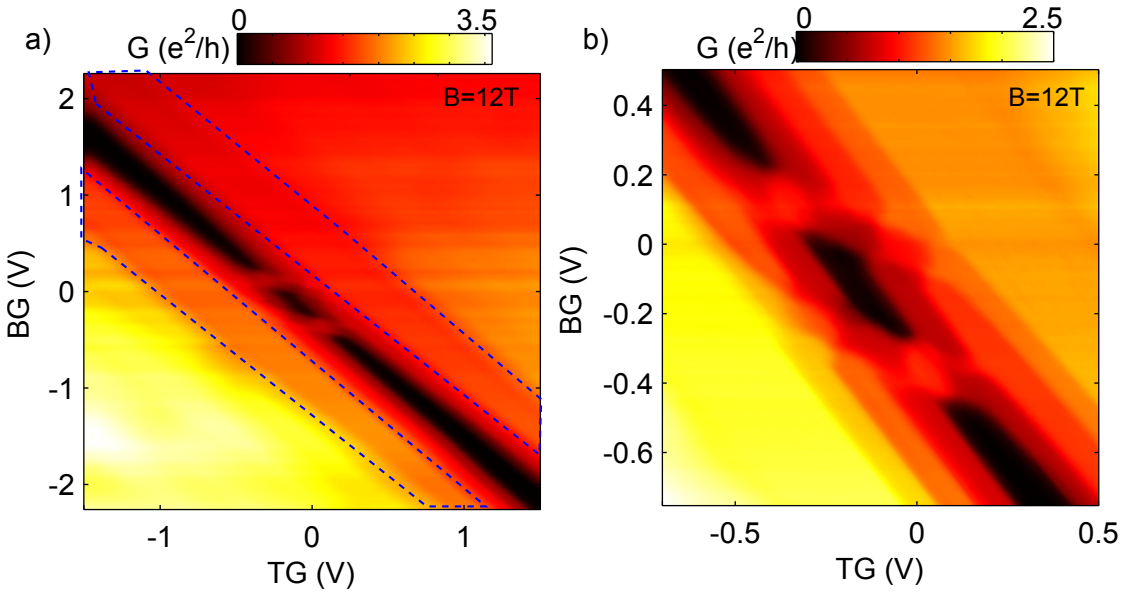

Figure 4.9. Broken symmetry states in TwBLG. 2-probe conductance colorplots of a dual-gated twisted bilayer graphene device (called "Portal") as a function of topgate voltage (TG) and backgate voltage (BG). **a**) Dashed lines indicate $\nu_{tot} = \pm 4$ plateaus which frame the zero total density line. **b)** Zoom-in on the TwBLG zeroth Landau level. A complex sequence of conductance plateaus are observed due to the broken spin-valley-layer degeneracy in the zeroth Landau level due to electron-electron interaction effects and the applied electric field.

gate voltages weighted by the gate capacitances. The result of this transformation is seen in Figure 4.10, which is the data from Figure 4.9b replotted in terms of $TG+c_{BT}BG$ and $TG - c_{BT}BG$ where $c_{BT} = C_{BG}/C_{TG}$ is the ratio of the gate capacitances. Recalling the discussion from Section 4.4, the symmetric combination of gate voltages controls the total charge density on the bilayer while the antisymmetric combination will correspond to an applied transverse displacement field which imbalances the charge between the layers. We will use the terms interchangeably for the rest of this section, although in general the mapping from voltage space to charge density/displacement field space is non linear due to quantum capacitance effects in our thin dielectric gates (thickness of 5-50nm). In the coordinate transformation, we also subtract a voltage offset from both axis so that the central conductance dip is located at the origin. This is the dual charge neutrality point of both layers. Asymmetric gate voltages along the y-axis from this point will then correspond to transferring charge from one layer to the other while keeping the total charge density zero; we call this the "zero density line".

In Figure 4.10a, the conductance increases with the magnitude of symmetric gate voltage in a sequence of plateau steps. Two wide plateaus are observed on the edges of the plot which we attribute to $\nu_{tot} = \pm 4$, where ν_{tot} is the total filling factor of the bilayer. The measured value of the conductance in these plateaus is almost half of the expected $G = 4e^2/h$. This is due to the effects of contact resistance, which add a series

resistance to the current through the quantum Hall edge modes. The contact resistance is observed to be backgate dependent, and is also sharply different for p- and n-type charge carriers, ranging from about 6 to 12kΩ (Figure 4.10c). To extract the backgate dependence of the contact resistance, we make a linear fit to the backgate dependence of the $\nu_{tot} = \pm 4$ plateaus (Figure 4.10c gray lines) and subtract the constant resistance $R = h/4e^2$. We then take this backgate-dependent contact resistance and subtract it from each of the backgate traces in the dataset, resulting in the contact resistance-corrected map G' in Figure 4.10b. The origin of this contact resistance is discussed in more detail in the next section.

By fitting the $\nu_{tot} = \pm 4$ plataeus, the rest of the conductance plateaus fall onto all the integer multiples of e^2/h between 0 and 4 (Figure 4.10d). The presence of the odd integer values of 1 and $3e^2/h$ indicates that the both the spin and valley degeneracies are broken, which we attribute to the effects of electron interactions. We can also identify the following plateau trends away from the zero density line: (1) symmetric gate voltages cause the conductance to monotonically increase in steps of e^2/h; (2) antisymmetric gate voltages do not change the plateau conductance until, at a certain point, it causes the plateau to collapse and then reemerge.

Motivated by the success of the double-layer charging model in explaining the non-interacting quantum Hall effect in TwBLG (Section 4.4), we attempt to explain the conductance map in terms of a pair of monolayer graphene layers conducting in parallel. In this case though, we consider each graphene sheet to have its Landau level degeneracy fully broken. By recalling that $\nu_{tot} = \nu_1 + \nu_2$, where ν_i are the individual filling factors on each layer, we can model the 2-probe conductance behavior away from the $\nu_{tot} = 0$ line as following $G = \nu_{tot} e^2/h$ for all possible integer combinations of ν_1 and ν_2. Symmetric voltages will change the value of ν_{tot}. Antisymmetric voltages can cause transitions from states with the same value for ν_{tot}, but with different values of the interlayer filling factor imbalance $\nu_\Delta = \nu_2 - \nu_1$. This should only occur if the applied displacement field is strong enough to stabilize the imbalanced state.

A schematic of the expected conductance map following this model is shown in Figure 4.11, where each plateau is labeled in terms of the individual filling factor occupations of the layers as (ν_1, ν_2), where ν_1 is the filling factor of the bottom layer. All possible combinations of filling factors -2,-1,0,1,2 in the two layers are considered. The extent of the plateau in the displacement field axis is scaled according to the estimated gap size in the following order: $\text{gap}(\nu = 2) >> \text{gap}(\nu = 0) > \text{gap}(\nu = 1)$[242]. As we can see by comparing with Figure 4.10b, the map qualitatively reproduces the arrangement of observed plateaus.

Turning now to the $\nu_{tot} = 0$ zero density line, if we follow the trend of all the other plateau features we would expect zero conductance. Indeed, there are plateaus with nearly zero conductance both at $(\nu_1, \nu_2) = (0, 0)$ and at high interlayer displacements fields along the zero density line. But, these zero conductance features are separated by a pair of non-zero plateaus with conductance of order e^2/h. Following the map in Figure 4.11, we identify these plateaus with the layer occupations (1,-1) and (-1,1). Figure

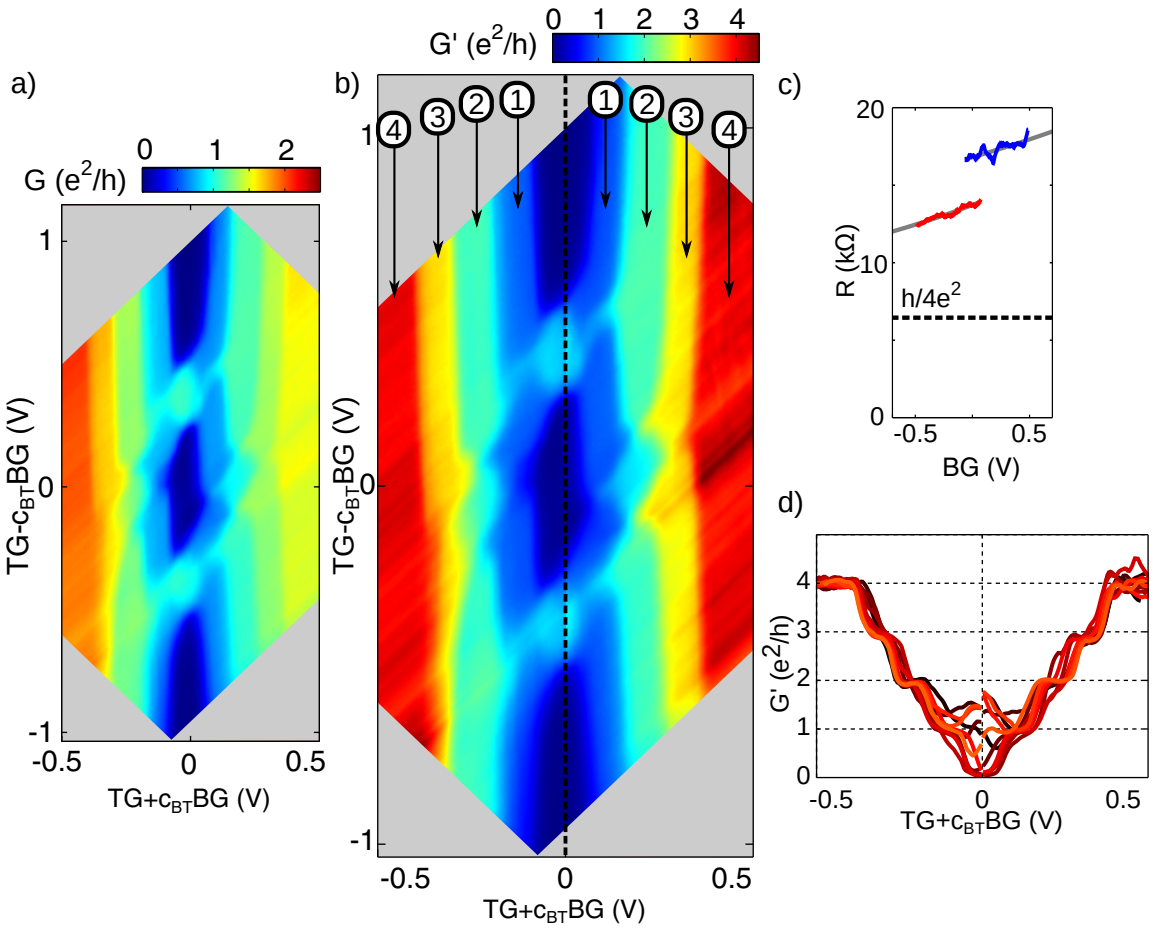

Figure 4.10. Measurement of broken symmetry plateau sequence. **a)** 2-probe conductance map of "Portal" as a function of symmetric and antisymmetric gate voltages. **b)** Same dataset with contact resistance removed by fitting to $\nu_{tot} = \pm 4$ plateaus. Circled numbers indicate value of plateau in units of e^2/h. **c)** Line cuts through $\nu_{tot} = \pm 4$ plateaus showing BG dependence of contact resistance. **d)** Symmetric voltage line cuts through data in (b) show conductance plateaus at all integer values from -4 to +4.

4.12 shows the raw conductance line cuts (no contact resistance subtracted) along the $\nu_{tot} = 0$ line, where the conductive features are observed to form smooth plateaus. The width of the features in the displacement field direction are also comparable to many of the other plateaus in Figure 4.10b, indicating that this is a feature corresponding to a bulk gapped state, as opposed to being a compressible transition region between two different insulating states at zero and high electric fields.

We can explain this sequence of features along the $\nu_{tot} = 0$ line by considering the possibility of interlayer tunneling/scattering along the edge. This concept was introduced in the previous section, but I review it again here. Large displacement fields

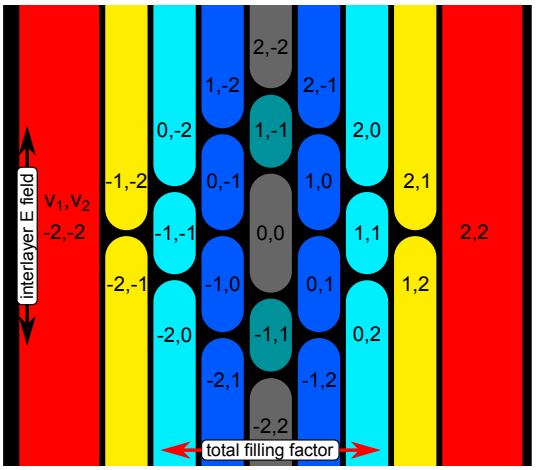

Figure 4.11. Schematic conductance map for TwBLG with broken symmetry states. Numbers indicate the filling factor on layers one and two as ν_1, ν_2.

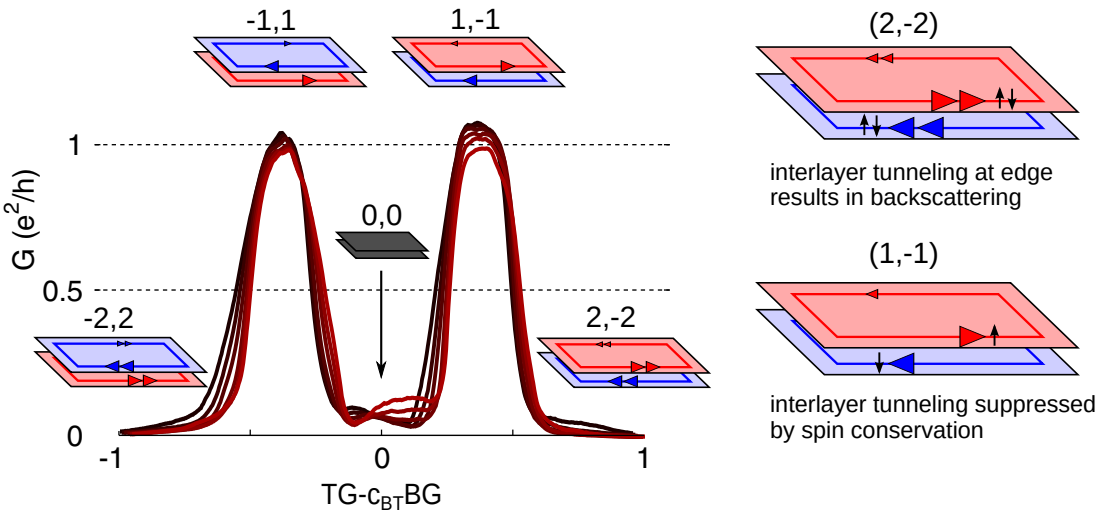

Figure 4.12. Electron-hole bilayer edge states can be protected. Left, Raw conductance near the zero-density line. Black to red lines correspond to cuts near $\nu_{tot} = 0$ where $TG + c_{BT}BG$=-25mV to +25mV. Bilayer cartoons show hypothesized edge states for each of the conductance regimes. **Right,** comparison of edge configurations for (2,-2) and (1,-1) states. The (2,-2) has the full spin degeneracy; and backscattering via interlayer tunneling is not prevented. For the (1,-1) state, the opposite spin polarizations of each layer prevents backscattering via interlayer tunneling.

should cause a transition to the electron-hole bilayer states (2,-2) or (-2,2), which are stabilized by the large cyclotron gaps between the zero and N=±1 index Landau levels. Each layer should then host a spin-degenerate edge state, each contributing $2e^2/h$ to

the total conductance. But instead of measuring $4e^2/h$, the conductance is heavily suppressed to values $<0.1e^2/h$. It seems likely that this is not a bulk disorder or contact resistance effect, given that all other features away from $\nu_{tot} = 0$ have much higher conductance. Rather, it is indicative that conduction is suppressed along the edge itself. In a chiral quantum Hall edge state, ballistic conduction is preserved due to the physical separation between backscattering modes. As can be seen in the bilayer schematics in Figure 4.12 though, for the cases (2,-2) or (-2,2), counterpropagating edge states are only separated by the tiny bilayer spacing of 0.34nm. If an electron scatters off of a rough edge or impurity, it can tunnel from one layer edge state to the other, backscatter, and reduce the total conductance. There is also the possibility that the tunnel coupling along the edge could be strong and coherent enough to directly open a gap in the edge states. Either way, the result will be a suppression of the conductance since the bulk is already localized due to the quantum Hall gaps in each layer.

Let us apply the same reasoning to the electron-hole bilayer (1,-1) and (-1,1) states. The picture should be nominally the same as the (2,-2) or (-2,2) cases, with each layer having opposite chirality edge states with the possibility of interlayer tunneling leading to backscattering. The key difference though is that the (1,-1) and (-1,1) states no longer have a spin degeneracy; and, in fact, the spins from each layer will be anti-aligned with respect to each other. If this were true, interlayer scattering would not be possible without a magnetic defect, which can provide a spin-flip mechanism when the electron tunnels from one layer to the other. The fact that the (1,-1) and (-1,1) states feature plateaus with G$>e^2/h$, even without accounting for contact resistance effects, indicates that the edge states are protected in a way which the (2,-2) and (-2,2) states are not. This is evidence that the (1,-1) and (-1,1) states are displaying the protected edge state behavior expected for a quantum spin Hall state. Although the measured conductance $\sim e^2/h$ is short of the expected $2e^2/h$, a majority of this reduction from the expected value can be accounted for by contact resistances effects, which we discuss further in the next subsection.

The magnetic field dependence of the (1,-1) and (-1,1) states is presented in Figure 4.13. Already at 5T the plateaus are separately identifiable and mostly saturated in value. They are observed to disperse linearly with magnetic field (Figure 4.13a), likely corresponding to both the magnetic field dependence of the (0,0) gap, which is observed to increase linearly with B in monolayer graphene, as well as the increasing charge density imbalance necessary to impose $\Delta\nu = 1 - (-1) = 2$.

By repeating the same measurements described above on other large-angle TwBLG devices, we have determined that the pattern of conductance plateaus observed in Figure 4.10b is the most universal phenomenology, with few exceptions. Figure 4.14 shows a side-by-side comparison between the same raw conductance dataset presented in Figure 4.10a ("Portal") and two other devices ("Octopus" and "Buendia"). All demonstrate the same behavior along the $\nu_{tot} = 0$ line, with two conductive plateaus separating insulating states at zero electric field and at high electric fields. They also all exhibit a majority of the expected plateaus features that are described in theoretical conductance map

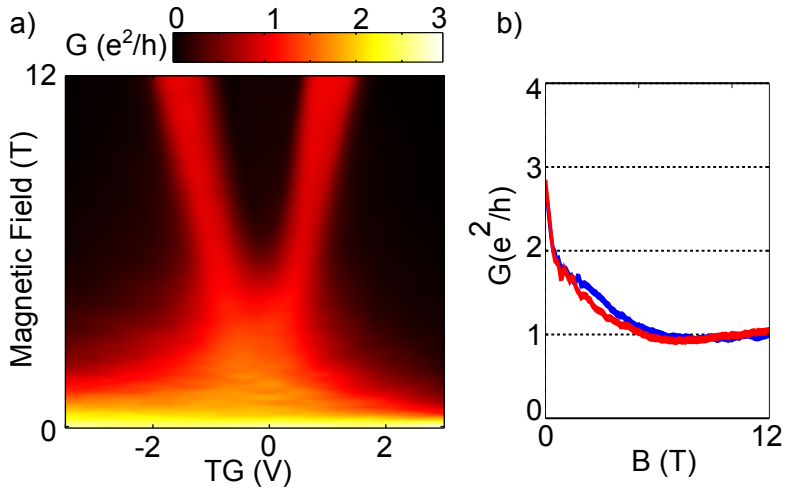

Figure 4.13. The protected electron-hole bilayer states onset near 5T. a) Magnetic field dependence of conductance along the $\nu_{tot} = 0$ line. **b)** Conductance of the (-1,1) and (1,-1) states (blue and red lines) as a function of magnetic field.
4.16

(Figure 4.11). All have varying contact resistances; in the case of the device "Buendia" there is clear evidence that the contacts are not equilibrating fully to all available edge states, which explains why some of the plateaus appear smeared or missing. In the following subsection we will discuss in more detail these contact resistance effects and their role in the measurement of the quantum spin Hall state.

■ 4.5.3 Contact resistance, gating and QSH

They are many specific departures from the measured datasets and the expected ideal behavior for twisted bilayer graphene with broken symmetry states. Most glaring is the fact the quantum spin Hall state ascribed to the (1,-1) and (-1,1) layer occupations should exhibit a two-probe conductance of $2e^2/h$, yet all measurements in these states yield $G \sim 0.6 - 1.5e^2/h$. In addition, there are some departures in the measured plateau sequence from the pattern described in Figure 4.11; for example, in Figure 4.14 some plateaus are observed to merge into others or are not well defined. Sample disorder can contribute to the weakening of specific quantum Hall plateaus, especially those corresponding to the comparatively weaker gaps involving the $\nu_i = \pm 1$ monolayer states[242]. Another source of systematic error can also arise from the contact and gate geometry which may affect the conductance measurements. We label these types of systematic errors as "contact resistance" effects, where the "contacts" are the portion of the electronic measurement circuit leading up to the "primary" TwBLG region that we want to know the conductance of. These contact effects will include our metallic measurement wires, the metallic leads, the metal-graphene interface, and the portion of the TwBLG which lies outside of the primary region controlled by the dual gates.

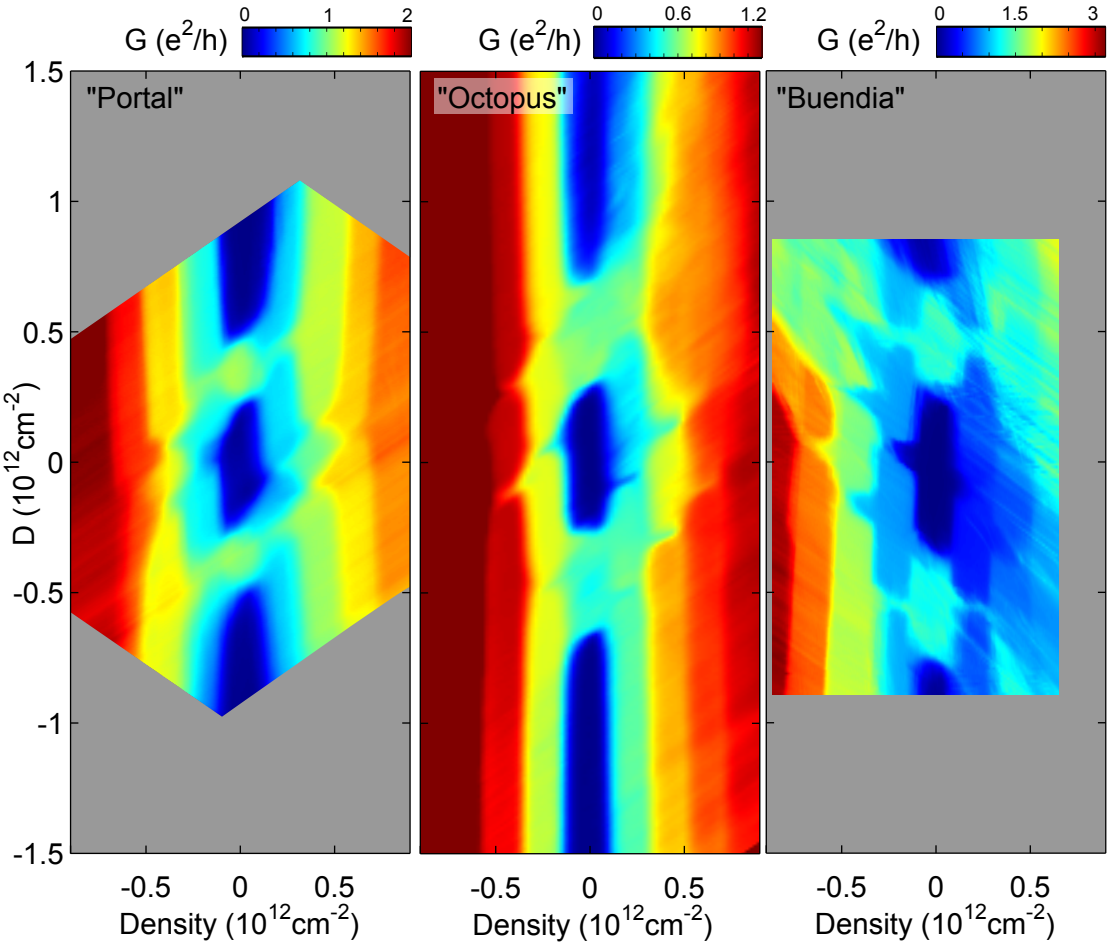

Figure 4.14. The zeroth Landau level of TwBLG looks similar for different samples. Raw 2-probe conductance colormaps of the TwBLG zeroth Landau level in three different samples called "Portal", "Octopus" and "Buendia". For comparison, data is plotted in terms of "Density"= $C_{TG}V_{TG} + C_{BG}V_{BG}$ and "Displacement field"= $C_{TG}V_{TG} - C_{BG}V_{BG}$.

Removing these systematic, non-intrinsic, errors is important because a conductance quantized at $2e^2/h$ is a clear hallmark of a quantum spin Hall state, and also because we want to identify any intrinsic backscattering mechanisms which may cause a departure from the quantized value.

Contact resistance due to contacts

The most obvious source of contact resistance is at the interfaces between lithographically defined metallic leads and the graphene. For all devices studied, the metallic leads are made of a 1nm layer of Cr and 60-150nm of Au. Since the Cr layer is too thin to be continuous, the assumption is that the Au will primarily define the contact

interface and the relevant work function difference. An extra resistance is associated with the barrier for electrons to tunnel from the gold into the graphene layer, which should contribute a fairly density-independent contact resistance. A more important effect is the contact doping caused by the work function difference between the metal and the graphene. This causes a p-doping of the graphene in the immediate vicinity of the metallic leads[68, 125]. Such contact-doping will result in an effective gate-dependent contact resistance, as the conduction from the contact-doped region into the primary region will vary depending on the formation of p-n junctions at the transition region[96]. Figure 4.15 shows a cartoon of this effect, in one case the primary region is doped by the gate to be n-type[2], opposite of the p-type doping near the contacts. The result is the creation of a p-n junction that will contribute additional contact resistance as compared to the case where the primary region has the same sign as the p-type graphene contacts (Figure 4.15 a).

The formation of p-n junctions offer a straightforward explanation for why the contact resistance will be lower for p-type graphene as compared to n-type graphene when using Au contacts. We observe this effect for each of our devices; in Figure 4.14, the p-type TwBLG (negative density) has a higher conductance than the n-type TwBLG (positive density) in each dataset. The p-n effect is dramatic because the measurements occur at high magnetic fields, where an interaction driven gap opens at charge neutrality. Since the p-n junction necessarily passes through charge neutrality, there will be a gap that separates the p- and n-type regions that can completely suppress conduction (Figure 4.15d). In this case the problem cannot be rectified by simply subtracting a constant contact resistance or even by measuring 4-probe; the edge states in the primary region are completely isolated from the contacts and the measurement could not be trusted to reflect the true conductance of the primary region.

Beating the p-n junctions and measuring a QSH state

The problem of sign-dependent contact resistances has a straightforward solution when measuring the quantum Hall effect in graphene monolayers: use n-type contacts to measure n-type graphene; use p-type contacts to measure p-type graphene. This could be done by varying the metals used for the contacts (from Au to Al), but a more practical solution for in-situ control is to use electrostatic gates to define the contact region. For example, an independent backgate underneath the contacts can dope the graphene n-type all the way up to the Au contacts. A separate gate can then control the primary region so that that the graphene conductance vs. carrier density can be studied for n-type graphene without the effects of p-n junctions. To study p-type graphene the "contact gate" can conversely be energized to be p-type. Such a strategy was used effectively in the work by Maher et. al. to study AB-bilayer graphene in high magnetic fields[139]. Figure 4.16 shows a device with independent contact gates which can dope the TwBLG leading up to each contact. When the contacts are p-type, the plateaus

[2]N-type graphene is has an electron carrier density greater than zero. P-type graphene has an electron carrier density less than zero.

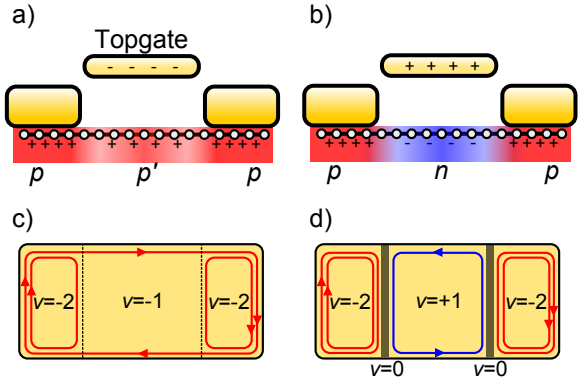

Figure 4.15. Contact doping can introduce a gate-dependent contact resistance. **a)** Graphene doping profile for negative gate voltages. Gold contacts (yellow squares) induce a local p-type doping in the graphene. **b)** Doping profile for positive gate voltages. p-n junctions are created at the graphene-gold interface. **c)** Edge state configuration for p-type graphene where the outer region has the same sign charge carriers as the inner region. **d)** When the inner region has the opposite sign charge carriers as the outer, the edge states may not be able to equilibrate across the insulating $\nu = 0$ state[9].

(1,-1)

on the p-side of the dataset are well defined and only have a contact resistance $\sim 100\Omega$, while the n-side of the data has heavily suppressed conductance. Flipping the polarity of the contacts from p-type to n-type flips the situation, with now the n-side having low contact resistance and the p-side being suppressed.

The strategy of matching the sign of the contact doping to that in the primary region only works when the sample has just one type of doping. This clearly is a problem when attempting to measure the bilayer QSH state, since one layer is n-type and the other is p-type. We need simultaneous p-type and n-type contacts. Figure 4.17 illustrates the problem of having only one type of contact. For example, a p-type contact will only be able to contact the layer with $\nu_i = -1$ effectively, since the layer with $\nu_i = 1$ will contain a p-n junction that will prevent equilibration of the edge states. This effect is seen quiet vividly in the measurements. For p-type contacts in Figure 4.16, most of the (-1,1) state in the bottom of the figure has a conductance of $1e^2/h$, and in fact smoothly connects to the (-1,0) state. Figures 4.18a,d show a more careful look at this behavior, where the conductance clearly does not change value when transitioning from the (-1,0) state to the (-1,1) state. Despite the presence of the extra edge state in the upper layer, no current flows through it for p-type contacts. In the lower portion of the (-1,1) state (Figure 4.18d), the conductance fluctuates with gate voltage, rising above $1e^2/h$. Following our model, it would appear that for this region of gate voltages there is some path by which the p-type contacts are able to conduct into the n-type $\nu_2 = +1$ edge state in addition to the $\nu_1 = -1$ state. Turning now to the (1,-1) state in the upper portion of the p-type colormap (Figure 4.18c), we see that the entire plateau has conductance greater than $1e^2/h$, although still less than $2e^2/h$. If we think of the (1,-1) state as having the sum of

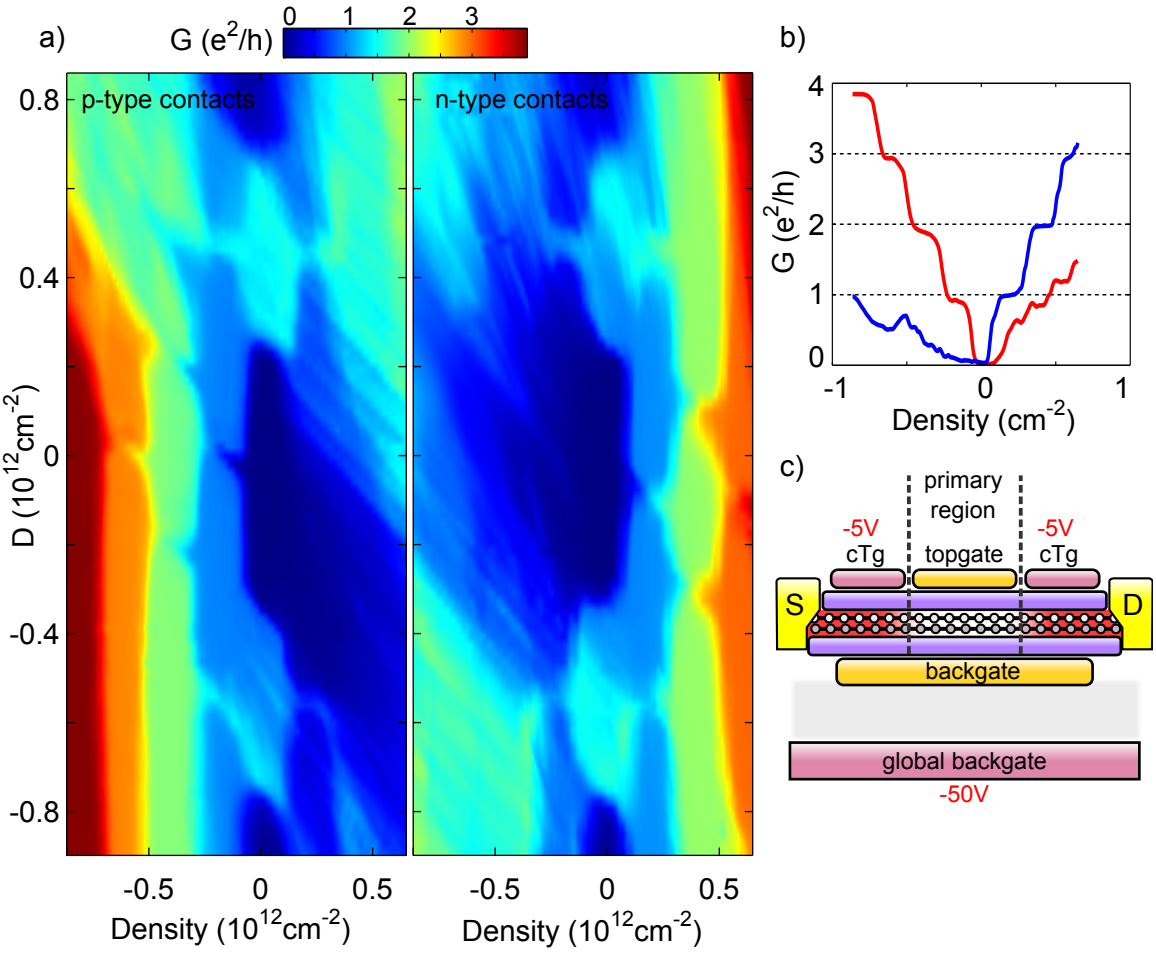

Figure 4.16. Contact gates can be used to control the effects of contact resistance. **a)** Conductance colorplots of the zeroth Landau level for sample "Buendia" with gate control of the contact doping. P-type contacts results in clear measurements of the negative density conductance plateaus and strong suppression of the positive density plateaus. The converse is true for n-type contacts. **b)** Density line cuts for p-type (red) and n-type (blue) contacts. **c)** Cartoon of device. The primary region is defined where the topgate and backgate overlap. The contact topgates (cTG) and global backgate control the doping of the TwBLG leading up to the metal leads.

the conductances of the (1,0) and (0,-1) states, then this fact is not too surprising since the conductance of the (1,0) plateau is not completely suppressed. Similar features are seen for measurements with n-type contacts, the (1,0) state connects smoothly with the (1,-1) state, and likewise the (0,1) state connects with the (-1,1) state (Figure 4.18e,f). In both cases then at least some portion of the electron-hole bilayer plateau is restricted to $1e^2/h$.

Given that both p- and n-type contacts seem capable of contacting at least one of the edge states effectively, a solution to the contact problem is to simultaneously

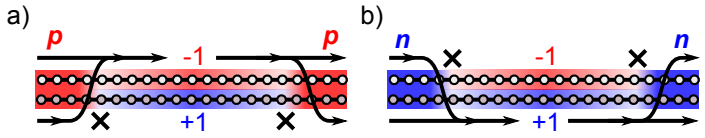

Figure 4.17. Contacts of a single doping type cannot simulatenously contact well both layers of a bilayer QSH state.

measure with p- and n-type contacts in parallel. In either case the (1,-1) and (-1,1) states are measured to have a conductance of at least $1e^2/h$, so if we were able to measure both in parallel we should measure a full $2e^2/h$, indicating that there are two independent edge states which are protected from scattering into each other. This would require at least four independent contacts to perform a pair of simultaneous 2-probe measurements, one with p-type contacts and the other with n-type contacts. An example of such a measurement is given in Figure 4.19, where the conductance values at the (-1,0), (-1,1) and (0,1) plateaus are measured while the contacts are changed from p-type, n-type, and mixed p-n type. This is accomplished by a set of four independent topgates which cover four independently contacted TwBLG regions which lead up to

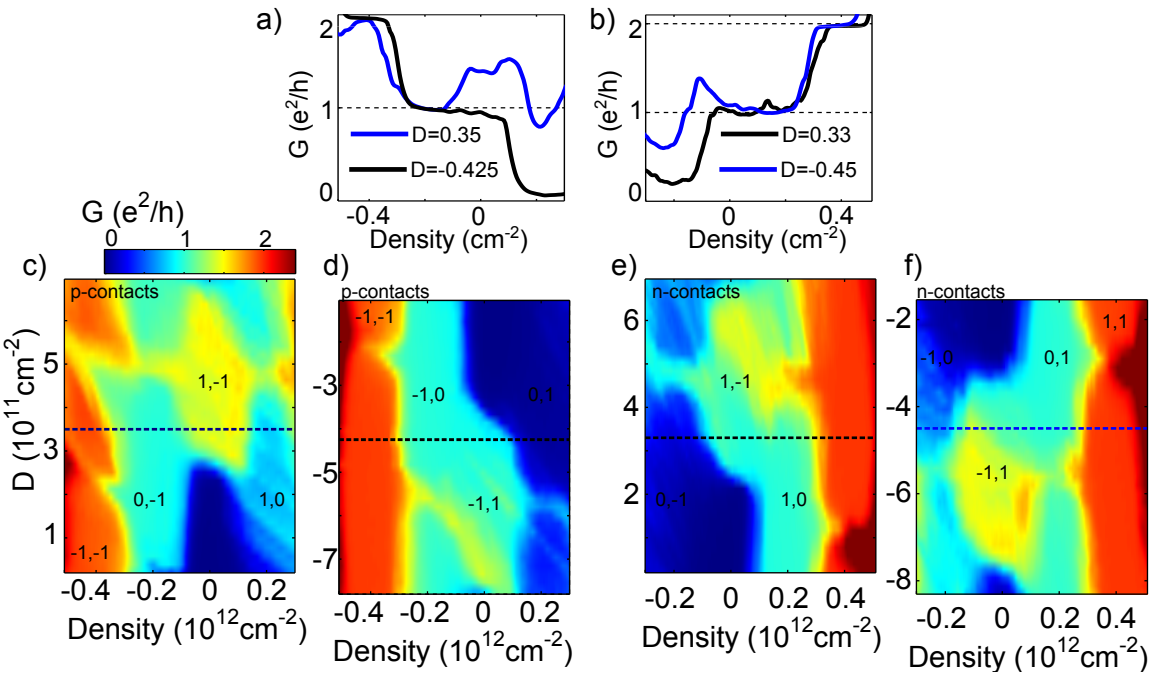

Figure 4.18. Contact effects limit the conductance of the (1,-1) and (-1,1) plateaus. a) Density traces for p-type contacts cutting through the (1,-1) state (blue) and the (-1,1) state (black). The conductance remains pinned to $1e^2/h$ when transitioning from the (-1,0) to (-1,1) state (black). **b)** Similar line cuts for n-type contacts. **c-f)** Zoom-in plots of the datasets from Figure 4.16 looking at the transitions from the $\nu_{tot} = \pm 1$ states to the (1,-1) and (-1,1) states.

the primary region. Each contact topgate (labeled cTG_i, where i=1–4) can be energized to dope the TwBLG layers beneath it to be either p-type or n-type, which will in turn change the device contact resistance while keeping the doping of the primary region constant (constant TG and BG voltages). The source bias contacts are connected to the leads under cTG_1 and cTG_2 while the drain contacts where current is measured from are connected to the leads under cTG_3 and cTG_4. For the (-1,0) plataeu we find that the conductance is increased when each pair of contact gates (cTG_{24} and cTG_{13}) drops below a threshold value, with the largest conductance occurring when all gates are negative. This is consistent with our previous analysis since negative contact gate values will result in p-type contacts which will most effectively contact the (-1,0) state. Conversely, for the (0,1) state there is an increase in conductance when the contact gates are pushed to positive values. Turning now to the (-1,1) state, we observe that the greatest conductance occurs for anti-symmetric combinations of the contact gates, when cTG_{24} has opposite sign to cTG_{13}. This suggests that the (-1,1) state is indeed made up of simultaneous p-type and n-type graphene layers—an electron-hole bilayer.

Although the mixed combination of p-type and n-type contacts increases the conductance of the (-1,1) compared to solely p-type and n-type contacts, it still maxs out around $1.3e^2/h$. This is because the contact topgates cannot fully dope the TwBLG all the way to where the metallic leads physically contact the graphene. The evidence for this is that by energizing the global Si backgate, which lies below the metal-graphene interface (see Figure 4.16), it is possible to reduce the contact resistance to about ~100Ω for either the p-side, or n-side, but not both simultaneously. The solution forward then is instead to have independent contact backgates which lie directy underneath the metal-graphene interfaces.

4.5.4 Conclusion - broken symmetries and quantum spin Hall state in TwBLG

In this section, we've seen how the quantum Hall effect behaves in twisted bilayer graphene as a function of the charge occupation on each layer. Because of the twist induced decoupling, there is no hybridization of the layers in the bulk. At the edge though, tunneling between the layers can occur depending on the the relative spin occupation of each layer. By doping each layer to $\nu = \pm 1$ we can induce a QSH state where backscattering along the edge is protected, and the edge states occupy different layers.

4.6 Final notes

4.6.1 Unanswered questions.

One big unanswered question is the nature of the interlayer tunneling at the edge of the sample. Somehow the roughness of the edge can provide the necessary valley scattering to cause the (2,-2) and (-2,2) states to be insulating, but it is not clear if this is a homogenous effect or not. Independent contacts on each layer may provide a route for probing the interlayer tunneling. It would also be interesting to try different edge

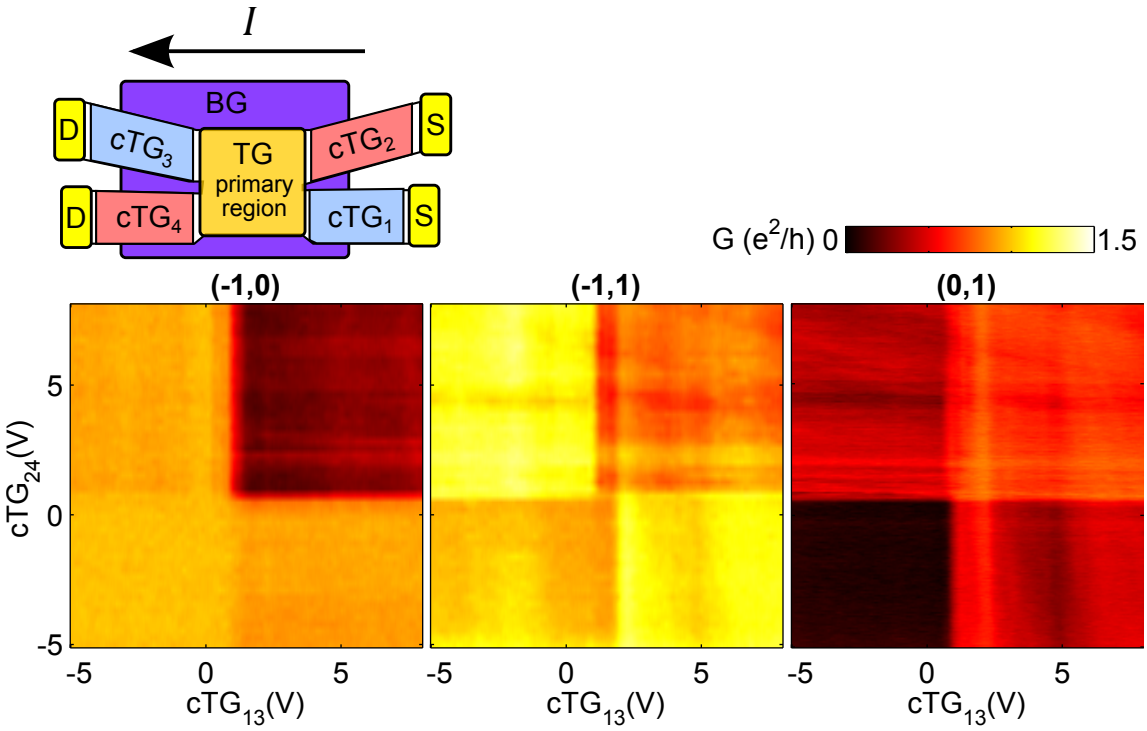

Figure 4.19. Simultaneous p-type and n-type contacts are the most effective in measuring the QSH state conductance. cTG scans in different plataeu regions. (-1,0) state at (TG,BG)=(0.38,0.04); (-1,1) state at (TG,BG)=(0.75,-0.167) ; (0,1) state at (TG,BG)=(0.71,0.12)

configurations, for example by having the edge defined by an electrostatic gate potential, instead of using the physical edge of the sample.

Missing from the above discussions is the possibility of new ground states due to interlayer interactions. All the data can be explained without invoking any kind of coherent interlayer coupling. This is somewhat surprising, given the clear importance of Coulomb interactions in breaking the degeneracy of the graphene zeroth Landau level. The magnetic length, which sets the scale for interactions within a layer, should always be larger than the inter-layer distance of 0.34nm, so why isn't there an interlayer ordered state (which is equivalent to a Bose-Einstein condensate of interlayer excitons[52])? The most obvious sign of this would be the presence of a new plateau corresponding to the half filling of a non-degenerate Landau level in each layer, for example at (1/2,1/2). So far, no such state is observed (Figure 4.14). One possibility is that the exchange gaps are smaller for the inter-layer coherent state, so higher quality samples and lower temperatures are necessary to observe it. Alternatively, the change in the interlayer tunneling conditions between the bulk and edge of the TwBLG sample may obscure the transport effects in the interlayer coherent states. In this case, alternative probes such as interlayer capacitance or tunneling measurements should be pursued to see if they

result in extra features.

■ 4.6.2 Future directions

TwBLG offers many interesting possibilities for future research. One direction is to realize non-Abelian defect states for quantum computing applications. Following the general route laid out for other QSH states, we could place superconducting contacts on the TwBLG to induce a Majorana bound state. Although the QSH state in TwBLG requires a magnetic field, with increasing sample quality the required magnetic field could be reduced to a range compatible with superconductors. This is informed by studies in monolayer graphene, where the $\nu = \pm 1$ states are observed to emerge at fields less than 1 Tesla[243]. A larger issue, which is a problem for all the QSH implementations of Majorana bound states, is that the proximitized 1d edge state must be gapped out to localize the Majorana mode. Gapping out a QSH requires mixing the two spins modes which are typically protected. It has been proposed that a ferromagnetic insulator could provide the mixing between the spins[62], while the insulating gap would prevent direct coupling to the Majorana bound state by the ferromagnet.

Generalizing the concept of a quantum spin Hall state is also an interesting direction. We have completed initial studies that demonstrate a clear fractional quantum Hall effect in TwBLG samples, with the trend following similar behavior to the integer quantum Hall effect. This bodes well for future work towards realizing a fractional quantum spin Hall effect.

Recent new proposals suggest that a fractional bilayer quantum Hall system could be used to realize non-Abelian defects, without the use of superconductors of ferromagnets[14]. Instead of a superconducting or magnetic gap, the resulting quantum defects would exist at the boundary of a quantum Hall gap and an interlayer gapped state. For this application, the TwBLG may offer a useful limit of the double layer graphene system where an interlayer gapped state could be introduce via controlled interlayer tunneling at the edge.

Lastly, there is predicted to be many new behaviors to explore in low-twist TwBLG. Initial studies from our group demonstrate very strong departures from monolayer or AB-bilayer for low twist angle samples. Further work will be necessary to understand the effects of electron-electron interactions and strain in these layer hybridize structures which have large superlattice potentials.

Appendix A

Fabrication Details

A.1 Overview

All the experiments discussed in this thesis involve measurements of graphene-hBN heterostructures. In this appendix, I summarize the various transfer techniques used to make the devices. All the methods have the following steps in common:

1. Graphene and hBN flakes are exfoliated onto a polymer or SiO_2 substrate.
2. A dry transfer method is used to stack the graphene and hBN layers to create a heterostructure. For the first generations of devices this was done one transfer at a time, with an anneal and AFM step in-between each transfer. In the final twisted bilayer graphene devices, the stack was created consecutively without any intermediate cleaning step.
3. The geometry of the device is defined by a dry etching process, so that only flat and clean regions remain.
4. Nanolithography is used to add gold contact leads and, if necessary, a topgate to the device.

An example of the fabrication process for a particular device is presented in Figure A.1.

The biggest limiting factor for all the fabrication steps is the transfer and stacking process. When graphene and hBN layers are stacked together, there will inevitably be bubbles of trapped residue and wrinkles at the interface (see Figure A.1d). These features will limit the size of the final device, since we only want to use the regions which are completely flat and free of impurities. The first generation of transfer techniques limited the device sizes to a few square microns. Recent improvements to the transfer process now result in heterostructures which are more than 10 microns in lateral size.

A.2 Flake transfer methods

Over the course of this thesis research, we developed various types of dry transfer methods to stack layers of graphene and hBN. The original method was inspired by the wet

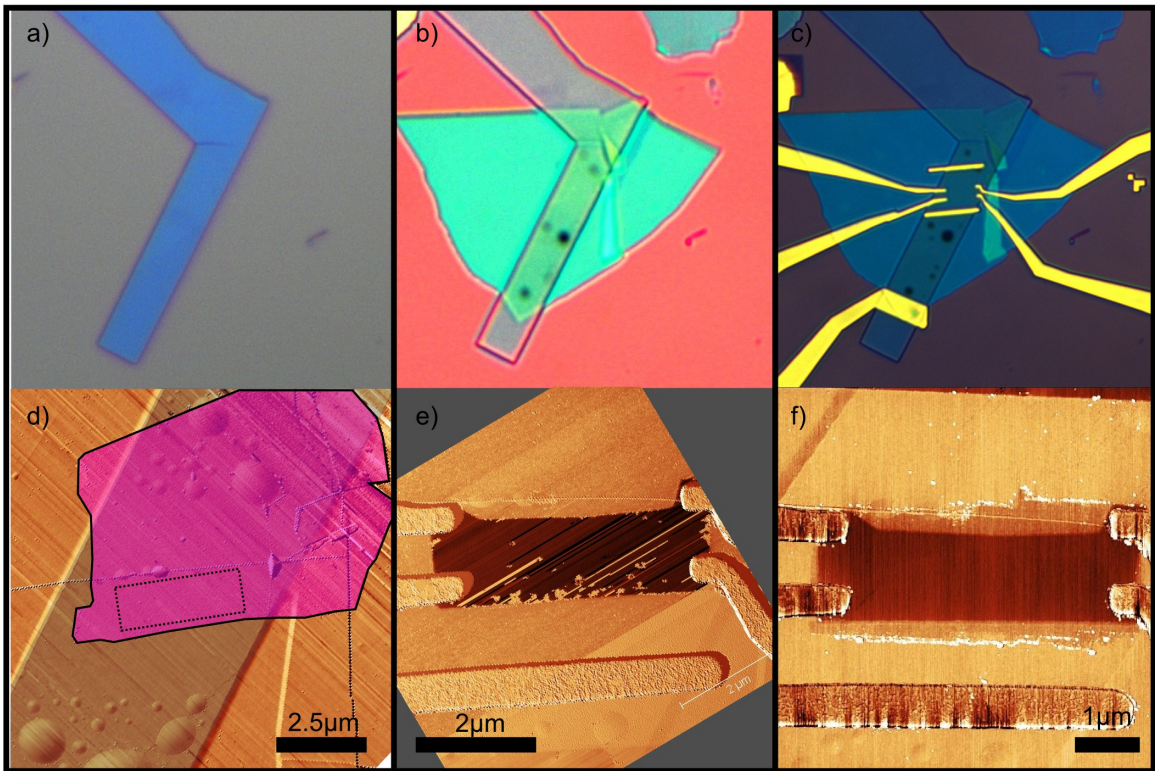

Figure A.1. Fabrication steps for a monolayer graphene quantum spin Hall device. The data measured from this device is presented in Figure 2.5 and 2.6. Optical images (a-c) and atomic force microscopy (AFM) phase images (d-f) **a)** An etched graphite flake serves as a local backgate electrode. **b)** After transfer of hBN and graphene flakes. **c)** Nanolithography is used to attach gold electrodes to the graphene. The next step is to etch the flake into its final shape. **d)** AFM phase image of a graphene flake (purple false color) on top of hBN on top of a graphite bar (gray false color). Bubbles and wrinkles are evident in the stack. The rectangle (dashed lines) indicates the location of the final device in a flat region of the graphene. **e)** AFM phase image of the final etched device with four contacts. Dark rectangle is etched graphene flake. Polymer residue can be observed towards the bottom of the graphene flake, this is removed in a subsequent AFM tip cleaning step. **f)** AFM image of device after tip cleaning process.

(solvent-release) transfer method by Dean et. al. [43], which we adapted into an all-dry method. All the techniques require some form of a transparent polymer layer, which is used to support a thin flake of graphene or hBN. A micromanipulator under a microscope is used to align the polymer supported flake with a target substrate. The flake and polymer are then slowly brought into contact with the substrate while applying heat. The heat causes the polymer and flake to attach and transfer to the substrate. The polymer layer is subsequently removed using solvents, leaving behind the transferred flake.

The mechanics of the transfer process are still not well understood, but certain methods have been empirically determined to produce heterostructures reliably with large flat areas. A primary requirement is that the starting flake material and substrates be very clean and free of obvious contamination, which is determined by an AFM pre-screening process. Despite this pre-screening, hydrocarbon residue is still observed to become trapped between stacked layers[82]. One theory is that the residue is due to unavoidable hydrocarbons from the environment which adsorb to the flakes. This residue is presumed to not be visible in the AFM topography scans. If this is the case, then the only reason why flat heterostructures are possible is because the hydrocarbon residue is pushed out in a "self-cleaning" process during the engage step. This theory is supported by our observation that engaging flakes very slowly results in much less trapped residue at the interface. The best results occur when the engage step occurs over the course of a hour, with stability ensured by a vibration isolation table and a heating source with low fluctuations.

■ A.2.1 PC-based pick-up method

This transfer method is designed to pick up and transfer flakes that have been exfoliated on a SiO_2 substrate. This is a great advantage because flakes can be exfoliated, cleaned, and even etched into geometries before being picked up to form a stack. It is based on the methods developed in references[224] and [254], and relies on the ability of PC (Poly(Bisphenol A carbonate)) to adhere to many 2d layered materials. The devices used for the experiments in Section 4.5 were made using this method.

PC film preperation

1. Make a film of PC on a glass slide in the following method. Take a 6% solution of PC dissolved in chloroform and drop it on a glass slide. Place the another glass slide on top and press down gently so that the solution spreads out to cover the whole slide. Smoothly and quickly slide the top glass off, leaving behind a flat film on top of the original.

2. Use a dropper to paint a frame of thicker PC around the edge of the top surface of the glass slide. This reinforces the film so you can peel it off.

3. Leave 10 mins to dry.

Figure A.2. Micromanipulator transfer setup. Under the microscope (Bausch & Lomb Microzoom II) there is a heated stage that holds the substrate. To the right is a micromanipulator (Karl Suss) that has been modified to hold a glass slide at a controllable tilt with respect to the stage.

4. Take a glass slide and attach a window frame of double sided tape on the surface towards the end of the slide. Place a square of PDMS (2x2mm) in the hole of the frame, so that it only touches the glass slide, not the tape.

5. Peel off the film of PC from the glass using a piece of tape. Simply attach the tape to one side of the PC film and then peel up. The film will peel off and the thicker PC frame will help it retain its form. Lay the film gently on top of the PDMS, ensuring that it lands flat. Use the flat edge of a razor blade to press the PC so that it sticks to the double sided tape on all sides surrounding the PDMS.

6. Use a razor blade to cut off the excess PC. The result is a flat film of PC on the PDMS, that is held down on the sides to the glass by the double sided tape.

Pickup Method

1. This method is described for picking up hBN flakes, although the same technique can be used for other materials, including monolayer graphene. For the easiest pickup, the SiO_2 wafer should be cleaned with a Piranha solution (3:1 solution of H_2SO_4:H_2O_2 at 80C for 20 mins), and then finished with a 15 second soak in a 1:20 solution of HF:H_2O. Flakes are exfoliated onto the substrates within a week of cleaning, and then individually imaged in an atomic force microscope to prescreen for flakes which are flat and clean.

2. The PC on PDMS square is mounted in a transfer setup at a 3-5° angle to the substrate. The PDMS square is centered on the flake that is desired to be picked up and then brought into contact at room temperature.

3. Once in contact, the substrate is heated to 70°C -130°C. The higher the temperature, the increased chance of pick up, but also the greater the risk that the PC film will detach and transfer to the substrate. Once the high temperature is reach, the substrate is cooled back down to room temperature.

4. Slowly disengage to pickup the flake from the substrate.

Picking up a second flake

1. A flake of graphite or hBN can be used to pickup sequential layers. The flakes are aligned under the microscope, and then the PC film is engage with the substrate at an angle so that it engages in a slow rolling motion.

2. The slower the engage, the less likely there will be trapped bubbles. To get the most slow engage, it is necessary to apply a slow ramping temperature increase of 10-20°C over the course of a hour. As the temperature increases, the film will slowly engage as the substrate thermally expands.

3. As soon as the flakes have completely engaged, cool down to room temperature and disengage the film. The flake should be picked up by the other flake.

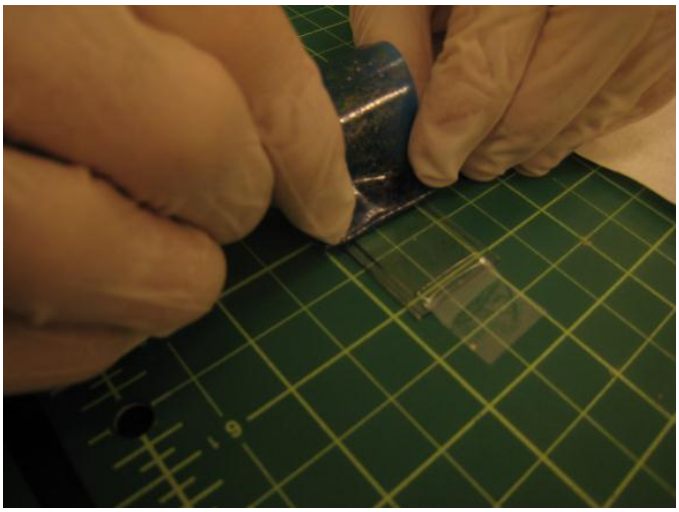

Figure A.3. MMA-based transfer method. Step

Transferring

1. To transfer the complete stack, engage at room temperature and then heat up the film to 130°C.

2. At 130°C, disengage slightly so that the PDMS detaches from the PC film. The PC film will still be attached at the edges.

3. Heat up to 155°C. At this temperature, the PC film will melt at the edges and completely detach from the glass slide.

4. The PC film can then be removed in chloroform.

■ A.2.2 MMA-based transfer method

This transfer method uses a soft layer of PDMS (Polydimethylsiloxane) as the support for the polymer membrane, instead of the membrane being suspended. This allows for a much simpler preparation process. This was the method used for making the devices discussed in Chapters 2 and 3.

1. Place a thin piece of PMDS film on a glass slide support. The PMDS used is a 1mm thick film of Sylgard 184 Silicone elastomer.

2. Radiate the PMDS+glass slide in a UV ozonator for 15 mins. This helps the packing tape (next step) to stick better to the PDMS.

3. Place a layer of very clear packing tape (Duck, HD Clear heavy duty packing tape), sticky-side down, so that it covers the PDMS and glass slide. Cut out the excess

material. The tape will mediate the adhesion between the PDMS and the MMA, since the MMA cannot stick directly on the PDMS well.

4. Spin a layer of MMA (Microchem, Methyl methacrylate MMA 8.5 EL9) at 1200rpm for 70s on top of the tape which sits on the PDMS. After, bake at 120°C for 10 mins. Repeat this step twice.

5. Flake deposition. Use a low tack tape to exfoliate layers of graphite or hBN (we use Ultron Systems R1011 "blue tape) and then press the tape gently onto the MMA layer. Apply low pressure by rubbing with a soft teflon tweezer.

6. Very slowly peel the tape off over the course of a few minutes, to avoid tearing the MMA film.

7. Find desired flakes under a microscope using a black background. Graphene monolayers will appear as a faint layer of contrast. Identify flakes by marking the underside of the glass with a black marker.

8. Using a sharp scalpel, cut out the PDMS+tape+MMA+desired flake and then mount the PDMS square on the end of a glass slide which can be mounted in the transfer setup. Multiple squares can be cut from the same PDMS layer.

9. Transfer method. Align the flake with the target substrate and bring into contact at room temperature. Heat up to 130°C and then disengage. The MMA will stick and transfer to the silicon oxide substrate, while the tape and PDMS will remain on the glass slide. The process can be repeated for multiple regions of the chip.

■ A.2.3 PVA-based transfer method

This was the first transfer method that our group developed, and was used to create the devices discussed in Section 4.4. It relies on the weak adhesion of polyvinyl alcohol (PVA) to both SiO_2 and Poly(methyl methacrylate) (PMMA).

1. Spin a layer of PVA (Fiberlay, PVA fiberlease) at 3000rpm for 60s on a Si/SiO_2 substrate and bake the chip at 75°C for 4 minutes.

2. Spin a layer of PMMA 950 A5 (Microchem, 5% by weight in Anisole) on top of the PVA layer at 1500 rpm for 60 s and subsequently bake the chip at 75°C for 10 minutes. It will appear as in Figure A.4a.

3. Cover the chip in a window of tape. This prevents the polymer from peeling off during the exfoliation process (Figure A.4b).

4. Exfoliate graphene or boron nitride onto the PMMA layer by using a piece of tape with flake material on it (Figure A.4c. Rub gently and peel the tape off slowly so that the PMMA does not tear or get ripped off. Find desired flakes under an optical microscope. Monolayers of graphene will appear as very faint features, but are still visible.

5. The entire polymer membrane can be suspended by gently peeling the tape window off from the substrate. The PVA+PMMA film will pop off from the silicon substrate. The entire window should be supported on glass slides for ease of handling.

6. The membrane can now be mounted in a transfer apparatus, ideally with a raised ring support that will force the desire flake on the membrane to be the lowest point. One method to do this is as follows:

7. Under a microscope, drop tiny metallic washers onto the back of the suspended membrane so that the flakes sits in the middle of the washer. Gently apply a thin layer of tape to fix the washer to the back of the membrane. In the case of a transmission mode microscope, a transparent tape layer should be used. The individual washers can then be cut out, each supporting a suspended polymer with a flake of graphene

8. Using a flip chip bonder, we align the polymer-support flake with a flake exfoliated on a substrate. We then bring them into contact, and heat the substrate to 120°C , cool down to room temperature, and then disengage. The result will be that the PMMA layer will detach from the PVA and transfer with the flake onto the substrate.

9. The PMMA layer is dissolved in acetone. The flakes on the substrate are then heat annealed under forming gas flow (300 sccm of Ar and 700 sccm of H_2) at 350°C for 2 hours.. This serves the dual purpose of removing polymer residue on top of the flakes, and also generally increases the flatness of the graphene transferred onto the hBN.

A.3 Additional nanofabrication details

A.3.1 Source materials

The source for the graphene in all experiments was from a graphite mine in India. The distributor was NGS Naturgraphit. The hexagonal boron nitride was grown by collaborators Takashi Taniguchi and Kenji Watanabe at the National Institute for Materials Science in Japan[228].

A.3.2 Contacts

Electric contacts are made to the graphene using a nanolithography process to define a PMMA polymer evaporation mask. A 1nm layer of Cr and then at 60-150nm layer of Au is evaporated using a thermal evaporator at a pressure of 1e-6Torr. The thin 1nm Cr layer is necessary to make the gold stick to the SiO_2. It is kept this thin because thicker layers of Cr will become strained when cooling/heating the sample, which will damage the contact.

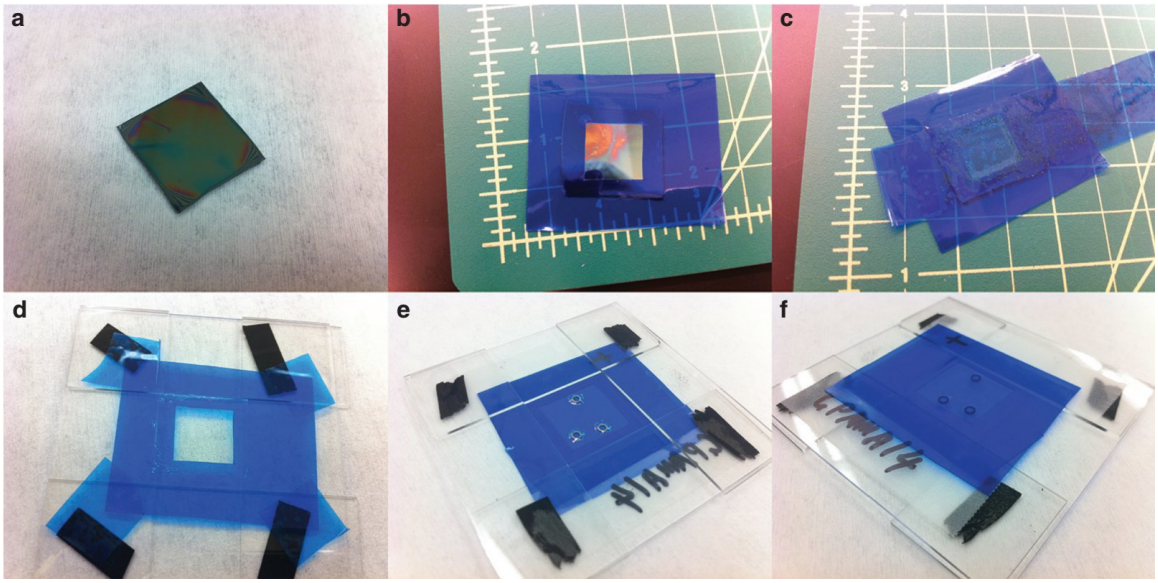

Figure A.4. PVA-based transfer method. **a)** Silicon chip with PVA and PMMA spun on. **b)** Tape window for supporting polymer film. **c)** With tape for depositing flake material. **d)** After suspending membrane. **e)** After placing washers and fixing with backing tape layer. **f)** Other side of window with tape backing layer.

Appendix B

Additional details for graphene quantum spin Hall state experiment

B.1 Fabrication

The samples for the monolayer graphene QSH experiments (Section 2.4) consisted of graphene-hBN-graphite stacks fabricated by a dry transfer process (see Appendix A). Samples were annealed in H_2-Ar atmosphere at 350^oC[43] after each transfer step and after patterning of contacts by standard electron beam lithography techniques. Images of the final devices can be seen in Figure B.2. Before measurement, residual debris from the fabrication process was swept off the graphene flake with an atomic force microscope tip operated in contact mode[77, 100] (the evidence of this is visible in the AFM micrograph inset to Figure 2.6b). The methods used produce a random alignment angle between graphene and hBN flakes. However, in the samples reported on in Section 2.4, we did not see any evidence for moiré-induced band structure reconstructions (see Chapter 3), suggesting that either the twist angle between graphene and hBN lattices is large, or the coupling is weak (see Figure B.9 for additional information).

B.2 Conductance measurements

Conductance measurements were made using ∼300 Hz voltage bias, with V_{ac}=100μV. The sample was immersed in ^{3}He liquid at 300mK for all measurements in Section 2.4 except those shown in Figure 2.8a, where the temperature is indicated, and those shown in Figure 2.7, which were taken at 150mK with the sample immersed in ^{3}He/^{4}He mixture. The angle between the magnetic field and graphene plane was controlled by a mechanical rotator. The sample was aligned using high density Shubnikov de Haas oscillations, ensuring reproducible alignment to better than $.025^o$ in the large tilt angle regime, $B_\perp \ll B_T$. For multiterminal devices (A and C), all measurements were done between two pairs of contacts (top configuration of Figure 2.7a) unless otherwise indicated, ensuring that only two uninterrupted edges are being measured.

B.3 Capacitance measurements

To measure capacitance, we used a HEMT-based amplifier to construct a low temperature capacitance bridge-on-a-chip[12]. A schematic representation of the bridge geometry and electronics appears in Figure B.8. In this geometry, an AC excitation on the graphene sample is balanced against a variable phase and amplitude excitation on a known reference capacitor, which is located near the sample. The sample bias was 900μV for the data set in Figure 2.5b and 100μV for that in Figure 2.7a, both of which were measured at 78 kHz. The signal at the input of the HEMT amplifier was first nulled by adjusting the reference excitation using a home-built dual-channel AC signal generator, after which data were acquired off-balance by monitoring the in- and out-of phase voltage at the balance point as a function of the applied DC sample bias. Biasing the transistor amplifier raised the base temperature of the cryostat, so that the temperature was 400mK during acquisition of the data in Figure 2.5b and 250 mK for Figure 2.7a.

Extracting density of states information from capacitance measurements requires that the measurement frequency, f, be lower than the inverse charging time of the experimental system[75]. Because incompressible regimes in quantum Hall samples are also highly resistive, contrast in the capacitance signal can be generated by the swing in sample resistance rather than density of states. In this case, capacitance minima appear because the sample can no longer charge on timescales of f^{-1}. Experimentally, such a transition is accompanied by a peak in the out-of-phase (dissipation) signal, which reaches a a maximum when the sample resistance $R \sim 1/fC$, where C is the sample capacitance. In the capacitance data shown in Figures 2.5b and 2.7a, the dissipation signal is less than $\sim 10\%$ of the capacitive signal, suggesting that the observed features are mostly due to density of states. We note that whether the capacitance dip associated with the metallic, high field $\nu = 0$ state is due to incompressibility or high bulk resistance is immaterial to the conclusions in Section 2.4: in either case, any metallic transport should be via edge states.

B.4 Additional data

Sample Name	BN Thickness (nm)	Sample Dimensions LxW (μm)	Aspect Ratio (L/W)
A	14	3.6 x 1.4	2.6
B	9	1.8 x 0.9	2
C	8.4	1.2 x 1.2	1
D	4.2	2.1 x 0.7	3
E	3.4	1.6 x 0.7	2.2
F	4	1.1 x 0.9	1.2
G	4.4	1 x 1	1
H	2.2	1.4 x 2	0.7
I	3.8	0.7 x 1.8	0.4

Figure B.1. Physical parameters of measured samples. The studied devices consisted of sequentially stacked flakes of thin graphite, h-BN, and monolayer graphene on an insulating Si wafer with 285nm of thermally-grown SiO_2. The bottom graphite layer serves as a local gate electrode as well as to screen charge inhomogeneity in the graphene. The table lists the details of the samples discussed in the Section 2.4 (Samples A, B, and C), as well as for additional samples which are presented in this appendix (Samples D-I).

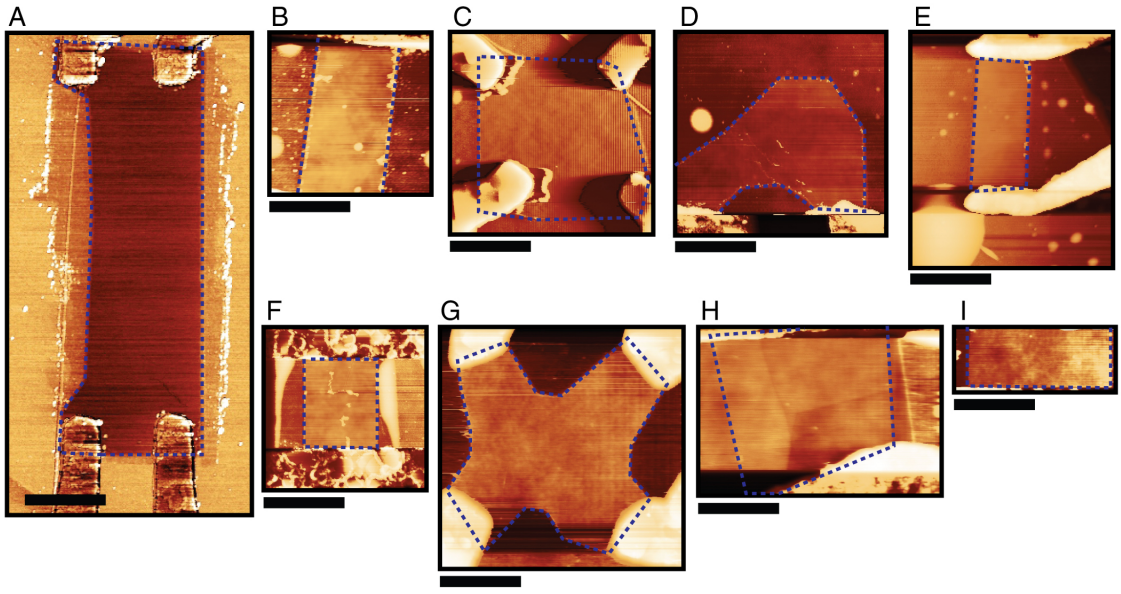

Figure B.2. Images of measured devices. False color AFM images of the devices enumerated in Table B.1. Dashed lines outline the graphene boundary. Black scale bars correspond to 1 μm.

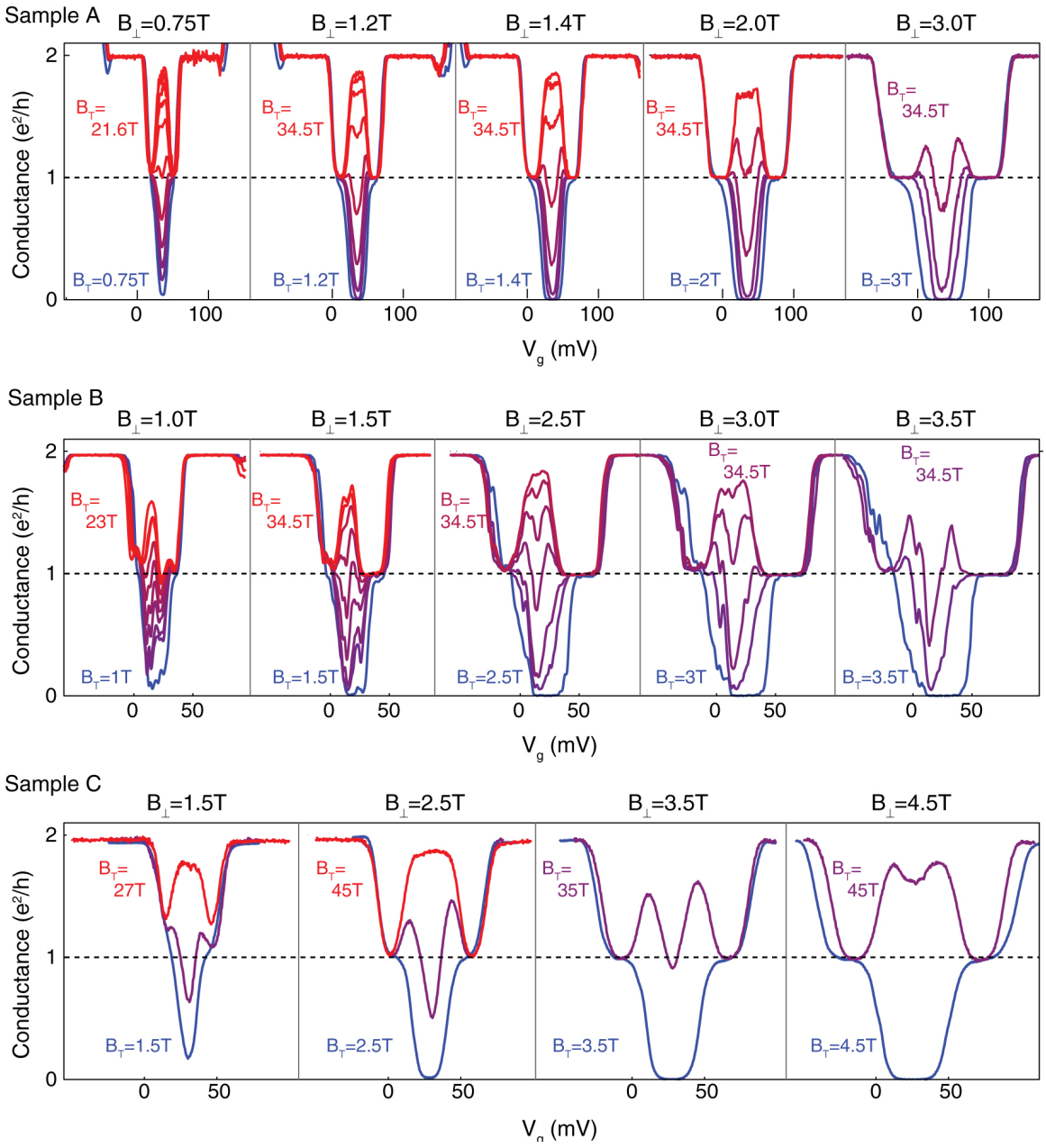

Figure B.3. Conductance as a function of $B_\perp$, B_T, and gate voltage for samples A, B and C. Coloring of lines from blue to red indicates increasing B_T, with $B_\perp$ as indicated at the top of each panel.

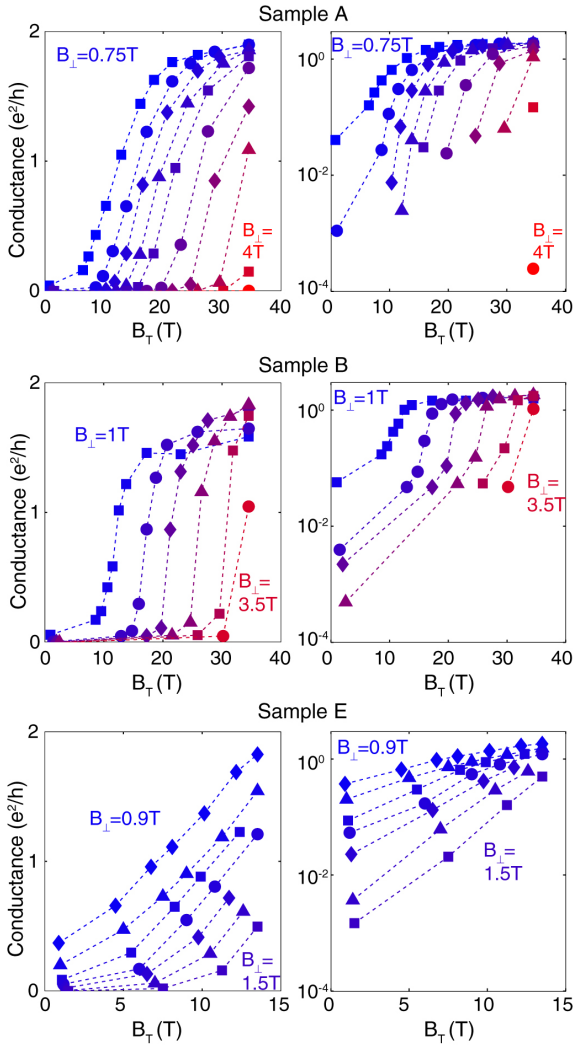

Figure B.4. $G_{\mathbf{cnp}}$ **as a function of** $B_\perp$ **and** B_T **for samples A, B and E.** Correspondingly higher values of B_T are required to induce the transition for higher values of $B_\perp$. For Sample A, the curves correspond to (blue to red) $B_\perp$=0.75, 1, 1.2, 1.4, 1.6, 2, 2.5, 3, 3.5, and 4T. For Sample B, the curves correspond to (blue to red) $B_\perp$=1, 1.5, 2, 2.5, 3, and 3.5 T. For Sample E, the curves correspond to (blue to red) $B_\perp$=0.9, 1, 1.1, 1.2, 1.3, 1.4, and 1.5T.

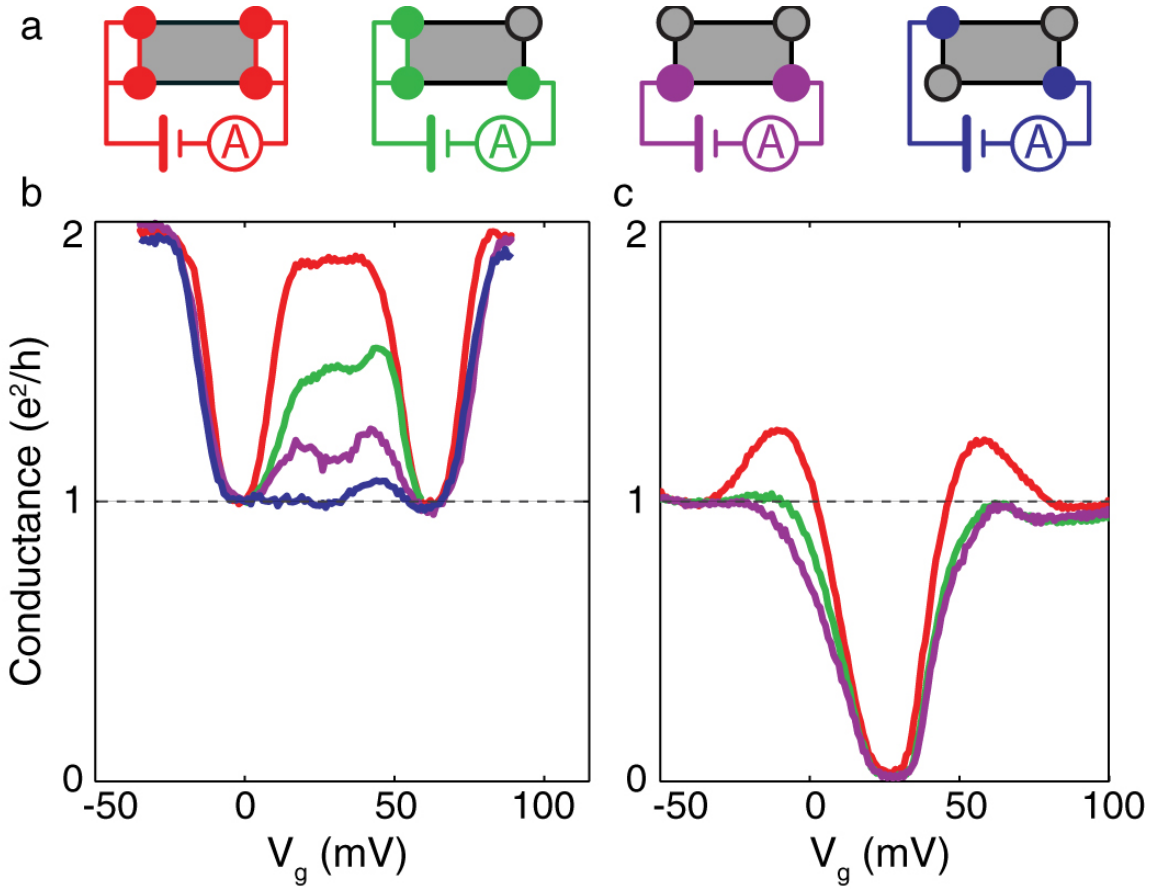

Figure B.5. Nonlocal measurements for sample C in the QSH and CAF regime. In Section 2.4, evidence for conduction via edge states in the QSH and CAF regimes is provided by nonlocal transport measurements in Sample A (Figures 2.6b and 2.8b). Due to conduction through counter-propagating edge states, interrupting an edge with a floating contact decreases the 2-terminal conductance much more than would be expected in a diffusive transport model. Here we provide an additional example of this behavior for sample C. **a,** Schematic of distinct 2-terminal measurement topologies with different number of floating contacts (hollow circles). **b,** QSH regime, $B_\perp$=2.7T and B_T=45T. **c,** CAF regime, $B_\perp$=5.9T and B_T=45T. Curves are color coded according to the measurement schematics, as in the main text. Due to a small gate leak in one of the contacts, these specific nonlocal measurements underestimate the conductance by a scale factor which was adjusted for by fitting the $\nu = -1$ plateau to a conductance of e^2/h.

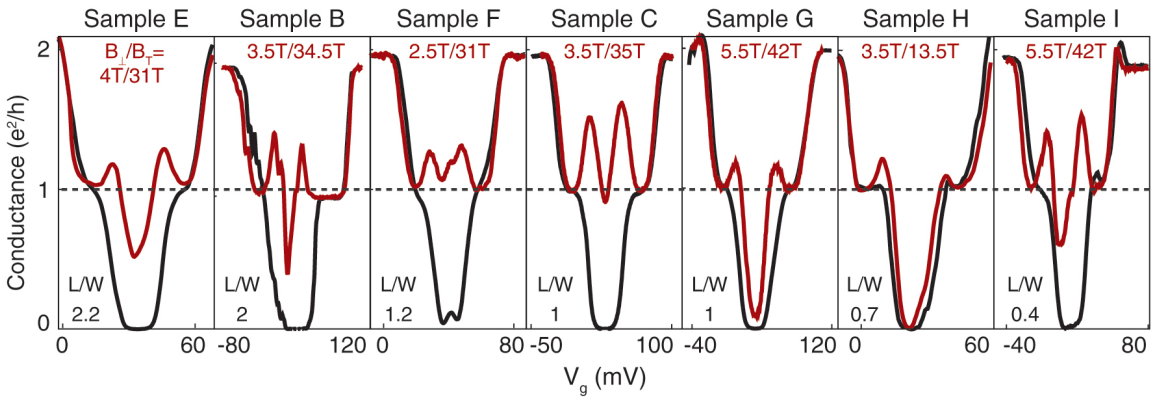

Figure B.6. Double conductance peaks in seven different samples. A generic feature of the intermediate regime between the insulating and metallic QSH regimes is the appearance of double conductance peaks close to $\nu = 0$. The figure shows two-terminal conductance vs. backgate voltage V_G. Purely perpendicular magnetic field only ($B_{\rm T} = B_\perp$, black lines) results in an insulating state at $\nu = 0$. Increasing the total magnetic field while keeping the perpendicular component constant ($B_{\rm T} > B_\perp$, red lines), induces a transition to the CAF with associated double conductance peak feature. Samples are ordered from left to right by descending aspect ratio.

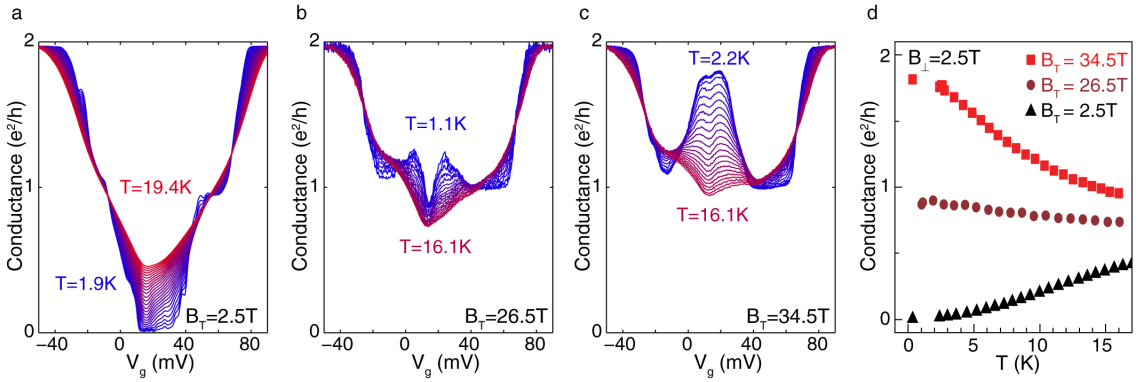

Figure B.7. Temperature dependence of the charge-neutrality point conductivity for Sample B. a-c, Gate sweeps for sample B at constant $B_\perp = 2.5$T and $B_{\rm T} = 2.5$T, 26.5T and 34.5T for a, b, and c, respectively. **d,** Conductance at the charge neutrality point as a function of temperature for the data in a, b, and c. A clear insulating dependence ($\partial G/\partial T > 0$) is observed for $B_\perp = B_{\rm T}$. With increased $B_{\rm T}$, in the intermediate regime, the double conductance peaks between $\nu = 0$ and $\nu = \pm 1$ display a weakly metallic temperature dependence ($\partial G/\partial T < 0$) while G_{cnp} is very weakly insulating. In the QSH regime ($B_{\rm T} \gg B_\perp$), where the conduction is along edge channels, the temperature dependence at $\nu = 0$ is metallic.

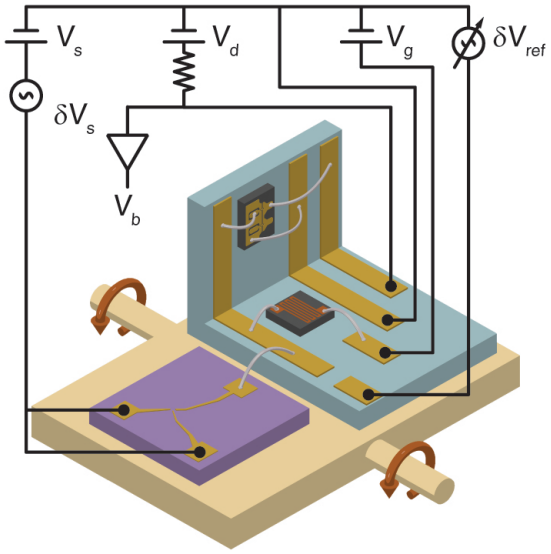

Figure B.8. Schematic of the capacitance bridge-on-a-chip in tilted magnetic field. The magnetic field points up in the schematic. Beige: sample stage, showing axis of rotation (red arrows). Purple: graphene sample mount. Blue: transistor mount with 90° bend. The HEMT is mounted on the face angled 90° from the graphene sample mount and with the plane of its 2D conduction channel perpendicular to the sample stage axis of rotation. A single wire bond connects the two mounts, from the graphite back gate to the balance point of the capacitance bridge. The transistor is gated by applying V_g to the balance point/graphite back gate through a 100 MΩ chip resistor. Combined with total capacitance of the balance point to ground ($\sim$ 3 pF), this sets the low frequency cutoff for the measurement at $\sim$ 1 kHz. The density of electrons in the graphene sample is determined by the DC voltage difference between the graphene sample and the graphite back gate, namely by $V_s - V_g$. In the data presented in Section 2.4, this is compensated for, and all capacitance measurements are shown as a function of the graphite gate voltage relative to grounded graphene. All components shown in black are at room temperature.

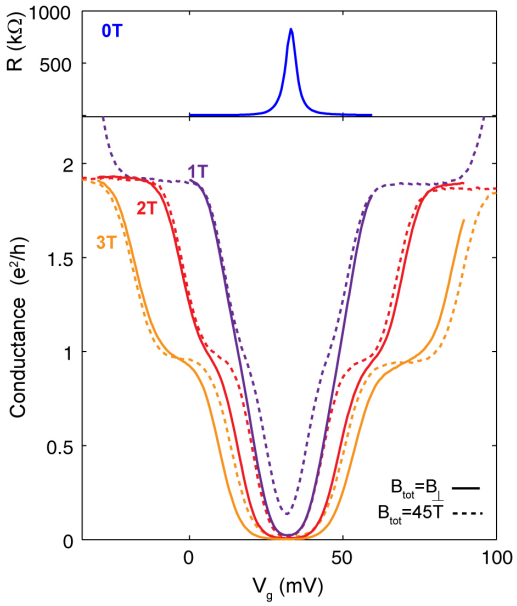

Figure B.9. Tilted-field magnetotransport in zero-field insulating monolayer graphene. In a fraction of devices having the identical geometry to those presented in Section 2.4, we find that rather than a conductivity of $\sim e^2/h$ at charge neutrality these devices instead exhibit insulating behavior at the CNP at zero applied magnetic field. We ascribe this insulating behavior to the opening of a bandgap at the CNP due to the effect of an aligned hBN substrate (see Chapter 3). The top panel shows resistance of the device in zero magnetic field. This device has a resistance of 825 kΩ at the CNP in zero magnetic field and T=.3K. As with the devices described in Chapter 2, the insulating state becomes stronger in a perpendicular magnetic field. In the bottom panel, solid lines are gate sweeps at constant $B_\perp$=1, 2 and 3T and $B_\mathrm{T} = B_\perp$. Dashed lines are for the corresponding sequence of $B_\perp$=1, 2 and 3T but with B_T=45T for each. Data taken at 0.3K. Semiconducting graphene samples do not show any sign of QSH-type physics, at least up to 45T. Even for $B_\perp$=1T and B_T=45T, the conductance at the CNP increases only slightly, from 0.02 e^2/h with zero in-plane field to $0.14e^2/h$ with B_T=45T. This is understandable, as even neglecting interaction effects, closing a moiré-induced band gap of $\Delta = 10$ meV requires a Zeeman field of nearly $\Delta/(g\mu_B) \approx 85$ T. We note that in these samples, the ground state at $B_\mathrm{T} = B_\perp$ may not be an antiferromagnet.

Appendix C

Additional details for graphene-hBN superlattice experiments

C.1 Zero and low-field transport measurements

Figure C.1 shows magnetotransport measurements performed on the four semiconducting graphene devices discussed in Section 3.4 at the base temperature of 150 mK. They attest to the high quality of our devices: well-formed plateaus at filling factor $\nu = 2$ appear for $B_Q \approx 100$ mT, implying that the quantum mobility $\mu_Q \equiv 1/B_Q$ is at least 10^5 cm^2/(V·s). This is in agreement with our measurements of the field-effect mobility $\mu_{FE} = e^{-1}(d\sigma/dn)$ close to charge neutrality (Figure C.2). Note that the field-effect mobility for all devices is an underestimate due to the effects of contact resistance and quantum capacitance, which reduces the capacitance used in calculating the charge density n in this simple estimate.

The transport data in Figure C.1A is the analogue of the capacitance data presented in Section 3.4 (Figure 3.10), and similarly shows the insulating state at zero field persisting as the field is raised. The insulator appears as a dark vertical band centered at the charge neutrality point (CNP), further confirming that a Landau level never forms at zero energy. A line trace of conductance at a single fixed density inside the gap (Figure C.1C) shows that the conductance is a monotonically decreasing function of $|B|$, decreasing by two orders of magnitude between $B = 0$ and $B = 2$ T before dropping below the noise floor of our measurement.

In addition to the four devices studied in Section 3.4, we measured a fifth graphene-hBN-graphite device that displayed insulating behavior at charge neutrality in zero field (Figure C.3). This device was fabricated in the identical manner to the other four but using a different, 5.9-nm-thick hBN flake as the substrate. This two-terminal device was approximately 1 μm × 1 μm. Its resistance at 0.3K at the CNP was 825 kΩ, and the width (in gate voltage) of the insulating state was comparable to the device A2.

C.2 Moire superlattices

A graphene-hBN heterostructure naturally leads to a moiré superlattice due to the $\delta = 1.8\%$ lattice mismatch and the rotational misalignment between the layers (quantified

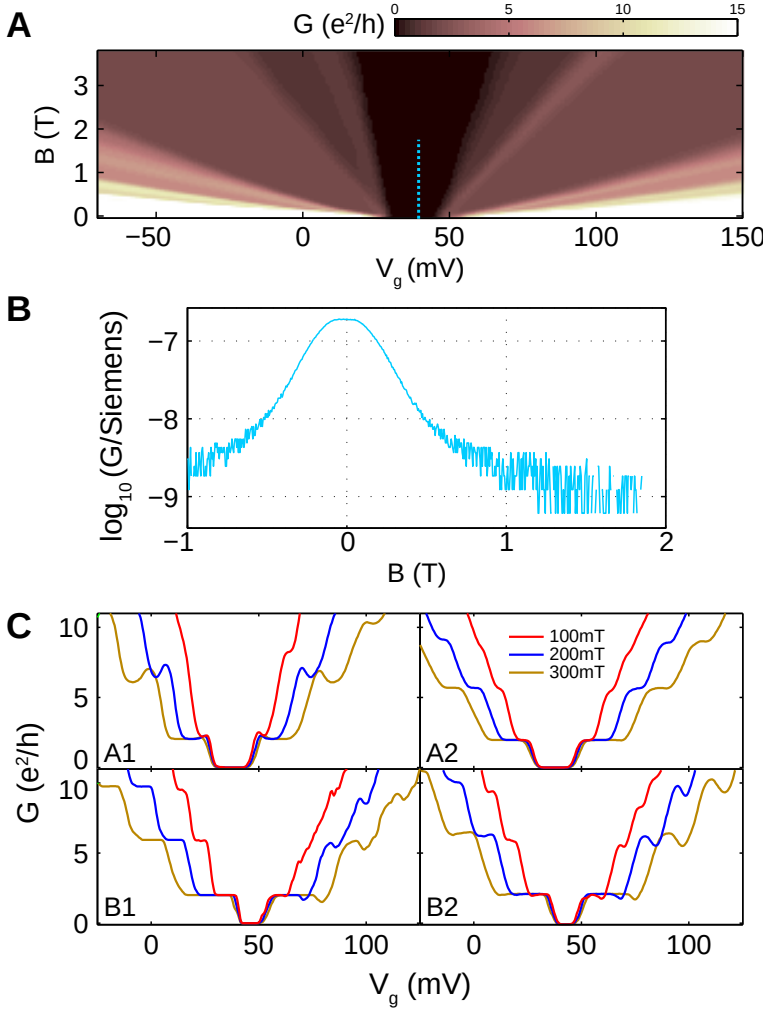

Figure C.1. Magnetotransport measurements of insulating graphene devices. (A) Conductance of device A1 as a function of gate voltage and magnetic field. **(B)** Conductance trace at $V_g = 40$ mV, showing that G_{CNP} is a monotonically decreasing function of $|B|$. **(C)** Gate sweeps at low field of the four devices, at B=100 (red), 200 (blue) and 300 mT (tan) . Well-quantized $\nu = \pm 2$ plateaus appear at $B \lesssim 100$ mT for all devices.

by the twist angle θ). The wavelength λ of the moiré is related to θ by [240]

$$\lambda = \frac{(1+\delta)a}{\sqrt{2(1+\delta)(1-\cos\theta)+\delta^2}}, \tag{C.1}$$

where a is the graphene lattice constant.

The wavelength λ of the moiré superlattice can be determined from its effects on the graphene magnetotransport measurements (Figure C.4 and C.5). At zero field, λ can

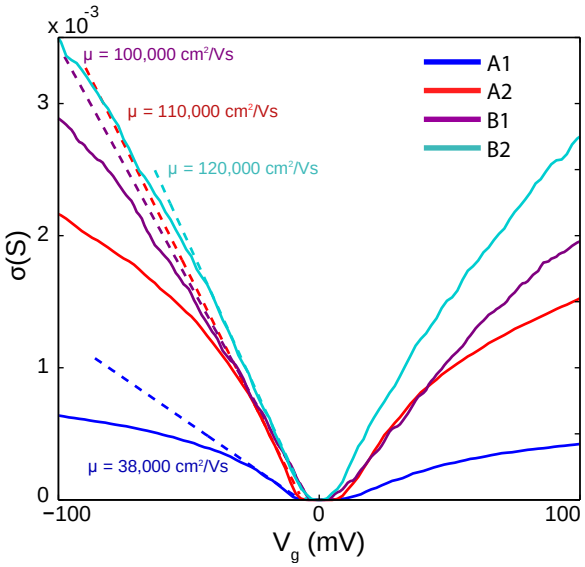

Figure C.2. Zero-field transport and field-effect mobility of insulating graphene devices. Conductivity vs. gate voltage for the four devices discussed in main text. Dashed lines are low-density tangents whose slope corresponds to the field-effect mobility

be estimated from the location in gate voltage of the superlattice Dirac points, which occur at carrier density $n = 4n_0$, where n_0 is the inverse superlattice unit cell area.

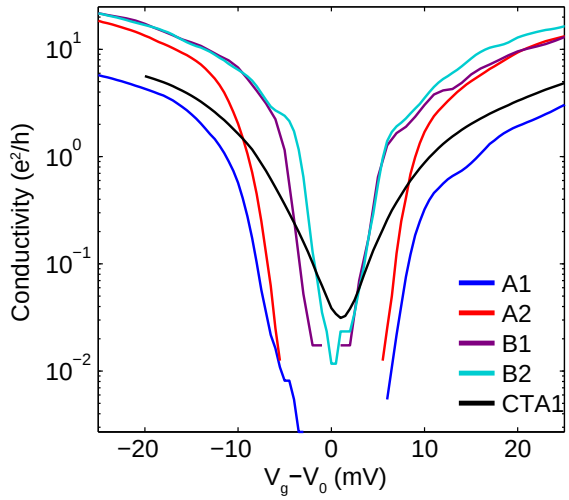

Figure C.3. Additional zero-field-insulating graphene-hBN device. Data for this (fifth) device, CTA1, are shown in black and compared with the four devices studied in the Section 3.4. The data ranges are the same as in Figure 3.8B of Chapter 3 but on a semilog scale. The CNP offset V_0=37, 37, 46 and 42 mV respectively for A1, A2, B1 and B2, as in Figure 3.8B, and V_0=32 mV for CTA1.

This requires knowledge of the carrier density as a function of gate voltage, which can be inferred from a charging model of the device that includes the effect of quantum capacitance $\tilde{C}_Q \equiv e^2(dn/d\mu)$ close to the CNP to give

$$n(V_g) = \frac{\tilde{C}_{geom}V_g}{e} - n_Q\left(\sqrt{1+\frac{\tilde{C}_{geom}V_g}{en_Q}} - 1\right), \tag{C.2}$$

where $n_Q \equiv (\pi/2)(\tilde{C}_{geom}\hbar v_F/e^2)^2$ [38] and $\tilde{C} \equiv C/A$ denotes capacitance per unit area A of the device. From the observed location of the superlattice Dirac points at 1.45V and 2.80V we estimate λ =11-13.5nm and 7.5-9.5nm for samples A1 and A2, respectively. This simple model does not take into account any modifications of the graphene band structure by electron-electron interactions or the moiré, but these effects are small in comparison to the error due to the uncertainty in the hBN dielectric constant.

A more accurate method for extracting λ is to fit the magnetotransport features associated with the Hofstadter spectrum. This method is purely geometric, and does not require knowledge of the carrier density, as it directly connects the superlattice unit cell area with the applied magnetic field. Figure C.4 shows magnetotransport measurements of samples A1, A2, and B1. Data from both samples A1 and A2 show secondary Landau fans centered at the high density resistance peaks discussed in Chapter 3, with a clear beating pattern arising from the interpenetrating Landau fans. When plotted on $V_G - 1/B$ axes (Figure C.5), it is clear that these bands of conductance peaks and intersecting gap features are uniformly spaced in $1/B$. Within the Wannier picture [227], integer Landau level gaps for different Landau fans are expected to intersect when $\phi/\phi_0 = 1/q$, where q is an integer. For example, the te^2/h gap features associated with the first Landau level of the $s = -4$ miniband and the $t'e^2/h$ state of the $s = 0$ fan will intersect at a density, such that

$$n/n_0 = t(\phi/\phi_0) - 4 = t'(\phi/\phi_0) \tag{C.3}$$

$$\phi/\phi_0 = -4/(t'-t) = 1/q \tag{C.4}$$

as long as t and t' are both integers in the main graphene sequence, $t^{(\prime)} = 4(N + 1/2)$. The positions of these features are fit by a single parameter B_0, the magnetic field at which one flux quantum threads the superlattice unit cell. Measuring B_0 allows us to infer the superlattice unit cell area n_0^{-1} and by extension $\lambda = \sqrt{2/\sqrt{3}n_0}$. Fitting the data in Figure C.5 produces values for samples A1 and A2 of $B_0 = 28.7 \pm 1.0$ T and 57.0 ± 1.2 T, giving λ=12.9 ± 0.2 nm and 9.2 ± 0.1 nm, respectively.

The most direct method to determine λ is to perform scanning tunneling microscopy measurements of the graphene-hBN heterostructure, where the moiré pattern can be directly imaged in a topographic scan. Figure C.6 shows topographic maps of sample B2 which clearly show a long-wavelength hexagonal moiré pattern. In this way we were able to independently measure λ for each of the devices to be: $\lambda_{B2} = 3.45 \pm 0.07$ nm, $\lambda_{B1} = 3.77 \pm 0.09$ nm, $\lambda_{A2} = 9.37 \pm 0.14$ nm and $\lambda_{A1} = 13.5 \pm 0.5$ nm.

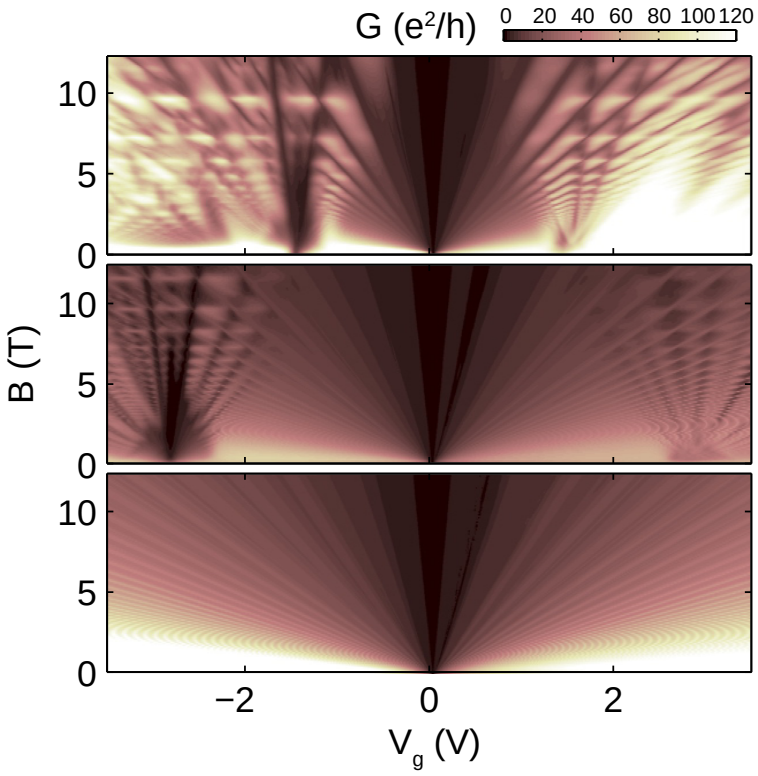

Figure C.4. Magnetotransport and superlattice Dirac points. Top to bottom: devices A1, A2 and B2.

■ C.3 Theoretical model for Hofstadter spectrum of monolayer graphene on hBN

For the numerical calculation of the Hofstadter band structure shown in Figure 3.9D, graphene and hBN are modeled by honeycomb lattices with lattice periods $a = 0.246$ nm and $a_{\mathrm{hBN}} = 0.2504$ nm, repectively [132]. We assume that graphene monolayer and hBN monolayer are aligned with zero rotation angle, and the ratio between the two lattice constants is round to a rational number $a_{\mathrm{hBN}}/a = 56/55$ to give a finite moiré superlattice period $56a \approx 13.8$ nm. The interlayer distance between hBN and graphene is set to 0.322 nm [69]. We consider the p-type orbital state on each atomic site within the tight binding model, and set the on-site potential to 0, 3.34eV and -1.40eV for the C, B and N atoms, respectively[208]. For the hopping amplitudes between different sites, we adopt the Slater-Koster parametrization [157] irrespective of the atomic species under consideration. To compute the low-energy spectrum in magnetic field, we take the low-lying Landau levels ($|E| < 1.5$ eV) of isolated monolayer graphene as the basis [157], and the coupling with hBN states is included as an on-site potential on the graphene atomic sites within second-order perturbation theory [41]. The spectrum obtained by

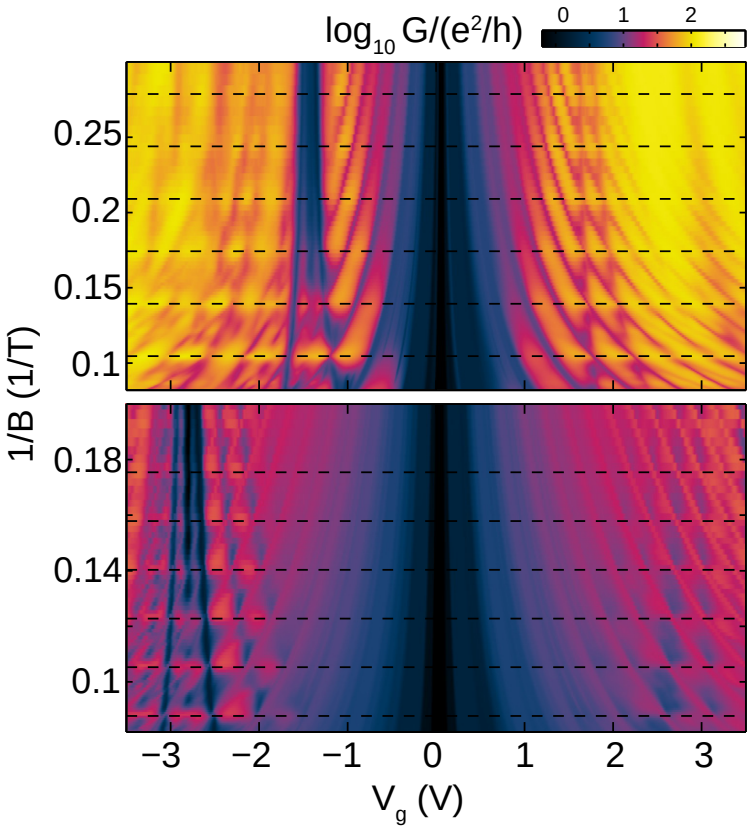

Figure C.5. Fits to Landau level crossings of Hofstadter spectrum and Hofstadter oscillations. Magnetotransport of samples A1 (top) and A2 (bottom) plotted as a function of $1/B$. Dashed lines are a fit to the Landau level crossings with the equation $B_0/B = q$, where q is an integer and B_0 is the flux quantum per superlattice unit cell. B_0 is equal to 28.7 T and 57.0 T for samples A1 and A2 respectively.

this method is nearly valley degenerate, and exactly spin degenerate. At high fields, the valley and spins are split, likely due to a combination of Zeeman effect, the band gap, and exchange effects. To simulate this, we add a phenomenological energy splitting $\delta E = (s + \xi/2)\Delta$, where $s = \pm 1$ and $\xi = \pm 1$ are spin and valley quantum numbers, respectively, and $\Delta = 8B/B_0(\text{meV})$ is the splitting width. Results of this calculation are shown in Figure C.7.

■ C.4 Landau level spectrum

In this section we describe the single particle spectrum of monolayer graphene in the presence of a mass gap. Using the basis $(\psi_{KA}, \psi_{KB}, \psi_{K'B}, -\psi_{K'A})$, the Hamiltonian in

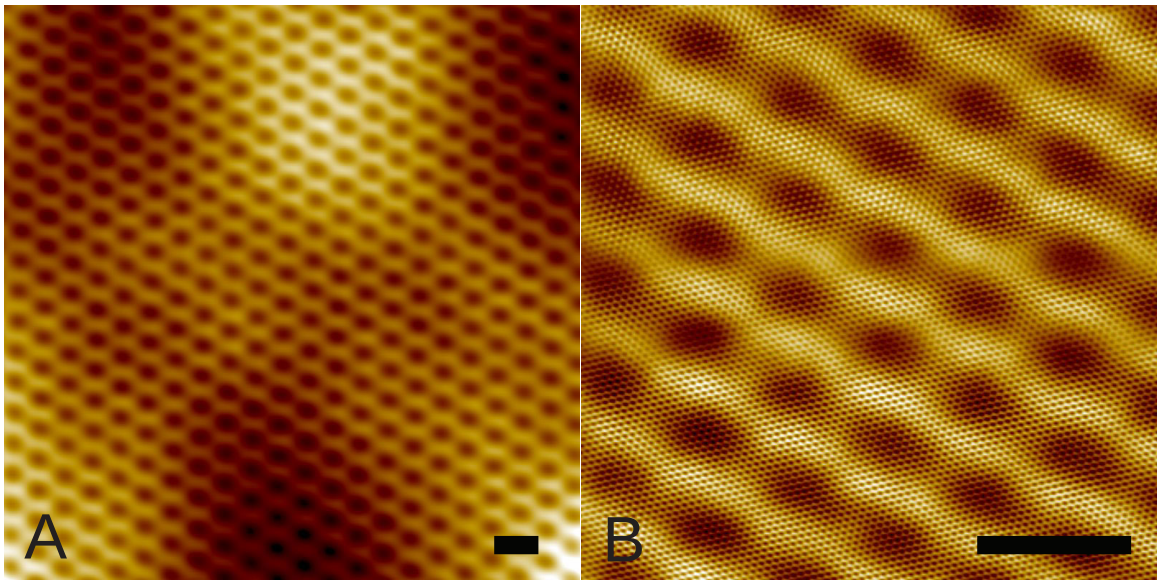

Figure C.6. STM topography map of sample B2. Topography map taken at a sample voltage of 0.3 V and a constant tunnel current of 100 pA. The scale bars for both images are 5 nm.

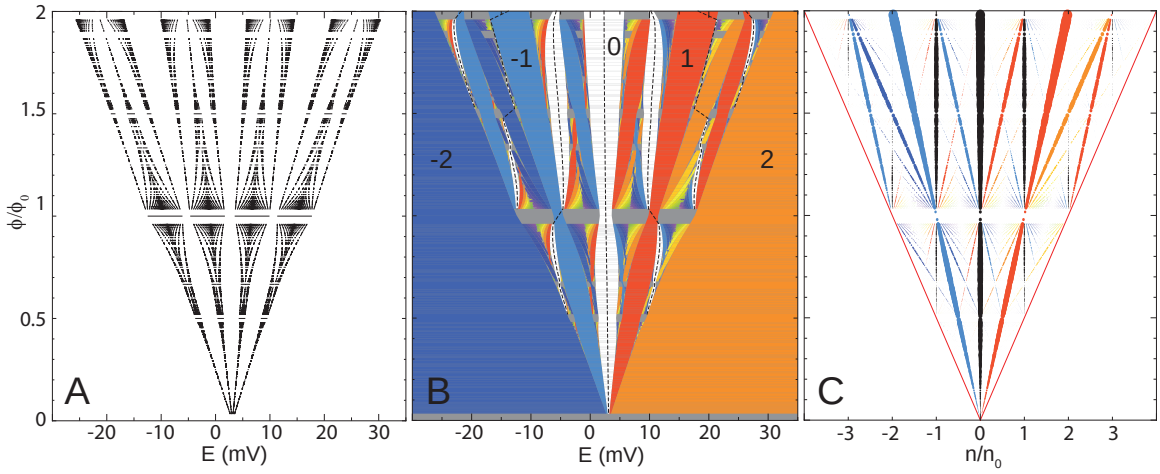

Figure C.7. Calculated Hofstadter spectrum, Hall conductivity, and Wannier diagram for the N=0 LL with fully broken spin and valley symmetry. (A) Hofstadter butterfly spectrum calculated from a tight binding model with an additional valley and spin splitting. (B) The same data, with gaps color-coded to reflect the quantized Hall conductance. The numbers indicate the corresponding value of the Hall conductance. The dashed curves mark constant density within the energy spectrum, specifically integer multiples of n_0. (C) Wannier diagram for the N=0 Landau level. The depicted features are gaps, color coded as in (B). Gapped features follow linear trajectories [213, 217, 227].

zero magnetic field simplifies in each valley to

$$\hat{H} = \begin{pmatrix} \xi m^* v_F^2 & v_F(p_x - ip_y) \\ v_F(p_x + ip_y) & -\xi m^* v_F^2 \end{pmatrix} \tag{C.5}$$

where $\xi = \pm 1$ labels the valley. Working in the Landau gauge $\mathbf{A} = -By\hat{x}$, the Hamiltonian is independent of x so that the wavefunctions are parameterized by the conserved quantum number p_x, where $\langle \mathbf{r}|\Psi\rangle = e^{ip_x x/\hbar}\boldsymbol{\phi}(y)$. After introducing the identities

$$\boldsymbol{\pi} \equiv \mathbf{p} - e\mathbf{A} \qquad \hat{a}^{(\dagger)} \equiv \frac{\ell_B}{\hbar\sqrt{2}}(\hat{\pi}_x \mp i\hat{\pi}_y) \qquad \ell_B = \sqrt{\frac{\hbar}{eB}}$$

we arrive at the Hamiltonian

$$\hat{H} = \frac{\hbar v_F \sqrt{2}}{\ell_B} \begin{pmatrix} \xi\mu & \hat{a}^\dagger \\ \hat{a} & -\xi\mu \end{pmatrix} \tag{C.6}$$

where $\hat{a}$ and $\hat{a}^\dagger$ obey $[a, a^\dagger] = 1$, so that they are creation and annihilation operators operating in the space of quantum harmonic oscillator states $|n\rangle$, and

$$\mu = \frac{m^* v_F^2 \ell_B}{\hbar v_F \sqrt{2}}$$

parameterizes the effective mass, written in units of the cyclotron energy. The eigenstates differ in form for $n = 0$ and $n > 0$. For the latter, there are two solutions for every positive n, with eigenvectors and corresponding eigenvalues

$$|\phi_{n>0}\rangle = \frac{1}{\sqrt{2}} \begin{pmatrix} \xi\sqrt{1 \pm \frac{\mu}{\sqrt{n+\mu^2}}}|n\rangle \\ \pm\sqrt{1 \mp \frac{\mu}{\sqrt{n+\mu^2}}}|n-1\rangle \end{pmatrix} \tag{C.7}$$

$$\epsilon_n = \pm\xi \frac{\hbar v_F \sqrt{2}}{\ell_B}\sqrt{n + \mu^2} \tag{C.8}$$

For $n = 0$ the solution is

$$|\phi_0\rangle = \begin{pmatrix} |0\rangle \\ 0 \end{pmatrix} \tag{C.9}$$

$$\epsilon_n = \xi m^* v_F^2 \tag{C.10}$$

The choice of basis means that the wavefunctions in the two valleys are fully polarized on different sublattices. The combined spectrum can be rewritten more transparently in terms of a quantum number N spanning all integers so that we recover the spectrum given in Chapter 3,

$$\epsilon_N = \begin{cases} \frac{\hbar v_F \sqrt{2}}{\ell_B}\mathrm{sgn}(N)\sqrt{2(\hbar v_F)^2|N|/\ell_B + (m^* v_F^2)^2} & N \neq 0 \\ \xi m^* v_F^2 & N = 0 \end{cases} \tag{C.11}$$

For $m^* = 0$, the spectrum is identical for both the valleys, as shown in Figure C.8A. While a nonzero m^* leads to shifts in all the energy levels, it leaves the valley degeneracy of the $N \neq 0$ levels intact. Not so the $N = 0$ LL, which splits into two doubly degenerate (when real spin is accounted for) levels (Figure C.8B). Like the zero mode of the massless equation, these levels do not disperse with magnetic field (Figure C.8C).

C.5 Gap measurements

C.5.1 Temperature dependence of conductivity at B=0

The temperature dependence of the minimum conductivity of the devices discussed in Section 3.4 were measured to elucidate the nature of the observed insulating state. This data is presented in Figure C.9, where the horizontal temperature axis is plotted as $1/T$. All samples exhibit a strong temperature dependence at high temperatures (200K to 20K), with the conductivity decreasing by orders of magnitude as the temperature decreases. We fit this high temperature regime with an Arrhenius dependence $\sigma \propto \exp(-\Delta/2T)$ to extract a gap, Δ, for each sample (Figure C.10). An Arrhenius dependence describes the high temperature conductance variation, especially in the samples with the largest Δ (samples A1 and A2). As the temperature is further reduced the conductivity deviates from a single gap Arrhenius law, with samples B1 and B2 showing the largest deviations. Such a deviation from simply activated behavior is expected as disorder effects set in and has been observed in other graphene systems with gaps induced by electric field [216] or by magnetic field [58]. Indeed, for intermediate temperatures (40K - 20K) our data can be fit by a variable-range hopping model with $\sigma(T) \propto \exp(-\sqrt{T^*/T})$ (Figure C.11) [206], although its validity is restricted to a narrow range with Arrhenius behavior more appropriate in the high-temperature limit. What is clear is that a single model cannot account for the entire temperature dependence from 200K to 2K. Given that the distribution of disorder at small energy scales in our samples is unknown, we focus on the high-temperature region of the conductance change to extract an energy scale associated with the gap of the devices.

C.5.2 Magnetic field dependence of the gap

Δ is not field independent at low fields, varying non-monotonically as the field is increased (Figure C.12). The gap is determined by fitting the temperature dependence of the minimum conductivity for each sample to an Arrhenius dependence from T =20-50K over a factor of 10 change in conductance at various magnetic fields. We note that this effect is absent in the single-particle model of [113].

C.6 Capacitance measurements

C.6.1 Principle of measurement

We measure capacitance between the graphene sheet and the graphite back gate by using a low-temperature capacitance bridge, based on a high-electron mobility transistor (HEMT). Our "bridge-on-a-chip" has very high sensitivity (approximately $10^{-1}e/\sqrt{\text{Hz}}$; e is the electron charge) and has been used to measure, among other things, single-electron charging of semiconductor quantum dots [12]. This technique is particularly well suited for measuring small-area graphene devices. It is based on the principle of applying a known AC excitation V_{meas} to the top plate of the unknown capacitance C_{meas} and a second AC excitation V_{std}, approximately 180° out of phase with V_{meas} to the top plate of a known, standard capacitor C_{std} Figure C.13. The bottom plates are connected at a common point–the "balance point"– and V_{std} is adjusted until the potential modulation at the balance point is zero. The unknown capacitance is then given by

$$C_{meas} = (V_{std}/V_{meas})\, C_{std}. \tag{C.12}$$

We typically use an excitation V_{meas} of 100 μV to 1 mV.

In practice, to measure the capacitance $C_{meas}(V_g, B)$, we balance once at the beginning of a V_g sweep and then measure the off-balance signal to determine the capacitance. Placing the gate of the HEMT at the balance point reduces the capacitance to ground at that point by a factor of C_{gs}/C_{cable}, where $C_{gs} \approx 0.4$ pF is the gate-source capacitance of the HEMT and $C_{cable} \approx 200$ pF is the capacitance to ground of the coaxial cable used to measure the signal at the (cold) balance point. Thus, even when the gain of the transistor is of order unity (and in practice we operate at higher gain of $\sim 3-4$), the transistor mitigates the shunting effect of the coaxial cable and consequently improves the signal-to-noise by a factor of $C_{cable}/C_{gs} \approx 500$.

C.6.2 Additional capacitance measurements

When the bulk resistance R of the device becomes large, the equation relating the measured capacitance $C_{meas} \equiv C$ and the density of states,

$$\frac{1}{C} = \frac{1}{C_{geom}} + \frac{1}{eA(\partial n/\partial \mu)}, \tag{C.13}$$

is no longer valid when the measurement frequency ω is larger than $\sim (RC)^{-1}$. This can happen, for example, when the chemical potential μ lies in the gap between Landau levels. Measuring a reduction in capacitance in this regime reflects the inability of the device to charge on the time scale ω^{-1}, rather than a direct measurement of the density of states as per Equation C.13 [75]. However, dips in the capacitance still qualitatively signify the formation of a gap in the energy spectrum.

The resistance of the device will introduce a phase shift in the balance-point signal. We keep track of this phase shift by recording both the X (capacitive) and Y (resistive)

quadratures of the balance-point voltage. In finite field, as the gate voltage (and chemical potential) are swept, the measurement oscillates between the high-frequency regime $\omega > (RC)^{-1}$, when μ lies in a Landau gap, and the low-frequency regime $\omega < (RC)^{-1}$, when filling a highly-degenerate Landau level. Transitions between the two regimes are marked by pronounced peaks in the Y quadrature, as can be seen in Figure C.14.

For measurements at higher frequencies, a small phase shift δ, unrelated to the resistance of the device, can be introduced into the measurement by, for example, mismatched cables or attenuators. We rotate the signal according to $X' = X\cos(\delta) - Y\sin(\delta)$ and $Y' = X\sin(\delta) + Y\cos(\delta)$, where δ is chosen such that $Y' \equiv 0$ in a highly compressible regime where $C \approx C_g$, e.g when μ lies in an orbital Landau level at low field. Figure C.15 shows capacitance $C = X' \cdot C_{std} - C_p$ and "loss" (defined as $Y' \cdot C_{std}$) for the semimetallic and insulating graphene capacitors (shown in Figure 3.10 main text). Here C_p is the parasitic background capacitance due to, for example, the capacitance between adjacent wire bonds or pins on the device mount.

Capacitance measurements are sensitive to the bulk of the sample in both the high and low frequency limits, making it a complementary measurement technique to transport. For example, Figure C.16 shows both transport and capacitance data taken on device A1 in the regime of Hofstadter minigaps. Well developed quantum Hall plateaus in conductance have corresponding dips in capacitance indicating a poorly conducting bulk associated with a spectral gap. Remarkably, dips in capacitance appear even when the expected transport features associated with Hofstadter minigaps are poorly developed.

■ C.7 Extracting an upper bound on the gap $\Delta\mu$ from gate dependence of transport and capacitance

In Figure 3.11C, we present an additional estimate of the bandgap by taking the width in gate voltage ΔV for the region defined by $\sigma < e^2/h$. This estimate is based on the assumption that conductance exponentially increases when the gate voltage is large enough to overcome the gap at the CNP. The chemical potential change ($\Delta\mu$) across this insulating region can be estimated from capacitance measurements, which, in the low frequency limit, can be analyzed to extract

$$\Delta\mu = \int_{dip} e\left(1 - \frac{C}{C_{geom}}\right) dV_g, \tag{C.14}$$

which follows from Eq. C.13 after substituting $dn = (eA)^{-1}CdV_g$. Figure C.17 shows transport and capacitance data from device B2. Over the range defined by $\sigma < e^2/h$, the capacitance is never greater than 20% of the geometric capacitance. Compared with our naive estimate, then, the second term under the integral reduces the $\Delta\mu$ by $\approx 20\%$. We thus can apply this estimate even when capacitance data is not available, producing an upper bound on $\Delta\mu$. This estimate is enabled by the high geometric capacitance of our devices, C_g, which suppresses disorder-induced localized state contributions $\Delta\mu$.

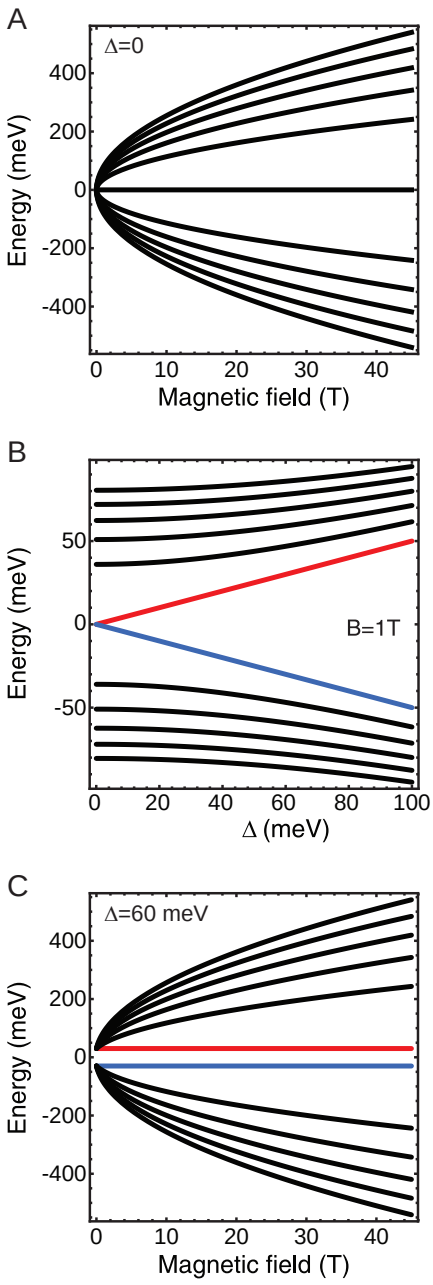

Figure C.8. Landau level energy spectrum for $-5 < N < -5$. **(A)** LL spectrum for $m^* = 0$ as a function of magnetic field, showing the zero mode and $\sqrt{B}$ dependence of the cyclotron energies. **(B)** Splitting of the zero mode with increasing $\Delta = 2m^* v_F^2$. Black curves indicate valley degenerate LLs, while red and blue indicate sublattice polarized levels in which the valley degeneracy has been lifted. Within these calculations, which neglect the Zeeman splitting, the black levels are fourfold degenerate while the red and blue levels are twofold degenerate. **(C)** LL spectrum with $\Delta = 60$ meV showing the sublattice polarized zero mode, which does not disperse with magnetic field.

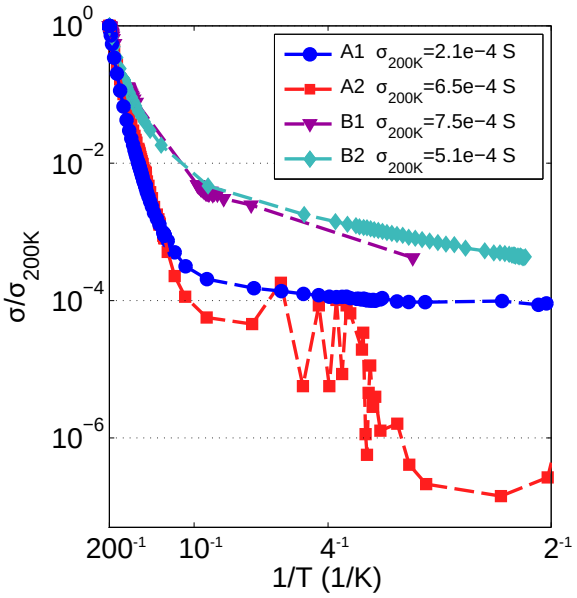

Figure C.9. Temperature dependence of conductivity from 200K to 2K. Normalized conductivity plotted against 1/T. All samples exhibit a strong temperature dependence at high temperatures (200K to 20K) and a weaker dependence for $T < 20$K.

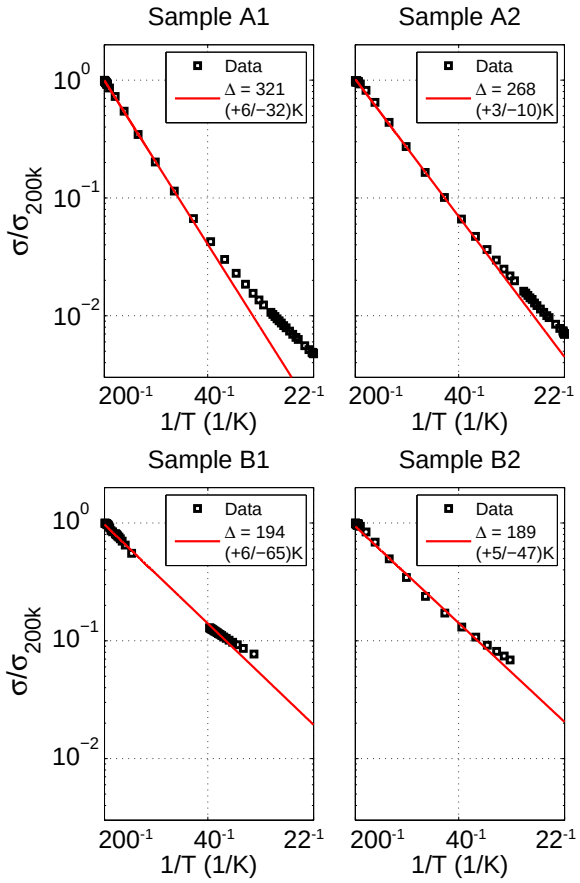

Figure C.10. Arrhenius fits. Data (black symbols) and high temperature fits (red line). Measured values of Δ are presented in the legend for each sample along with the spread in gap values (in parentheses) due to uncertainty in the range of the high temperature regime. These gap values appear in Figure 3.11C.

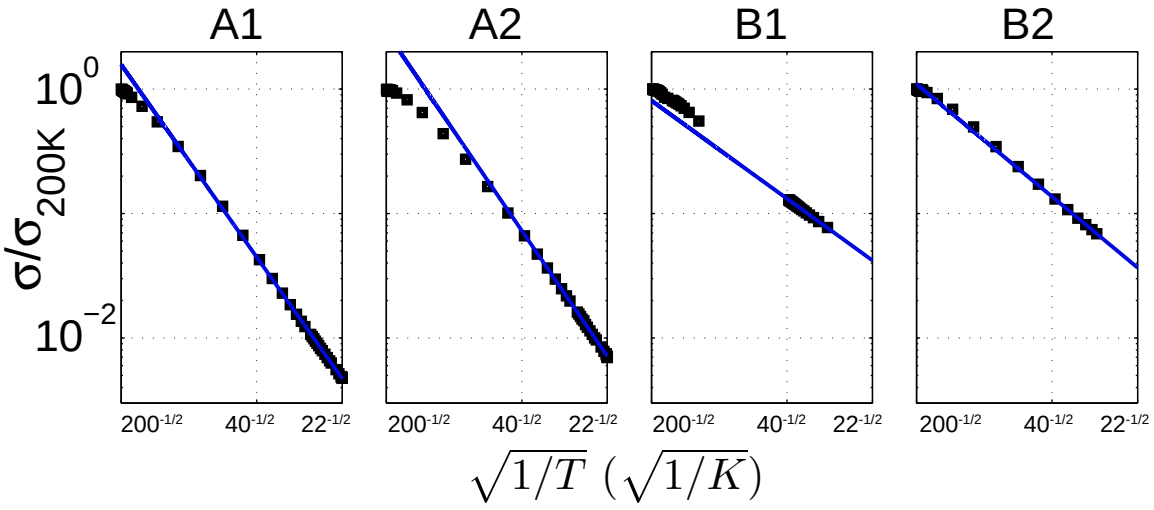

Figure C.11. Variable-range hopping (VRH) fits. Data (black symbols) and intermediate temperature fits (blue lines) to a VRH model $\sigma(T) \propto \exp(-\sqrt{T^*/T})$. Fits have $T^* = 1681$, 1764, 441 and 576K for samples A1, A2, B1 and B2 respectively.

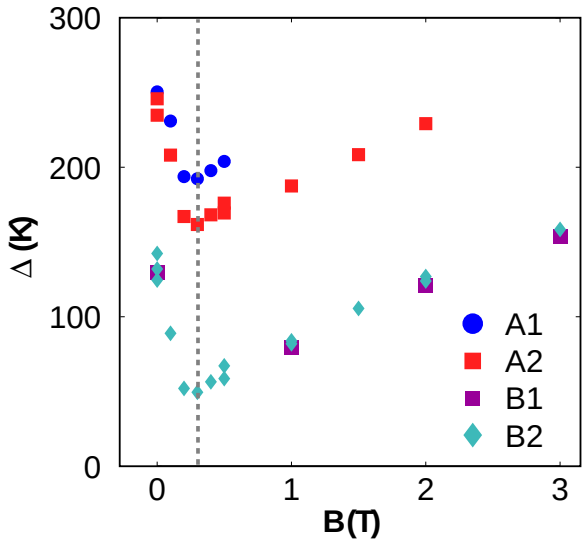

Figure C.12. Dependence of Arrhenius gap on magnetic field. Gap extracted by fitting to Arrhenius behavior from 10 K to 50 K at different magnetic fields. Gaps for all samples exhibit nonmonotonic behavior, with an apparent minimum at $B \simeq 0.25$ T (gray dashed line).

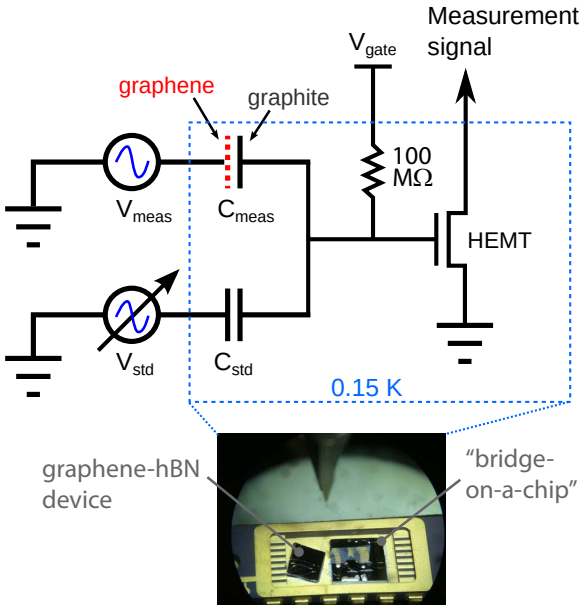

Figure C.13. Schematic of high-sensitivity capacitance measurement.

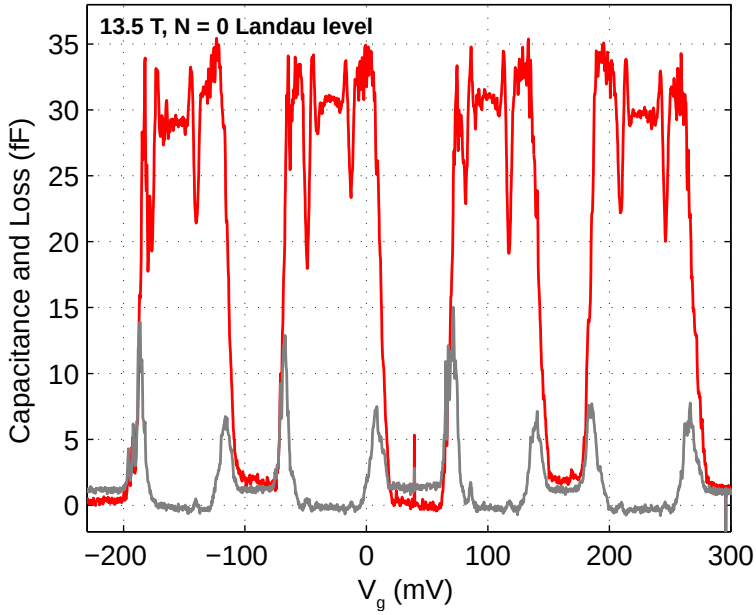

Figure C.14. Capacitance and loss of the insulating graphene capacitor in the $N = 0$ Landau level at 13.5T Capacitance is shown in red and loss in grey.

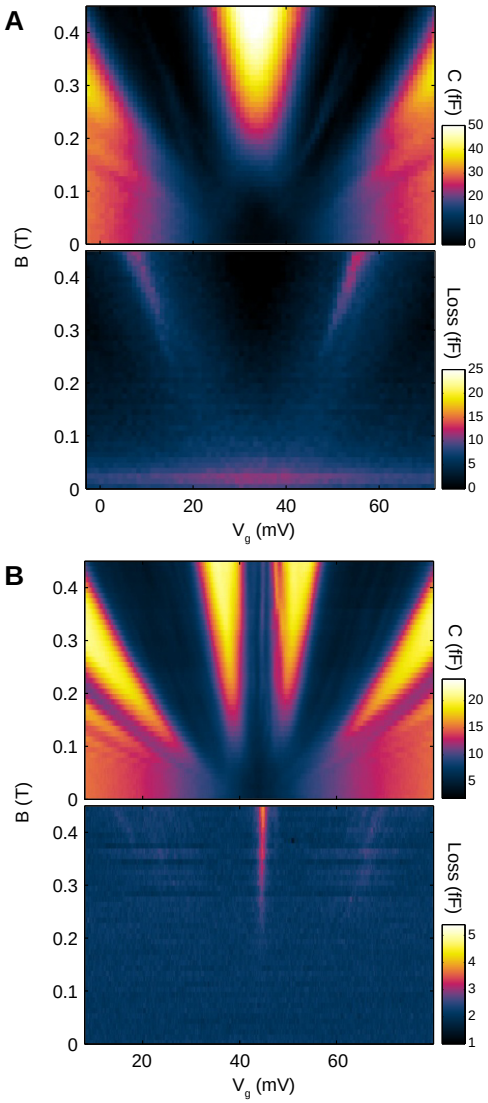

Figure C.15. Capacitance and loss of the semimetallic and insulating graphene-hBN capacitors. (A) The same measurement of the capacitance of the semimetallic graphene capacitor depicted in Figure 3.10A of the main text, alongside a concurrent measurement of the loss signal. The measurement frequency was 173.5 kHz. A parasitic background capacitance C_p=2 pF was subtracted from the capacitance signal after a rotation of $\delta = -7.2°$. The scale of the capacitance color bar is twice as large as that of the loss. **(B)** The same measurement of the capacitance of the insulating graphene capacitor (device B1) depicted in Figure 3.10B, alongside a concurrent measurement of the loss signal. The measurement frequency was 56.2 kHz. A parasitic background capacitance C_p=57 fF was subtracted from the capacitance signal after a rotation of $\delta = -1.1°$. The scale of the capacitance color bar is five times as large as that of the loss.

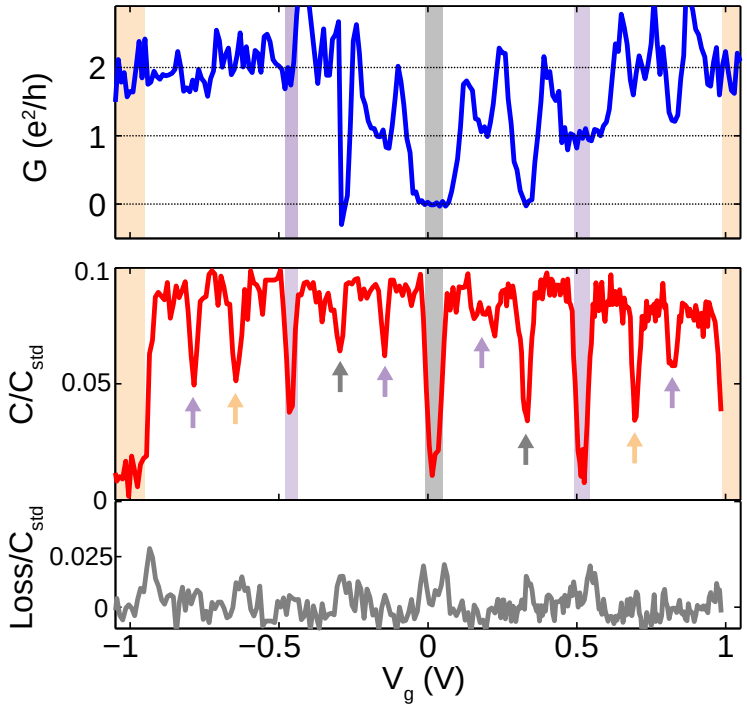

Figure C.16. Comparison of transport and capacitance at 45 T. Top: transport measurement. Features are similar to the measurement in Figure 3.9C, top panel (at 43T). Bottom: capacitance and loss measurement at 45 T. Measurement frequency was 48 kHz. Shaded rectangles indicate normal quantum Hall states at filling factors $\nu = 0, \pm 1$ and ± 2, as in Figure 3.9C. Colored arrows indicate bulk insulating states associated with Hofstadter minigaps in the $N = 0$ LL for $\phi/\phi_0 > 1$.

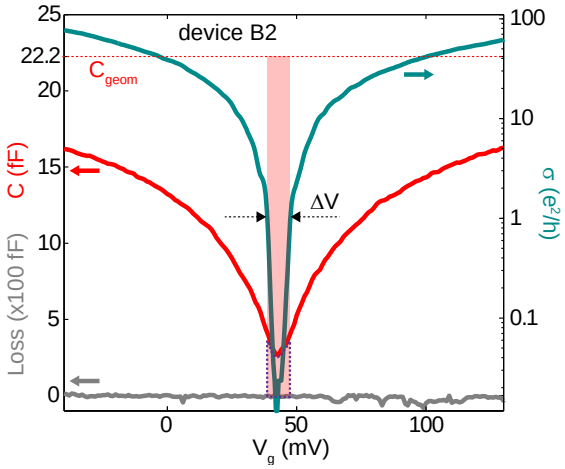

Figure C.17. Estimate of zero-field gap from chemical potential change $\Delta\mu(\Delta V)$. Simultaneous measurement of zero-field capacitance (red) and conductivity (blue) of device B2. Over a range of gate voltage ΔV, $\Delta\mu = e\Delta V - \int(C/C_{geom})dV$ (Equation C.14); that is, the shaded red rectangle minus the area indicated by the purple outline. Here, C_{geom}=22.2 fF is indicated by a dashed red line. Thus, $\Delta\mu = e\Delta V$ serves as an upper bound on the magnitude of the gap.

Appendix D

Additional details for twisted bilayer graphene experiments

D.1 Fabrication details

These are the fabrication details for the devices discussed in Section 4.4. Our twisted bilayer graphene samples were fabricated on a hexagonal Boron Nitride (h-BN) substrate, using a PMMA-transfer technique (see Appendix A.2.3). Flakes of h-BN were used as substrates for the twisted bilayer graphene to ensure high sample quality and low impurity doping [43, 236]. First, h-BN was mechanically exfoliated onto Si substrates with 285 nm of thermally grown oxide, and then flat h-BN flakes were identified using optical and atomic force microscopy. Two graphene sheets were then sequentially transferred to the same h-BN flake such that they overlap to form a bilayer region. Because we cannot determine or control the crystallographic orientation of the graphene sheets, the transfer process results in a random twist angle between the lattices of the two graphene layers. Atomic force microscopy measurements indicate a step height between the layers that varies from 3.4 to 4.1 Å across three different samples, which is very close to the inter-layer distance of 3.4 Å observed in graphite [46].

Next, the graphene layers were lithographically patterned and then etched in an Oxygen reactive ion etcher to isolate the overlapping region where the twisted bilayer graphene is formed. The isolated twisted bilayer graphene was then contacted using thermally evaporated Cr/Au (Figure D.1). Finally, a topgate was made by transferring a thin h-BN flake on top of the contacted twisted bilayer graphene, followed by the fabrication of additional Cr/Au contacts for the topgate electrodes.

After each step where the graphene encountered PMMA or solvents the entire device was heat annealed for 3 hours at 350°C under Ar and H flow.

D.2 Contact geometry for TwBLG quantum Hall study

In the experiments discussed in Section 4.4, twisted bilayer graphene was made by stacking two monolayer graphene sheets which overlap to form a bilayer region. For these samples, the monolayer graphene sheets extended beyond the overlap region, allowing for metal electrodes to be deposited which only contact one of the layers (Figure D.1).

We found that current flowed freely between the layers: measuring the resistance of the overlap region with probes on separate layers shows no measurable increase compared to probes on the same layer. In addition, inter-layer current vs voltage measurements were found to be linear down to 0.1 mV. The net result is that we see no layer-specific effects due to our contact geometry and we treat the probes as contacting the bilayer as a single unit.

■ D.3 Displacement field, density and screening

In Section 4.4, I presented magnetoresistance measurements of twisted bilayer graphene as a function of the total carrier density on the bilayer and the displacement field applied normal to the layers. As stated in that chapter, the total density n_{tot} and displacement field D are given as follows:

$$en_{\text{tot}} = (C_{\text{T}}V_{\text{TG}} + C_{\text{B}}V_{\text{BG}}),\ D = (C_{\text{T}}V_{\text{TG}} - C_{\text{B}}V_{\text{BG}})/2, \tag{S1}$$

where e is the elementary charge, $C_{\text{T(B)}}$ is the capacitance per unit area to ground of the top (bottom) gate, and $V_{\text{TG(BG)}}$ is the potential difference between the top (bottom) gate and the graphene layer closest to it. This potential difference will be primarily determined by the voltage $V_{\text{T,B}}$ applied to the top (bottom) gate, with a small correction due to the graphene chemical potential as: $V_{\text{TG}} = V_{\text{T}} - \mu_{\text{U}}$ and $V_{\text{BG}} = V_{\text{B}} - \mu_{\text{L}}$, where $\mu_{\text{U(L)}}$ is the chemical potential of the upper (lower) graphene layer.

The value of $\mu_{\text{U(L)}}$ in response to the applied gate voltages will be determined by the inter-layer screening and charging behavior as the bilayer responds to the applied field D, while keeping n_{tot} as given in equation S1. As discussed in Section 4.4, D will be screened by the layer density imbalance as well as the inter-layer dielectric environment. The resulting chemical potential difference between the two layers is given by the following

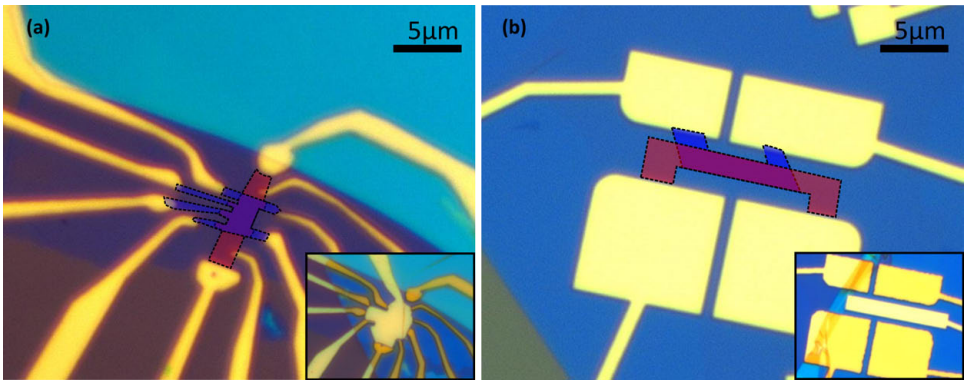

Figure D.1. Optical images of twisted bilayer graphene devices before topgate fabrication. Etched graphene flakes are outlined, with the bottom graphene flake highlighted in red and the top graphene flake highlighted in blue. The inset shows the same devices after fabrication of topgate electrodes

equation:

$$C_{\mathrm{GG}}\frac{(\mu_{\mathrm{U}}-\mu_{\mathrm{L}})}{e}=D-e\frac{(n_{\mathrm{U}}-n_{\mathrm{L}})}{2}, \tag{S2}$$

where $n_{\mathrm{U(L)}}$ is the carrier density on the upper (lower) layer and C_{GG} is the inter-layer capacitance.

The graphene chemical potential at zero magnetic field is given by $\mu=\hbar v_F\sqrt{\pi n}$ [27], where n is the density of the monolayer graphene sheet, $\hbar$ is the reduced Planck constant and v_F is the graphene Fermi velocity. Although the density dependence of μ will change in a magnetic field due to Landau level (LL) formation, this formula will still hold when the chemical potential lies at the graphene LL energy, and in most cases offers a better approximation than completely neglecting the chemical potential term.

The above equations can be solved numerically to produce a relation between the applied gate voltages and the chemical potential of the graphene sheets, as well as the actual value of n_{tot} and D which are used throughout Section 4.4. The importance of the chemical potential terms can be seen in Figure D.2, where the background subtracted longitudinal resistance is plotted as a function of D and $\nu_{\mathrm{tot}}=n_{\mathrm{tot}}h/eB$, without the chemical potential correction (Figure D.2a), and with the chemical potential correction (Figure D.2b). For the uncorrected values, the layer degenerate crossings do not match $D=0$, and do not occur at the right filling factors. Taking into account the chemical potential terms and the inter-layer screening results in more accurate values for n_{tot} and D (Figure D.2b), with the layer degenerate crossings occurring at $D=0$ and at integer multiples of filling factor 8.

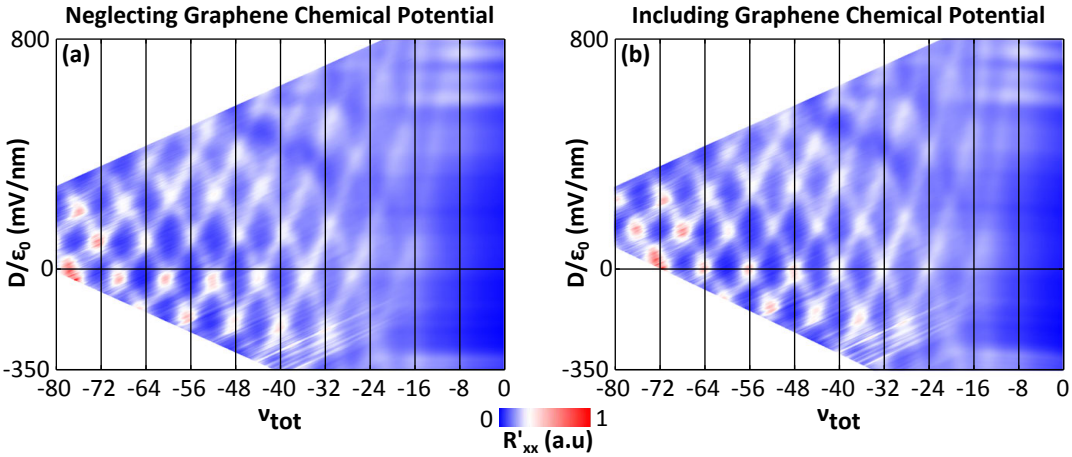

Figure D.2. **(a)** Background subtracted longitudinal resistance R'_{xx} at B=4T, as a function of the displacement field D and filling factor ν_{tot}, neglecting the graphene chemical potential. The layer degenerate crossings do no occur at $D=0$ and the filling factors do not match the correct crossings. **(b)** Same R'_{xx}, but with D and ν_{tot} calculated to include the graphene chemical potential and the screening properties of the twisted bilayer. Layer degenerate crossings now occur at $D=0$ and at integer multiples of filling factor 8. The plot in (b) is the same data that appears in Figure 4.7f.

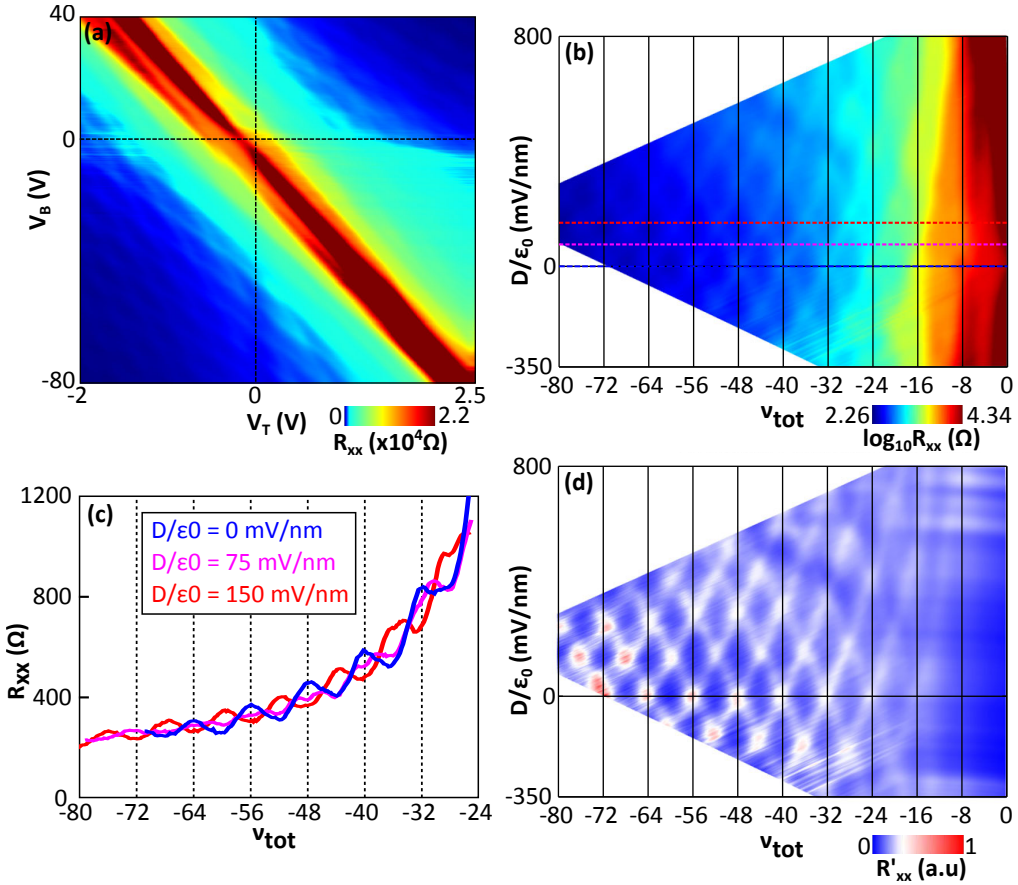

Figure D.3. **(a)** Measured longitudinal resistance R_{xx} as a function of V_T and V_B. **(b)** Same R_{xx} data as a function of displacement field D and total filling factor ν_{tot} with log color scale. **(c)** R_{xx} line-scans corresponding to the dashed lines in (b). **(d)** Same R_{xx} data, but with the background subtracted. Crossings visible in (d) occur in the same location as in (b).

■ D.4 Magnetoresistance measurement and background subtraction for TwBLG quantum Hall study

In Figure 4.7f I presented a longitudinal resistance measurement R_{xx} with the background subtracted. The raw data is presented in Figure D.3a, which is a measurement of R_{xx} at $B = 4T$ as a function of V_T and V_B. This same data is replotted as a function of D and ν_{tot} in Figure D.3b. Peaks in R_{xx} can be clearly observed in both figures, but are obscured by a background resistance which increases as the density is lowered (Fig D.3c). We subtract this background by removing a linear fit from $1/R_{xx}$ and then scaling uniformly for high color contrast (Fig D.3d), resulting in the figure appearing in Section 4.4 (Fig 4.7f). As can be seen in Figure D.3d, the peaks in the background subtracted R'_{xx} occur in the exact same location as the original R_{xx} measurement in Figure D.3b.

■ D.5 Consistency between zero and high magnetic field measurements

I now show that our zero magnetic field measurements (Figure 4.4d) are consistent with our high-field data and inter-layer screening model. At the charge neutrality point (CNP), where $n_{\mathrm{tot}} = 0$, the resistance is observed to decrease with increasing D, and at the highest displacement fields (D/ϵ_0=900 mV/nm) a small splitting of the resistance peak begins to develop. From our high field measurements we know that the effect of D is to induce density imbalances between the two layers. For the case where $n_{\mathrm{tot}} = 0$, this density imbalance must result in equal but opposite sign charge densities on the two layers. Each individual layer then is doped away from its CNP, lowering its resistance, and in turn lowering the parallel resistance of the two layers. At high enough D, the density difference between the layers should be large enough to separately resolve the CNP of each layer. For the case of the device in Figure 4.4d, a splitting of the resistance peak by $\Delta n_{\mathrm{tot}} = 6 \times 10^{11}$ cm^{-2} is observed at D/ϵ_0=900 mV/nm. This corresponds to a chemical potential difference of $\Delta\mu = 128$ meV between the two layers. Applying equation S2 to these values for D, Δn_{tot} and $\Delta\mu$ results in a value for the interlayer capacitance of $C_{\mathrm{GG}} \sim 6\ \mu$F/cm^{-2}. This value is very similar to that extracted from our high magnetic field analysis of the same sample ($C_{\mathrm{GG}} = 6.8\ \mu$F/cm^2), and shows that the screening analysis is consistent for zero and high magnetic fields.

Appendix E

Basic electronic theory of twisted bilayer graphene

This section outlines a simple model for the twisted bilayer graphene electronic structure that captures the most important physics. I will follow the model developed in two papers by Lopes dos Santos [45, 134], but with some extra figures plotted to highlight the key parts. We'll begin by discussing geometry and the conditions for producing commensurate structures. From there we will build a continuum model where the low energy states of graphene are modeled in a nearly-free electron model under the perturbation of the other layer. The most important result is to demonstrate that twist-induced decoupling between the layers.

■ E.1 Geometry

We construct a twisted bilayer graphene lattice model by starting with an AB stacked bilayer and then rotating with respect to an origin centered on an A_1B_2 site (sub-index 1,2 indicates the lower or upper layer respectively). The graphene honeycomb lattice is described by the following lattice vectors.

$$\boldsymbol{a_1} = a\left\{\frac{1}{2}, \frac{\sqrt{3}}{2}\right\},\ \boldsymbol{a_2} = a\left\{-\frac{1}{2}, \frac{\sqrt{3}}{2}\right\}$$

The A sublattice sites occupy the lattice sites and the B sublattice are shifted by $\boldsymbol{\delta}_1 = (\boldsymbol{a_1} + \boldsymbol{a}_2)/3$. Their spatial positions will be:

$$\boldsymbol{r_A}(m,n) = m\boldsymbol{a}_1 + n\boldsymbol{a}_2,\ \boldsymbol{r_B}(m,n) = \boldsymbol{r_A}(m,n) + \boldsymbol{\delta_1}$$

where m, n are integers.

Layer 2 is stacked such that initially its B atoms (B_2) are aligned with the A atoms of layer 1 (A_1). The origin is set at an A_1B_2 site such that $\boldsymbol{r_{B2}}(0,0) = \boldsymbol{r_{A1}}(0,0)$.

To create a twisted bilayer we rotate layer 2 relative to layer 1 by an angle θabout the common A_1B_2 site at the origin. For a commensurate structure to be created, a B_2site at location $\boldsymbol{r_{B2}}(k,l) = k\boldsymbol{a} + l\boldsymbol{a}_2$must be rotated to an A_1site $\boldsymbol{r_{A1}}(m,n) = m\boldsymbol{a}+n\boldsymbol{a}_2$. This is only possible if $(k^2+l^2) = (m^2+n^2)$. An example of a commensurate

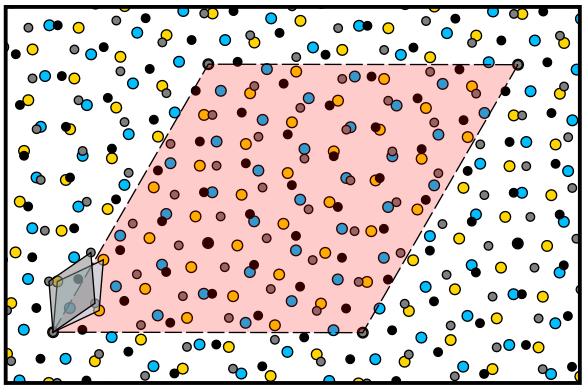

Figure E.1. Commensurate twisted bilayer graphene superlattice

structure is shown in Figure E.1. The solutions to this Diophantine equation give all the possible commensurate structures and were originally solve by Shallcross et. al.[201] and Mele[147]. Lopes dos Santos et. al.[45] present an elegant solution based on the graphene point symmetries. The result is the following equation for the commensurate angles as a function of two coprime positive integers m and r, with $0 < \theta < \pi/3$:

$$cos\theta(m,r) = \frac{3m^2 + 3mr + r^2/2}{3m^2 + 3mr + r^2},$$

and with primitive vectors of the superlattice given by:

$$gcd(r,3) = 1, \quad \begin{bmatrix} \boldsymbol{t_1} \\ \boldsymbol{t_2} \end{bmatrix} = \begin{bmatrix} m & m+r \\ -(m+r) & 2m+r \end{bmatrix} \begin{bmatrix} \boldsymbol{a_1} \\ \boldsymbol{a_2} \end{bmatrix}$$

$$gcd(r,3) = 3, \quad \begin{bmatrix} \boldsymbol{t_1} \\ \boldsymbol{t_2} \end{bmatrix} = \begin{bmatrix} m+\frac{r}{3} & \frac{r}{3} \\ -\frac{r}{3} & m+\frac{2r}{3} \end{bmatrix} \begin{bmatrix} \boldsymbol{a_1} \\ \boldsymbol{a_2} \end{bmatrix}$$

It turns out that there are two types of solutions to the commensurability problem depending on whether r is a multiple of 3. These different structures were identified by Mele[147] and termed sublattice exchange even ($gcd(r,3) = 3$) and sublattice exchange odd ($gcd(r,3) = 1$) which have different symmetry properties. In monolayer graphene an inversion operation will map one sublattice into another ($A \rightarrow B$). TwBLG is not inversion symmetric, but can be symmetric under both inversion in-plane and an exchange of layers. This operation will exchange sublattices for an SE-even structure ($A_1 \rightarrow B_1, A_2 \rightarrow B_2$). For an SE-odd structure, the same operation will exchange the sublattices and also invert the lattice in-plane ($A_1 \rightarrow -B_1, A_2 \rightarrow -B_2$). These structures differ in their electronic properties because the SE-even lattice directly couples the Dirac $\boldsymbol{K}$ points of each layer, i.e. the vector $\boldsymbol{K} - \boldsymbol{K}^\theta$ is a superlattice reciprocal lattice vector, where $\boldsymbol{K}^\theta$ is the rotated $\boldsymbol{K}$ in layer 2 (Figure E.2, left). Since this vector is short, it is predicted to open a gap at zero energy. This effect has yet to be observed experimentally. SE-odd structures couple $\boldsymbol{K}$ to $\boldsymbol{K}'^\theta$, but it requires a much

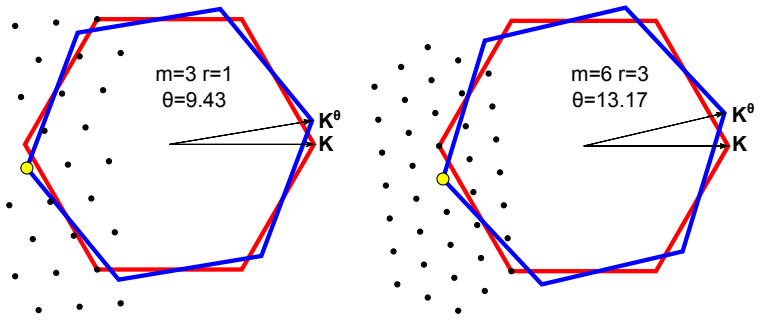

Figure E.2. SE-odd and SE-even structures have different interlayer couplings. Plots of Brillouin zones for the unrotate (red) and rotated layer (blue). Black dots are constructed by adding reciprocal superlattice vectors to a K-point in layer 2 and represent interlayer scattering processes. **Left)** In SE-odd structures, the superlattice does not couple $\boldsymbol{K}$ into $\boldsymbol{K}^{\theta}$. **Right)** In a SE-even structure, the sublattice couples $\boldsymbol{K}$ into $\boldsymbol{K}^{\theta}$.

larger reciprocal lattice vector; and so correspondingly the matrix element will be heavily reduced (Figure E.2, right).

There are predictions that the gap in the SE-even structures host symmetry-protected edge states and are due to SE-even TwBLG being a topological crystalline insulator[111]. The gap is predicted to be on the order of 10meV, although it has yet to be observed.

■ E.2 Continuum model

We are primarily interested in the low energy physics of the twisted bilayer graphene, since that is the energy scale that is accessed by transport experiments, which are limited by electrostatic gating ($n \sim 10^{13}\text{cm}^{-2}, \epsilon_F \sim 0.4\text{eV}$). This fact, along with the weak interlayer coupling ($t_\perp \sim 0.4\text{eV}$) compared to the graphene nearest-neighbor hopping ($t \sim 2.7\text{eV}$) motivates a nearly-free electron approach where the interlayer coupling acts as a perturbation on the monolayer graphene low energy states. The detailed derivation of the below results can be found in Lopes dos Santos et. al. [45]. This model accurately captures a large part of the TwBLG graphene low-energy electronic properties, specifically it predicts a decoupling of the layers at large twist angles, a reduction of the Fermi velocity for low twist angles, as well as the presence of low-energy van Hove singularities where the layers bands strongly hybridize.

We start by considering the intra-layer Hamiltonian for states near the Dirac point in each layer: $\mathbf{K} = \frac{4\pi}{3}(1,0)$ for layer 1, $\mathbf{K}^{\boldsymbol{\theta}} = \frac{4\pi}{3}(cos\theta, sin\theta)$ for layer 2. By defining the two component Dirac fields $\phi_{i,\boldsymbol{k}}$ for each layer $i = 1, 2$ such that they correspond to a plane wave with the same momentum k in each layer we get:

$$\mathcal{H}_0 = \hbar\sum_k \phi^\dagger_{1,\boldsymbol{k}} v_F \boldsymbol{\sigma}\cdot\left(\boldsymbol{k}+\frac{\Delta\mathbf{K}}{2}\right)\phi_{1,\boldsymbol{k}} + \hbar\sum_k \phi^\dagger_{2,\boldsymbol{k}} v_F \boldsymbol{\sigma^\theta}\cdot\left(\boldsymbol{k}-\frac{\Delta\mathbf{K}}{2}\right)\phi_{2,\boldsymbol{k}},$$

where $\Delta\mathrm{K} = \mathbf{K} - \mathbf{K}^\theta$, $\boldsymbol{\sigma} = (\sigma_x, \sigma_y)$ are Pauli matrices and $\boldsymbol{\sigma^\theta} = e^{+i\theta\sigma_z/2}\boldsymbol{\sigma}e^{-i\theta\sigma_z/2}$.

Note that the momentum mismatch, ΔK , is taken up in the form of the matrix element as opposed to in the definition of the fields themselves.

In the presence of interlayer coupling, states with momentum $\boldsymbol{k}$ in one layer can scatter with momentum $\boldsymbol{k}+\boldsymbol{G}$ into the second layer, where $\boldsymbol{G}$ is a reciprocal lattice vector of the superlattice. The resulting form of the interlayer Hamiltonian is:

$$\mathcal{H}_\perp = \sum_\alpha\sum_\beta \widetilde{t}^{\beta\alpha}_\perp(\mathbf{G})\phi^\dagger_{1,\boldsymbol{k}+\boldsymbol{G},\alpha}\phi_{2,\boldsymbol{k},\beta} + \mathrm{H.c.}, \tag{E.1}$$

where $\widetilde{t}^{\alpha\beta}_\perp(\mathbf{G})$ are the Fourier components of the interlayer hopping process coupling sublattice sites $\alpha = A_1, B_1$ and $\beta = A_2, B_2$. A typical approximation for the interlayer coupling is to consider only the hopping of each site in layer 1 to its closest neighbor in layer 2, more details can be found in Lopes dos Santos et. al. [45].

For small twist angles, the resulting moiré pattern will be smooth and it can be expected that the dominant Fourier components in equation E.1 will be for the smallest amplitude $\boldsymbol{G}$ vectors, corresponding to the superlattice reciprocal lattice basis vectors $\boldsymbol{G_1}$and$\boldsymbol{G_2}$. The most important couplings are between states with momentum$\boldsymbol{k}$ in layer 1 to states in layer 2 of momentum $\boldsymbol{k}$,$\boldsymbol{k}-\boldsymbol{G_1}$,$\boldsymbol{k}-\boldsymbol{G_1}-\boldsymbol{G_2}$ and then conversely states of momentum $\boldsymbol{k}$ in layer 2 coupling to states in layer 1 of momentum $\boldsymbol{k}$,$\boldsymbol{k}+\boldsymbol{G_1}$,$\boldsymbol{k}+\boldsymbol{G_1}+\boldsymbol{G_2}$(see Figure E.3). All of these terms have the same magnitude coupling coefficient, differing only by a sublattice-dependent phase factor:

$$\widetilde{t}_\perp(\mathbf{0}) = t_\perp\begin{pmatrix}1 & 1\\ 1 & 1\end{pmatrix}$$

$$\widetilde{t}_\perp(\mathrm{G_1}) = t_\perp\begin{pmatrix}z^* & 1\\ z & z^*\end{pmatrix},\ \widetilde{t}_\perp(\mathrm{G_1}+\mathrm{G_2}) = t_\perp\begin{pmatrix}z & 1\\ z^* & z\end{pmatrix};\ z = e^{i2\pi/3}$$

The resulting continuum model Hamiltonian will have 12x12 elements associated with the 2 sublattice states, 2 layer states, and 3 possible scattering momenta. Computing its eigenenergies results in the low-energy band structure shown in Figure E.4. Two isolated Dirac cones are clearly visible centered near $\boldsymbol{K}$ and $\boldsymbol{K^\theta}$with states in each of these cones being localized to only one of the layers. Where the Dirac cones intersect, the two layers hybridize, resulting in a van Hove singularity in the band structure. This interlayer mixing will cause a flattening on the Dirac cones as the twist angle is reduced. Figure E.5 shows the dependence of the Fermi velocity, relative to its unperturbed value, which shows a sharp dropoff for $\theta < 5°$.

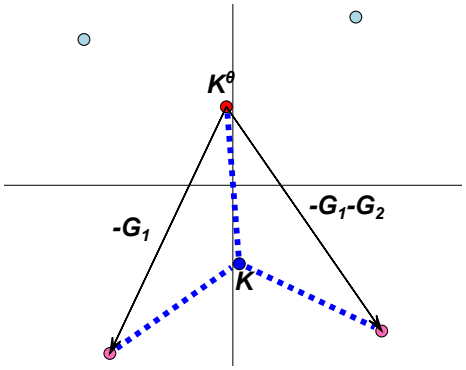

Figure E.3. States in layer 1 near the $\boldsymbol{K}$ point couple to states in layer 2 with added momentum of $0, -\boldsymbol{G_1}$, or $-\boldsymbol{G_1} - \boldsymbol{G_2}$.

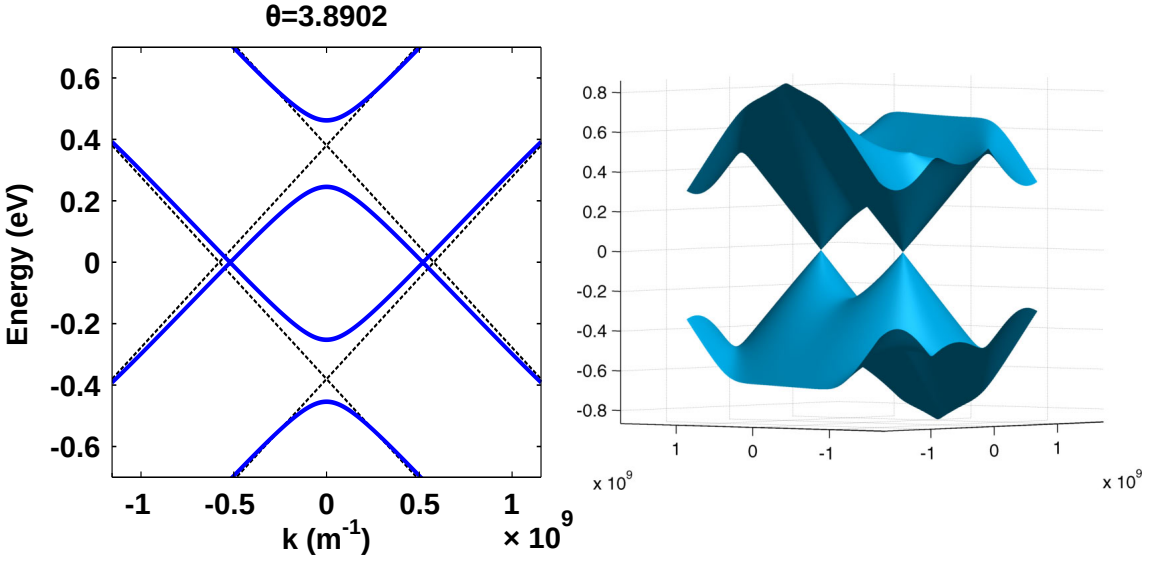

Figure E.4. Low energy band structure for twisted bilayer graphene.

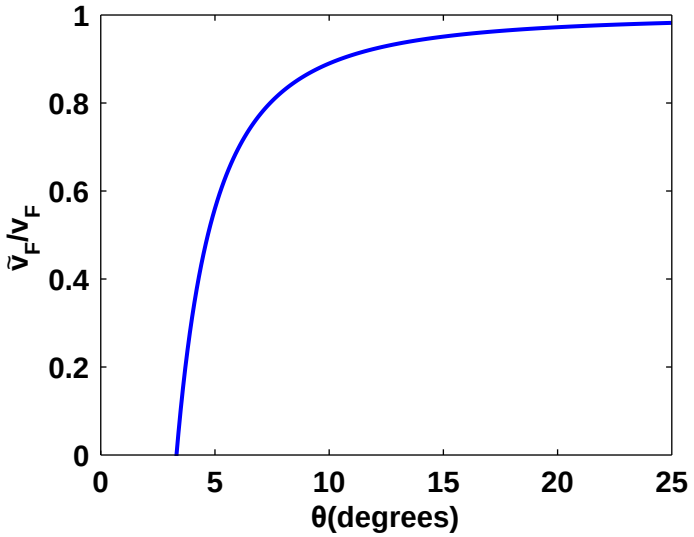

Figure E.5. Fermi velocity reduction with twist angle

■ E.3 Different families of commensurate structures

There are many remaining mysteries regarding the expected electronic behavior of TwBLG. Because of the tight constraints of the commensurability condition, the wavelength of a TwBLG superlattice will vary widely and discontinuously as a function of twist angle. This can be seen by plotting the wavelength of the commensurate structures as a function of twist angle (Figure E.6). The wavelength is normalize with respect to the moiré wavelength $\lambda_{moir} = a/[2sin(\theta/2)]$, which is well defined at each twist angle. Notice that the $r = 1$ structures have the shortest wavelengths, which is equal to the moiré wavelength at the same angle. At low twist angles, the commensurate solutions become very dense, so a structure with $r = 3$ will be a near periodic repetition of a shorter wavelength $r = 1$ structure. At larger twist angles though, it would appear that slight changes in the twist angle could cause the superlattice scale to change drastically. These types of effects have yet to be observed experimentally.

■ E.4 Conclusions from basic electronic theory

The conclusion of this section is that for a large majority of possible twist angles the low energy electronic states are decoupled between the layers: the energy eigenstates are nearly completely localized onto either one layer or the other for the range of energies accessible with electrostatic gates.

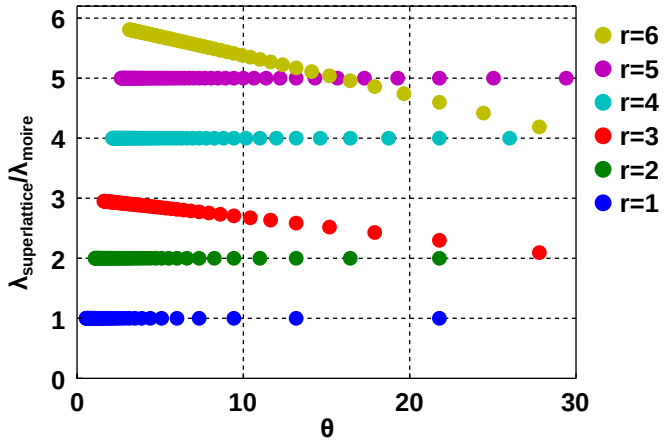

Figure E.6. Dependence of superlattice wavelength on twist angle. Wavelength is normalized to the value of the moiré wavelength at the same twist angle.

Bibliography

[1] Abanin, D. A., Lee, P. A. & Levitov, L. S. Spin-filtered edge states and quantum Hall effect in graphene. *Phys. Rev. Lett.* **96**, 176803– (2006).

[2] Abanin, D. A. & Levitov, L. S. Conformal invariance and shape-dependent conductance of graphene samples. *Phys. Rev. B* **78**, 035416 (2008).

[3] Aidelsburger, M., Atala, M., Lohse, M., Barreiro, J., Paredes, B. & Bloch, I. Realization of the hofstadter hamiltonian with ultracold atoms in optical lattices. *Phys. Rev. Lett.* **111**, 185301 (2013).

[4] Albrecht, C., Smet, J. H., von Klitzing, K., Weiss, D., Umansky, V. & Schweizer, H. Evidence of hofstadter's fractal energy spectrum in the quantized hall conductance. *Phys. Rev. Lett.* **86**, 147–150 (2001).

[5] Alicea, J. Majorana fermions in a tunable semiconductor device. *Phys. Rev. B* **81**, 125318 (2010).

[6] Alicea, J. & Fisher, M. P. A. Graphene integer quantum Hall effect in the ferromagnetic and paramagnetic regimes. *Phys. Rev. B* **74**, 075422 (2006).

[7] Alicea, J. & Fisher, M. P. Interplay between lattice-scale physics and the quantum Hall effect in graphene. *Solid State Communications* **143**, 504–509 (2007).

[8] Amet, F., Williams, J. R., Watanabe, K., Taniguchi, T. & Goldhaber-Gordon, D. Insulating behavior at the neutrality point in single-layer graphene. *Physical Review Letters* **110**, 216601 (2013).

[9] Amet, F., Williams, J. R., Watanabe, K., Taniguchi, T. & Goldhaber-Gordon, D. Selective equilibration of spin-polarized quantum hall edge states in graphene. *Phys. Rev. Lett.* **112**, 196601 (2014).

[10] Amet, F., Williams, J., Garcia, A., Yankowitz, M., Watanabe, K., Taniguchi, T. & Goldhaber-Gordon, D. Tunneling spectroscopy of graphene-boron-nitride heterostructures. *Physical Review B* **85**, 073405 (2012).

[11] Apalkov, V. M. & Chakraborty, T. Fractional quantum hall states of dirac electrons in graphene. *Physical Review Letters* **97**, – (2006).

[12] Ashoori, R. C., Stormer, H. L., Weiner, J. S., Pfeiffer, L. N., Pearton, S. J., Baldwin, K. W. & West, K. W. Single-electron capacitance spectroscopy of discrete quantum levels. *Phys. Rev. Lett.* **68**, 3088–3091 (1992).

[13] Azbel, M. Y. Energy spectrum of a conduction electron in a magnetic field. *Sov. Phys. JETP* **19**, 634 (1964).

[14] Barkeshli, M. & Qi, X.-L. Synthetic topological qubits in conventional bilayer quantum hall systems. *Phys. Rev. X* **4**, 041035 (2014).

[15] Berger, C., Song, Z., Li, X., Wu, X., Brown, N., Naud, C., Mayou, D., Li, T., Hass, J., Marchenkov, A. N., Conrad, E. H., First, P. N. & de Heer, W. A. Electronic confinement and coherence in patterned epitaxial graphene. *Science* **312**, 1191–1196 (2006).

[16] Berman, O. L., Lozovik, Y. E. & Gumbs, G. Bose-Einstein condensation and superfluidity of magnetoexcitons in bilayer graphene. *Physical Review B* **77**, 155433 (2008).

[17] Bernevig, B. A., Hughes, T. L. & Zhang, S.-C. Quantum spin Hall effect and topological phase transition in HgTe quantum wells. *Science* **314**, 1757–1761 (2006).

[18] Bistritzer, R. & MacDonald, A. H. Moire butterflies in twisted bilayer graphene. *Phys. Rev. B* **84**, 035440– (2011).

[19] Bistritzer, R. & MacDonald, A. H. Moire bands in twisted double-layer graphene. *Proceedings of the National Academy of Sciences* **108**, 12233–12237 (2011).

[20] Boebinger, G. S., Jiang, H. W., Pfeiffer, L. N. & West, K. W. Magnetic-field-driven destruction of quantum hall states in a double quantum well. *Physical Review Letters* **64**, 1793–1796 (1990).

[21] Bolotin, K. I., Sikes, K. J., Jiang, Z., Klima, M., Fudenberg, G., Hone, J., Kim, P. & Stormer, H. L. Ultrahigh electron mobility in suspended graphene. *Solid State Communications* **146,**, 351–355 (2008).

[22] Bolotin, K. I., Ghahari, F., Shulman, M. D., Stormer, H. L. & Kim, P. Observation of the fractional quantum Hall effect in graphene. *Nature* **462**, 196–199 (2009).

[23] Brune, C., Roth, A., Buhmann, H., Hankiewicz, E. M., Molenkamp, L. W., Maciejko, J., Qi, X.-L. & Zhang, S.-C. Spin polarization of the quantum spin hall edge states. *Nat Phys* **8**, 485–490 (2012).

[24] Buckley, J. E., Wragg, J. L., White, H. W., Bruckdorfer, A. & Worcester, D. L. Large scale periodic features associated with surface boundaries in scanning tunneling microscope images of graphite. *Journal of Vacuum Science & Technology B* **9**, 1079–1082 (1991).

[25] Bunch, J. S., van der Zande, A. M., Verbridge, S. S., Frank, I. W., Tanenbaum, D. M., Parpia, J. M., Craighead, H. G. & McEuen, P. L. Electromechanical resonators from graphene sheets. *Science* **315**, 490–493 (2007).

[26] Büttner, B., Liu, C. X., Tkachov, G., Novik, E. G., Brüne, C., Buhmann, H., Hankiewicz, E. M., Recher, P., Trauzettel, B., Zhang, S. C. & Molenkamp, L. W. Single valley Dirac fermions in zero-gap HgTe quantum wells. *Nature Physics* **7**, 418–422 (2011).

[27] Castro Neto, A. H., Guinea, F., Peres, N. M. R., Novoselov, K. S. & Geim, A. K. The electronic properties of graphene. *Rev. Mod. Phys* **81**, 109 (2009).

[28] Chang, M.-C. & Niu, Q. Berry phase, hyperorbits, and the hofstadter spectrum: Semiclassical dynamics in magnetic bloch bands. *Phys. Rev. B* **53**, 7010–7023 (1996).

[29] Checkelsky, J. G., Li, L. & Ong, N. P. Zero-energy state in graphene in a high magnetic field. *Phys. Rev. Lett.* **100**, 206801 (2008).

[30] Checkelsky, J. G., Li, L. & Ong, N. P. Divergent resistance at the dirac point in graphene: Evidence for a transition in a high magnetic field. *Phys. Rev. B* **79**, 115434 (2009).

[31] Chen, X., Gu, Z.-C., Liu, Z.-X. & Wen, X.-G. Symmetry-protected topological orders in interacting bosonic systems. *Science* **338**, 1604–1606 (2012).

[32] Chen, Y. L., Chu, J.-H., Analytis, J. G., Liu, Z. K., Igarashi, K., Kuo, H.-H., Qi, X. L., Mo, S. K., Moore, R. G., Lu, D. H., Hashimoto, M., Sasagawa, T., Zhang, S. C., Fisher, I. R., Hussain, Z. & Shen, Z. X. Massive Dirac fermion on the surface of a magnetically doped topological insulator. *Science* **329**, 659–662 (2010).

[33] Chen, Z., Lin, Y.-M., Rooks, M. J. & Avouris, P. Graphene nano-ribbon electronics. *Physica E* **40**, 228 – 232 (2007).

[34] Cheng, M. Superconducting proximity effect on the edge of fractional topological insulators. *Physical Review B* **86**, 195126 (2012).

[35] Cheng, S.-H., Zou, K., Okino, F., Gutierrez, H., Gupta, A., Shen, N., Eklund, P., Sofo, J. & Zhu, J. Reversible fluorination of graphene: Evidence of a two-dimensional wide bandgap semiconductor. *Phys. Rev. B* **81**, 205435 (2010).

[36] Chu, Z.-D., He, W.-Y. & He, L. Coexistence of van hove singularities and superlattice dirac points in a slightly twisted graphene bilayer. *Phys. Rev. B* **87**, 155419 (2013).

[37] Clarke, D. J., Alicea, J. & Shtengel, K. Exotic non-abelian anyons from conventional fractional quantum hall states. *Nature communications* **4**, 1348 (2013).

[38] Das Sarma, S., Adam, S., Hwang, E. H. & Rossi, E. Electronic transport in two dimensional graphene. *Rev. Mod. Phys.* **83** (2011).

[39] Das Sarma, S. & Yang, K. The enigma of theν=0 quantum Hall effect in graphene. *Solid State Communications* **149**, 1502–1506 (2009).

[40] de Gail, R. *et al.* Topologically protected zero modes in twisted bilayer graphene. *Phys. Rev. B* **84**, 045436 (2011).

[41] Dean, C., Young, A. F., Wang, L., Meric, I., Lee, G. H., Watanabe, K., Taniguchi, T., Shepard, K., Kim, P. & Hone, J. Graphene based heterostructures. *Solid State Communications* **152**, 1275–1282 (2012).

[42] Dean, C. R., Young, A. F., Cadden-Zimansky, P., Wang, L., Ren, H., Watanabe, K., Taniguchi, T., Kim, P., Hone, J. & Shepard, K. L. Multicomponent fractional quantum Hall effect in graphene. *Nature Physics* **7**, 693–696 (2011).

[43] Dean, C. R., Young, A. F., Meric, I., Lee, C., Wang, L., Sorgenfrei, S., Watanabe, K., Taniguchi, T., Kim, P., Shepard, K. L. & Hone, J. Boron nitride substrates for high-quality graphene electronics. *Nature Nanotechnology* **5**, 722–726 (2010).

[44] Decker, R., Wang, Y., Brar, V. W., Regan, W., Tsai, H.-Z., Wu, Q., Gannett, W., Zettl, A. & Crommie, M. F. Local electronic properties of graphene on a bn substrate via scanning tunneling microscopy. *Nano Letters* null–null (2011).

[45] dos Santos, J. L., Peres, N. & Neto, A. C. Continuum model of the twisted graphene bilayer. *Physical Review B* **86**, 155449 (2012).

[46] Dresselhaus, M. S. & Dresselhaus, G. Intercalation compounds of graphite. *Adv. Phys.* **51**, 1–186 (2002).

[47] Du, L., Knez, I., Sullivan, G. & Du, R.-R. Observation of quantum spin Hall states in InAs/GaSb bilayers under broken time-reversal symmetry. *arXiv/cond-mat: 1306.1925* (2013).

[48] Du, X., Skachko, I. & Andrei, E. Y. Towards ballistic transport in graphene. *International Journal of Modern Physics B* **22**, 4579–4588 (2008).

[49] Du, X., Skachko, I., Duerr, F., Luican, A. & Andrei, E. Y. Fractional quantum Hall effect and insulating phase of dirac electrons in graphene. *Nature* **462**, 192–195 (2009).

[50] Eckmann, A., Park, J., Yang, H., Elias, D., Mayorov, A. S., Yu, G., Jalil, R., Novoselov, K. S., Gorbachev, R. V., Lazzeri, M., Geim, A. K. & Casiraghi, C. Raman fingerprint of aligned graphene/h-bn superlattices. *Nano Letters* **13**, 5242–5246 (2013).

[51] Eisenstein, J., Boebinger, G., Pfeiffer, L., West, K. & He, S. New fractional quantum hall state in double-layer two-dimensional electron systems. *Phys. Rev. Lett.* **68**, 1383–1386 (1992).

[52] Eisenstein, J. P. & MacDonald, A. H. Bose-Einstein condensation of excitons in bilayer electron systems. *Nature* **432**, 691–694 (2004).

[53] Eisenstein, J. P., Pfeiffer, L. N. & West, K. W. Independently contacted two-dimensional electron systems in double quantum wells. *Applied Physics Letters* **57**, 2324–2326 (1990).

[54] Elias, D. C., Nair, R. R., Mohiuddin, T. M. G., Morozov, S. V., Blake, P., Halsall, M. P., Ferrari, A. C., Boukhvalov, D. W., Katsnelson, M. I., Geim, A. K. & Novoselov, K. S. Control of graphene's properties by reversible hydrogenation: Evidence for graphane. *Science* **323**, 610–613 (2009).

[55] Emtsev, K. V., Bostwick, A., Horn, K., Jobst, J., Kellogg, G. L., Ley, L., McChesney, J. L., Ohta, T., Reshanov, S. A., Roehrl, J., Rotenberg, E., Schmid, A. K., Waldmann, D., Weber, H. B. & Seyller, T. Towards wafer-size graphene layers by atmospheric pressure graphitization of silicon carbide. *Nature Materials* **8**, 203–207 (2009).

[56] Enderlein, C., Kim, Y. S., Bostwick, A., Rotenberg, E. & Horn, K. The formation of an energy gap in graphene on ruthenium by controlling the interface. *New Journal of Physics* **12**, 033014 (2010).

[57] Feldman, B. E., Krauss, B., Smet, J. H. & Yacoby, A. Unconventional sequence of fractional quantum hall states in suspended graphene. *Science* **337**, 1196–1199 (2012).

[58] Feldman, B. E., Martin, J. & Yacoby, A. Broken-symmetry states and divergent resistance in suspended bilayer graphene. *Nature Physics* **5**, 889–893 (2009).

[59] Fertig, H. A. & Brey, L. Luttinger liquid at the edge of undoped graphene in a strong magnetic field. *Phys. Rev. Lett.* **97**, 116805 (2006).

[60] Fu, L. Topological crystalline insulators. *Phys. Rev. Lett.* **106**, 106802– (2011).

[61] Fu, L. & Kane, C. L. Superconducting proximity effect and majorana fermions at the surface of a topological insulator. *Phys. Rev. Lett.* **100**, 096407– (2008).

[62] Fu, L. & Kane, C. L. Josephson current and noise at a superconductor/quantum-spin-hall-insulator/superconductor junction. *Physical Review B* **79**, 161408 (2009).

[63] Geim, A. K. & Grigorieva, I. V. Van der waals heterostructures. *Nature* **499**, 419–425 (2013).

[64] Geim, A. K. & Novoselov, K. S. The rise of graphene. *Nature Materials* **6**, 183–191 (2007).

[65] Geim, A. K. & MacDonald, A. H. Graphene: Exploring carbon flatland. *Phys. Today* **60**, 35–41 (2007).

[66] Geisler, M., Smet, J., Umansky, V., Von Klitzing, K., Naundorf, B., Ketzmerick, R. & Schweizer, H. Detection of landau band coupling induced rearrangement of the hofstadter butterfly. *Physica E: Low-dimensional Systems and Nanostructures* **25**, 227–232 (2004).

[67] Giesbers, A., Ponomarenko, L., Novoselov, K., Geim, A., Katsnelson, M., Maan, J. & Zeitler, U. Gap opening in the zeroth landau level of graphene. *Physical Review B* **80** (2009).

[68] Giovannetti, G., Khomyakov, P., Brocks, G., Karpan, V., van den Brink, J. & Kelly, P. Doping graphene with metal contacts. *Phys. Rev. Lett.* **101**, 026803 (2008).

[69] Giovannetti, G., Khomyakov, P. A., Brocks, G., Kelly, P. J. & van den Brink, J. Substrate-induced band gap in graphene on hexagonal boron nitride: Ab initio density functional calculations. *Phys. Rev. B* **76**, 073103 (2007).

[70] Girvin & Prange (eds.) *The Quantum Hall Effect* (Springer-Verlag, 1987).

[71] Goerbig, M. O., Moessner, R. & Doucot, B. Electron interactions in graphene in a strong magnetic field. *Physical Review B* **74**, – (2006).

[72] Goerbig, M. O. Quantum hall effects. *arXiv preprint arXiv:0909.1998* (2009).

[73] González, J. Kohn-luttinger superconductivity in graphene. *Phys. Rev. B* **78**, 205431 (2008).

[74] González, J. Magnetic and kohn-luttinger instabilities near a van hove singularity: Monolayer versus twisted bilayer graphene. *Physical Review B* **88**, 125434 (2013).

[75] Goodall, R. K., Higgins, R. J. & Harrang, J. P. Capacitance measurements of a quantized two-dimensional electron gas in the regime of the quantum Hall effect. *Phys. Rev. B* **31**, 6597–6608 (1985).

[76] Goossens, A. M., Calado, V. E., Barreiro, A., Watanabe, K., Taniguchi, T. & Vandersypen, L. M. K. Mechanical cleaning of graphene. *Applied Physics Letters* **100**, 073110 (2012).

[77] Goossens, A. M., Driessen, S. C. M., Baart, T. A., Watanabe, K., Taniguchi, T. & Vandersypen, L. M. K. Gate-defined confinement in bilayer graphene-hexagonal boron nitride hybrid devices. *Nano Letters* **12**, 4656–4660 (2012).

[78] Gorbachev, R. V., Geim, A. K., Katsnelson, M. I., Novoselov, K. S., Tudorovskiy, T., Grigorieva, I. V., MacDonald, A. H., Morozov, S. V., Watanabe, K., Taniguchi, T. & Ponomarenko, L. A. Strong coulomb drag and broken symmetry in double-layer graphene. *Nat Phys* **8**, 896–901 (2012).

[79] Gorbachev, R. V., Song, J. C. W., Yu, G. L., Kretinin, A. V., Withers, F., Cao, Y., Mishchenko, A., Grigorieva, I. V., Novoselov, K. S., Levitov, L. S. & Geim, A. K. Detecting topological currents in graphene superlattices. *Science* **346**, 448–451 (2014).

[80] Gramila, T. J. *et al.* Mutual friction between parallel two-dimensional electron systems. *Phys. Rev. Lett.* **66**, 1216–1219 (1991).

[81] Guinea, F., Katsnelson, M. I. & Geim, A. K. Energy gaps and a zero-field quantum hall effect in graphene by strain engineering. *Nat Phys* **6**, 30–33 (2010).

[82] Haigh, S. J., Gholinia, A., Jalil, R., Romani, S., Britnell, L., Elias, D. C., Novoselov, K. S., Ponomarenko, L. A., Geim, A. K. & Gorbachev, R. Cross-sectional imaging of individual layers and buried interfaces of graphene-based heterostructures and superlattices. *Nat Mater* **11**, 764–767 (2012).

[83] Haldane, F. D. M. Model for a quantum hall effect without landau levels: Condensed-matter realization of the "parity anomaly". *Phys. Rev. Lett.* **61**, 2015–2018 (1988).

[84] Halperin, B. I. Quantized Hall conductance, current-carrying edge states, and the existence of extended states in a two-dimensional disordered potential. *Phys. Rev. B* **25**, 2185–2190 (1982).

[85] Han, M., Ozyilmaz, B., Zhang, Y. & Kim, P. Energy band gap engineering of graphene nanoribbons. *Physical Review Letters* **98**, 206805 (2007).

[86] Hasan, M. Z. & Kane, C. L. Colloquium: Topological insulators. *Rev. Mod. Phys* **82**, 3045–3067 (2010).

[87] Hass, J., Varchon, F., Millán-Otoya, J., Sprinkle, M., Sharma, N., de Heer, W., Berger, C., First, P., Magaud, L. & Conrad, E. Why multilayer graphene on 4H-SiC(0001Â¯) behaves like a single sheet of graphene. *Physical Review Letters* **100**, 125504 (2008).

[88] Havener, R. W., Zhuang, H., Brown, L., Hennig, R. G. & Park, J. Angle-resolved raman imaging of interlayer rotations and interactions in twisted bilayer graphene. *Nano Letters* **12**, 3162–3167 (2012).

[89] Herbut, I. F. Theory of integer quantum Hall effect in graphene. *Phys. Rev. B* **75**, 165411 (2007).

[90] Hernandez, Y., Nicolosi, V., Lotya, M., Blighe, F. M., Sun, Z., De, S., T., M., Holland, B., Byrne, M., Gun'Ko, Y. K., Boland, J. J., Niraj, P., Duesberg, G., Krishnamurthy, S., Goodhue, R., Hutchison, J., Scardaci, V., Ferrari, A. C. & Coleman, J. N. High-yield production of graphene by liquid-phase exfoliation of graphite. *Nat Nano* **3**, 563–568 (2008).

[91] Hofstadter, D. *Gödel, Escher, Bach: An Eternal Golden Braid* (Basic Books, 1979).

[92] Hofstadter, D. R. Energy levels and wave functions of bloch electrons in rational and irrational magnetic fields. *Phys. Rev. B* **14**, 2239–2249 (1976).

[93] Hsieh, D., Qian, D., Wray, L., Xia, Y., Hor, Y. S., Cava, R. J. & Hasan, M. Z. A topological dirac insulator in a quantum spin Hall phase. *Nature* **452**, 970–974 (2008).

[94] Hsieh, T. H., Lin, H., Liu, J., Duan, W., Bansil, A. & Fu, L. Topological crystalline insulators in the SnTe material class. *Nature Communications* **3**, 982– (2012).

[95] Huang, Y., Wu, J. & Hwang, K. C. Thickness of graphene and single-wall carbon nanotubes. *Physical Review B* **74**, 245413 (2006).

[96] Huard, B., Sulpizio, J. A., Stander, N., Todd, K., Yang, B. & Goldhaber-Gordon, D. Transport measurements across a tunable potential barrier in graphene. *Phys. Rev. Lett.* **98**, 236803 (2007).

[97] Hunt, B., Sanchez-Yamagishi, J. D., Young, A. F., Yankowitz, M., LeRoy, B. J., Watanabe, K., Taniguchi, T., Moon, P., Koshino, M., Jarillo-Herrero, P. & Ashoori, R. C. Massive dirac fermions and hofstadter butterfly in a van der waals heterostructure. *Science* **340**, 1427–1430 (2013).

[98] Hwang, E. H. & Das Sarma, S. Dielectric function, screening, and plasmons in two-dimensional graphene. *Phys. Rev. B* **75**, 205418 (2007).

[99] Jaksch, D. & Zoller, P. Creation of effective magnetic fields in optical lattices: the hofstadter butterfly for cold neutral atoms. *New Journal of Physics* **5**, 56 (2003).

[100] Jalilian, R., Jauregui, L. A., Lopez, G., Tian, J., Roecker, C., Yazdanpanah, M. M., Cohn, R. W., Jovanovic, I. & Chen, Y. P. Scanning gate microscopy on graphene: charge inhomogeneity and extrinsic doping. *Nanotechnology* **22**, 295705 (2011).

[101] Jiang, Z., Zhang, Y., Stormer, H. L. & Kim, P. Quantum Hall states near the charge-neutral dirac point in graphene. *Phys. Rev. Lett.* **99**, 106802– (2007).

[102] Jung, J. & MacDonald, A. H. Theory of the magnetic-field-induced insulator in neutral graphene sheets. *Phys. Rev. B* **80**, 235417 (2009).

[103] Jungwirth, T. & MacDonald, A. H. Pseudospin anisotropy classification of quantum hall ferromagnets. *Phys. Rev. B* **63**, 035305 (2000).

[104] Kane, C. L. & Mele, E. J. Quantum spin Hall effect in graphene. *Phys. Rev. Lett.* **95**, 226801 (2005).

[105] Kato, Y. K., Myers, R. C., Gossard, A. C. & Awschalom, D. D. Observation of the spin hall effect in semiconductors. *Science* **306**, 1910–1913 (2004).

[106] Kharitonov, M. Phase diagram for the $\nu = 0$ quantum hall state in monolayer graphene. *arxiv* (2011).

[107] Kharitonov, M. Phase diagram for the ν=0 quantum Hall state in monolayer graphene. *Phys. Rev. B* **85**, 155439 (2012).

[108] Ki, D.-K., Fal'ko, V. I., Abanin, D. A. & Morpurgo, A. F. Observation of even denominator fractional quantum hall effect in suspended bilayer graphene. *Nano Letters* **14**, 2135–2139 (2014).

[109] Kim, K. S., Zhao, Y., Jang, H., Lee, S. Y., Kim, J. M., Kim, K. S., Ahn, J.-H., Kim, P., Choi, J.-Y. & Hong, B. H. Large-scale pattern growth of graphene films for stretchable transparent electrodes. *Nature* **457**, 706–710 (2009).

[110] Kim, S., Lee, K. & Tutuc, E. Spin-Polarized to Valley-Polarized Transition in Graphene Bilayers at nu = 0 in High Magnetic Fields. *Phys. Rev. Lett.* **107**, 16803 (2011).

[111] Kindermann, M. Topological crystalline insulator phase in graphene multilayers. *ArXiv e-prints* (2013).

[112] Kindermann, M. & Mele, E. J. Landau quantization in twisted bilayer graphene: The dirac comb. *Physical Review B* **84**, 161406 (2011).

[113] Kindermann, M., Uchoa, B. & Miller, D. L. Zero-energy modes and gate-tunable gap in graphene on hexagonal boron nitride. *Phys. Rev. B* **86**, 115415– (2012).

[114] Kitaev, A. Y. Unpaired majorana fermions in quantum wires. *Physics-Uspekhi* **44**, 131 (2001).

[115] Klitzing, K. v., Dorda, G. & Pepper, M. New method for high-accuracy determination of the fine-structure constant based on quantized hall resistance. *Phys. Rev. Lett.* **45**, 494–497 (1980).

[116] Knez, I., Du, R.-R. & Sullivan, G. Evidence for helical edge modes in inverted InAs/GaSb quantum wells. *Phys. Rev. Lett.* **107**, 136603– (2011).

[117] König, M., Wiedmann, S., Brüne, C., Roth, A., Buhmann, H., Molenkamp, L. W., Qi, X.-L. & Zhang, S.-C. Quantum spin Hall insulator state in HgTe quantum wells. *Science* **318**, 766–770 (2007).

[118] König, M., Wiedmann, S., Brüne, C., Roth, A., Buhmann, H., Molenkamp, L. W., Qi, X.-L. & Zhang, S.-C. Quantum spin hall insulator state in hgte quantum wells. *Science* **318**, 766–770 (2007).

[119] Koshino, M. & Ando, T. Transport in bilayer graphene: Calculations within a self-consistent born approximation. *Physical Review B* **73**, 245403 (2006).

[120] Kretinin, A. V., Cao, Y., Tu, J. S., Yu, G. L., Jalil, R., Novoselov, K. S., Haigh, S. J., Gholinia, A., Mishchenko, A., Lozada, M., Georgiou, T., Woods, C. R., Withers, F., Blake, P., Eda, G., Wirsig, A., Hucho, C., Watanabe, K., Taniguchi, T., Geim, A. K. & Gorbachev, R. V. Electronic properties of graphene encapsulated with different two-dimensional atomic crystals. *Nano Letters* **14**, 3270–3276 (2014).

[121] Kubota, Y., Watanabe, K., Tsuda, O. & Taniguchi, T. Deep ultraviolet light-emitting hexagonal boron nitride synthesized at atmospheric pressure. *Science* **317**, 932–934 (2007).

[122] Landgraf, W., Shallcross, S., Türschmann, K., Weckbecker, D. & Pankratov, O. Electronic structure of twisted graphene flakes. *Physical Review B* **87**, 075433 (2013).

[123] Latil, S. & Henrard, L. Charge carriers in few-layer graphene films. *Phys. Rev. Lett.* **97**, 036803 (2006).

[124] Lee, D., Riedl, C., Beringer, T., Castro Neto, A., von Klitzing, K., Starke, U. & Smet, J. Quantum hall effect in twisted bilayer graphene. *Phys. Rev. Lett.* **107**, 216602 (2011).

[125] Lee, E. J. H., Balasubramanian, K., Weitz, R. T., Burghard, M. & Kern, K. Contact and edge effects in graphene devices. *Nat Nano* **3**, 486–490 (2008).

[126] Lee, P. A. & Ramakrishnan, T. V. Disordered electronic systems. *Rev. Mod. Phys.* **57**, 287–337 (1985).

[127] Li, G. & Andrei, E. Y. Observation of landau levels of dirac fermions in graphite. *Nature Physics* **3**, 623–627 (2007).

[128] Li, G., Luican, A. & Andrei, E. Y. Scanning tunneling spectroscopy of graphene. *Available at http://arxiv.org/abs/0803.4016v1* (2009).

[129] Li, G., Luican, A., Dos Santos, J. L., Neto, A. C., Reina, A., Kong, J. & Andrei, E. Observation of van hove singularities in twisted graphene layers. *Nature Physics* **6**, 109–113 (2009).

[130] Li, X., Wang, X., Zhang, L., Lee, S. & Dai, H. Chemically derived, ultrasmooth graphene nanoribbon semiconductors. *Science* **319**, 1229–1232 (2008).

[131] Lindner, N. H., Berg, E., Refael, G. & Stern, A. Fractionalizing majorana fermions: Non-abelian statistics on the edges of abelian quantum hall states. *Phys. Rev. X* **2**, 041002– (2012).

[132] Liu, L., Feng, Y. P. & Shen, Z. X. Structural and electronic properties of h-bn. *Phys. Rev. B* **68**, 104102– (2003).

[133] Lopes dos Santos, J., Peres, N. & Castro Neto, A. Continuum model of the twisted graphene bilayer. *Phys. Rev. B* **86**, 155449 (2012).

[134] Lopes dos Santos, J. M. B., Peres, N. M. R. & Castro Neto, a. H. Graphene bilayer with a twist: Electronic structure. *Physical Review Letters* **99**, 256802 (2007).

[135] Luican, A., Li, G., Reina, A., Kong, J., Nair, R., Novoselov, K., Geim, A. & Andrei, E. Single-layer behavior and its breakdown in twisted graphene layers. *Physical Review Letters* **106**, 126802 (2011).

[136] Luryi, S. Quantum capacitance devices. *Applied Physics Letters* **52**, 501–503 (1988).

[137] MacDonald, A. H. Landau-level subband structure of electrons on a square lattice. *Phys. Rev. B* **28**, 6713–6717 (1983).

[138] Maher, P., Dean, C. R., Young, A. F., Taniguchi, T., Watanabe, K., Shepard, K. L., Hone, J. & Kim, P. Evidence for a spin phase transition at charge neutrality in bilayer graphene. *Nature Physics* **9**, 154–158 (2013).

[139] Maher, P., Wang, L., Gao, Y., Forsythe, C., Taniguchi, T., Watanabe, K., Abanin, D., Papic, Z., Cadden-Zimansky, P., Hone, J., Kim, P. & Dean, C. R. Tunable fractional quantum hall phases in bilayer graphene. *Science* **345**, 61–64 (2014).

[140] Marchenko, D., Varykhalov, A., Scholz, M., Bihlmayer, G., Rashba, E., Rybkin, A., Shikin, A. & Rader, O. Giant Rashba splitting in graphene due to hybridization with gold. *Nature Communications* **3**, 1232 (2012).

[141] Martin, J., Akerman, N., Ulbricht, G., Lohmann, T., Smet, J. H., von Klitzing, K. & Yacoby, A. Observation of electron-hole puddles in graphene using a scanning single-electron transistor. *Nature Physics* **4**, 144–148 (2008).

[142] Mayorov, A. S., Elias, D. C., Mukhin, I. S., Morozov, S. V., Ponomarenko, L. A., Novoselov, K. S., Geim, A. K. & Gorbachev, R. V. How close can one approach the dirac point in graphene experimentally? *Nano Letters* **12**, 4629–4634 (2012).

[143] Mazo, V., Huang, C.-W., Shimshoni, E., Carr, S. T. & Fertig, H. A. Superfluid-insulator transition of quantum hall domain walls in bilayer graphene. *ArXiv e-prints* (2013).

[144] McCann, E. Asymmetry gap in the electronic band structure of bilayer graphene. *Phys. Rev. B* **74,**, 161403 (2006).

[145] McCann, E. & Fal'ko, V. I. Landau-level degeneracy and quantum hall effect in a graphite bilayer. *Phys. Rev. Lett.* **96**, 086805 (2006).

[146] McChesney, J. L., Bostwick, A., Ohta, T., Seyller, T., Horn, K., González, J. & Rotenberg, E. Extended van hove singularity and superconducting instability in doped graphene. *Phys. Rev. Lett.* **104**, 136803 (2010).

[147] Mele, E. J. Commensuration and interlayer coherence in twisted bilayer graphene. *Physical Review B* **81**, 161405 (2010).

[148] Mele, E. J. Band symmetries and singularities in twisted multilayer graphene. *Physical Review B* **84**, 235439 (2011).

[149] Melinte, S., Berciu, M., Zhou, C., Tutuc, E., Papadakis, S. J., Harrison, C., De Poortere, E. P., Wu, M., Chaikin, P. M., Shayegan, M., Bhatt, R. N. & Register, R. A. Laterally modulated 2D electron system in the extreme quantum limit. *Phys. Rev. Lett.* **92**, 036802– (2004).

[150] Meyer, J. C., Geim, A. K., Katsnelson, M. I., Novoselov, K. S., Booth, T. J. & Roth, S. The structure of suspended graphene sheets. *Nature* **446**, 60–63 (2007).

[151] Miller, D. L., Kubista, K. D., Rutter, G. M., Ruan, M., de Heer, W. A., Kindermann, M., First, P. N. & Stroscio, J. A. Real-space mapping of magnetically quantized graphene states. *Nature Physics* **6**, 811–817 (2010).

[152] Min, H., Bistritzer, R., Su, J.-J. & MacDonald, A. H. Room-temperature superfluidity in graphene bilayers. *Phys. Rev. B* **78**, 121401 (2008).

[153] Min, H., Hill, J. E., Sinitsyn, N. A., Sahu, B. R., Kleinman, L. & MacDonald, A. H. Intrinsic and Rashba spin-orbit interactions in graphene sheets. *Phys. Rev. B* **74**, 165310 (2006).

[154] Min, H., Sahu, B., Banerjee, S. K. & MacDonald, A. H. Ab initio theory of gate induced gaps in graphene bilayers. *Phys. Rev. B* **75**, 155115– (2007).

[155] Miyake, H., Siviloglou, G., Kennedy, C., Burton, W. & Ketterle, W. Realizing the harper hamiltonian with laser-assisted tunneling in optical lattices. *Phys. Rev. Lett.* **111**, 185302 (2013).

[156] Moon, K., Mori, H., Yang, K., Girvin, S. M., MacDonald, A. H., Zheng, L., Yoshioka, D. & Zhang, S.-C. Spontaneous interlayer coherence in double-layer quantum Hall systems: Charged vortices and kosterlitz-thouless phase transitions. *Phys. Rev. B* **51**, 5138 (1995).

[157] Moon, P. & Koshino, M. Energy spectrum and quantum hall effect in twisted bilayer graphene. *Phys. Rev. B* **85**, 195458– (2012).

[158] Mourik, V., Zuo, K., Frolov, S. M., Plissard, S. R., Bakkers, E. P. A. M. & Kouwenhoven, L. P. Signatures of majorana fermions in hybrid superconductor-semiconductor nanowire devices. *Science* **336**, 1003–1007 (2012).

[159] Murakami, S., Nagaosa, N. & Zhang, S.-C. Dissipationless quantum spin current at room temperature. *Science* **301**, 1348–1351 (2003).

[160] Murakami, S., Nagaosa, N. & Zhang, S.-C. Spin-hall insulator. *Phys. Rev. Lett.* **93**, 156804– (2004).

[161] Nadj-Perge, S., Drozdov, I. K., Li, J., Chen, H., Jeon, S., Seo, J., MacDonald, A. H., Bernevig, B. A. & Yazdani, A. Observation of majorana fermions in ferromagnetic atomic chains on a superconductor. *Science* **346**, 602–607 (2014).

[162] Nandi, D., Finck, A., Eisenstein, J., Pfeiffer, L. & West, K. Exciton condensation and perfect coulomb drag. *Nature* **488**, 481–484 (2012).

[163] Nandkishore, R., Levitov, L. S. & Chubukov, A. V. Chiral superconductivity from repulsive interactions in doped graphene. *Nat Phys* **8**, 158–163 (2012).

[164] Nayak, C., Simon, S. H., Stern, A., Freedman, M. & Das Sarma, S. Non-abelian anyons and topological quantum computation. *Rev. Mod. Phys.* **80**, 1083–1159 (2008).

[165] Nicks, L., Nehl, F. & Chambers, M. Recovering flake graphite from steelmaking kish. *JOM* **47**, 48–51 (1995).

[166] Nomura, K. & MacDonald, A. H. Quantum hall ferromagnetism in graphene. *Physical Review Letters* **96**, 256602 (2006).

[167] Nomura, K., Ryu, S. & Lee, D.-H. Field-induced kosterlitz-thouless transition in the n=0 landau level of graphene. *Physical Review Letters* **103**, 216801 (2009).

[168] Novoselov, K. S., Geim, A. K., Morozov, S. V., Jiang, D., Katsnelson, M. I., Grigorieva, I. V., Dubonos, S. V. & Firsov, A. A. Two-dimensional gas of massless Dirac fermions in graphene. *Nature* **438**, 197 (2005).

[169] Novoselov, K. S., Geim, A. K., Morozov, S. V., Jiang, D., Zhang, Y., Dubonos, S. V., Grigorieva, I. V. & Firsov, A. A. Electric field effect in atomically thin carbon films. *Science* **306**, 666–669 (2004).

[170] Novoselov, K. S., Jiang, Z., Zhang, Y., Morozov, S. V., Stormer, H. L., Zeitler, U., Maan, J. C., Boebinger, G. S., Kim, P. & Geim, A. K. Room-temperature quantum hall effect in graphene. *Science* **315**, 1379–1379 (2007).

[171] Novoselov, K. S., McCann, E., Morozov, S. V., Fal'ko, V. I., Katsnelson, M. I., Zeitler, U., Jiang, D., Schedin, F. & Geim, A. K. Unconventional quantum hall effect and berry's phase of 2 pi in bilayer graphene. *Nature Physics* **2**, 177–180 (2006).

[172] Ohta, T., Bostwick, A., Seyller, T., Horn, K. & Rotenberg, E. Controlling the electronic structure of bilayer graphene. *Science* **313**, 951–954 (2006).

[173] Ohta, T., Robinson, J. T., Feibelman, P. J., Bostwick, A., Rotenberg, E. & Beechem, T. E. Evidence for interlayer coupling and moiré periodic potentials in twisted bilayer graphene. *Physical Review Letters* **109**, 186807 (2012).

[174] Oostinga, J. B., Heersche, H. B., Liu, X., Morpurgo, A. F. & Vandersypen, L. M. K. Gate-induced insulating state in bilayer graphene devices. *Nature Materials* **7**, 151–157 (2008).

[175] Ostrovsky, P. M., Gornyi, I. V. & Mirlin, A. D. Theory of anomalous quantum Hall effects in graphene. *Phys. Rev. B* **77**, 195430– (2008).

[176] Park, C.-H., Yang, L., Son, Y.-W., Cohen, M. L. & Louie, S. G. Anisotropic behaviours of massless dirac fermions in graphene under periodic potentials. *Nature Physics* **4**, 213–217 (2008).

[177] Park, C.-H., Yang, L., Son, Y.-W., Cohen, M. L. & Louie, S. G. New generation of massless dirac fermions in graphene under external periodic potentials. *Phys. Rev. Lett.* **101**, 126804– (2008).

[178] Petrone, N., Dean, C. R., Meric, I., van der Zande, A. M., Huang, P. Y., Wang, L., Muller, D., Shepard, K. L. & Hone, J. Chemical vapor deposition-derived graphene with electrical performance of exfoliated graphene. *Nano Letters* **12**, 2751–2756 (2012).

[179] Petta, J. R., Johnson, A. C., Taylor, J. M., Laird, E. A., Yacoby, A., Lukin, M. D., Marcus, C. M., Hanson, M. P. & Gossard, A. C. Coherent manipulation of coupled electron spins in semiconductor quantum dots. *Science* **309**, 2180–2184 (2005).

[180] Pfeiffer, L. N. Devices including graphene layers epitaxially grown on single crystal substrates (2009). US Patent 7,619,257.

[181] Ponomarenko, L. A., Geim, A. K., Zhukov, A. A., Jalil, R., Morozov, S. V., Novoselov, K. S., Grigorieva, I. V., Hill, E. H., Cheianov, V. V., Fal/'ko, V. I., Watanabe, K., Taniguchi, T. & Gorbachev, R. V. Tunable metal-insulator transition in double-layer graphene heterostructures. *Nature Physics* **7**, 958–961 (2011).

[182] Ponomarenko, L. A., Gorbachev, R. V., Yu, G. L., Elias, D. C., Jalil, R., Patel, A. A., Mishchenko, A., Mayorov, A. S., Woods, C. R., Wallbank, J. R., Mucha-Kruczynski, M., Piot, B. A., Potemski, M., Grigorieva, I. V., Novoselov, K. S., Guinea, F., Fal/'ko, V. I. & Geim, A. K. Cloning of dirac fermions in graphene superlattices. *Nature* **497**, 594–597 (2013).

[183] Qi, X.-L. & Zhang, S.-C. Topological insulators and superconductors. *Rev. Mod. Phys.* **83**, 1057–1110 (2011).

[184] Reina, A., Jia, X., Ho, J., Nezich, D., Son, H., Bulovic, V., Dresselhaus, M. S. & Kong, J. Large area, few-layer graphene films on arbitrary substrates by chemical vapor deposition. *Nano Letters* **9**, 30–35 (2009).

[185] Rodriguez-Vega, M., Fischer, J., Das Sarma, S. & Rossi, E. Ground state of graphene heterostructures in the presence of random charged impurities. *Phys. Rev. B* **90**, 035406 (2014).

[186] Rong, Z. & Kuiper, P. Electronic effects in scanning tunneling microscopy: Moiré pattern on a graphite surface. *Phys. Rev. B* **48**, 17427–17431 (1993).

[187] Roth, A., Brüe, C., Buhmann, H., Molenkamp, L. W., Maciejko, J., Qi, X.-L. & Zhang, S.-C. Nonlocal transport in the quantum spin Hall state. *Science* **325**, 294–297 (2009).

[188] Rycerz, A., Tworzydlo, J. & Beenakker, C. W. J. Valley filter and valley valve in graphene. *Nature Physics* **3**, 172–175 (2007).

[189] Ryu, S., Schnyder, A. P., Furusaki, A. & Ludwig, A. W. W. Topological insulators and superconductors: tenfold way and dimensional hierarchy. *New Journal of Physics* **12**, 065010– (2010).

[190] Sachs, B., Wehling, T. O., Katsnelson, M. I. & Lichtenstein, A. I. Adhesion and electronic structure of graphene on hexagonal boron nitride substrates. *Phys. Rev. B* **84**, 195414 (2011).

[191] San-Jose, P. & Prada, E. Helical networks in twisted bilayer graphene under interlayer bias. *Phys. Rev. B* **88**, 121408 (2013).

[192] Sanchez-Yamagishi, J. D., Taychatanapat, T., Watanabe, K., Taniguchi, T., Yacoby, A. & Jarillo-Herrero, P. Quantum hall effect, screening, and layer-polarized insulating states in twisted bilayer graphene. *Phys. Rev. Lett.* **108**, 076601– (2012).

[193] Sato, M. & Fujimoto, S. Topological phases of noncentrosymmetric superconductors: Edge states, majorana fermions, and non-abelian statistics. *Phys. Rev. B* **79**, 094504 (2009).

[194] Sau, J. D., Lutchyn, R. M., Tewari, S. & Das Sarma, S. Generic new platform for topological quantum computation using semiconductor heterostructures. *Phys. Rev. Lett.* **104**, 040502 (2010).

[195] Schlösser, T., Ensslin, K., Kotthaus, J. P. & Holland, M. Landau subbands generated by a lateral electrostatic superlattice - chasing the hofstadter butterfly. *Semiconductor Science Technology* **11**, 1582–1585 (1996).

[196] Schmidt, H. *et al.* Tunable graphene system with two decoupled monolayers. *Appl. Phys. Lett.* **93**, 172108 (2008).

[197] Schmidt, H., Lüdtke, T., Barthold, P. & Haug, R. J. Mobilities and scattering times in decoupled graphene monolayers. *Physical Review B* **81**, 121403 (2010).

[198] Schmidt, H., Lüdtke, T., Barthold, P. & Haug, R. Temperature dependent measurements on two decoupled graphene monolayers. *Physica E: Low-dimensional Systems and Nanostructures* **42**, 699–702 (2010).

[199] Schwierz, F. Graphene transistors. *Nat Nano* **5**, 487–496 (2010).

[200] Semenoff, G. W. Condensed-matter simulation of a three-dimensional anomaly. *Phys. Rev. Lett.* **53**, 2449 (1984).

[201] Shallcross, S., Sharma, S., Kandelaki, E. & Pankratov, O. A. Electronic structure of turbostratic graphene. *Physical Review B* **81**, 165105 (2010).

[202] Shallcross, S., Sharma, S. & Pankratov, O. Emergent momentum scale, localization, and van hove singularities in the graphene twist bilayer. *Physical Review B* **87**, 245403 (2013).

[203] Shallcross, S., Sharma, S. & Pankratov, O. A. Quantum interference at the twist boundary in graphene. *Physical Review Letters* **101**, 056803 (2008).

[204] Shibata, N. & Nomura, K. Coupled charge and valley excitations in graphene quantum Hall ferromagnets. *Phys. Rev. B* **77**, 235426 (2008).

[205] Shitade, A., Katsura, H., KuneÅ¡, J., Qi, X.-L., Zhang, S.-C. & Nagaosa, N. Quantum spin Hall effect in a transition metal oxide Na_2IrO_3. *Phys. Rev. Lett.* **102**, 256403– (2009).

[206] Shklovskii, B. I. & Efros, A. L. *Electronic Properties of Doped Semiconductors* (Springer, New York, 1984).

[207] Sinova, J., Culcer, D., Niu, Q., Sinitsyn, N. A., Jungwirth, T. & MacDonald, A. H. Universal intrinsic spin hall effect. *Phys. Rev. Lett.* **92**, 126603 (2004).

[208] Slawinska, J., Zasada, I. & Klusek, Z. Energy gap tuning in graphene on hexagonal boron nitride bilayer system. *Phys. Rev. B* **81**, 155433– (2010).

[209] Snoke, D., Denev, S., Liu, Y., Pfeiffer, L. & West, K. Long-range transport in excitonic dark states in coupled quantum wells. *Nature* **418**, 754–757 (2002).

[210] Song, J. C. W., Shytov, A. V. & Levitov, L. S. Engineering interaction effects and gap opening in graphene superlattices. *ArXiv e-prints* (2012).

[211] Spielman, I. B., Eisenstein, J. P., Pfeiffer, L. N. & West, K. W. Resonantly enhanced tunneling in a double layer quantum hall ferromagnet. *Physical Review Letters* **84**, 5808–5811 (2000).

[212] Sprinkle, M., Siegel, D., Hu, Y., Hicks, J., Tejeda, A., Taleb-Ibrahimi, A., Le FÃšvre, P., Bertran, F., Vizzini, S., Enriquez, H., Chiang, S., Soukiassian, P., Berger, C., de Heer, W. A., Lanzara, A. & Conrad, E. H. First direct observation of a nearly ideal graphene band structure. *Physical Review Letters* **103**, 226803 (2009).

[213] Streda, P. Quantised hall effect in a two-dimensional periodic potential. *J. Phys. C: Solid State Phys.* **15**, L1299 (1982).

[214] Suárez Morell, E. *et al.* Flat bands in slightly twisted bilayer graphene: Tight-binding calculations. *Phys. Rev. B* **82**, 121407 (2010).

[215] Taychatanapat, T., Watanabe, K., Taniguchi, T. & Jarillo-Herrero, P. Quantum hall effect and landau-level crossing of dirac fermions in trilayer graphene. *Nature Physics* **7**, 621–625 (2011).

[216] Taychatanapat, T. & Jarillo-Herrero, P. Electronic transport in dual-gated bilayer graphene at large displacement fields. *Phys. Rev. Lett.* **105**, 166601– (2010).

[217] Thouless, D. J., Kohmoto, M., Nightingale, M. P. & den Nijs, M. Quantized Hall conductance in a two-dimensional periodic potential. *Phys. Rev. Lett.* **49**, 405 (1982).

[218] Toke, C., Lammert, P. E., Crespi, V. H. & Jain, J. K. Fractional quantum Hall effect in graphene. *Phys. Rev. B* **74**, 235417 (2006).

[219] Trambly de Laissardière, G., Mayou, D. & Magaud, L. Localization of dirac electrons in rotated graphene bilayers. *Nano Letters* **10**, 804–808 (2010).

[220] Tsu, R. *Superlattice to nanoelectronics* (Elsevier, 2010).

[221] Vaezi, A. Fractional topological superconductor with fractionalized majorana fermions. *Physical Review B* **87**, 035132 (2013).

[222] Wallace, P. R. The band theory of graphite. *Phys. Rev.* **71**, 622– (1947).

[223] Wallbank, J. R., Patel, A. A., Mucha-Kruczynski, M., Geim, A. K. & Fal'ko, V. I. Generic miniband structure of graphene on a hexagonal substrate. *arXiv:1211.4711* (2012).

[224] Wang, L., Meric, I., Huang, P. Y., Gao, Q., Gao, Y., Tran, H., Taniguchi, T., Watanabe, K., Campos, L. M., Muller, D. A., Guo, J., Kim, P., Hone, J., Shepard, K. L. & Dean, C. R. One-dimensional electrical contact to a two-dimensional material. *Science* **342**, 614–617 (2013).

[225] Wang, Q. H., Kalantar-Zadeh, K., Kis, A., Coleman, J. N. & Strano, M. S. Electronics and optoelectronics of two-dimensional transition metal dichalcogenides. *Nat Nano* **7**, 699–712 (2012).

[226] Wang, Z. F., Liu, F. & Chou, M. Y. Fractal landau-level spectra in twisted bilayer graphene. *Nano Letters* **12**, 3833–3838 (2012).

[227] Wannier, G. H. A result not dependent on rationality for bloch electrons in a magnetic field. *phys. stat. sol. (b)* **88**, 757–765 (1978).

[228] Watanabe, K., Taniguchi, T. & Kanda, H. Direct-bandgap properties and evidence for ultraviolet lasing of hexagonal boron nitride single crystal. *Nature Materials* **3**, 404–409 (2004).

[229] Weitz, R. T., Allen, M. T., Feldman, B. E., Martin, J. & Yacoby, A. Broken-symmetry states in doubly gated suspended bilayer graphene. *Science* **330**, 812–816 (2010).

[230] Woods, C. R., Britnell, L., Eckmann, A., Ma, R. S., Lu, J. C., Guo, H. M., Lin, X., Yu, G. L., Cao, Y., Gorbachev, R. V., Kretinin, A. V., Park, J., Ponomarenko, L. A., Katsnelson, M. I., Gornostyrev, Y. N., Watanabe, K., Taniguchi, T., Casiraghi, C., Gao, H.-J., Geim, A. K. & Novoselov, K. S. Commensurate-incommensurate transition in graphene on hexagonal boron nitride. *Nat Phys* **10**, 451–456 (2014).

[231] Wu, X. S., Li, X. B., Song, Z. M., Berger, C. & de Heer, W. A. Weak antilocalization in epitaxial graphene: Evidence for chiral electrons. *Physical Review Letters* **98**, – (2007).

[232] Wunderlich, J., Kaestner, B., Sinova, J. & Jungwirth, T. Experimental observation of the spin-hall effect in a two-dimensional spin-orbit coupled semiconductor system. *Phys. Rev. Lett.* **94**, 047204 (2005).

[233] Xia, Y., Qian, D., Hsieh, D., Wray, L., Pal, A., Lin, H., Bansil, A., Grauer, D., Hor, Y. S., Cava, R. J. & Hasan, M. Z. Observation of a large-gap topological-insulator class with a single dirac cone on the surface. *Nature Physics* **5**, 398–402 (2009).

[234] Xiao, D., Yao, W. & Niu, Q. Valley-contrasting physics in graphene: Magnetic moment and topological transport. *Physical Review Letters* **99**, 236809 (2007).

[235] Xu, S.-Y., Neupane, M., Liu, C., Zhang, D., Richardella, A., Andrew Wray, L., Alidoust, N., Leandersson, M., Balasubramanian, T., Sanchez-Barriga, J., Rader, O., Landolt, G., Slomski, B., Hugo Dil, J., Osterwalder, J., Chang, T.-R., Jeng, H.-T., Lin, H., Bansil, A., Samarth, N. & Zahid Hasan, M. Hedgehog spin texture and Berry's phase tuning in a magnetic topological insulator. *Nature Physics* **8**, 616–622 (2012).

[236] Xue, J., Sanchez-Yamagishi, J., Bulmash, D., Jacquod, P., Deshpande, A., Watanabe, K., Taniguchi, T., Jarillo-Herrero, P. & LeRoy, B. J. Scanning tunnelling microscopy and spectroscopy of ultra-flat graphene on hexagonal boron nitride. *Nature Materials* **10**, 282–285 (2011).

[237] Yang, K., Das Sarma, S. & MacDonald, A. H. Collective modes and skyrmion excitations in graphene SU(4) quantum Hall ferromagnets. *Phys. Rev. B* **74**, 075423 (2006).

[238] Yang, K., Moon, K., Zheng, L., MacDonald, A. H., Girvin, S. M., Yoshioka, D. & Zhang, S.-C. Quantum ferromagnetism and phase transitions in double-layer quantum Hall systems. *Phys. Rev. Lett.* **72**, 732– (1994).

[239] Yang, L., Park, C.-H., Son, Y.-W., Cohen, M. & Louie, S. Quasiparticle energies and band gaps in graphene nanoribbons. *Phys. Rev. Lett.* **99**, 186801 (2007).

[240] Yankowitz, M., Xue, J., Cormode, D., Sanchez-Yamagishi, J. D., Watanabe, K., Taniguchi, T., Jarillo-Herrero, P., Jacquod, P. & LeRoy, B. J. Emergence of superlattice dirac points in graphene on hexagonal boron nitride. *Nature Physics* **8**, 382–386 (2012).

[241] Yao, Y., Ye, F., Qi, X.-L., Zhang, S.-C. & Fang, Z. Spin-orbit gap of graphene: First-principles calculations. *Phys. Rev. B* **75**, 041401– (2007).

[242] Young, A. F., Dean, C. R., Wang, L., Ren, H., Cadden-Zimansky, P., Watanabe, K., Taniguchi, T., Hone, J., Shepard, K. L. & Kim, P. Spin and valley quantum hall ferromagnetism in graphene. *Nature Physics* **8**, 550–556 (2012).

[243] Young, A. F., Sanchez-Yamagishi, J. D., Hunt, B., Choi, S. H., Watanabe, K., Taniguchi, T., Ashoori, R. C. & Jarillo-Herrero, P. Tunable symmetry breaking and helical edge transport in a graphene quantum spin hall state. *Nature* **505**, 528–532 (2014).

[244] Young, A. F. *Quantum transport in graphene heterostructures.* Ph.D. thesis, Columbia University (2012).

[245] Zhang, C. H. & Joglekar, Y. N. Excitonic condensation of massless fermions in graphene bilayers. *Physical Review B* **77**, 233405 (2008).

[246] Zhang, L., Camacho, J., Cao, H., Chen, Y. P., Khodas, M., Kharzeev, D. E., Tsvelik, A. M., Valla, T. & Zaliznyak, I. A. Breakdown of the N=0 quantum Hall state in graphene: Two insulating regimes. *Phys. Rev. B* **80**, 241412– (2009).

[247] Zhang, L., Zhang, Y., Khodas, M., Valla, T. & Zaliznyak, I. A. Metal to insulator transition on the N=0 Landau level in graphene. *Phys. Rev. Lett.* **105**, 046804– (2010).

[248] Zhang, Y., Jiang, Z., Small, J. P., Purewal, M. S., Tan, Y.-W., Fazlollahi, M., Chudow, J. D., Jaszczak, J. A., Stormer, H. L. & Kim, P. Landau-level splitting in graphene in high magnetic fields. *Phys. Rev. Lett.* **96**, 136806– (2006).

[249] Zhang, Y., Brar, V. W., Girit, C., Zettle, A. & Crommie, M. F. Origin of spatial charge inhomogeneity in graphene. *Nature Physics* **5**, 722 (2009).

[250] Zhang, Y., Tan, Y.-W., Stormer, H. L. & Kim, P. Experimental observation of the quantum Hall effect and berry's phase in graphene. *Nature* **438**, 201 (2005).

[251] Zhang, Y., Tang, T.-T., Girit, C., Hao, Z., Martin, M. C., Zettl, A., Crommie, M. F., Shen, Y. R. & Wang, F. Direct observation of a widely tunable bandgap in bilayer graphene. *Nature* **459**, 820–823 (2009).

[252] Zhao, Y., Cadden-Zimansky, P., Jiang, Z. & Kim, P. Symmetry breaking in the zero-energy Landau level in bilayer graphene. *Phys. Rev. Lett.* **104**, 066801 (2010).

[253] Zhou, S. Y., Gweon, G.-H., Fedorov, A. V., First, P. N., de Heer, W. A., Lee, D.-H., Guinea, F., Castro Neto, A. H. & Lanzara, A. Substrate-induced bandgap opening in epitaxial graphene. *Nature Materials* **6**, 770–775 (2007).

[254] Zomer, P. J., Guimaraes, M. H. D., Brant, J. C., Tombros, N. & van Wees, B. J. Fast pick up technique for high quality heterostructures of bilayer graphene and hexagonal boron nitride. *Applied Physics Letters* **105**, – (2014).